# FLOWABLE FIBROUS CONCRETE FOR THIN PAVEMENT INLAYS

BY

AMANDA CHRISTINE BORDELON

DISSERTATION

Submitted in partial fulfillment of the requirements
for the degree of Doctor of Philosophy in Civil Engineering
in the Graduate College of the
University of Illinois at Urbana-Champaign, 2011

Urbana, Illinois

Doctoral Committee:

Associate Professor Jeffery R. Roesler, Chair and Director of Research
Professor Imad Al-Qadi
Professor Leslie Struble
Professor David Lange

## ABSTRACT

Synthetic fibers within a flowable fibrous concrete (FFC) mixture were characterized by relating their spatial distribution and orientations, determined from x-ray computed tomography (CT), with the measured toughness or fracture energy response of a FFC specimen. This new type of concrete, FFC, was developed to provide a workable, flowable mixture that could be utilized to rapidly construct thin concrete pavement inlays. A full-scale demonstration project verified the feasibility of constructing the FFC as a 5 cm thick inlay bonded to an existing asphalt pavement. In order to quantify this new FFC material, flexural beam properties were measured to determine the material's toughness and fracture properties. Unnotched beams of the FFC material verified that the measured nominal strength and measured toughness increased as the specimen size was reduced. A high energy x-ray CT and image processing technique were utilized to identify the synthetic fibers in the hardened FFC through contrast and shape-based filtering from the 3D images. The filtered images showed the number of fibers across any given vertical plane in a FFC specimen was directly correlated with the measured total fracture energy. Fibers located near a surface (cast or mold) within a boundary zone size estimated at ¼ to ½ of the fiber length, were found to have a higher alignment parallel to the surface with a lower number of fibers in this boundary zone, than the interior of the specimen. Fiber alignment in the FFC fracture beams had a less significant contribution, relative to the number of fibers, on the measured total fracture energy. For the FFC mixture, volumetric segregation of fibers occurred within a 15 cm cast beam, based on the analysis of the CT images. A finite element analysis using a tri-linear softening model successfully simulated the behavior of FFC for larger (15 cm) notched

beam specimens and for some smaller (5 cm) beam specimens. However, a deflection hardening response occurred in some of these other 5 cm beam FFC specimens due to the higher local fiber content, for which the tri-linear softening modeling approach could not accurately simulate this post-cracking response.

To my parents for their constant support

## ACKNOWLEDGEMENTS

I would like to thank my research defense committee for their advice and guidance over the years. I thank the Federal Highway Administration and National Highway Institute through the Dwight D. Eisenhower Graduate Fellowship, the Illinois Chapter of the American Concrete Pavement Association, and the Illinois Department of Transportation for funding this doctoral research.

The donations and recommendations on fiber usage were from Klaus Alex-Rieder and Kumar Ranganathan at W.R. Grace Construction Products and Antonio Gallovich at Maccaferri. I thank Meredith Price at BitPlane Scientific Software and Dr. Robert Shephard for assistance in learning the IMARIS software.

I thank the other transportation graduate students who assisted in construction of the full-scale project in Rantoul, predominantly Alex Brand with all the mixture optimization testing assistance. I also thank Dr. Gregorz Banas for assisting on small-scale testing in the laboratory.

I want to thank Leilei Yin and Darren Stevenson at Beckman Institute along with Dr. Balasingam Muhunthan and Kalehiwot Nega at Washington State University for assistance in setting up and running the x-ray CT scanning.

I thank the encouragement and mentoring from my colleagues and friends: Dr. Eshan Dave, Dr. Matthew George, Dr. Kerry Hall, and Dr. Jacob Hiller.

# TABLE OF CONTENTS

## LIST OF FIGURES

# LIST OF TABLES

# CHAPTER 1. INTRODUCTION

## 1.1. Motivation

Rehabilitation and repair of existing pavements are the leading directions for current infrastructure improvements, rather than construction of new or total reconstruction of existing pavement structures. A new pavement structure can lead to a longer performance life; however with limited resources, many agencies require short-term overlays which extend the pavement service life by 10 to 15 years. Asphalt concrete surfaces are historically the choice for thin overlays of existing pavement structures due to their rapid placement, ability to construct in a thin layer, and ability to open for traffic shortly after placement. Likewise, several recent projects and studies have experimented with constructing thin portland cement concrete overlays with similar objectives to the asphalt overlays. With the concrete material as a thin overlay, the design service life is dependent on several important factors such as interlayer bond, material strength and fracture properties, slab size, slab thickness, and underlying material condition. The service life of a thin bonded concrete overlay or inlay (a thin layer cast over a milled asphalt section) is dependent on the concrete-asphalt interface bond condition. Concrete overlays (5 cm thick) have been found to exhibit large crack spacing and large crack widths in the presence of debonding (Carlswärd 2006). However, in the presence of a debonded interface, Carlswärd also found that macro-fiber-reinforced concrete (FRC) mixtures reduced these crack widths. Thus, thin concrete overlays or inlays should include FRC in order to match or exceed the life of existing asphalt overlays. There is motivation to further optimize and design a thin concrete inlay bonded to an underlying asphalt pavement, which can be placed rapidly, and have reduced crack widths through

high FRC toughness. The research presented describes the development and characterization of such a mixture, referred to as flowable fibrous concrete (FFC) illustrated in Figure 1-1, which is an unique combination of other current concrete research concepts, i.e., self-consolidating concrete, FRC, and ultra-thin whitetopping.

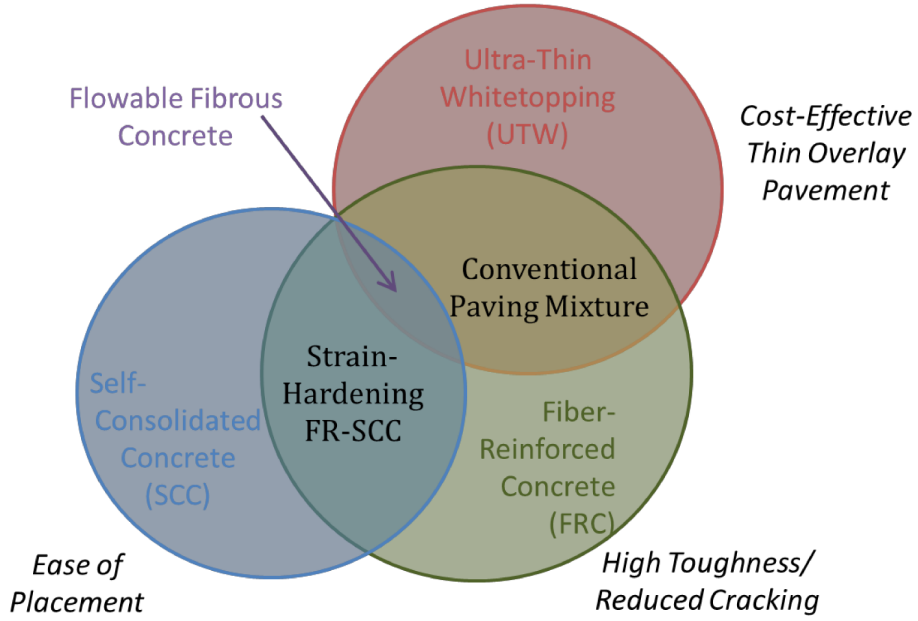


**Figure 1-1 Diagram illustrating the combination of research technologies (UTW, SCC, and FRC) used to classify flowable fibrous concrete (FFC).**

### 1.1.1. Fiber-Reinforcement Benefits

The benefits of FRC for thin concrete surfaces are known to increase the material toughness, increase the load carrying capacity of slabs, minimize spalling of joints and cracks, and reduce the rate of crack growth (Falkner et al. 1995; Li 2003b; Beckett 2004; Roesler et al. 2004; Roesler et al. 2006; Roesler et al. 2008). The post-cracking toughness performance for macro-fiber-reinforced concrete mixtures was found to be linked with reduced crack widths in 5 cm thick 2.5 m long beams (Carlswärd 2006) and increased slab load carrying capacity (Altoubat et al. 2008). Recent accelerated pavement testing of 9 cm thick 1.8 m square slabs at 0.38% volume fraction synthetic FRC demonstrated

reduced deflection magnitudes, reduced deflection variability, lowered percentage of slabs cracked for the same load repetitions, and slower crack deterioration rates compared to plain un-reinforced concrete slabs (Cervantes and Roesler 2009; Bordelon and Roesler 2011). Similar reductions in deflection and extended load repetitions until failure have also been achieved in the laboratory with strain-hardening concrete for un-bonded overlay bridge decks (Zhang and Li 2002).

For a thin concrete overlay or inlay, the length of fiber, volume fraction, and concrete mixture workability impact how the fibers orient themselves within the slab height. These impacting factors were studied for the development of the FFC mixture in terms of the effect on post-cracking performance. Different fiber sizes and types were compared for the effect on flow and measured toughness. For example, a hybrid fiber mixture consisting of two fiber lengths could have similar flow effects as aggregate blending (Nehdi and Ladanchuk 2004), as well as reduced crack widths at the micro and macro-scales (Bentur and Mindess 1990; Rossi 1997).

### 1.1.2. Concrete Overlay Thickness

Thin concrete pavements (less than 7.5 cm) have been constructed in the past, e.g., slabs of 6.3 cm height with 4.6 m slab lengths were constructed as part of the AASHO road test (Highway Research Board 1961). Ultra-thin whitetopping (UTW) technology has gained recent popularity as a thin concrete overlay bonded to an existing asphalt pavement (Gucunski 1998; Mack et al. 1998; Harrington 2008) as illustrated Figure 1-2. High shear stresses exist at the concrete-asphalt interface due to large surface-to-volume ratios in thin pavements (Mack et al. 1997; Harrington 2008). With UTW, the magnitude of the interface stresses was traditionally reduced by decreasing the slab size to roughly 1.2 to

1.8 m (American Concrete Pavement Association 1998). Still, challenges such as rapid deterioration rates of thin un-reinforced concrete slabs and an intense joint saw-cutting requirement (potentially 0.6 x 0.6 m slab sizes for a 5 cm thick pavement) have prohibited widespread acceptance of thin overlay technologies. By implementing fiber-reinforcement, the fracture energy (measured from a notched specimen) and toughness (measured from an unnotched specimen) significantly increase, as shown in the UTW pavement mixture examples listed in Table 1-1. Fresh properties and strength or initial fracture parameters listed in Table 1-1 were influenced primarily by the concrete mixture proportioning and not the fiber content. Increasing the dosage of fiber reinforcement, for the same fiber type and for similar concrete mixture strengths, results in an increase in the post-cracking performance ($R_{150}^{150}$ or $G_{FRC}$). Current performance-based FRC design for UTW pavements allows for a pavement thickness reduction based on the measured mixture residual strength properties (Roesler et al. 2008b). A residual strength ratio $R_{150}^{150}$ of 20 percent determined from the standard flexural beam test (ASTM Standard C1609 2007) is used by the Illinois Department of Transportation as the recommended minimum for FRC overlay designs. By increasing the amount of macro-fibers in a paving mixture, a reduction in the required pavement thickness is anticipated, with the reduction related to the residual strength ratio from a flexural beam toughness test. Typically for thin concrete pavements, a reduction in thickness brings down the total cost for construction materials and makes thin concrete overlays/inlays economically competitive. As the concrete slab thickness is reduced to 5 cm, a mixture with a higher macro-fiber content is required to establish the minimum recommended residual strength ratio.

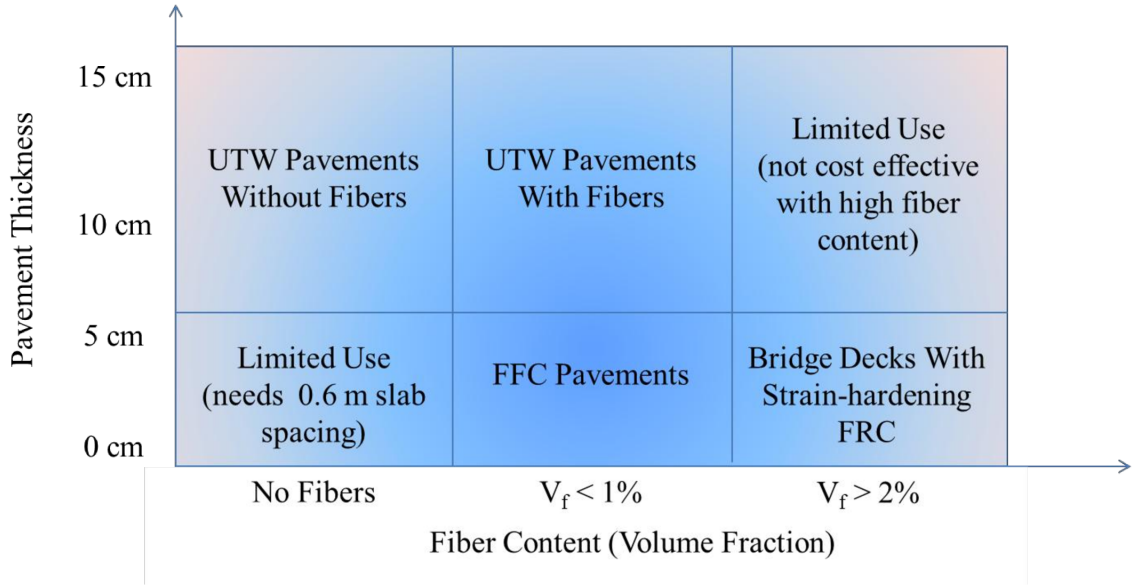


**Figure 1-2 Chart of thin concrete pavement applications containing various macro-fiber contents.**

**Table 1-1 Mixture Designs and Properties for Thin Concrete Overlays**

| | | Thin Concrete Overlay Mixtures† | | | |
|---|---|---|---|---|---|
| Volume Fraction of Fibers | | 0.0% | 0.2% | 0.3% | 0.4% |
| Mixture Proportions | | | | | |
| Cement | $kg/m^3$ | 307 | 257 | 307 | 310 |
| Fly Ash | $kg/m^3$ | 83 | 80 | 83 | 84 |
| Water | $kg/m^3$ | 159 | 132 | 159 | 161 |
| Coarse Aggregate* | $kg/m^3$ | 1174 | 1145 | 1176 | 1186 |
| Fine Aggregate | $kg/m^3$ | 596 | 730 | 597 | 602 |
| 40 mm Macro-Fiber | $kg/m^3$ | 0.0 | 1.8 | 2.4 | 3.6 |
| AEA | $ml/m^3$ | 400 | 0 | 100 | 101 |
| Water Reducer | $ml/m^3$ | 600 | 808 | 601 | 0 |
| HRWR | $ml/m^3$ | 0 | 0 | 0 | 606 |
| w/cm ratio | - | 0.41 | 0.39 | 0.41 | 0.41 |
| Fresh Properties | | | | | |
| Vertical Slump | cm | 1.3 | NA | 1.2 | 2.5 |
| Flow Diameter | mm | - | - | - | - |
| Unit Weight | $kg/m^3$ | 2150 | NA | 2287 | 2313 |
| Air Content | % | 10.3 | NA | 5.3 | 4.4 |
| Hardened Strengths | | | | | |
| Test Age | days | 14 | 28 | 14 | 28 |
| Compressive | MPa | 22.6 | 36.0 | 34.8 | 39.7 |
| Split-Tensile | MPa | 2.29 | 3.95 | 3.81 | 4.07 |
| MOR | MPa | NA | 5.87 | 3.14 | NA |
| $R_{150}^{150}$ | % | 0 | NA | 18 | NA |
| Fracture Properties (15 cm SEN[B]) | | | | | |
| $P_c$ | kN | 2.36 | 3.94 | 2.33 | 4.34 |
| $K_{IC}$ | $MPa\text{-}m^{1/2}$ | 0.86 | 1.14 | 0.82 | 1.33 |
| $CTOD_c$ | mm | 0.031 | 0.015 | 0.025 | 0.024 |
| $G_f$ | N/m | 43.7 | 46.9 | 33.8 | 65.2 |
| $G_F$ | N/m | 60.5 | - | - | - |
| $G_{FRC}$ | N/m | - | 1137 | 1715 | 3553 |

† Example concrete overlay mixtures are restated from Roesler et al. (2008b).
* Traditional overlay mixtures have a nominal maximum aggregate size (NMAS) of 19 mm.
Strength and fracture properties are an average of two specimens.
NA= not available.

### 1.1.3. Fiber Content

Fiber-reinforced concrete (FRC) has primarily been considered a feasible option for thinner (38 to 50 mm) overlay projects such as for bridge decks (Zhang and Li 2002;

Carlswärd 2006; Kunieda and Rokugo 2006) as shown in Figure 1-2. A strain-hardening post-cracking performance demonstrates a higher flexural strength as the concrete exhibits multiple cracking (Naaman and Reinhardt 2006). This type of strain-hardening concrete is typically produced by using fiber volume contents greater than 2 percent along with a mortar-based (no coarse aggregate) mixture (Li 2003; Benson et al. 2005; Wille et al. 2011). This strain-hardening material may be ideal for improving the toughness performance of a bridge decks; however, the material cost associated with constructing pavements with this strain-hardening material is not economically feasible, especially for thicker pavements (Figure 1-2). The FFC mixture was designed in this research study to be economical with a fiber volume fraction similar or slightly higher than found with existing UTW pavements, but with superior toughness induced by more aligned fibers in a 5 cm thick concrete slab.

A challenge of increasing the dosage of fibers in the concrete mixture is this can lead to fiber clumping, reduced workability, non-uniform dispersion, and poor consolidation. A reduction and higher variation in toughness performance are expected to occur due to poor consolidation. Thus to improve consolidation, self-consolidating concrete (SCC) technology developed for highly reinforced concrete structures was implemented for this FFC research. SCC mixture designs often consist of higher cementitious contents (Kosaka et al. 1996; Assaad et al. 2003; Nehdi and Ladanchuk 2004; Wang et al. 2005; Carlswärd 2006) and improved aggregate blending (Hu 2005; Koehler 2007; Shen 2007) to improve workability of a concrete mixture. By utilizing a more flowable concrete mixture in combination with the addition of fibers (volume fraction < 1%), the likelihood of voids from poor compaction/consolidation efforts are expected to be reduced and the

toughness performance can be maintained. The additional benefits of using a flowable concrete material are a rapid placement during the inlay construction, with minimal consolidation energy and improved contact of the concrete on the existing asphalt interface.

## 1.2. Goals and Methodology

### 1.2.1. Flowable Fibrous Concrete Mixture

Based on past research experience using synthetic macro-fibers in concrete (Roesler et al. 2008b; Bordelon and Roesler 2009; Bordelon et al. 2009), it was estimated that a required residual strength ratio of 50 percent would provide adequate fracture performance for a 10 to 15 year thin inlay pavement service life. This residual strength ratio would be achievable with a fiber volume fraction of 0.5 percent. Flexural unnotched and fracture notched beam tests are described in Chapter 2 and were used to quantify the toughness performance and fracture properties of the FFC mixture, respectively. A suitable FFC mixture was developed, as described in Chapter 2, to contain fiber contents up to 0.5 percent along with mixture proportioning for improved consolidation and higher workability for rapid placement. Alternative synthetic fibers, either individual types of macro-fibers or a hybrid of macro- and micro-fibers are studied, as presented in Chapter 2, for optimal workability and toughness performance. Mixture proportioning techniques developed for SCC, such as increased cementitious material content and improved aggregate gradation, are used to increase the flow of the FFC material. A full-scale inlay pavement project was constructed with the FFC mixture. Workability was characterized based on an inverted slump flow test, commonly used to

classify SCC, along with the casting of the full-scale demonstration project to verify the fresh concrete material properties in the field and to understand construction challenges associated with the FFC material.

### 1.2.2. FRC Inlay Representative Specimen Size

The current standard flexural (unnotched) (ASTM Standard C1609 2007) and notched fracture beam tests for measuring post-cracking performance of FRC are based on a 15 cm beam height, which is practical for concrete slab applications of similar magnitude of thickness. However, among thinner pavement sections, the proximity of mold surface boundaries was expected to have an impact on the alignment of fibers and alter the measured toughness performance. Thus, potential representative flexural test samples to quantify the enhanced toughness of a 5 cm thick pavement are reported and discussed in Chapter 3. The effect of test sample size on the nominal strength (Planas et al. 1997; Bažant and Planas 1998) is addressed in Chapter 3 for geometrically similar toughness beam samples from 5 to 15 cm in height. Additionally, the influence on the measured post-cracking performance due to surface boundary-effects on cast specimens, compared to specimens centrally-cut from the interior of a larger beam, is reviewed in Chapter 3 and characterized further in Chapter 5. A prediction of flexural response of fracture beam tests has been successfully used in the past with cohesive zone tri-linear softening finite element modeling (FEM) to simulate 2D fracture beam specimen responses (Roesler et al. 2007; Park et al. 2010) and 3D FRC slab responses (Gaedicke 2009). The compatibility of this FEM approach to describe the deflection hardening and enhanced fracture energy of the FFC mixture, particularly with smaller beam sizes, is discussed in Chapter 3.

### 1.2.3. Distribution of Synthetic Fibers within Concrete

In order to properly understand the beam toughness results from Chapters 2 and 3, information on the fiber spatial distribution and orientation within the FFC specimens was needed. A literature review of existing techniques to identify and count fibers as well as determine fiber orientation is summarized in Chapter 4. Furthermore, researchers to date have not published techniques to locate and identify individual synthetic fibers within concrete. Thus, a non-destructive technique using x-ray computed tomography (CT) combined with post-processing image analysis to locate individual synthetic macro-fibers inside the concrete is described in Chapter 4. The results of 3D reconstructed images of FFC fracture specimens and analysis to determine the synthetic fiber spatial distribution are presented in Chapter 4. Statistical variation in the number of fibers located at any fracture plane is used to predict the range of expected fracture performance for the FFC mixture.

### 1.2.4. Boundary Effects on Fiber Orientation and Distribution

Recent publications concluded that steel fibers in a SCC mixture were more aligned with the direction of flow (Stähli et al. 2008) and resulted in higher concrete toughness (Zerbino et al. 2011) due to re-orientation of fibers in close proximity to a molded surface. Chapter 5 reviews current literature on construction technique and boundary surface effects on fiber orientation. For thin pavements cast with the synthetic FFC mixture, it was anticipated that the majority of fibers would similarly be parallel with the cast or mold surfaces and result in a higher measured toughness. The orientation of fibers is computed in Chapter 5 based on the x-ray CT imaging sample results from Chapter 4. In addition, the distribution of fibers with respect to the height distance from a cast or

mold surface is presented in Chapter 5. Analyses on both the distribution and orientation of the fibers with respect to a boundary surfaces or a concrete placement technique are summarized and compared to the measured fracture test results. The size of the boundary affected zone is also estimated based on both the distribution and orientation of x-ray imaged fibers.

# CHAPTER 2. FLOWABLE FIBROUS CONCRETE CONCEPT AND PROPERTIES

## 2.1. Motivation

An economically competitive 5 cm thick concrete inlay pavement which can be rapidly placed and have an extended service life through enhanced fracture properties was employed by using a flowable fibrous concrete (FFC) mixture. This thin FFC inlay was achievable through careful selection and analysis of concrete material constituents and proportioning. The improved workability and placement efficiency of FFC was designed using mixture proportioning strategies from structural self-consolidating concrete (SCC). To achieve the desired toughness, macro-fiber-reinforcement was added to the mixture at greater volume fractions than typical ultra-thin whitetopping (UTW) pavement designs. Overall, the FFC mixture, as presented and evaluated in this chapter, is a modification of a SCC mixture, containing fiber-reinforced concrete (FRC), and is used as a 5 cm thin bonded inlay.

### 2.1.1. Adaptation of SCC Technology

SCC technology has been used for structural concrete to rapidly construct walls and beams, and minimize the amount of vibration energy necessary for proper consolidation (De Schutter et al. 2008; Lange et al. 2008). For enhanced flow, SCC mixtures have been proportioned to use a well-graded blending of aggregates (Hu 2005; Koehler 2007; Shen 2007), higher cementitious material contents than seen in typical paving mixtures (Kosaka et al. 1996; Assaad et al. 2003; Nehdi and Ladanchuk 2004; Wang et al. 2005; Carlswärd 2006), and high range water reducer (HRWR). A recent experiment was

completed to determine the feasibility of using structural SCC for thin concrete pavement overlays (Riley 2005). This experiment, conducted in a ready-mixed concrete yard, determined that an un-reinforced concrete layer, with 44 mm height cast into formwork, over an existing concrete pavement could successfully be constructed rapidly and withstood truck traffic 24 hours after casting. This type of un-reinforced concrete as such a thin layer may be easier to construct, but it may not have a long service life. Macro-fiber-reinforcement will be utilized in the more workable FFC mixture to generate the necessary crack resistance and to improve pavement's service life.

Typical structural SCC mixtures do not have the ability to maintain a "green" strength, which the fresh concrete is stiff enough to hold its shape, for pavement applications on a grade or to be placed with a slip-form paver. However, Wang et al. (2005) introduced a "slip-form SCC" mixture for pavements consisting of a higher slump than typical slip-form paving mixtures with a certain level of green strength (see Figure 2-1). This slip-form SCC was consolidated not with internal vibration, but through an optimized mixture which was extruded as a 10 cm thick pavement. The slip-form SCC mixture was optimized by adjusting the content of fine aggregates, HRWR, and mineral admixtures (Wang et al. 2005) until the desired workability (around 200 to 350 mm slump flow diameter) was stiff enough such that the fresh concrete will retain vertical slab edges after being extruded. The slip-form SCC was reported to reduce construction costs (despite higher material costs) by increased construction speed and reduce $CO_2$ emissions generated due to use of paver vibrators (Lomboy et al. 2011) .

The FFC mixture was similar to SCC in terms of greater workability, flowability, and consolidation over conventional concrete. In order to improve the efficiency and cost of

construction, a vibratory screed instead of a slip-form paver was used to consolidate, strike-off, and level the 5 cm thick concrete inlay pavement surface. The FFC mixture was designed to be primarily placed as an inlay and utilize the edges of an existing asphalt pavement after milling, like a curb and gutter on city streets, as longitudinal formwork along the pavement. With the FFC cast as an inlay, the only "green" strength required was to prevent excessive flow on a longitudinal or transverse grade, which could occur with a typical structural SCC.

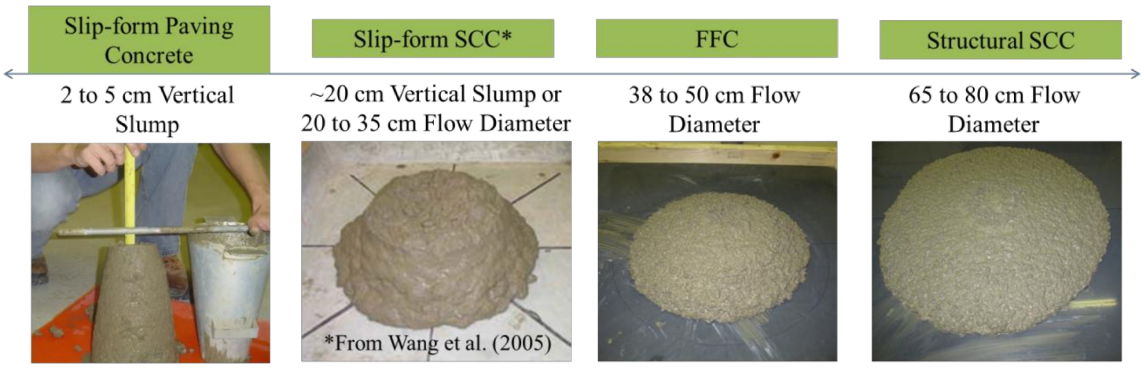


**Figure 2-1 Example images and desired slump measurements from slip-form concrete paving to structural SCC.**

2.1.2. Incorporating Macro-Fiber-Reinforcement

FRC has been known to increase toughness, reduce the rate of crack growth in slabs, increase load carrying capacity of slabs, and minimize spalling. Typically, the use of FRC in pavements (at less than 1 percent volume fraction) has allowed for reduced slab height requirements, e.g. with bonded concrete overlay applications. Higher volume fractions of FRC, e.g. 2.0 percent of polyvinyl alcohol fibers (Zhang and Li 2002; Kunieda and Rokugo 2006), have been successfully used as 38 to 50 mm thick bridge deck overlays.

FRC pavement design has reportedly employed a dosage of fiber-reinforcement based on trial-and-error and experience (Carlswärd 2006; Roesler et al. 2008b; Bordelon and Roesler 2009). Research has shown that generating a concrete mixture design based on specific dosage rate or volume fraction does not guarantee the same toughness performance for varying fiber types (Bordelon 2007; Roesler et al. 2008a; Bordelon and Roesler 2009). The Concrete Society was one of the first organizations to incorporate a more performance-based approach to designing slabs-on-grade with macro-fibers based on a measured residual strength or toughness parameter (The Concrete Society 2003). Standard tests have evolved with more applications of fiber reinforcement (Japan Concrete Institute 1984; ASTM Standard C1018 1997; European Standard EN 14651 2005; ASTM Standard C1399a 2007; ASTM Standard C1609 2007; ASTM Standard C1550 2008), enabling better quantification of various flexural strength performance parameters.

A design methodology used by the Illinois Department of Transportation for 7.5 to 15 cm thick concrete pavement overlay bonded to asphalt or UTW (Illinois Department of Transportation 2008; Roesler et al. 2008b) utilizes a performance-based (residual strength ratio $R_{150}^{150}$) input to describe the benefit of using FRC. The recommended minimum residual strength ratio (the load capacity after a given deflection compared to the peak flexural load) was set at 20 percent for a 7.5 cm or thicker FRC overlay. For placing a thin FFC inlay of 5 cm, a higher toughness performance between 40 to 50 percent residual strength was desired based on the anticipated serviceability requirements for a thin concrete inlay. Thus, FFC mixtures containing various combinations of hybrid fiber-reinforcement were tested for optimal resistance to cracking based on results from two

types of laboratory beam tests (unnotched beam toughness and single-edged notched beam fracture).

## 2.2. Material Property Tests

### 2.2.1. Fresh Property Tests

A test commonly used to measure the workability of SCC was selected for characterizing the flow properties of the FFC mixtures. The inverted slump flow test (ASTM Standard C1611b 2009) was developed for estimating horizontal flow of a concrete mixture. Potential segregation of fresh mortar from the aggregates and fiber particles was estimated using the visual stability indexing described in ASTM C1611. A typical SCC mixture requires a slump flow diameter from around 650 to 800 mm (Self-Compacting Concrete European Project Group 2005), as illustrated in Figure 2-1, to fill large highly-reinforced structures and still consolidate without internal vibration. Since the FFC mixture only needs to flow a short distance in the thin inlay and will be consolidated with the assistance of a vibratory screed for paving applications, a higher yield strength than SCC was desired with a target slump flow diameter of 380 mm (shown in Figure 2-1). With the slump flow measurement less than 500 mm in diameter the FFC mixture is therefore excluded from being classified as a typical SCC mixture. Additional fresh properties such as the unit weight (ASTM Standard C138 2009) and the air content from a pressure air-meter (ASTM Standard C231a 2009) were monitored for consistency between FFC mixtures.

### 2.2.2. Unnotched Specimen Toughness Tests

Both notched fracture and unnotched toughness tests were performed on the hardened FFC mixture to estimate the post-cracking performance. The unnotched toughness test for the FFC used a four-point bending beam to determine the flexural strength (MOR) and residual strength ratio values of the mixture (ASTM Standard C1609 2007; Roesler et al. 2008b). A diagram of the samples and loading for the unnotched flexural test can be seen in Figure 2-2a. With the unnotched test, specimen geometry can alter the nominal strength values measured from the test (Gopalaratnam and Gettu 1995; Bažant and Planas 1998). Additionally, the post-cracking toughness performance of geometrically similar beams have been found to be dependent on the sample height from 10 to 15 cm (Altoubat et al. 2004; Jiang and Banthia 2010), as is discussed further in Chapter 3. The unnotched flexural test beams studied in this research were all geometrically similar with a constant span-to-height ratio S/d of 3 and width-to-height b/d ratio of 1. Jiang and Banthia (2010) suggested a normalized load-deflection curve be plotted when comparing the geometrically similar specimens of different height.

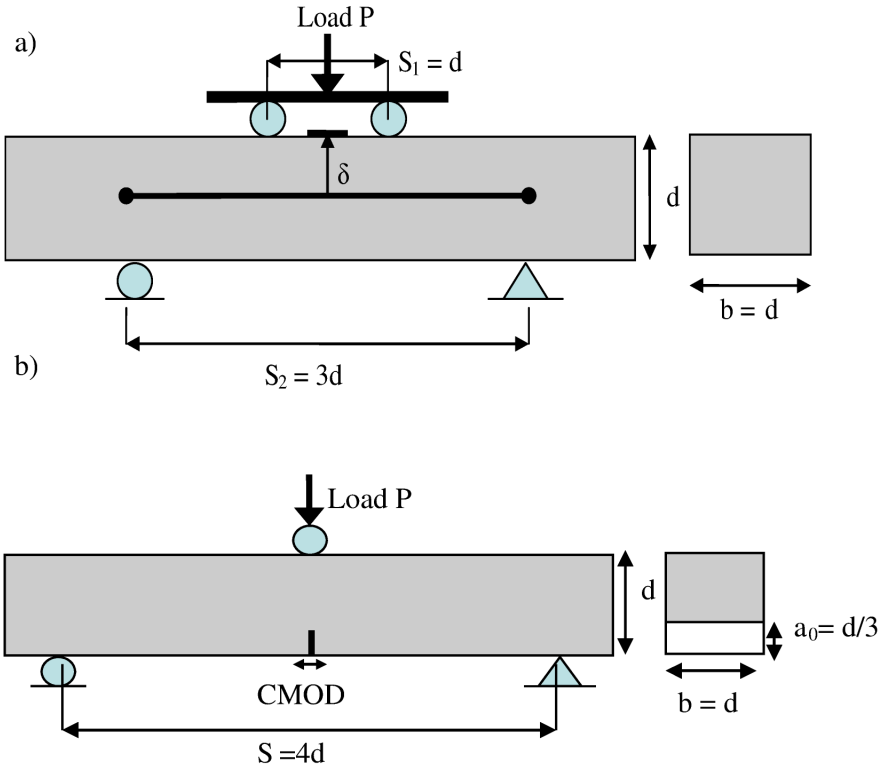


**Figure 2-2 Schematics of a) the unnotched flexure four-point bending test configuration and b) the SEN[B] fracture test configuration with center-point loading.**

A load versus midspan deflection curve was recorded from the unnotched beam test and the load values at various deflection levels were used to compute a residual stress, as represented in Figure 2-3 for 7.5 cm beam height. A residual stress ratio (residual stress measured at a given deflection $\delta$ divided by the peak flexural strength) was also computed for 7.5 cm and 15 cm beam heights, as $R_{S/\delta}^{75}$ and $R_{S/\delta}^{150}$, respectively.

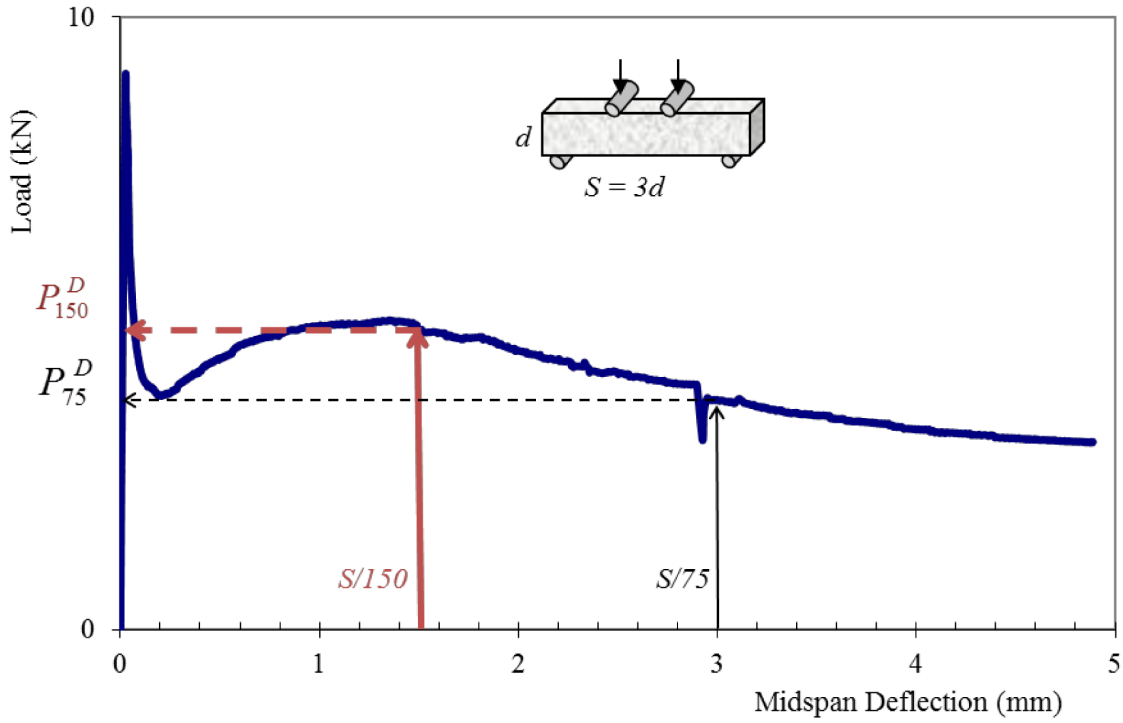


**Figure 2-3 Schematic shows an example load versus deflection result of an unnotched flexural beam of height 7.5 cm.**

2.2.3. Notched Specimen Fracture Tests

Although the unnotched flexural strength test provides an index on the relative toughness performance, the material's size-independent properties (Bažant and Gopalaratnam 1991; Struble and Lange 1997; Bažant and Planas 1998; Anderson 2005) can be determined using a notched fracture test, e.g., a single edge notched beam (SEN[B]). The computed fracture properties from the SEN[B] laboratory specimens are necessary inputs for finite element-based fracture models capable of characterizing the load versus displacement response of beams and load capacity of concrete slabs (Gaedicke 2009).

The fracture test used a center-loaded SEN[B], as shown in Figure 2-2b, with a span-to-height (S/d) ratio of 4 and a notch-to-beam height $a_0$/d of 1/3. The results of fracture test selected were used to compute the material's size-independent fracture properties – the

critical mode I stress intensity factor ($K_{Ic}$), critical crack tip opening displacement ($CTOD_c$), and initial fracture energy ($G_f$) – based on the two-parameter analysis method (Jenq and Shah 1985; Shah 1990). The area under the applied load versus crack mouth opening displacement (CMOD) was used to compute the work of fracture or total fracture energy ($G_{FRC}$) originally proposed by Hillerborg (Hillerborg 1985). This measured total fracture energy does depend on the specimen size and geometry. An example of the calculations for fracture properties of concrete paving mixtures based on the load versus CMOD curves can be found in past publications (Bordelon 2007; Roesler et al. 2008b).

## 2.3. Material Selection and Proportioning

### 2.3.1. FFC Mixture Design

The FFC mixture, shown in Table 2-1, was originally based on a slip-form SCC mixture presented by Wang et al. (2005), but modified to achieve a more typical SCC high slump flow by adjusting the coarse and fine aggregate blending and HRWR amount. In comparison to a typical UTW pavement mixture (Table 1-1), the control flowable mixture was designed to be classified as a SCC by adjusting the following: slightly higher cement content, 30 percent of the cementitious binder as fly ash instead of 21 to 24 percent, higher fine aggregate to coarse aggregate ratio, and use of HRWR. To further make the FFC from the flowable concrete mixture, a hybrid of micro-fibers and macro-fibers were also added to provide crack resistance and the appropriate "green" stiffness for placing on a grade. In addition, the FFC mixture was designed with a smaller nominal maximum coarse aggregate size of 9.5 mm instead of the typical 19 mm for UTW, as this reduced aggregate size for 5 cm inlay is proportional to the thickness of a

10 cm UTW. Consolidation was verified for the FFC mixture by comparing bulk specific gravities of hardened FFC specimens to that of the batched mixture with a difference of only 3 to 4 percent.

**Table 2-1 Summary of Mixture Designs**

| Material | | Control SCC Mixture | Field FFC Mixture* | 5 cm Test Beam Mixture† |
|---|---|---|---|---|
| Water | kg/m$^3$ | 187 | 168 | 187 |
| Type I Cement | kg/m$^3$ | 328 | 292 | 328 |
| Type C Fly Ash | kg/m$^3$ | 140 | 128 | 140 |
| Coarse Aggregate (9.5 mm) | kg/m$^3$ | 1052 | 1068 | 1052 |
| Sand | kg/m$^3$ | 857 | 890 | 857 |
| Micro-fiber (6 mm) | kg/m$^3$ | 0.59 | 0.63 | 0 |
| Macro-fiber (40 or 48 mm) | kg/m$^3$ | 0 | 4.4 | 4.6 |
| HRWR | mL/m$^3$ | 1028 | 2759 | 1028 |
| AEA | mL/m$^3$ | 107 | 101 | 107 |

w/cm = 0.4; CA/FA (by mass) = 1. 22

*Field FFC mixture was an average of 5 truck batches. This mixture was also designed for the 7.5 and 15 cm unnotched test samples presented in Chapter 3.

† These mixture proportions with macro-fibers and without the micro-fibers were used for the 5 cm beam unnotched and all fracture test samples presented in Chapter 3 through 5.

### 2.3.2. Chemical Admixtures

High range water reducers (HRWR) have been added to reduce viscosity and increase flow of the paste (Hu 2005) without affecting segregation, setting time, or strength of the concrete. The amount of polycarboxylate-based super-plasticizer AdvaCast® 575 varied up to 1486 mL/m$^3$ for each FFC mixture studied in order to achieve a desired slump flow diameter near 400 mm. Of all the FFC mixtures designed, the average HRWR amount utilized was 888 mL/m$^3$ and produced slump flow diameters between 330 and 451 mm. In order to demonstrate the importance of the HRWR in the FFC, a mixture was designed without HRWR. This mixture without HRWR had a significantly reduced workability as tested by a vertical slump (ASTM Standard C143/C143M 2008) of 75 mm similar to a typical slip-form concrete paving mixture (see Figure 2-1) and required external

consolidation. Fracture testing verified that the addition of HRWR did not have a quantifiable impact on toughness performance.

An air-entraining admixture (AEA) was also employed for the FFC mixtures because the climate exhibited in Illinois generally requires entrained air for freeze-thaw resistance. The use of AEA was known to decrease viscosity and reduce segregation of the concrete (Hu 2005). The amount of air-entraining admixture Daravair® 1400 was proportioned at the minimum recommended dosage rate (30 mL/100 kg cement). Air contents measured with a pressure meter ranged from 1.5 to 7.5 percent among all tested FFC mixtures.

### 2.3.3. Aggregate Blending

A well-graded aggregate blend corresponding to the maximum blended packing density was utilized (Shen 2007) to achieve the desired flow at the minimum cement content. A variety of aggregate blends were selected and batched, including the suggested optimal packing density by Shen (2007) using a combination of two limestone coarse aggregates (at 19 mm and 9.5 mm maximum aggregate size) and natural sand. Because the FFC was designed to be placed as a 50 mm concrete inlay, a smaller maximum limestone coarse aggregate size of 9.5 mm was preferred. The optimal aggregate packing density with the Toufar model for the combination of 9.5 mm limestone aggregate and natural sand (Shen 2007) resulted in a blend that was 55 percent by mass limestone coarse aggregate and 45 percent by mass fine aggregate sand. Although the workability was greatest (producing a slump flow diameter of 451 mm) with the three aggregate blend, the 55 percent CA to 45 percent FA by mass blending also had a similar flow diameter of 438 mm. The gradations of the coarse and fine aggregates with the FFC mixture blended combination are shown in Figure 2-4.

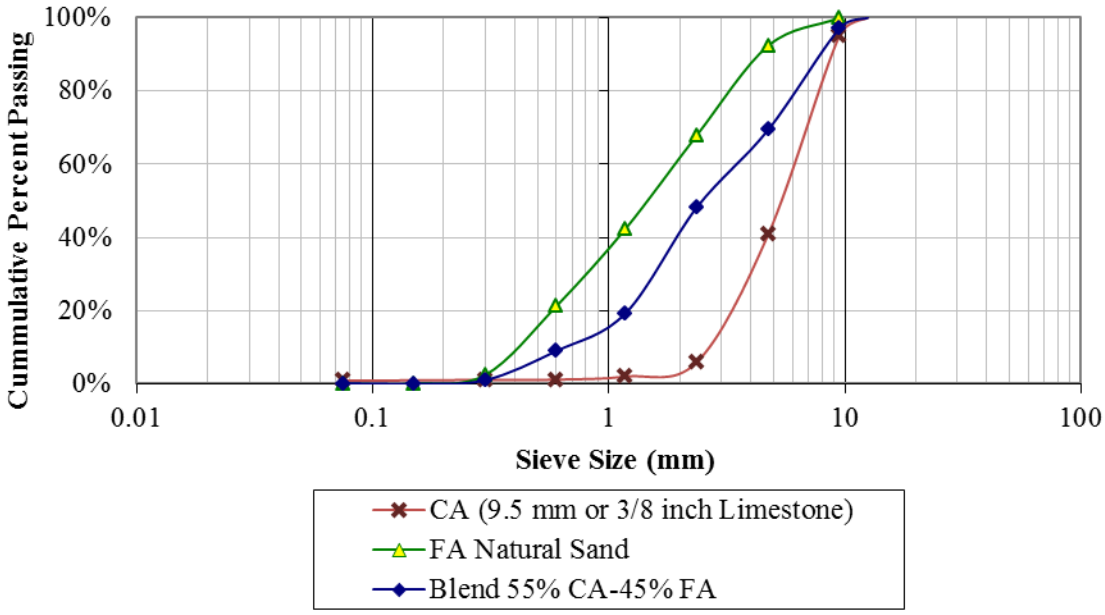


**Figure 2-4 Gradation curves for individual aggregate sources and the blended combination (at a coarse aggregate/fine aggregate mass ratio of 1.22).**

2.3.4. Cement Content

Typical SCC mixture designs contain significantly higher cementitious contents, around 450 to 550 kg/m$^3$ (Kosaka et al. 1996; Assaad et al. 2003; Nehdi and Ladanchuk 2004; Wang et al. 2005; Carlswärd 2006), than utilized in typical concrete pavement mixtures. The FFC control mixture contained 468 kg/m$^3$ of total cementitious material, with 30 percent Class C fly ash replacement and a water-cementitious (w/cm) ratio of 0.40. A more cost effective FFC mixture was explored containing a lower total cementitious content of 308 kg/m$^3$, which is more typically utilized in paving concrete mixtures (Table 1-1). The lower cementitious content mixture had a reduced workability, with a measured vertical slump of 38 mm. The workability and 7 day strengths (35 MPa compressive and 3.7 MPa split-tensile strengths) were similar to that expected for slip-form paving concrete. As a result, this lower cementitious content mixture was consolidated with internal vibration. Fracture SEN[B] results, illustrated in Figure 2-5, of

the reduced total cementitious content mixture produced a considerably lower average fracture energy of 1,598 N/m relative to the higher cementitious FFC mixture (6,345 N/m). This reduced post-cracking response is attributed to the lack of cement paste for bonding with the fibers, which generates friction during fiber pull-out. Therefore, it is required for the FFC mixture to contain an increased amount of cementitious material compared to UTW or slip-form paving mixtures in order to provide enough coating along the fiber surface area for a good bond and pull-out friction.

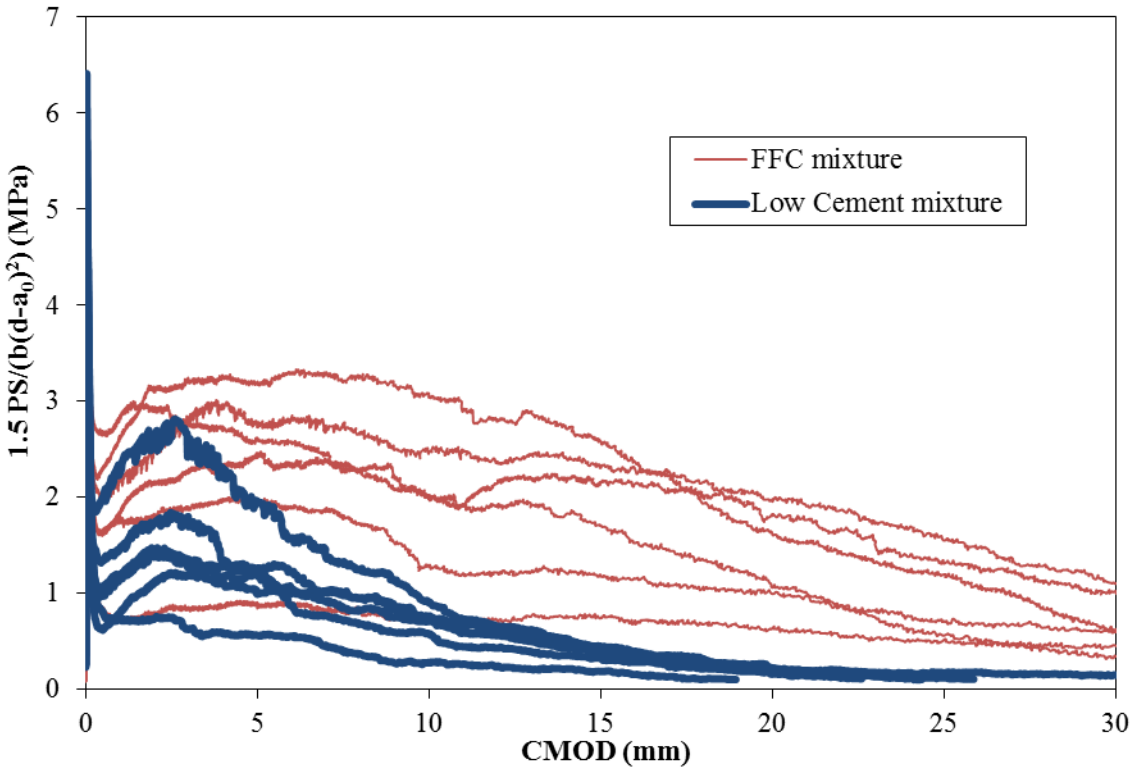


**Figure 2-5 Fracture test stress curves for 5 cm beams cast as 5 cm plates with different cement contents.**

2.3.5. Synthetic Macro-Fiber Type

Construction of higher fiber volume fractions in FRC slabs can be difficult, as fibers tend to clump or ball within the mixture. The addition of fibers requires extra cement paste to coat fibers, and traditionally external vibration energy is used to facilitate consolidation

and finishing of the concrete. The addition of both fibers and cement can increase the cost of the material design. However, the cost for construction can be reduced by using a more workable, or flowable, concrete mixture to promote a rapid concrete pavement placement. The improved workability and flow of the FFC was expected to reduce the likelihood of fiber clumping, reduce air voids from poor compaction/consolidation efforts, and produce better and more uniform fiber alignment to increase the overall toughness performance.

The FFC mixture contains a hybrid of both synthetic micro- and synthetic macro-fibers. Synthetic macro-fibers are more commonly accepted for pavement projects (Altoubat et al. 2008; Roesler et al. 2008b; Bordelon and Roesler 2009) due to their similar toughness performance as that of steel macro-fibers. The synthetic (polypropylene/ polyethylene blend) macro-fibers shown in Figure 2-6a-d were added to the FFC mixtures to improve the toughness characteristics of the control mixture and provide the necessary crack resistance for achieving a high load capacity and long service life of the inlay. The 20 mm long fibers (Figure 2-6d) were cut from the 40 mm Strux® (Figure 2-6c); thus, the 20 mm fibers have a lower aspect ratio of 45. The 40 mm and 50 mm Strux® fibers contained similar aspect ratio of 90 and 85, respectively. Synthetic fibers often have a lower flexural stiffness than steel fibers, which may lead to bending and curling of these flexible fibers around aggregate particles or other fibers within the concrete. The flexibility of synthetic macro-fibers has been linked to an increase in the yield stress and reduced slump (Nehdi and Ladanchuk 2004; Rapoport and Shah 2005; Banfill et al. 2006; Martinie et al. 2010). With these macro-fibers at higher volume fractions, clumping was possible, which would produce higher yield stress and a potential for fiber segregation

during placement of the concrete. A synthetic fiber called "BT50" (Figure 2-6a) had a higher flexural stiffness and was studied in the FFC mixture to understand the effect fiber stiffness has on the dispersion and resulting toughness performance. Comparison of fracture results for FFC mixtures containing either the stiffer BT50 fibers or the more flexible fibrillated Strux® 90/40 fibers are presented in Chapter 4.

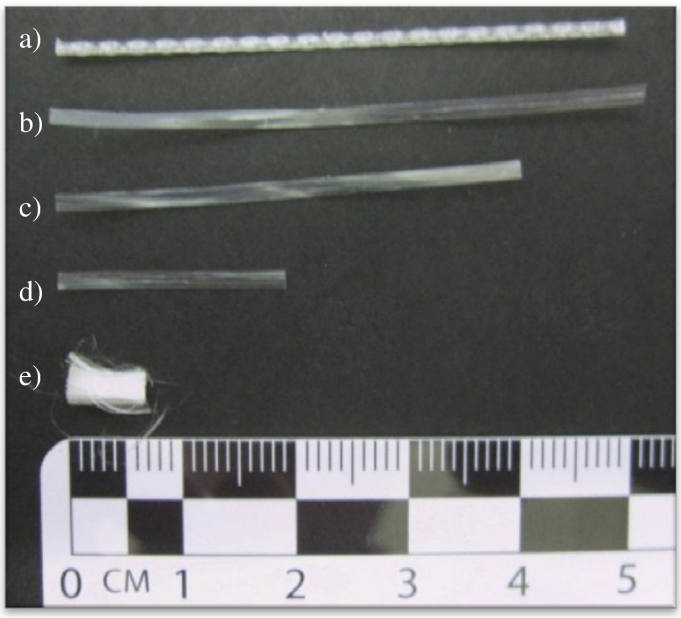


a) Bi-tapered ("BT50")*
$L_f$ = 48 mm, $L_f/d_f$ = 97, $E_f$ = N/A

b) Fibrillated (Strux® 85/50)
$L_f$ = 50 mm, $L_f/d_f$ = 85, $E_f$ = 9.5 GPa

c) Fibrillated (Strux® 90/40)
$L_f$ = 40 mm, $L_f/d_f$ = 90, $E_f$ = 9.5 GPa

d) Fibrillated (cut Strux® 90/40)
$L_f$ = 20 mm, $L_f/d_f$ = 45, $E_f$ = 9.5 GPa

e) Virgin Polypropylene (Fibromac® 6)
$L_f$ = 6 mm, $L_f/d_f$ = 330, $E_f$ = 3.5 GPa

*Geometry was measured manually for BT50 fibers.

**Figure 2-6 Synthetic fibers used in the various FFC mixtures.**

FFC mixtures containing either only micro-fibers or only macro-fibers produced slump flow diameters, shown in Table 2-2, similar in magnitude to typical SCC mixtures. The targeted slump flow diameter of the FFC mixture containing macro-fibers was achieved by adding HRWR. Different fiber blends in the FFC mixture demonstrated negligible impact on 7-day compressive and tensile strengths (Table 2-2). The slump flow diameters were reduced with mixtures of increasing fiber lengths (and similar fiber aspect ratios) or lower HRWR amounts.

**Table 2-2 FFC Fresh Properties and Strengths**

| | Air Content | HRWR Amount | Slump Flow | Test Age | Compressive Strength $f'_c$ | | Split-Tensile Strength $f'_{sp}$ | |
|---|---|---|---|---|---|---|---|---|
| | (%) | (mL/m$^3$) | (mm) | (day) | (MPa) | (psi) | (MPa) | (psi) |
| Micro-fiber Only (6 mm) | 5.2 | 721 | 438 | 28 | 46.6 | 6,753 | 4.78 | 693 |
| 20 mm Fiber | 7.3 | 1234 | 406 | 7 | 27.8 | 4,029 | 3.59 | 520 |
| 40 mm Fiber | NA* | 1196 | 425 | 7 | 30.8 | 4,470 | 3.21 | 466 |
| 50 mm Fiber | 6.8 | 738 | 305 | 7 | 29.5 | 4,281 | 2.94 | 426 |
| Blend of 40 and 20 mm Fibers | 7.5 | 1068 | 413 | 7 | 27.9 | 4,046 | 3.40 | 493 |
| | | | | 28 | 40.3 | 5,840 | 3.88 | 563 |
| Macro-Fiber Only (40 mm) | 2.6 | 1206 | 457 | 7 | 35.6 | 5,164 | 3.58 | 519 |

*Pressure air-meter not functioning properly.

The load versus midspan deflection curves for unnotched flexural beams (75 x 75 x 286 mm) of different hybrid fiber combinations are shown in Figure 2-7. Synthetic macro-fibers of lengths 20, 40 and 50 mm (Figure 2-6b-d) were investigated at 0.46 percent volume fraction (0.23 percent volume fraction for each macro-fiber in the blended mixture) in conjunction with the 6 mm polypropylene micro-fiber at 0.06 percent volume fraction. For these 75 mm height beams, the residual strength ratios measured at midspan deflections of 1.5 mm and 3 mm were recorded as $R_{150}^{75}$ and $R_{75}^{75}$, respectively. The average properties and coefficient of variation for three replicate beams are given in Table 2-3. All of the FFC mixtures containing the 20 mm length fiber, including the blend of the 40 and 20 mm fibers, produced residual strength ratios between 30 and 40 percent. The mixtures containing the 20 mm long fiber, either alone at 0.46% volume fraction or in combination with the 40 mm long fiber, also exhibited a higher variation (29 to 30% COV for $R^{75}{}_{75}$) among the replicate beam samples. The higher variation in toughness could be due to the fact that the 20 mm fibers were manually cut from the 40

mm fibers. At a 7-day age with the same volume fraction of 0.46 percent, the 40 and 50 mm fiber mixtures had the highest residual strength ratios over 54 percent. Overall, hybrid mixtures containing a volume fraction of 0.46% of macro-fibers at either 40 or 50 mm in length produced the desired toughness performance with residual strength ratios over 50 percent.

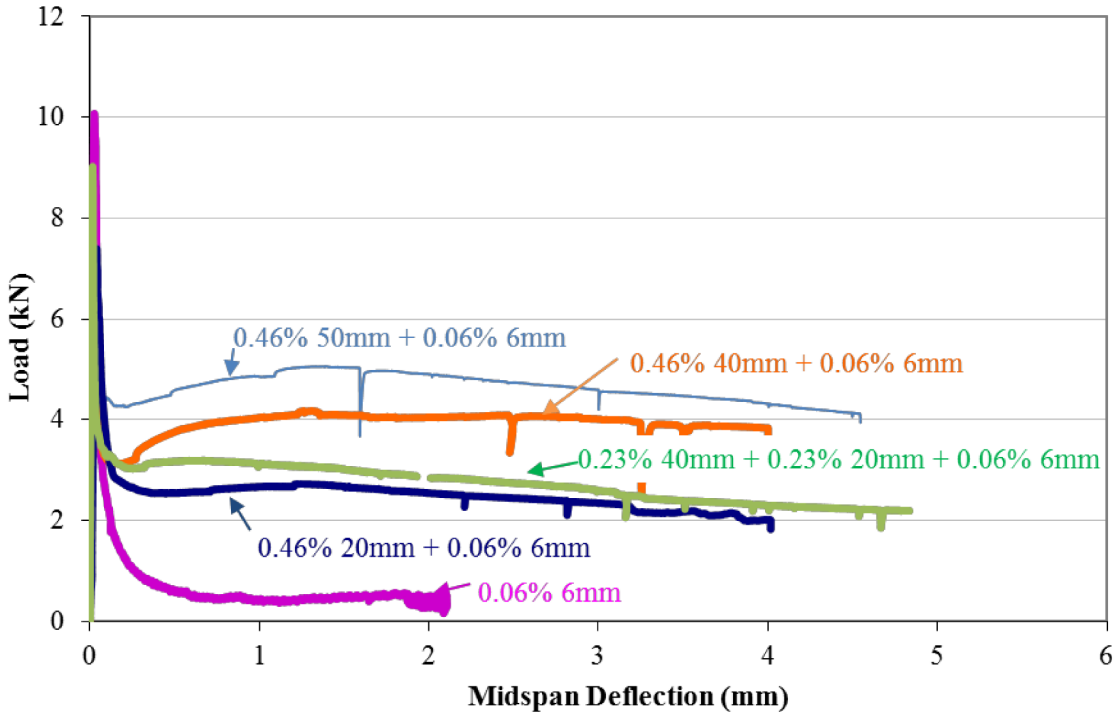


**Figure 2-7 Flexural load versus deflection curves plotted for one 7.5 cm beam of each FRC mixture.**

**Table 2-3 Flexural 7.5 cm Beam Properties of FRC Mixtures**

| | Peak Load (kN) | MOR (MPa) | $f^{75}_{150}$ (MPa) | $R^{75}_{150}$ | $f^{75}_{75}$ (MPa) | $R^{75}_{75}$ |
|---|---|---|---|---|---|---|
| Micro-fiber Only | 10.21* (3%) | 5.27 (3%) | 0.30 (27%) | 5.8% (28%) | 0.15 (NA) | 3.0% (NA) |
| 20 mm Fiber | 7.35 (5%) | 3.80 (5%) | 1.43 (13%) | 38.0% (19%) | 1.29 (22%) | 34.2% (30%) |
| 40 mm Fiber | 7.80 (19%) | 4.03 (19%) | 2.18 (5%) | 54.9% (14%) | 2.16 (6%) | 54.3% (13%) |
| 50 mm Fiber | 8.34 (5%) | 4.31 (5%) | 2.43 (11%) | 56.4% (10%) | 2.39 (1%) | 55.2% (7%) |
| Blend of 40 and 20 mm Fibers | 8.26 (10%) | 4.27 (10%) | 1.53 (22%) | 36.5% (30%) | 1.37 (19%) | 32.6% (29%) |

*Micro-fiber beams were tested at 28 days; all other tests were performed at 7 days.
Average values and coefficients of variation in parentheses are for three samples.
NA = not available (only one sample reached 3 mm deflection).

Past research of concrete paving mixtures with FRC (see Table 1-1) has indicated that volume fraction and fracture energy are linearly correlated for the same fiber type. Results of fracture SEN[B] test specimens of 5 cm in height, cut from either a cast 5 cm thick plate or a 15 cm thick beam (described in Chapter 3), containing the same batched 0.46% volume fraction of macro-fibers are illustrated in Figure 2-8. A linear relationship between the measured total fracture energy and the number of fibers crossing the fracture plane (manually counted after testing) was found for both synthetic macro-fibers "BT50" and Strux® 90/40 studied in this research.

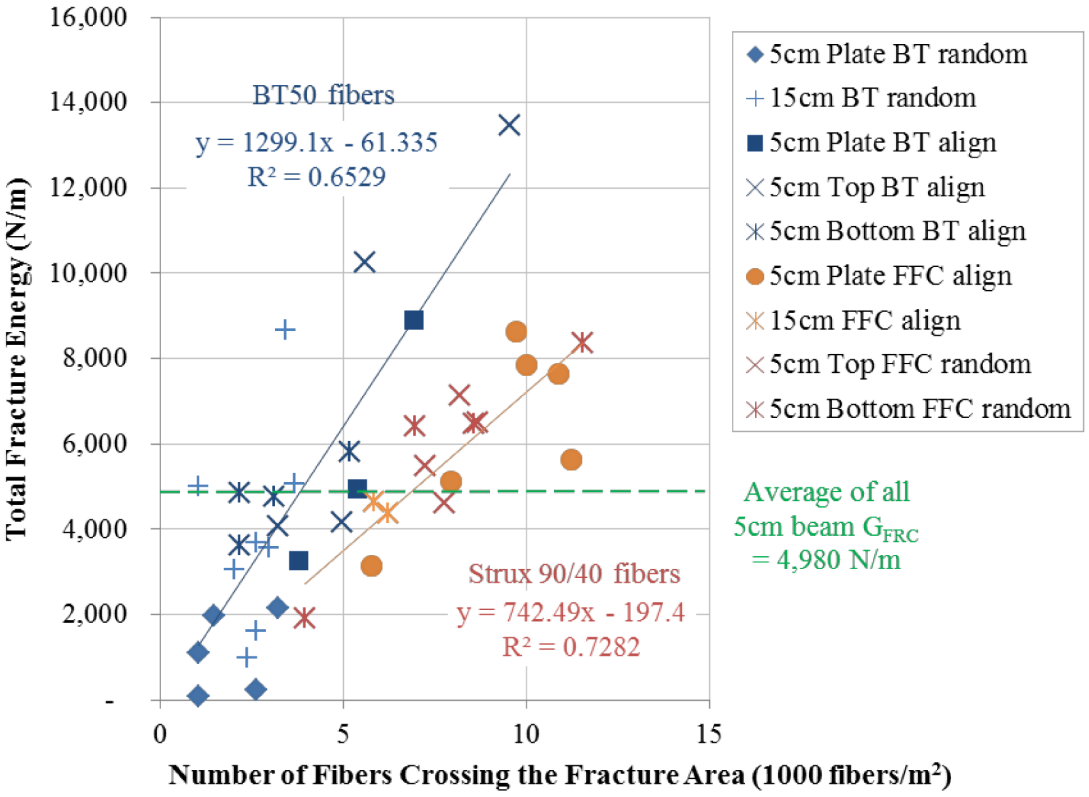


**Figure 2-8 Number of fibers intersecting fracture plane versus total fracture energy.**

2.3.6. Including Micro-Fiber-Reinforcement

Micro-fibers are traditionally added to concrete for slabs and pavements in order to control the widths of plastic shrinkage cracks. For the FFC mixture, micro-fibers were introduced to improve the fresh concrete mixture cohesion. While macro-fibers could possibly have clumping or potential fiber segregation during placement of the concrete, micro-fibers have been demonstrated (Rapoport and Shah 2005; Banfill et al. 2006) to increase segregation resistance and increase the viscosity of fresh concrete mixtures. The addition of microfibers has also been found to improve the "green" strength of fresh slip-form SCC mixtures (Voigt et al. 2010). An increase in yield stress from the use of synthetic micro-fibers in the FFC, compared to an un-reinforced SCC mixture, was

expected to provide a more cohesive mixture capable of holding a cross-slope or longitudinal grade.

The control FFC mixture contained a polypropylene fiber Fibromac® of 6 mm length (shown in Figure 2-6e) at the manufacturer's recommended volume fraction of 0.06 percent. The average and standard deviation of fresh properties of the FFC mixtures with or without the addition of micro-fibers are reported in Table 2-4. The use of micro-fibers in the FFC mixture reduced the slump flow diameter as expected, even in the presence of higher HRWR. The combination of AEA with micro-fibers in the FFC mixture resulted in higher measured air contents. Among the micro-fiber mixtures (without any macro-fibers), the post-cracking performance listed in Table 2-3 was highly variable with 27 percent of variation between replicate beams. However, the average post-cracking performance for these micro-fiber mixtures was low ($R_{150}^{75}$ of 6 percent) which inflated the significance of small changes in toughness values (see Figure 2-7). The micro-fibers were desired for field FFC mixtures to produce a stable and cohesive flow. However, laboratory testing mixtures as presented in Table 2-1 omitted the addition of micro-fibers mainly to focus on the benefits of macro-fibers alone on post-cracking performance and to simplify locating fibers within the concrete.

**Table 2-4 Fresh Properties for FFC Mixtures**

| | | Mixtures containing Micro-fibers | | Mixtures without Micro-fibers* | |
|---|---|---|---|---|---|
| | Unit | Average | Standard Deviation | Average | Standard Deviation |
| Unit Weight | kg/m$^3$ | 2251 | 40 | 2344 | 17 |
| Air Content | % | 5.9 | 1.2 | 2.1 | 0.6 |
| HRWR Amount | mL/m$^3$ | 1218 | 332 | 1119 | 231 |
| Slump Flow Diameter | mm | 439 | 73 | 509 | 48 |

*FFC mixtures using only macro-fibers were used for fracture testing beam samples.

## 2.4. FFC Properties

The strengths of the FFC mixture (constructed with the field mixture listed in Table 2-1) displayed in Table 2-5 were only slightly higher than for UTW pavements shown in Table 1-1of 36 to 40 MPa compressive and 4 MPa split-tensile strengths at 28 days. The increase in measured strengths compared to these past UTW mixtures, was assumed to be directly linked to the higher cementitious content utilized in the FFC. Initial fracture test properties of the FFC were found to be similar, e.g., 53 N/m $G_f$ of the FFC at 28 days was within the range measured by other UTW pavements from 47 to 65 N/m. The FFC also achieved a higher post-peak cracking performance than past paving mixtures as illustrated in Figure 2-9. This FFC toughness performance, based on either 7.5 or 15 cm beam heights, exceeded the minimum recommendation of 20 percent residual strength ratio (Roesler et al. 2008b) for UTW concrete overlay applications containing fiber-reinforcement. With the higher volume fraction of macro-fibers (at 0.5 percent) in the FFC mixture, the measured total fracture energy was 2 to 3 times greater than with FRC mixtures commonly used for paving thin overlays (at 0.3 percent or less volume fraction of macro-fibers).

**Table 2-5 Hardened Properties of the FFC**

| Strengths (10 cm diameter x 20 cm) | | | Flexural Properties (15 x 15 cm beams) | | | |
|---|---|---|---|---|---|---|
| Age (days) | $f'_c$ (MPa) | $f'_{sp}$ (MPa) | E (GPa) | MOR (MPa) | $f^{150}_{150}$ (MPa) | $R^{150}_{150}$ (%) |
| 7 | 35.8 (1%) | 3.49 (40%) | - | 3.78 (8%) | 1.80 (17%) | 47.6% (12%) |
| 28 | 41.5 (9%) | 4.25 (5%) | 31.7 (6%) | 5.02 (10%) | 1.41 (7%) | 28.0% (9%) |

Flexural Properties (7.5 x 7.5 cm beams)

| Age (days) | MOR (MPa) | $f^{75}_{150}$ (MPa) | $R^{75}_{150}$ (%) | $f^{75}_{75}$ (MPa) | $R^{75}_{75}$ (%) |
|---|---|---|---|---|---|
| 7 | 4.49 (5%) | 2.61 (13%) | 58.1% (15%) | 2.19 (18%) | 48.7% (18%) |
| 28 | 4.77 (2%) | 2.56 (4%) | 53.7% (5%) | 2.12 (12%) | 45.0% (12%) |

Fracture Properties (15 cm height SEN[B])

| Age (days) | $P_c$ (kN) | $K_{Ic}$ (MPa $m^{1/2}$) | $CTOD_c$ (mm) | $G_f$ (N/m) | $G_{FRC}$ (N/m) |
|---|---|---|---|---|---|
| 7 | 4.24 (8%) | 1.24 (6%) | 0.026 (3%) | 63.2 (14%) | 3691 (55%) |
| 28 | 4.21 (11%) | 1.26 (17%) | 0.019 (16%) | 52.8 (27%) | 3175 (14%) |

Averages are for three specimens from field batches.
Value in parentheses is the coefficient of variation.
All field concrete specimens were rodded for consolidation.
$f'_c$ = compressive strength
$f'_{sp}$ = split-tensile strength
E = elastic modulus
MOR = modulus of rupture or flexural strength
$f^d_X$ = residual stress of for beam height d (in mm) at deflection of span/x
$R^d_X$ = residual stress ratio of for beam height d (in mm) at deflection of span/x
$P_c$ = peak load

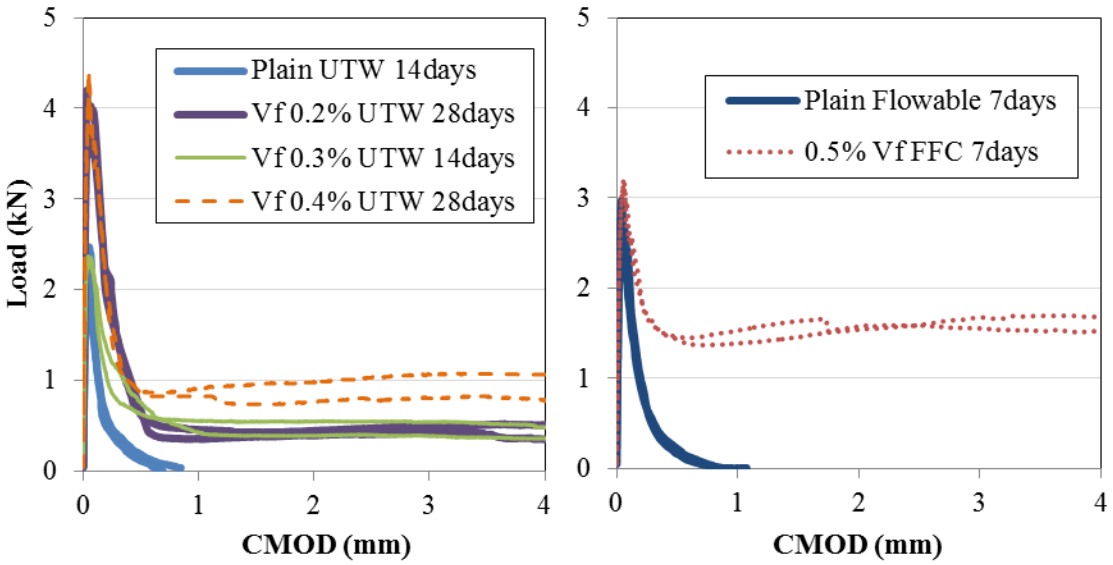


**Figure 2-9 Standard 15 cm fracture specimen curves for (a) typical ultra-thin whitetopping (UTW) mixtures for different volume fractions and (b) flowable fibrous concrete.**

A reduction in residual strength ratio with age was expected based on past experience (Zollinger et al. 1993; Bordelon 2007) for the 15 cm beam height samples. The cement matrix and bond strength increased with age and likely caused more fiber rupture, producing reduced total energy, compared to the pullout of fibers. With the FFC this reduction in $R^{150}_{150}$ was measured to be from 48% at 7 days to 28% at 28 days. However, flexural load versus midspan deflection curves for unnotched toughness test specimens of 7.5 cm beam height (illustrated in Figure 2-10) exhibited similar residual flexural properties at 7 and 28 days (both with 2.6 MPa $f^{75}_{150}$ and 2.2 MPa $f^{75}_{75}$). Because the 7.5 cm beam did not lose as much residual strength with age, it is likely that the thinner cast beam specimens had a higher degree of fiber alignment. The effect of fiber distribution and alignment on measured toughness in thinner specimens was investigated further in Chapters 4 and 5.

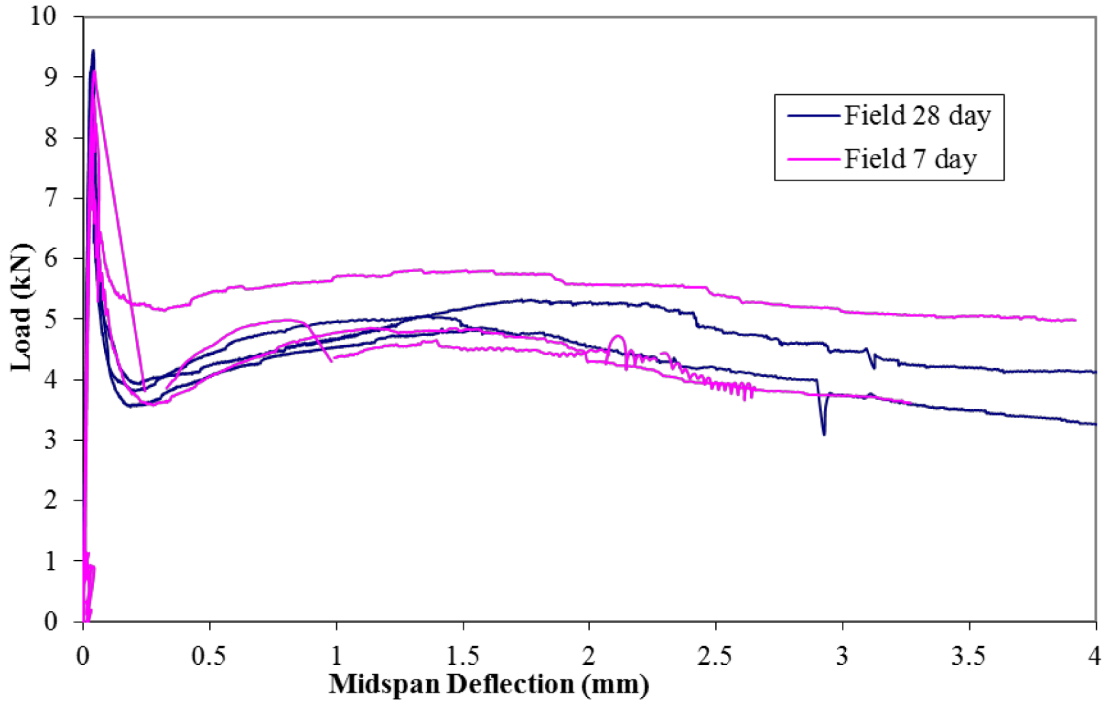


**Figure 2-10 Flexural load versus deflection curve for 75 mm beam specimens.**

## 2.5. FFC Inlay Pavement Test Section

A full-scale 5 cm thick inlay pavement was cast to demonstrate and observe any challenges related to the placement of the FFC material and to monitor the cracking and bonding performance of the hardened concrete pavement inlay. The full-scale demonstration project, 99 m in length, was cast at the Advanced Transportation Research and Engineering Laboratory in Rantoul, Illinois in July of 2009. Figure 2-11 illustrates the layout of three test sections which were all constructed at a thickness of 5 cm. The main variable between the three sections was the slab size (1.15 x 1.12 m, 1.73 x 1.68 m, or 1.72 x 3.35 m), where the smallest size corresponds to a typical slab size used for a 7.5 cm UTW design.

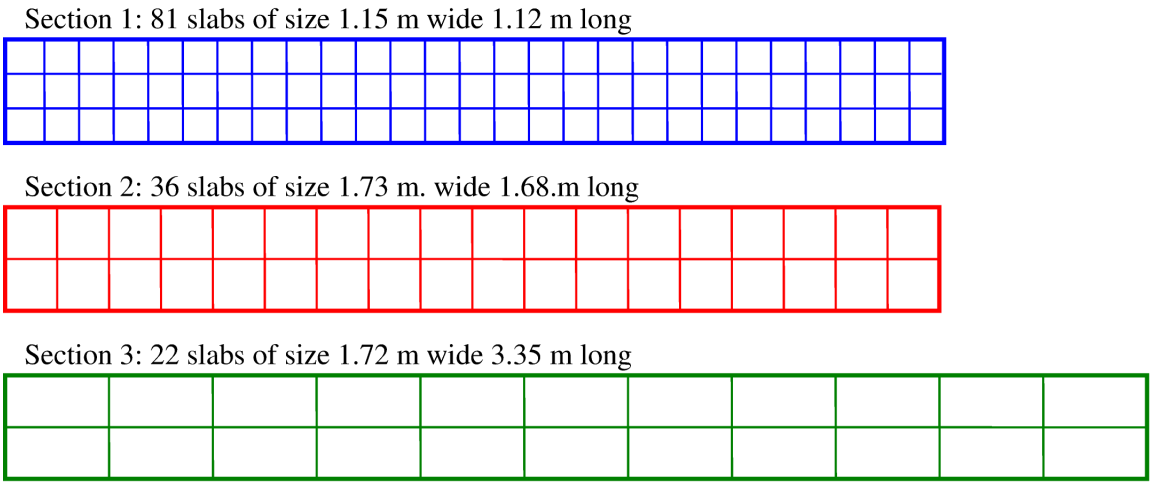


**Figure 2-11 Plan view of the full-scale section configurations.**

At the site location, existing aged hot-mixed asphalt concrete (HMA), as described in more detail in Appendix A, was milled 5 cm deep and roughly 3.3 m wide. Typical paving mixtures are stiff enough to be constructed through slip-form pavers and without the need for formwork. By having vertical edges along the FFC inlay, the flowable concrete could retain its shape in a location where a grade or cross-slope may exist. A 5 cm wide lip of the HMA remained on either side of the field constructed lane acting as the side (vertical) edge formwork to contain the FFC, similar to a curb or gutter on a city street.

### 2.5.1. FFC Construction

For enhanced concrete-to-asphalt bonding, researchers have all agreed that the underlying HMA surface should be cleaned prior to casting, yet there are inconsistent results on whether milling or grinding is necessary (Silfwerbrand and Paulsson 1998; Harrington 2008). With this field project, the milled HMA surface was cleaned using high pressure water to remove dust and loose asphalt pieces, then allowed to dry overnight before casting the FFC. During the FFC casting, the material was spread efficiently using the

chute from the ready mixed concrete truck. When necessary, the concrete was further moved in place with shovels and rakes, as shown in Figure 2-12. A vibratory screed was used to strike-off and externally consolidate the concrete surface. Internal vibration was not necessary on the FFC test sections. Small fiber clumps did occur occasionally in a few truck batches as a result of inadequate shearing during mixing. The visible clumps were removed by hand prior to finishing. A bull-float was used for finishing followed by the application of a curing compound. Roughly four hours after casting, an early-entry saw was used to cut joints, according to the plan in Figure 2-11, for a depth of 13 mm (approximately 1/4 of the slab thickness).

**Figure 2-12 Photograph from construction of the FFC inlay.**

2.5.2. Bonding of FFC to Asphalt

The field slabs were subjected only to thermal cyclic loading over the service life (currently 2 years) since casting. The interface bonding condition was investigated on the field project after the concrete had gained sufficient strength. Use of an in-situ torsion

test determined that the bond produced torque readings of 500 N-m, which was exceptionally high compared to typical HMA overlays at 400 N-m (Tashman et al. 2006). The individual torque readings and location details of the concrete-asphalt interface testing are described in Appendix A.

Section 1 originally contained an asphalt surface which was not completely removed in areas during milling, and therefore left the potential for debonding/sliding between the concrete and underlying asphalt. A chain drag on the surface of the slab further verified that debonding had occurred in some portions of the inlay, especially in section 1, yet no significant impact on crack development was observed.

### 2.5.3. Cracking of FFC Inlay

All transverse and longitudinal joints were cracked by 20 days after construction and joint cracking was induced by the concrete shrinkage and thermal cyclic loading of the slabs. The transverse joints in the largest slabs (section 3) exhibited the most percentage of joints cracked after one day. It was verified that joints which formed cracks after one thermal cycle remained the widest cracked joints at later ages (Roesler et al. 2008b). Joint crack width monitoring was ended due to difficulty of maintaining debris-free joints after the first month. Still, by 20 days, the widest joint cracks were found to be 1.25 mm regardless of the slab size. Average crack widths were found to be 0.4, 0.6, and 0.9 mm for slab lengths of 1.1, 1.7, and 3.4 m, respectively. As expected, the longer the slab length, the greater the measured crack width. Mid-slab cracking was only found after two years, and occurred as 0.2 mm wide corner crack formed after one applied heavy vehicle load event. Further description on the cracking locations and crack widths with age can be found in Appendix A.

## 2.6. Summary

A concrete mixture known as flowable fibrous concrete (FFC) was designed for placement as a 5 cm thin concrete inlay pavement. This FFC mixture was optimized to contain enough macro-fiber-reinforcement to have 2 times the toughness performance compared to typical fiber-reinforced concrete used in UTW applications. Compared to typical slip-form paving concrete, the w/cm ratio and air entraining admixture amounts were similar for paving mixtures, but the FFC mixture implemented a higher cementitious content, smaller maximum aggregate size, higher percentage of sand, micro-fibers, and HRWR to achieve the desired fresh and hardened concrete properties. The FFC required a higher cementitious content to have enough binder for coating all of the fibers while providing the desired workability and toughness performance to the mixture.

The constructability of FFC was evaluated with full-scale sections of the FFC mixture cast as 5 cm thick inlay on a milled asphalt pavement. A total of 99 m of FFC was placed within two hours and consolidated using a vibratory screed. Longer slab sizes produced the earliest and widest cracking at the joints, with these joints cracking before day one and residing as the largest crack widths measured at later ages. The inlay sections predominantly exhibited good interfacial bonding between the milled asphalt and new concrete. Debonding was only found in locations where loosely bonded HMA debris remained at the interface from insufficient milling and cleaning.

Residual strength ratios measured with a 15 cm standard flexural beam at 7 days were roughly 50 percent for FFC mixtures containing 40 or 50 mm long macro-fibers. The use of smaller fiber lengths, such as 20 mm, still achieved higher residual strength ratios than typical UTW pavements with FRC mixtures. Flexural test specimens of 7.5 cm height

resulted in greater toughness properties than the standard 15 cm height specimens for the same FFC mixture. Consequently, the standard toughness test beam size of 15 cm underestimated the post-cracking performance of a 5 cm thick concrete inlay.

# CHAPTER 3. REPRESENTATIVE SPECIMEN AND MODELING FOR FFC TOUGHNESS PERFORMANCE

## 3.1. Motivation

Improved flexural load capacity of slabs has been confirmed with the addition of macro-fibers in concrete and as a result the required concrete slab thickness can be reduced (The Concrete Society 2003; Altoubat et al. 2008; Roesler et al. 2008b). The higher toughness performance of the FFC mixture, due to a higher fiber content relative to that utilized in traditional UTW pavements and higher cementitious content to coat the fibers during pull-out, was anticipated to provide the necessary service life for the thin inlay and to make the design economically viable. A further increase in toughness was also expected due to the anticipated greater alignment of fibers in the FFC inlay by constructing the concrete pavement section with a thickness close to the magnitude to the fiber length. A question arises whether it is appropriate to use the standard 15 cm height flexural beam tests to characterize the enhanced toughness material response of this 5 cm FFC inlay pavement. The discussion in this chapter covers the selection of a beam test size and casting technique in order to properly represent the toughness performance of the 5 cm thin inlay. In addition, the effectiveness of using a finite element fracture-based model to simulate the cracking performance of the FFC at various thicknesses is also evaluated.

## 3.2. Selection of FFC Toughness Testing

### 3.2.1. Background

It is well known that concrete specimens exhibit a strength size effect (Planas et al. 1997; Bažant and Planas 1998). Part of the increased strength for smaller specimen sizes is due

to the existence of boundary surfaces (Bažant and Planas 1998), where the concrete material is predicted to have a different particle packing within a boundary-affected zone. For a FRC material, there was expected to be two different boundary zone sizes with one containing higher amounts of cementitious material rather than aggregates and fibers, and another where fibers become re-oriented due to limited fiber packing against a surface. Due to this boundary-affected zone, a reduced beam height is expected to demonstrate a higher measured nominal peak strength. According to the strength size effect theory, the measured nominal peak strength increases as the characteristic dimension, such as the beam specimen height, decreases. Thus, it was anticipated that by reducing the specimen height to 50 mm in order to represent the fracture response of the thin FFC inlay, the nominal strength would also increase.

Post-cracking residual stresses and residual strength ratios have also been found to increase for FRC flexural beams of reduced specimen sizes from 150 to 70 mm in height, for the same concrete mixture (Ward and Li 1990; Altoubat et al. 2004; Stähli and van Mier 2007; Giaccio et al. 2008; Jiang and Banthia 2010). Because the residual strength ratio has been found to correlate with the load carrying capacity of a FRC slab, a measured increase in this residual strength ratio of these smaller tested beams may result in the assumption that the FRC pavement slab thickness can be reduced. By constructing a 5 cm thick FRC inlay, the peak and post-peak strengths will both be apparently higher than for 10 to 15 cm thick UTW pavements. However it was anticipated that the measured increase, particularly in post-cracking strength was related to more fiber alignment within this boundary-affected zone. Further research was needed to

understand and characterize the effects of having a boundary surface on the measured post-cracking performance.

A variety of test methods and specimen geometries exist to capture the residual or post-cracking toughness performance of FRC (Gopalaratnam and Gettu 1995; ASTM Standard C1399a 2007; ASTM Standard C1609 2007; ASTM Standard C1550 2008). By measuring the post-cracking properties, the effect of fiber-reinforced on the overall performance of the concrete structure can be estimated. Standard flexural beam tests are used to determine the FRC material toughness based on either a 100 or 150 mm beam height cast specimen (ASTM Standard C1609 2007). These standard tests are appropriate for concrete pavements of similar or greater design thicknesses. Nevertheless, as the target thickness of the inlay design for FFC is reduced to 50 mm, a smaller, more representative sample beam height should be utilized in determining the toughness performance for these thin pavement designs. For thin concrete applications such as shotcrete walls, researchers have recommended using more plate-like test (e.g., ASTM 1550) specimens to characterize the toughness performance of implementing FRC (Gopalaratnam and Gettu 1995). The main problem with smaller specimens has been the increased statistical variability of the measured properties (Bažant and Planas 1998; Stähli and van Mier 2007), particularly as the specimen dimensions approached the physical size of the material components in the FRC mixture. Despite the expected increase in variation of a small sample, it is desired to find a representative test which can predict the enhanced toughness performance of a 5 cm thick concrete inlay.

### 3.2.2. FFC Toughness Test Specimens

Two beam test methods were examined for this research: an unnotched toughness beam and a single-edge notched beam (SEN[B]) fracture test. The unnotched flexural beam samples were utilized in this research to measure the post-cracking toughness performance of the FFC mixture, because the computed residual strength ratio from this test has been found to correlate with full-scale concrete slab performance (Roesler et al. 2006; Gaedicke et al. 2009). In addition, this standard unnotched beam test using a 15 cm height beam has been implemented for determining post-cracking performance of FRC use in designing UTW pavements (ASTM Standard C1609 2007; Roesler et al. 2008b). Fracture testing was also utilized in order to compute size-independent initial fracture properties useful for finite element modeling and is also based on a 15 cm height SEN[B]. The notched specimen is critical for modeling the material in different specimen geometries, while the unnotched test can be used for more practical engineering evaluation of a viable FFC mixture based on its toughness properties. The suitability of using these existing specimen standards (based on 15 cm height beams) to simulate the post-cracking response of the 5 cm FFC inlay was investigated. Table 3-1 summarizes alternative geometrically-similar beam dimensions and construction techniques that were explored.

**Table 3-1 Toughness Specimen Summary**

| | Final Specimen Height (cm) | | |
|---|---|---|---|
| | 5 | 7.5 | 15 |
| Unnotched Flexural Specimen Preparation* | | | |
| Cast as final height | x | x | X |
| Cut from 15 cm beam | x | x | |
| Cut from 5 cm plate thickness | x | | |
| SEN[B] Fracture Specimen Preparation† | | | |
| Cast as final height | x | | X |
| Cut from 15 cm beam | x | | |
| Cut from 5 cm plate thickness | x | | |

* Concrete for all unnotched flexural specimens was rodded for consolidation.
† Concrete for all SEN[B] fracture specimens was externally consolidated with a mallet.

Smaller beam sizes were considered, of the same thickness as the 5 cm thick inlay, aimed at having a representative toughness performance as the inlay pavement. For the unnotched toughness test, beam specimens were cast at various heights (5, 7.5 and 15 cm) to determine the magnitude of expected increase in post-cracking strength for a 5 cm FFC inlay. Similarly, fracture testing of 5 cm and 15 cm beams was performed to determine size-effects on the measured total fracture energy. The impact of boundary surface walls on the measured toughness was studied by comparing 7.5 cm beam specimens cut from the center of a cast 15 cm standard flexural beam to 7.5 cm beam with a mold surface on three sides. Thin 5 cm plate specimens were tested with both the unnotched toughness test, as presented herein, and with the fracture test, as found in Chapter 4, to compare post-cracking performance from having boundaries on two opposing sides (cast and mold).

### 3.2.3. Unnotched Flexural Toughness Test

The unnotched (four-point bending) flexural beam test using deformation control for pre- and post-peak behavior was performed for each prism beam of heights 5, 7.5 or 15 cm. The unnotched beam specimens had a constant span/height ratio of 3, a height-to-width

ratio of 1, and were tested on their side relative to the cast surface (see Figure 3-1), according to the ASTM C1609 standard geometry recommendations. These unnotched test beams (7.5 cm and 15 cm mold height) were originally cast during the field project (see Table 2-3 for FFC field mixture) and the FFC material was placed randomly into the molds and consolidated using a rodding technique. Similar placement and consolidation was performed in the laboratory on additional unnotched specimens. These laboratory FFC specimens contained only the Strux 90/40 macro-fibers (no micro-fibers), as listed in Table 2-3, to focus on the toughness enhancements from macro-fiber reinforcement. Additional to the molded specimens cast in the field, 15 cm height beams were constructed in the laboratory for which 5 and 7.5 cm beams were cut in order to determine the material properties without boundary wall effects. 5 cm thick plates were also constructed in the laboratory to simulate a realistic boundary effect found in a thin FFC inlay. Because the typical test geometry utilizes a beam rather than a plate, several 5 x 5 cm beams were cut from within the cast plate. Again, the measured residual strength ratios from specimens originally cast as a 5 cm plate were expected be the highest due to the reduced specimen height and the influence of boundary surfaces to produce better fiber alignment in the direction of the maximum tensile stress.

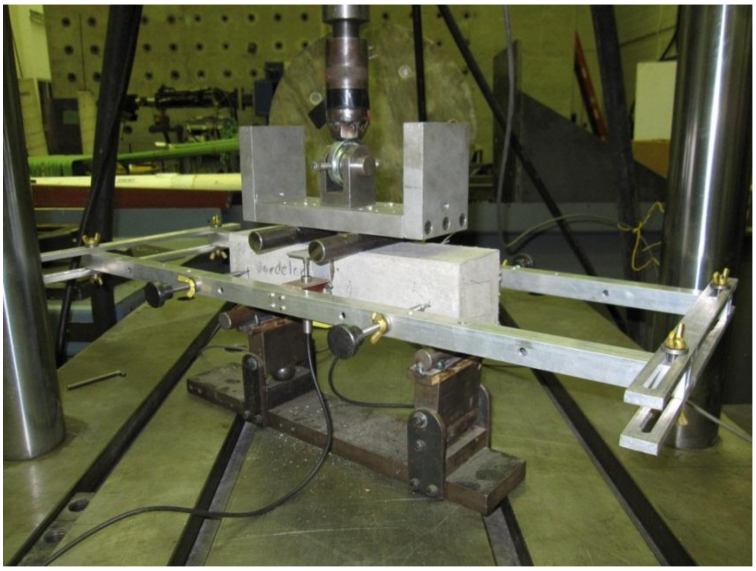

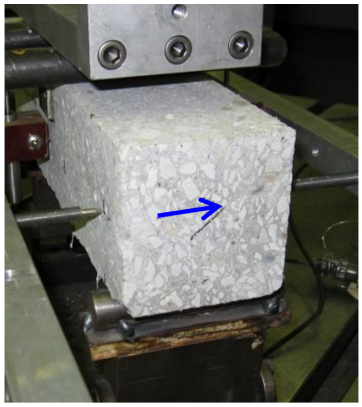

The arrow denotes the direction of cast surface with respect to loading.

**Figure 3-1 Loading frame and deflection gauge for 7.5 cm unnotched four-point bending beam test. Insert on right illustrates specimen loaded on side.**

## 3.3. Reduced Specimen Height Effect on Toughness

The unnotched beam results indicated that both the strength and post-cracking residual strength ratio increased for 7.5 cm cast specimens compared to 15 cm cast specimens. The apparent flexural strength, shown in Table 3-2, increased by about 10% for a 7.5 cm beam compared to the 15 cm beam. Among the cast and rodded FFC specimens, from 5 to 15 cm in height, the average residual strength ratios listed in Table 3-2 appeared not to vary significantly with the beam height. Furthermore, as seen in Figure 3-2, the post-cracking performance of a 5 cm height cast beam exhibited an increased toughness for deflections over the 1 mm used for computing residual strength ratio $R^{150}{}_{150}$ listed in Table 3-2. Regardless of specimen height, the desired 50 percent residual strength ratio (see Table 3-2) could be achieved with casting beam specimens of the FFC mixture containing the Strux 90/40 macro-fibers.

**Table 3-2 Flexure Results for Unnotched Beams**

| Tested Beam Dimensions | Construction Technique and Geometry | | Age (days) | Peak Flexural Strength (MPa) | | Residual Strength Ratio, $R_{150}$ * | |
|---|---|---|---|---|---|---|---|
| 5 x 5 x 20 cm‡ | Rodded | Plate† | 14 | 5.52 | (5%) | 68% | (30%) |
| | | Cast | 14 | 4.78 | (3%) | 51% | (13%) |
| | | Cut | 14 | 6.11 | (1%) | 68% | (4%) |
| 7.5 x 7.5 x 29 cm | Rodded | Cast | 7 | 4.16 | (3%) | 50% | (10%) |
| | | Cut | 7 | 4.33 | (1%) | 33% | (13%) |
| 15 x 15 x 53 cm | Rodded | Cast | 7 | 3.78 | (8%) | 48% | (17%) |

Average values and coefficients of variation in parentheses are for two (or †four) samples.

*Residual strength ratio is computed for a deflection of S/150 (i.e. 1 mm or 1.5 mm deflection for a 5 or 7.5 cm beam, respectively).

‡5 cm tested beams contained the laboratory FFC mixture with only 0.46% $V_f$ of Strux 90/40; all other beams contained the Strux 90/40 and Fibromac 6 fibers in FFC mixture from the field demonstration.

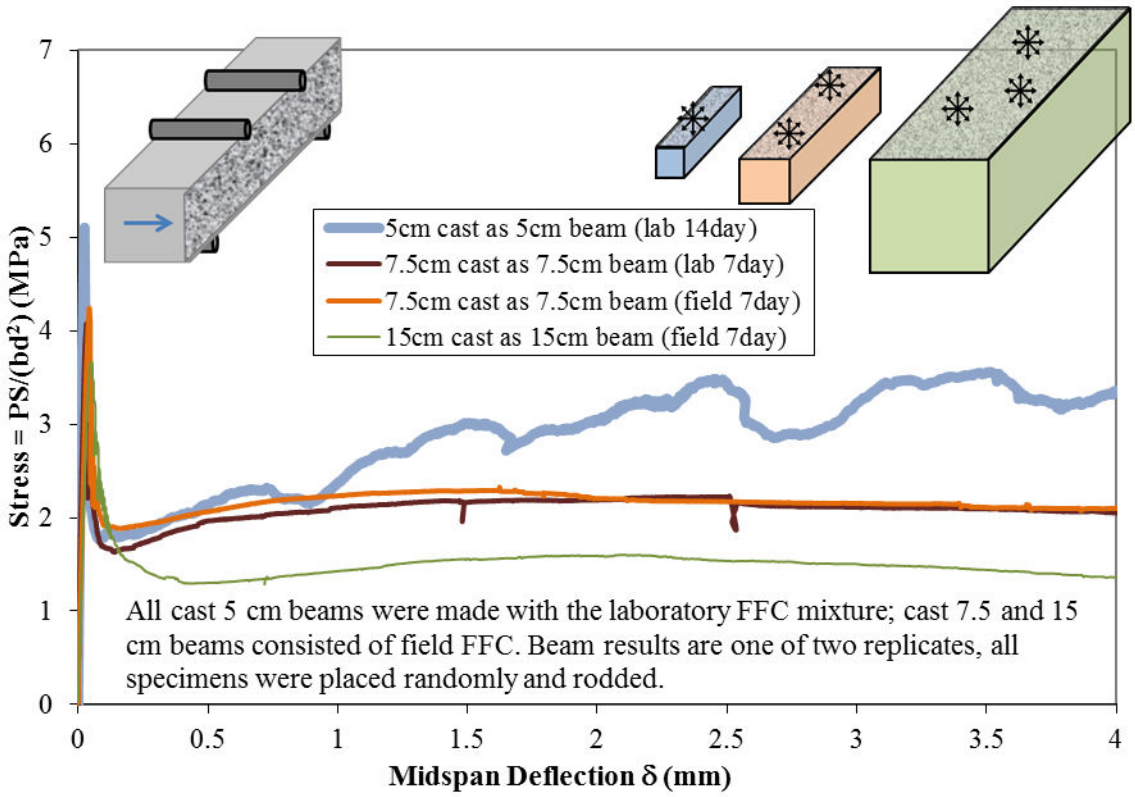


**Figure 3-2 Flexural unnotched beam stress versus a normalized deflection curves comparing cast specimens of 5, 7.5 or 15 cm in height.**

3.3.1. Influence of Boundary Wall on Toughness

The effects of the boundary wall were negated by cutting beams from the central interior of a 15 cm beam. In Figure 3-3, a 7.5 cm beam cut from within a 15 cm beam was shown to result in similar residual stresses as the standard 15 cm beam. On the contrary, a 7.5 cm beam when cast in a mold had an improved residual strength. The increased residual performance was similar to other research findings which stated that the influence of a mold surface improved toughness (Stähli and van Mier 2007). It was hypothesized that the proximity of the cast surface and molded walls relative to the fiber length would enhance the fiber alignment in the beam, and the overall residual strength of the material would improve for smaller beam sizes.

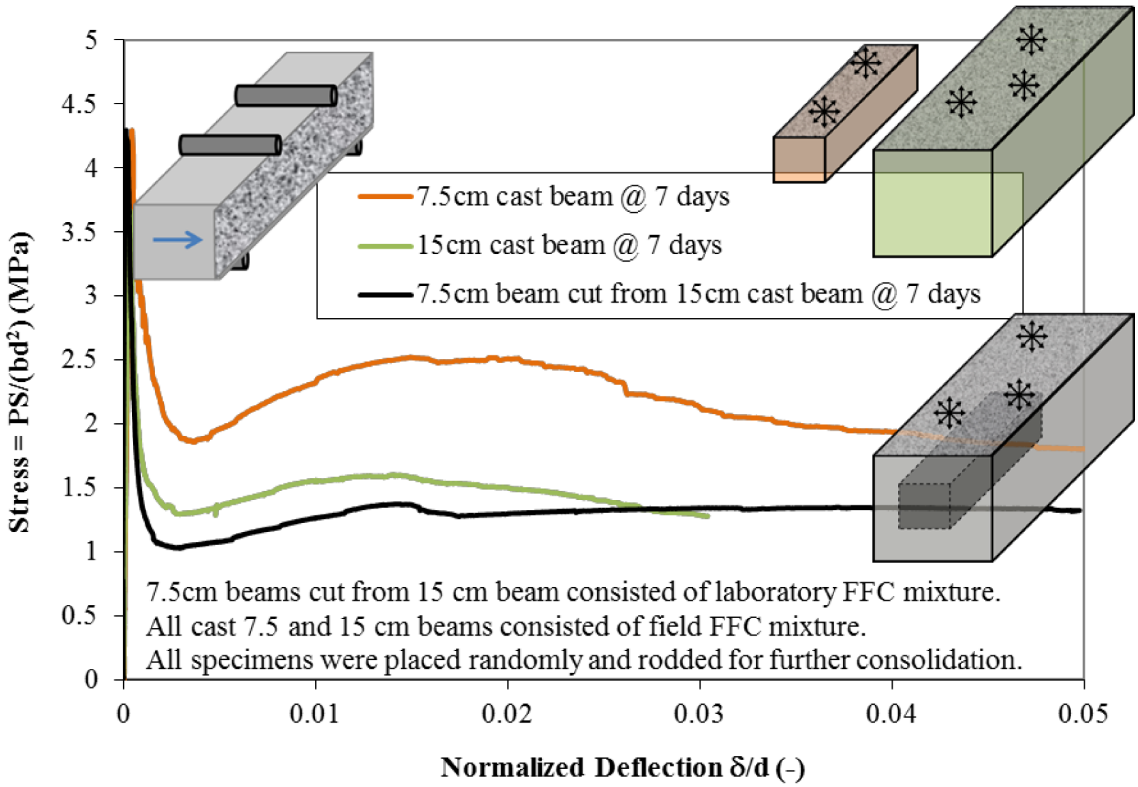


**Figure 3-3 Flexural stress versus a normalized deflection (midspan deflection/beam height) curves comparing between 7.5 beams either cut from 15 cm beam or cast in a 7.5 cm mold.**

The cut 7.5 cm and cast 15 cm beam produced similar residual strengths at 7 days, as both FFC specimens likely had similar fiber alignments. However, the cut 5 cm beam at 14 days had a significant jump in residual strength (see Figure 3-4 for a plot of beams cut from a 15 cm beam and normalized by the peak strength) which was not expected. The variation between two 5 cm beams cut from within a 15 cm beam was very low (with a COV of 4%). Thus, an explanation for this higher residual strength in the 5 cm cut beam was expected to be related to a potentially higher number of fibers found at the location of the cut 5 cm beam within the 15 cm beam. A technique to identify information on the synthetic fiber distribution and orientation within the concrete, such as with the x-ray computed tomographic imaging, is presented in Chapter 4.

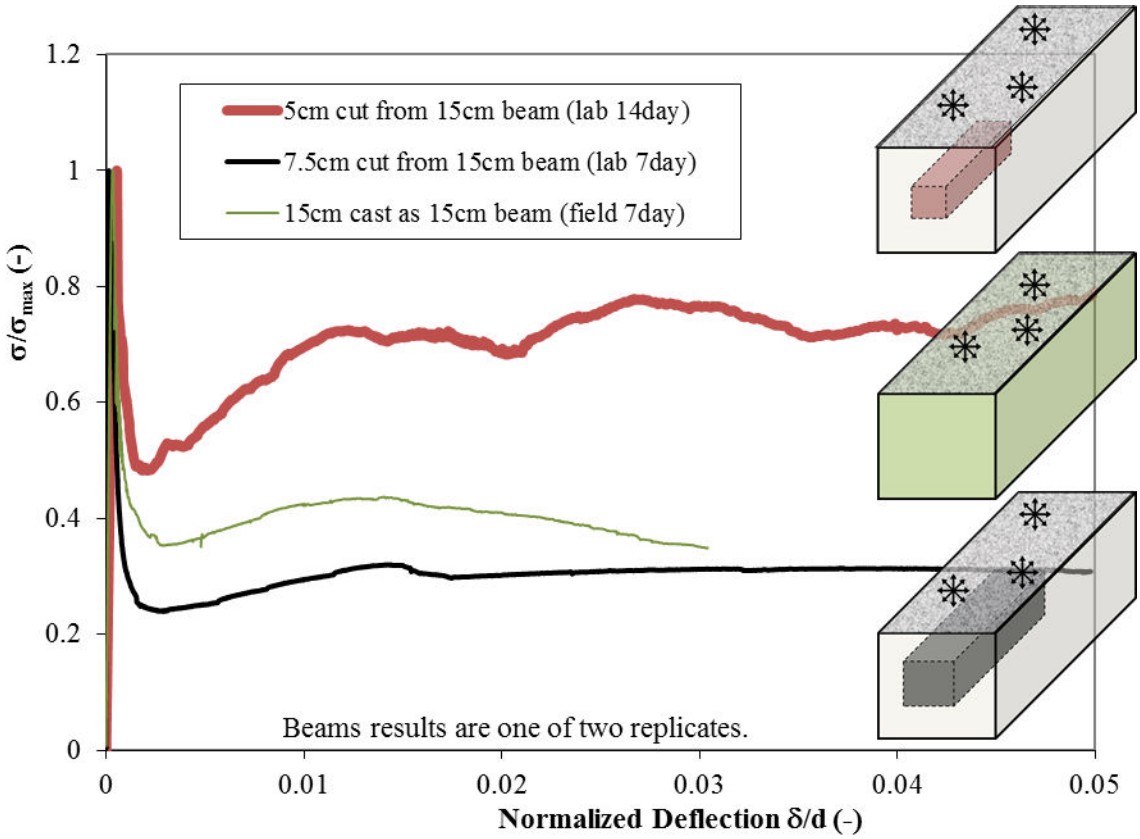


**Figure 3-4 Flexural stress normalized by the peak strength versus a normalized deflection (midspan deflection/specimen height) curves comparing a 5 cm and a 7.5 cm beams cut from the interior of a cast 15cm beam.**

From the 7.5 cm unnotched beam flexural behavior in Figure 3-3, it was clear that boundary surfaces contributed to the measured toughness performance. Additional testing was performed on specimens cast as a thin plate specimen of 5 cm in height. These plate specimens were expected to be the best representation of the same boundary conditions as the field inlay. For measuring the performance of the 5 cm thick plate, the same four-point bending unnotched flexural testing was either done for a full plate or for 5 x 5 cm beams cut from within the plate. In order to understand the impact on post-cracking residual strength from having two boundary surfaces of a thin pavement inlay, plate specimens 5 cm in height were also constructed and tested. The Figure 3-5 illustrates flexural results of full cast 5 cm plate which is 15 cm wide with a 45 cm span between supports versus small beams 5 x 5 cm (15 cm span) cut from a cast 5 cm thick plate. The tested 5 cm thick plate and the 5 cm beam cut from a plate were geometrically similar with a constant span to width of 3 (as opposed to a constant span to height of 3 among other unnotched beam tests). The average residual strength ratio was 68 percent (listed in Table 3-2) for the 5 cm beams cut from the plate. There was a high coefficient of variation of 30% for the residual strength ratio of these 5 cm beams cast as a plate. This higher COV was assumed to be related to the random distribution of fibers and the potentially altered alignment of these fibers due to the consolidation by rodding. As a result, the one 5 cm beam cut from the center of the thin plate which demonstrated significant deflection hardening in Figure 3-5, was anticipated to be due to a potentially higher fiber concentration or clumping at that location in the plate. By testing a full plate (15 cm width), the post-cracking flexural curves between specimens were more consistent due to a more average toughness from fibers across the entire plate width.

Results suggest that toughness measurements averaged from several 5 cm beams cut from a 5 cm thick plate did produce comparable results as a wide plate 5 cm thick containing the FFC material.

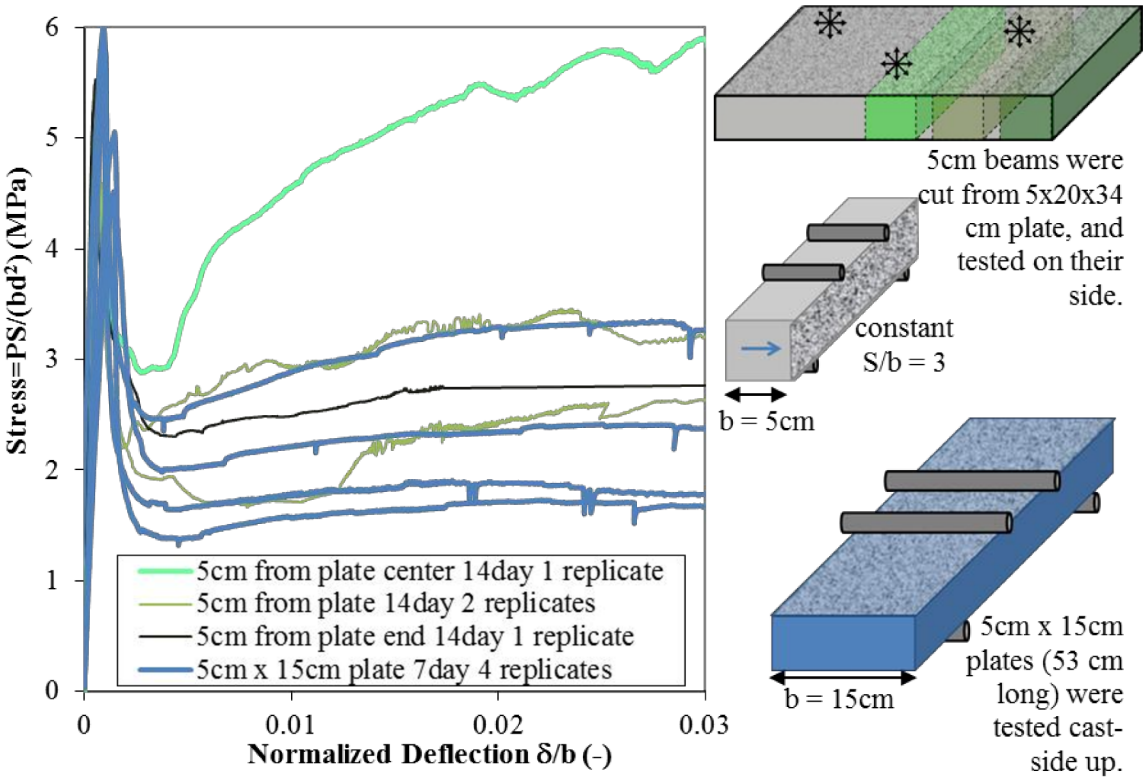


**Figure 3-5 Flexural stress versus a normalized deflection (midspan deflection/specimen width) curves of tested specimens cast as a 5 cm plate or cut 5x5 cm beams from a 5 cm plate.**

3.3.2. Consolidation Technique Effect

The rodding technique initially used to consolidate FFC specimens was not recommended for future specimens. It was assumed this rodding construction technique altered the fiber orientation, disrupting the natural fiber alignment produced by casting a thin 5 cm plate. Since the field FFC utilized some external compaction from the vibratory screed, further laboratory specimens (constructed for notched fracture testing) were consolidated externally using only the tapping of a mallet and a surface strike off.

### 3.3.3. Test Selection

The unnotched test results for specimens of 5 cm in height cut from a cast 5 cm plate were expected to have the best representation of toughness performance for the FFC inlay of the same thickness. Although standardized testing can still be performed using a 15 cm beam in order to achieve the material properties of the FFC mixture, the toughness properties measured will underestimate the potentially higher performance for the thin inlay pavement. A fracture test was suggested for further testing rather than unnotched beam tests for determining the performance of the FFC inlay, because the calculated initial fracture properties are known to be size-independent. The calculated fracture properties were expected to be the same for any specimen height, for the same FFC mixture and the same expected fiber alignment. Any increase in post-cracking flexural behavior of a notched specimen resulting in higher fracture energy measurements was assumed to be a directly result of either more fiber alignment or an increase in the fiber content localized at the fracture plane.

## 3.4. FFC Fracture Properties with 5 cm Beams

### 3.4.1. SEN[B] Fracture Test

The fracture testing described in Chapter 2 was selected for characterizing the FFC mixture through size-independent material properties, versus the residual strength index property determined from the unnotched flexural test. The fracture properties can also be incorporated into local cohesive fracture models with finite element modeling to simulate the global response of the material in various geometries.

Several 5x5x23 cm beams were cut from within a 15x15x53 cm cast beam and tested as a SEN[B] for fracture properties. In comparison, the standard 15 cm SEN[B] beam with the dimensions of 15x8x70 cm was also cast with the same FFC mixture and tested. All SEN[B] tests contained the same span/height ratio of 4. The FFC mixture used in the fracture testing (listed in Table 2-3) contained only the 0.46 percent Strux 90/40 macro-fibers (no micro-fibers) and all tests were performed at 7 days after costruction. All of these fracture FFC specimens were placed randomly into beam molds and were consolidated with a mallet tapped on the side of the molds.

### 3.4.2. Plain Concrete

Beams of un-reinforced flowable concrete were tested to determine the magnitude of anticipated increase in nominal strength of the FFC when reducing the thickness from 15 cm to 5 cm. The notched fracture beam height of 5 cm was found to have a significantly increased nominal strength of 59% (shown in Figure 3-6 and Table 3-3) compared to the standard 15 cm beam height. The initial fracture properties ($K_{Ic}$, $CTOD_c$, and $G_{Ic}$) derived for the plain concrete SEN[B] specimens were similar between both the 5 and 15 cm specimens, as expected for "size-independent" properties. The total fracture energies for the 5 and 15 cm beam height SEN[B] specimens were also within approximately 10% of each other. The fracture properties shown in Table 3-3 for this un-reinforced flowable concrete were also similar to that recorded for conventional un-reinforced concrete mixtures from past pavement projects (Roesler et al. 2008b) as listed in Table 1-1. Despite the differences in aggregate size and proportioning, the higher cementitious content, and increased workability, the fracture properties of the FFC matrix was at minimum similar to conventional concrete used for pavements.

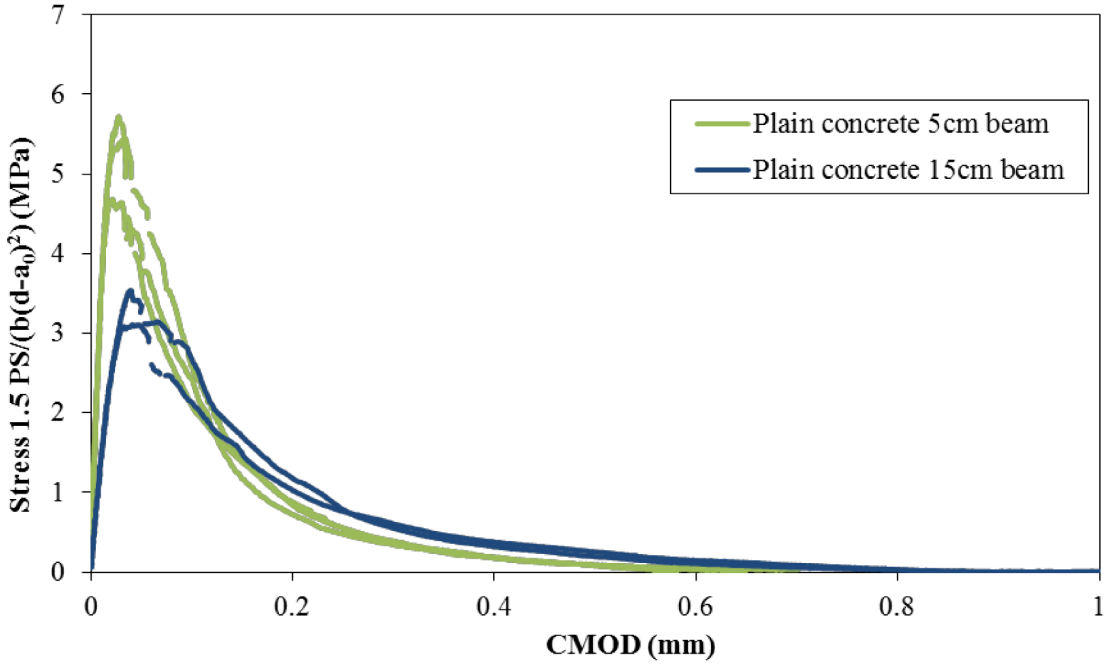


**Figure 3-6 Nominal stress curves for plain concrete of 5 cm beams cut from 15 cm and cast 15 cm height beams.**

**Table 3-3 Fracture Results for Beams Randomly-Placed**

| Mixture | Construction Method | Beam Height | Age | $1.5P_{max}S/(b(d-a_0))$ | $K_{Ic}$ | $CTOD_c$ | $G_{Ic}$ | $G_{PCC}$ or $G_{FRC}$ |
|---|---|---|---|---|---|---|---|---|
| | | | (days) | (MPa) | (MPa-$m^{1/2}$) | (mm) | (N/m) | (N/m) |
| Plain | Random | 5 cm† | 7 | 5.28 (10%) | 0.84 (7%) | 0.011 (7%) | 31 (17%) | 71 (7%) |
| | | 15 cm* | 7 | 3.32 (9%) | 0.87 (3%) | 0.017 (22%) | 32 (1%) | 80 (5%) |
| FFC | Random | 5 cm‡ | 7 | 5.10 (9%) | 0.78 (12%) | 0.010 (13%) | 28 (19%) | 5862 (33%) |
| | | 15 cm† | 7 | 3.66 (19%) | 1.06 (2%) | 0.024 (6%) | 47 (5%) | 5667 (13%) |

Values reported are averages of *two, †three or ‡eight specimens.
Numbers in parentheses are the computed coefficients of variation.
The SEN[B] 5 cm beams were all cut from a cast 15x15x53 cm beam.

### 3.4.3. FFC

With the addition of Strux 90/40 macro-fibers to the flowable concrete, there was a slight increase in the measured initial fracture properties for the 15 cm fracture beams (see Table 3-3). As expected, the total fracture energy of the FFC mixture increased by 71 times that of the un-reinforced flowable concrete, as measured from the 15 cm standard SEN[B]. The total fracture energy on average measured from the 5 cm SEN[B] specimens were in fact similar to that of the 15 cm SEN[B] near 6000 N/m (as shown in Table 3-3). This is unlike the residual strength ratio trend of the cast unnotched toughness testing specimens. Because these 5 cm SEN[B] specimens were cut from the interior of a cast 15 cm beam, it is reasonable that the average total fracture energy would be similar and the SEN[B] results are size-independent.

For both 5 and 15 cm fracture beams, the average total fracture energy was significantly higher than other FRC mixtures for pavement applications. Many of the UTW pavement mixtures produced total fracture energies of 3500 N/m for both 0.4 percent volume fraction of Strux 90/40 fibers (as shown in Table 1-1) or even at higher fiber content pavement mixtures at 0.78 percent volume fraction of the Strux 90/40 fiber (Roesler et al. 2007; Park et al. 2010). This means that by having a more flowable mixture could have resulted in more aligned fibers within the 15 cm beam or with a higher cement content to cover the fibers, an improved the fiber-matrix bond strength and friction during fiber pull-out may increase the total fracture energy. Therefore, by utilizing a FFC mixture instead of a conventional concrete pavement mixture, the total fracture energy measured even from a 15 cm standard SEN[B] can be improved by at least 60%.

The large variation of 33 percent in the total fracture energy of the 5 cm beams reported in Table 3-3 was attributed to the location within the 15 cm beam for which these 5 cm beams were extracted, as seen in Figure 3-7. It was anticipated that an increase in the fracture energy would occur in the FFC especially when there is more fiber alignment due to close proximity of boundary surfaces. Figure 3-7 illustrates the post-peak fracture response of these 5 cm beams with respect to their location within the 15 cm beam, as compared to the fracture response of the standard 15 cm SEN[B] test specimen. For these SEN[B] specimens containing the Strux 90/40 macro-fibers in FFC, a clear trend was observed that the 5 cm beams originating near the bottom mold of a 15 cm beam had higher fracture energy curves than a 5 cm beam from the top cast surface of a 15 cm beam.

Initially it was thought that segregation of fibers may have generated a non-uniform variation in the number of fibers found throughout the beam. However, the number of fibers crossing the fracture plane was found to be roughly equivalent (around 8000 fibers/$m^2$) for the 5 cm beams cut from the top and bottom of the 15 cm beam. Again, it was hypothesized that the fibers within the FFC were more aligned perpendicular to the fracture plane and thus improved the specimen fracture performance. Using a non-destructive imaging of the FFC specimens to determine the fiber orientation, further insight can be made into the fracture behavior of FFC specimens.

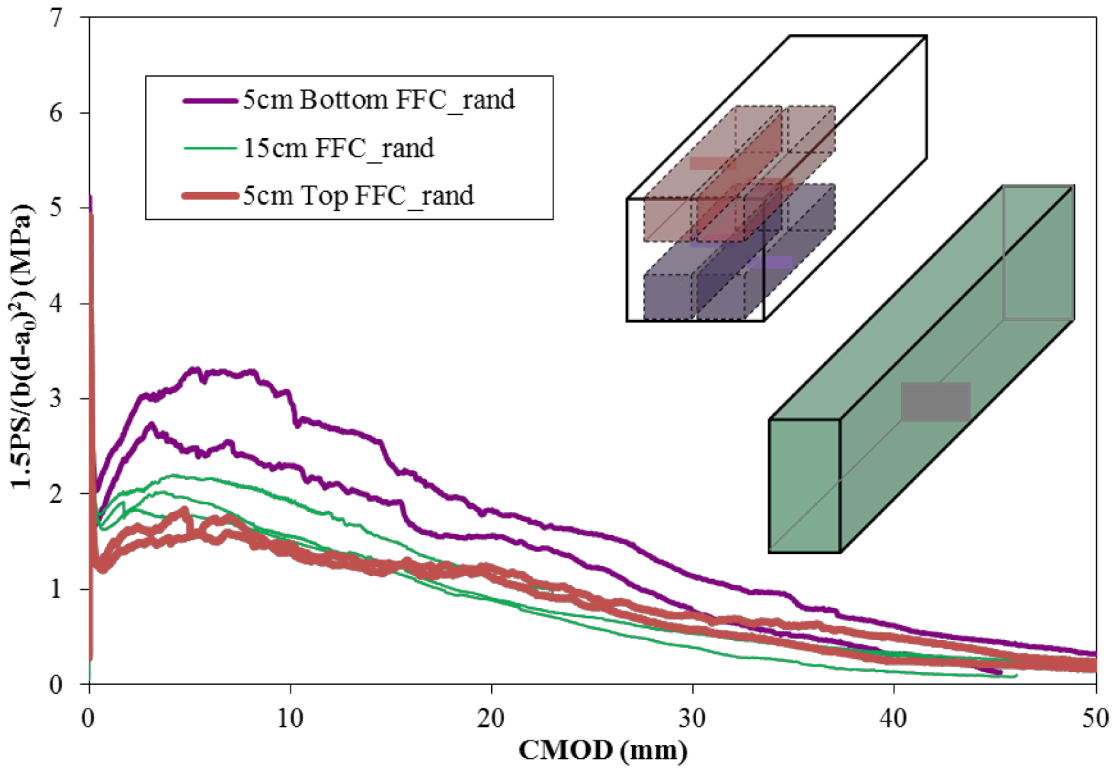


**Figure 3-7 Fracture beams stress versus CMOD curves for FFC placed randomly into 15 cm beam molds.**

## 3.5. Finite Element Analysis

Fracture properties can be used with finite element modeling (FEM) to predict cracking performance of concrete structures and pavements primarily in mode I (crack opening). A 2D finite element analysis using the cohesive zone model has been implemented in past research (Roesler et al. 2007; Park et al. 2010) to reproduce the toughness performance of FRC mixtures used in concrete pavements. The same FEM approach, using a tri-linear cohesive crack model, was utilized in this research to understand the applicability for characterizing the fracture performance of the FFC containing 0.46 percent volume fraction of macro-fibers. The FEM implementation used the measured fracture parameters from Table 3-3. Finally, analysis was needed to assist in determining

limitations of this modeling which may exist for certain specimen geometries with the FFC material.

The FEM approach, as illustrated in Figure 3-8, used the measured fracture parameters ($G_f$, $CTOD_c$, $G_{FRC}$, and $w_f$) and tensile strength of the FFC to predict the overall response of the SEN[B]. Computer software programs PATRAN® and ABAQUS® were utilized for generating the specimen mesh geometry and for performing the damage softening analysis of the cohesive crack elements, respectively.

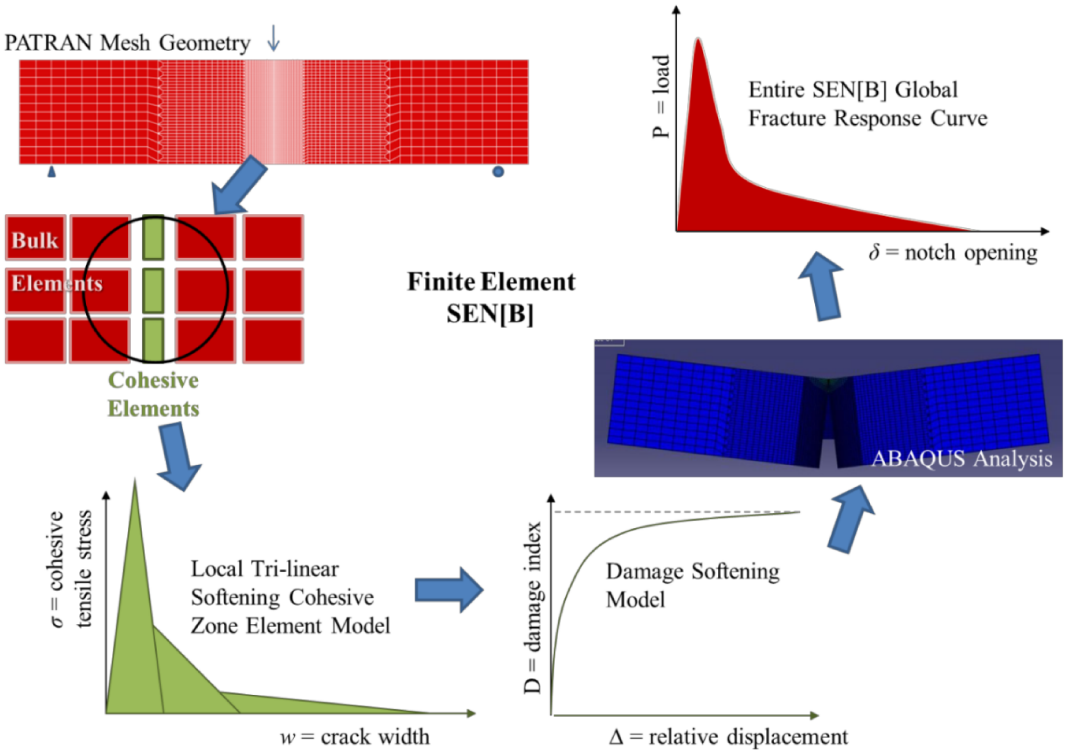


**Figure 3-8 Approach for using the finite element fracture-based method with meshing the specimen geometry and defining the cohesive zone element softening curve.**

## 3.6. Cohesive Zone Tension Softening Model Definition

A cohesive zone model (CZM) was used to describe the specified tension-softening behavior along the expected crack location. As bi-linear tension-softening curve models

(containing one post-cracking kink point) have been known to accurately simulate the fracture performance of un-reinforced concrete (Elices et al. 1992; Olesen 2001; Østergaard et al. 2004; Roesler et al. 2007; Park et al. 2008), this same model was utilized for simulating the flowable un-reinforced concrete mixture. For FRC, researchers have described the fracture performance with either tri-linear (Park et al. 2010) or poly-linear (Löfgren et al. 2008) softening curves requiring additional input parameters to describe the increase in total fracture energy due to the addition of fibers in the concrete.

Recent research of FRC (Löfgren et al. 2008; Shen et al. 2008; Park et al. 2010) with a wide range of macro-fiber types and specimen geometries have shown the CZM can be used to describe the global response of the FRC for larger specimen sizes (15 cm height). The tri-linear tension-softening curve was selected to define the constitutive relationship for the FFC mixture based on the experimentally measured fracture properties. The size-independent initial fracture energy $G_{f1}$ and other material properties measured from the FFC specimens (such as the total fracture energy for un-reinforced flowable concrete $G_{f2}$, total fracture energy for fiber-reinforced concrete $G_{FRC}$, and the split-tensile strength $f_{sp}$) were used to define the tri-linear softening model, as illustrated in Figure 3-9. Equations for the tri-linear softening cohesive zone element model were based on past definitions (Roesler et al. 2007; Gaedicke 2009; Park et al. 2010).

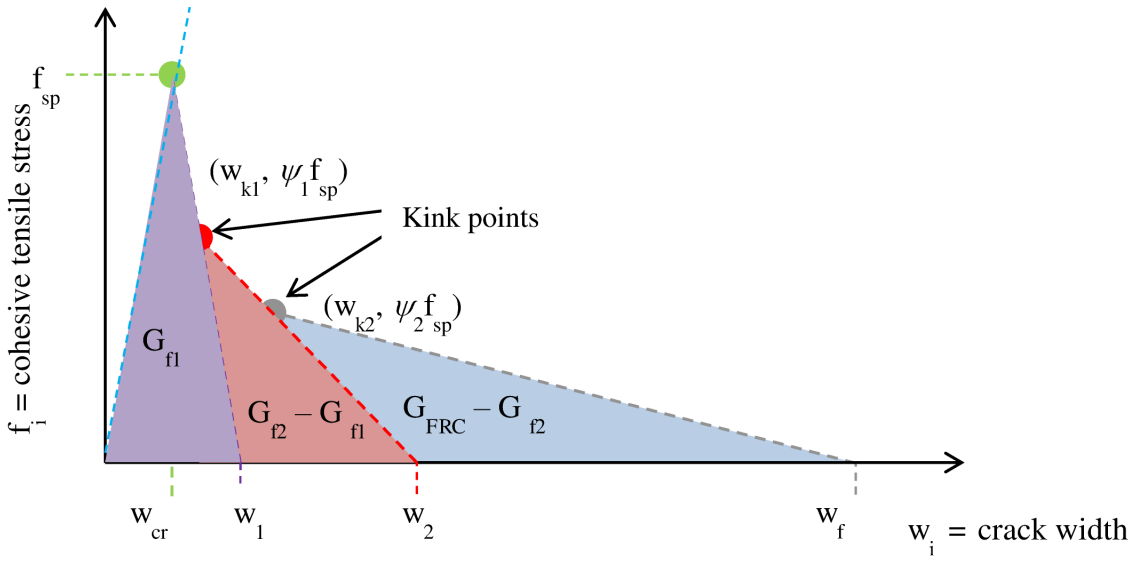


**Figure 3-9 Tri-linear tension-softening model based on the measured fracture properties and tensile strength of the concrete.**

The equations below were utilized based on the measured tensile strength and the computed initial fracture energy $G_{f1}$ of the FFC mixture in order to compute the first kink point $w_{k1}$. Due to the increase in initial fracture energy measured by the 15 cm SEN[B] with the FFC, compared to the un-reinforced flowable concrete and that of a 5 cm FFC specimen test, this first kink point as shown in Figure 3-10 was located at a slightly higher crack width for the 15 cm FFC fracture simulation.

$$w_{k1} = w_1 - \Psi_1 \; w_1 - w_{cr}$$

where:

$$w_1 = \frac{2G_{f1}}{f_{sp}}$$

$$\Psi_1 = 0.25$$

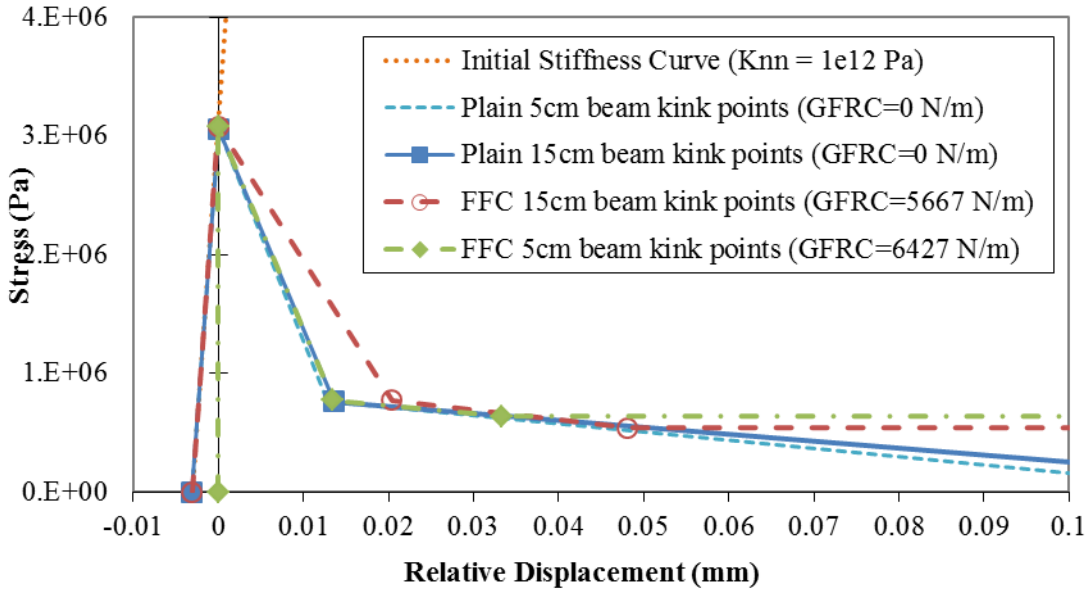


**Figure 3-10 Tri-linear tension softening curves used in for un-reinforced and Strux 90/40 fiber-reinforced FFC.**

The calculation of the second kink point was based on the following equations, which use the total fracture energy measured from the un-reinforced flowable concrete $G_{f2}$, the total fracture energy of the FFC $G_{FRC}$, and the final crack opening width $w_f$. The simulated global post-peak response is significantly impacted by the total fracture energy of the fiber-reinforced concrete, as well as the final crack opening width, defined relative to the length of the macro-fibers in the FFC.

$$w_{k2} = w_2 - \frac{\Psi_2}{\Psi_1}\ w_2 - w_{k1}$$

where:

$$w_2 = \frac{2}{\Psi_1 f_{sp}}\ G_{f2} - \ 1 - \Psi_1\ G_{f1}$$

$$\Psi_2 = \frac{2\ G_{FRC} - G_{f2}}{f_{sp}\ w_f - w_2}$$

Finite element simulations were run with the experimentally derived fracture properties of the FFC, both without reinforcement and with the macro-fiber reinforcement, and for two different specimen heights. The relevant properties required in defining the bi-linear and tri-linear curves for un-reinforced and FFC concrete were listed in Table 3-4. Some input property assumptions were made based on previous researcher's experience. For example, the initial penalty stiffness $K_{nn}$ of 1e12 Pa/m (Gaedicke 2009) was selected after some preliminary simulations were used to determine this stiffness was sufficient for the FEM to reach the tensile strength at a reasonable crack opening. The definition of the final crack width has been suggested by past researchers to be between $L_f/4$ and $L_f/2$ (Roesler et al. 2007; Gaedicke 2009; Park et al. 2010). For the opening displacement range of 0.2 to 1.0 mm, the larger final crack width of $L_f/2$ resulted in a closer post-cracking response to the experimental FFC data.

**Table 3-4 FEM Input and Calculated Properties**

| | | Plain Concrete | | FFC (Strux 90/40 fibers) | | FFC (BT50 fibers) † | |
|---|---|---|---|---|---|---|---|
| Beam Height = | | 5 cm | 15 cm | 5 cm | 15 cm | 5 cm | 5 cm |
| Input Properties | | | | | | | |
| E | GPa | 26.5 | 26.5 | 26.3 | 26.3 | 27.7 | 27.7 |
| υ | - | 0.15 | 0.15 | 0.15 | 0.15 | 0.15 | 0.15 |
| ρ | $kg/m^3$ | 2,313 | 2,313 | 2,318 | 2,318 | 2,350 | 2,350 |
| fsp | MPa | 3.05 | 3.05 | 3.08 | 3.08 | 3.70 | 3.70 |
| Gf1 | N/m | 30.9 | 32.2 | 27.7 | 46.6 | 28.0 | 28.0 |
| Gf2 | N/m | 71 | 80 | 71 | 80 | 71 | 71 |
| GFRC | N/m | - | - | 6,427 | 5,667 | 990 | 8,677 |
| CTODc | mm | 11.1 | 16.9 | 10.3 | 24.0 | 9.2 | 12.8 |
| Lf | mm | 40 | 40 | 40 | 40 | 48 | 48 |
| Knn | Pa/m | 1e12 | 1e12 | 1e12 | 1e12 | 1e12 | 1e12 |
| Kss | GPa/m | 435 | 435 | 435 | 435 | 435 | 435 |
| wcr | μm | 3.05 | 3.05 | 3.08 | 3.08 | 3.70 | 3.70 |
| Calculated Properties | | | | | | | |
| w1 | μm | 20.2 | 21.1 | 18.0 | 30.2 | 15.1 | 15.1 |
| wk1 | μm | 15.9 | 16.6 | 14.3 | 23.5 | 12.3 | 12.3 |
| Ψ1 | - | 0.25 | 0.25 | 0.25 | 0.25 | 0.25 | 0.25 |
| w2 | μm | 125.4 | 146.4 | 130.4 | 117.0 | 108.1 | 108.1 |
| wf | mm | - | - | 20 | 20 | 24 | 24 |
| Ψ2 | - | - | - | 0.28 | 0.24 | 0.02 | 0.19 |
| wk2 | μm | - | - | 33.9 | 48.7 | 100.1 | 33.5 |

Mixtures were randomly placed into beam specimens.
†Values are from a single 5 cm fracture beam result; cut from the bottom of a 15 cm cast beam.

## 3.7. Finite Element Analysis versus Experimental Results

### 3.7.1. Un-reinforced Flowable Concrete Results with Bilinear Softening

Finite element modeling using a bi-linear softening curve verified that the test results of un-reinforced flowable concrete for 5 cm and 15 cm height SEN[B] specimens could be reasonably predicted. Figure 3-11 shows the global FEM response versus the experimental results for these the 5 and 15 cm SEN[B] un-reinforced specimens. As anticipated (Roesler et al. 2007; Park et al. 2008), there was a good fit for the FEM response curve of the 15 cm SEN[B] with the experimental data. However, the 5 cm height SEN[B] simulations (estimating a 30% increase in nominal strength compared to a

15 cm beam height) underestimated the peak strength of the experimental results (with a 59% increase) shown in Figure 3-11. It was presumed that the underestimation of the global peak response SEN[B] specimen strength was primarily a result of using the same indirect split-tensile strength for all simulations, without adjusting for a strength size-effect. Like the flexural nominal strength, it was hypothesized that the indirect split-tensile strength also should be increased with smaller size specimens and therefore the split-tensile strength based on a 10 cm diameter specimen may not be appropriate for simulating a 5 cm height SEN[B].

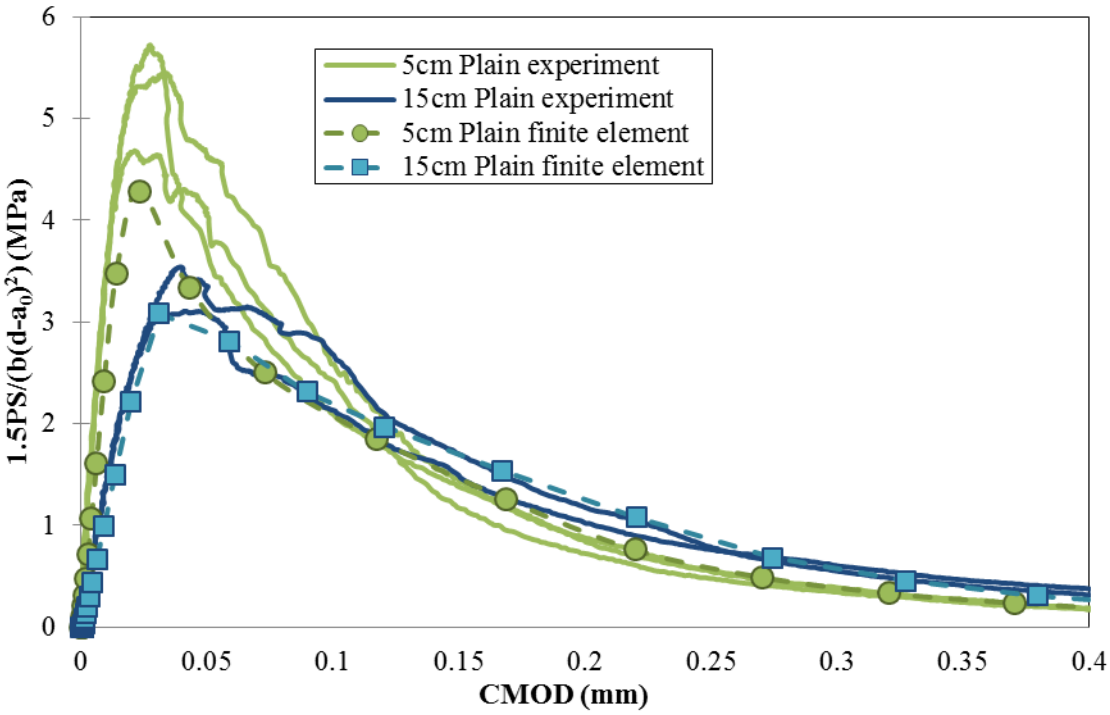


**Figure 3-11 Comparison between experiment and finite element model for un-reinforced concrete beams of 5 and 15 cm depth.**

3.7.2. Applicability of Using CZM for FFC

The experimental and simulated fracture behavior of 15 cm beams containing 0.78% volume fraction of Strux fibers were presented in past literature (Roesler et al. 2007; Park

et al. 2010) as represented in Figure 3-13a. The response of this 15 cm beam with the higher fiber content has a monotonic decrease in load with the beam opening displacement. There is a slight secondary peak exhibited in the experimental curve due to a deflection hardening response of the FRC specimen which cannot be captured with the CZM. In ABAQUS, the cohesive crack model damage response curve must be continuously increasing and therefore any significant deflection hardening response of an FFC specimen cannot be reproduced with this model. The FFC 15 cm SEN[B] specimen response is plotted in Figure 3-13b for 0.46% volume fraction of fibers and total fracture energy of 5700 N/m. The tri-linear softening model can be utilized to simulate the experimental FFC 15 cm height SEN[B] results, with the best fit occurring for crack opening widths less than 2 mm. Overall, the tri-linear softening model does reasonably well as a conservative estimation for the entire global response of the FFC. With the FFC mixture, especially placed randomly and consolidated with a mallet into a 15 cm SEN[B] mold, it was hypothesized that fiber alignment was less likely to occur within the 15 cm beam height, and therefore the deflection softening fracture response of thicker specimens can be sufficiently predicted using the CZM.

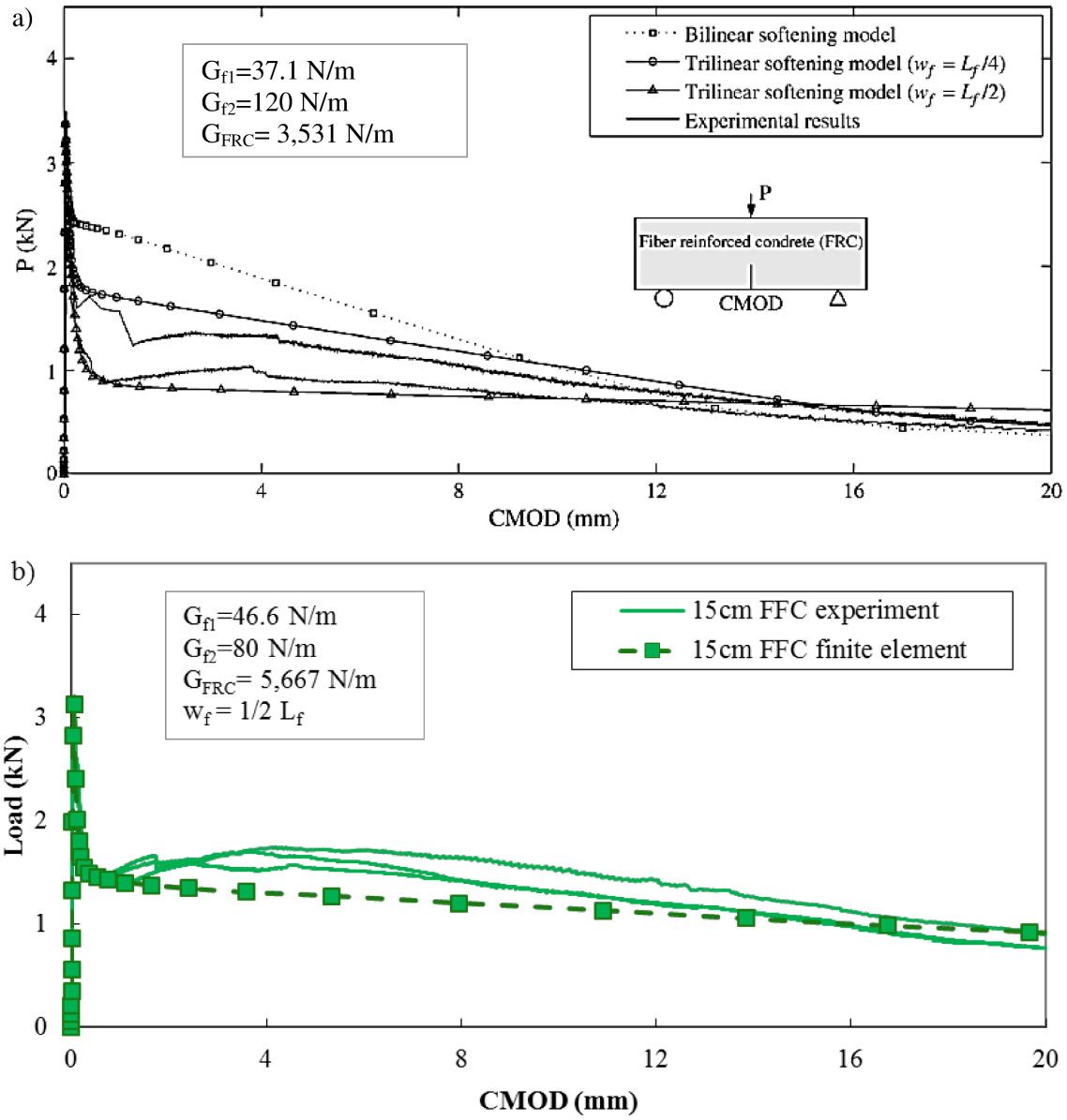


**Figure 3-12 SEN[B] 15 cm height experimental and FEM global response curves for a) 0.78% volume fraction FRC (Park et al. 2010) and b) FFC with 0.46% volume fraction of Strux fibers.**

The thin FFC inlay was anticipated to potentially have higher fracture energies (with an average of 6,427 N/m). As shown in Figure 3-13, the tri-linear softening curve response was a good fit especially for some of the FFC fracture specimens with a lower secondary peak, or at least for crack opening displacements less than 2 mm. Due to potential fiber alignment or a higher localized volume of fibers within some FFC specimens, an

expected increase in the secondary peak or deflection hardening response, led to a higher measured total fracture energy for that FFC fracture specimen.

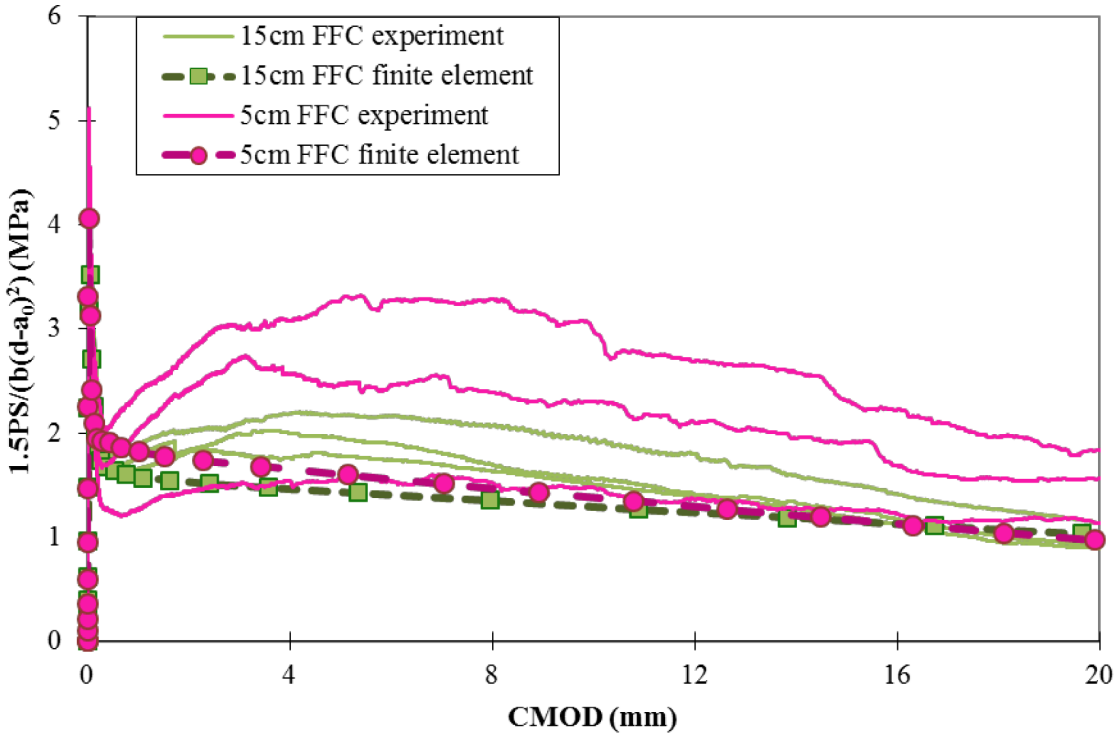


**Figure 3-13 Comparison between experiment and finite element model results for the FFC SEN[B] with Strux 90/40 of 5 and 15 cm height.**

3.7.3. Total Fracture Energy

An important issue with modeling the FFC material was that among some of the 5 cm specimens, there can be a significant deflection hardening response (see Figure 3-14), which is much greater than the secondary peak load seen for the 15 cm beam in Figure 3-13b. The FFC material containing alternative macro-fiber types or alternative construction techniques can be demonstrated through experimental testing to have the capability of reaching higher total fracture energies in excess of 5,000 N/m. For example, the FFC mixture containing 0.46 percent volume fraction of BT fibers when cast under directional flow as a 5 cm thick plate (as utilized in Chapters 4 and 5) had the

potential to exhibit up to 13,500 N/m in the measured total fracture energy for a single specimen. A higher fracture performance was expected of fibers being well coated by the cement matrix which increases fiber-matrix bonding and pull-out resistance of the FFC, as well as a higher fracture energy due to potentially more aligned fibers induced from casting the FFC with a directional flow into a 5 cm plate. With the potentially higher fracture energy measured for the 5 cm SEN[B] FFC material, a bi-linear softening CZM was anticipated to be more applicable to characterize the FFC material response (utilized to simulate the 13,500 /m specimen in Figure 3-14).

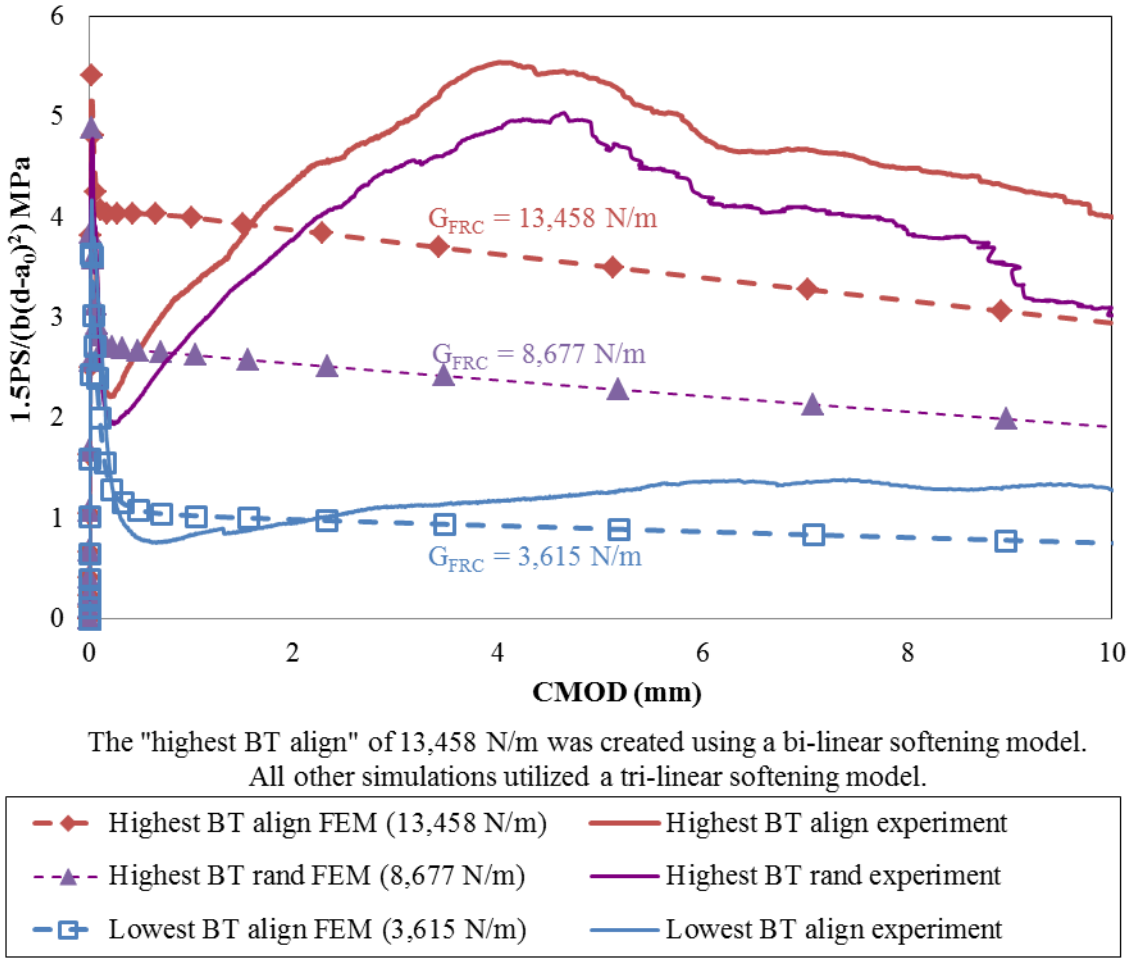


**Figure 3-14 Finite element analysis results of a 5 cm fracture BT fiber FFC beams of varying total fracture energy values.**

For fracture energies greater than 9,000 N/m, as can occur with some 5 cm FFC specimens, the computed second kink point stress of the tri-linear softening CZM was higher than the first kink point, as represented in Figure 3-15. Thus for a high fracture energy, a recommended bi-linear curve was considered sufficient to describe the global response of the FFC. One negative side of using the bi-linear softening model was that it is known to overestimate the early post-peak response of FRC SEN[B] as shown in Figure 3-13a (Park et al. 2010) and was also found for the 13,500 N/m sample in Figure 3-14. Overall, for specimens with fracture energies less than 9,000 N/m, the tri-linear softening model can still be used to simulate the global response of the FFC material.

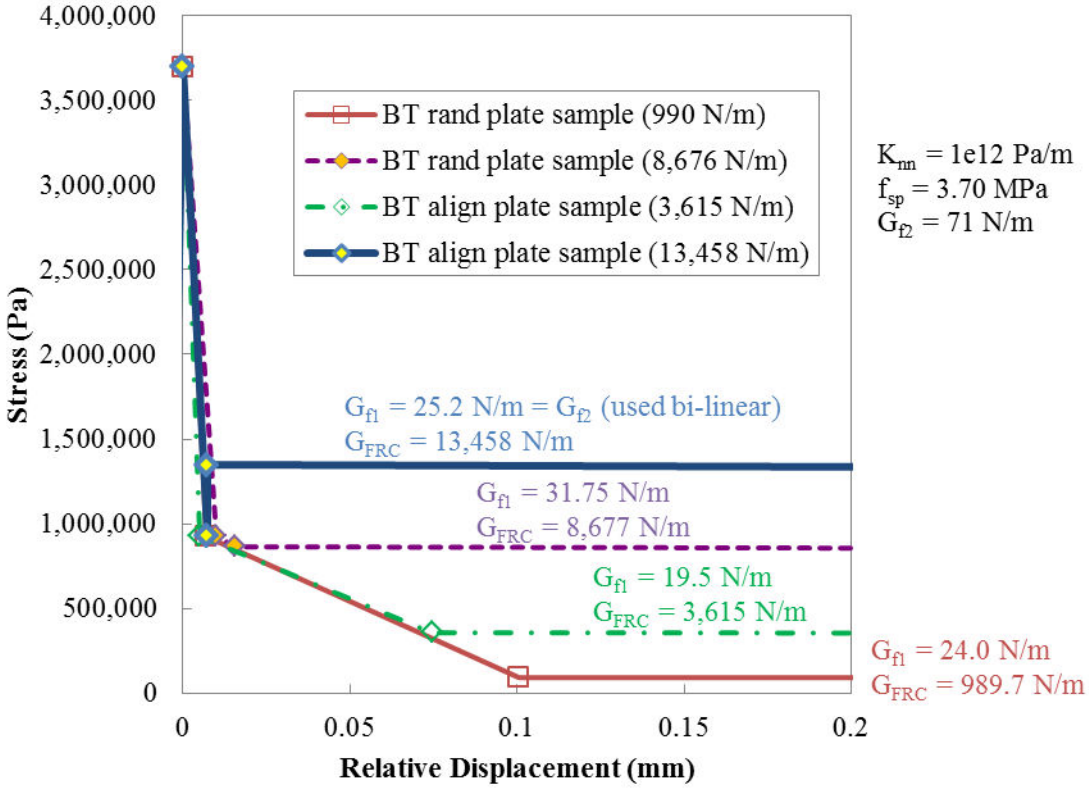


**Figure 3-15 Tension softening models for BT FFC fracture beams cast as a 5 cm plate.**

### 3.7.4. FFC Post-cracking Deflection Hardening Response

While the finite element fracture-based CZM was able to simulate an increase in the global response related to the increased fracture energy of the FFC material SEN[B], the model could not accurately simulate the post-cracking secondary peak of the experimental FFC beam specimens (see the example in Figure 3-15 for the BT fiber mixture 5 cm SEN[B] specimens). The secondary peak reached after crack initiation in the concrete has been known to generally occur in flexural bending tests with higher fiber content mixtures (Naaman and Reinhardt 2006). Several mechanical interactions and responses of the fibers in the concrete are also predicted to contribute to higher energy requirements and result in a larger post-peak fracture behavior of the FRC material. These mechanisms are: crack initiation and propagation along the fiber and concrete matrix interface, elastic stretching of the fibers, and frictional slip between a debonded fiber and the concrete matrix. A combined phenomenon of fiber pull-out, fiber content and fiber orientation on a tested beam resulting in a secondary stress peak after the concrete is cracked has been referred to as deflection hardening in the literature. As shown in Figure 3-15 for some of the 5 cm SEN[B] specimens with the FFC, modeling of deflection hardening responses for fiber-reinforced concrete materials is still a topic of current research and cannot be accurately simulated with this tri-linear softening CZM.

## 3.8. Summary

Various specimen sizes, test configurations, and consolidation techniques were studied to find a beam geometry that represents the toughness response of the FFC material used to cast the thin concrete inlay pavement. The standard 15 cm unnotched flexural beams

used in ASTM C1609 were insufficient for measuring an accurate prediction the post-cracking performance of a 5 cm thick FFC pavement. Higher residual strength ratios measured for reduced specimens sizes was attributed to the nearby cast or mold surfaces creating fiber alignment in the thinly cast specimens. A 15 cm standard SEN[B] fracture test was found to be the best for predicting size-independent initial fracture properties. The SEN[B] of 15 cm in height were thicker than the design application of the FFC and were found to significantly underestimate the toughness found from a 5 cm thick plate specimen.

As expected, 5 cm SEN[B] specimens exhibited significantly higher peak strengths than 15 cm beams (59% greater at 7 days for the flowable concrete mixture). A post-cracking deflection hardening behavior was found along with higher residual strength ratios for some of the 5 cm beams consisting of the FFC mixture. A rodding technique utilized commonly for traditional concrete mixtures was found to produce reduced toughness performances, as it likely disrupts the internal fiber orientation in the material.

The finite element analysis utilizing fracture properties of a 15 cm SEN[B] test in a tri-linear damage softening model simulated peak and post-cracking fracture responses of the FFC of the same SEN[B] height specimens. Although, for some 5 cm SEN[B] FFC specimens exhibiting a deflection hardening behavior, a damage softening model in FEM was unable to simulate the secondary peak produced. In addition, the tri-linear softening model was no longer valid for simulating post-peak cracking of the FFC SEN[B] specimens with high measured total fracture energies over 9,000 N/m.

# CHAPTER 4. SYNTHETIC MACRO-FIBER DISTRIBUTION IN CONCRETE

## 4.1. Motivation

An increased toughness was measured experimentally for FFC specimens cast as thin plates relative to 15 cm molded beam specimens. This increase in toughness was hypothesized to be due to more effective alignment or a re-distribution of the fibers as the concrete flowed into the cast forms, particularly because the height of the forms were on a scale proportional to the fiber length. Thus a method is needed to link fiber orientation and distribution with the measured toughness. Past studies have investigated the influence of a single fiber's orientation on toughness performance with cement composites based on a single fiber pull out test (Stang and Shah 1986; Bentur and Mindess 1990; Li et al. 1990; Stang et al. 1990). Micromechanical tensile stress models (Gopalaratnam and Shah 1987; Leung and Li 1990; Li et al. 1991; Li 1992; Li et al. 1993; Lange-Kornbak and Karihaloo 1997) describe FRC as having a random 3D orientation and distribution of fibers, often neglecting the specimen geometry influence on fiber distribution and fiber orientation. Therefore, for the FFC mixture cast as a thin inlay, an understanding of the fiber distribution and orientation are useful for improving such modeling.

To properly understand the benefits of the FFC mixture in thin inlay pavement, a means to identify the fibers within the concrete was required. The identification method must be able to quantify the net orientation of fibers, the spatial distribution of fibers, and the expected number of fibers crossing any given fracture plane. A technique which could non-destructively locate the synthetic macro-fibers in the concrete was considered a

challenge since most literature on FRC fiber distribution had been with locating steel fibers. Stereological techniques, commonly used in the past, could be implemented for estimating the two-dimensional distribution of fibers from cross-sectional slices. Locating the fiber in a 3D space was preferred and could be done using a non-destructive technique such as x-ray computed tomography (CT). X-ray CT has been demonstrated to be effective at locating steel fibers within concrete (Benson et al. 2005; Stähli et al. 2008; Barnett et al. 2010; Krause et al. 2010), as illustrated in Figure 4-1. By using the x-ray CT technique in combination with image post-processing of the 5 cm specimens, a 3D reconstruction of the synthetic fiber distribution within the FFC mixture could be made. Figure 4-2 illustrates an example of the potential synthetic fiber dispersion and the actual fiber distribution found from within a 5 cm thick FFC specimen. The results of the fracture testing in Chapter 3 were used in selecting the 5 cm beam specimens to be scanned with the x-ray CT based on their expected range in fiber distribution and fiber orientations.

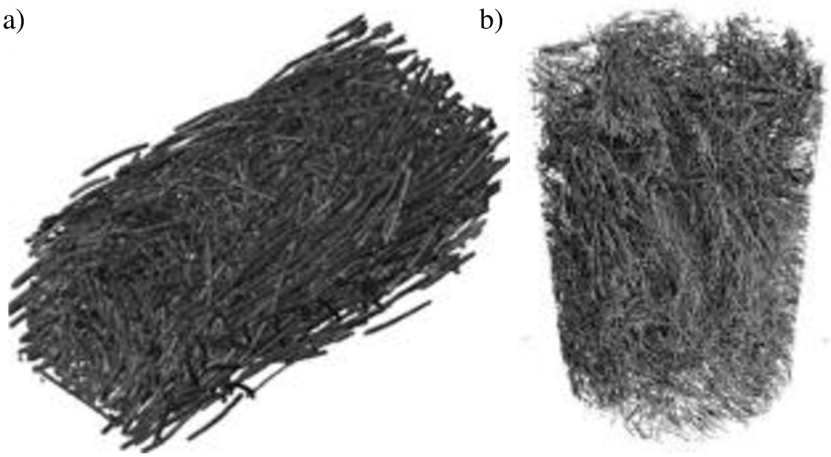


**Figure 4-1 Reconstructed x-ray CT image for a) 3 percent volume fraction steel FRC within a beam sample (Stähli et al. 2008), or b) core sample (Krause et al. 2010).**

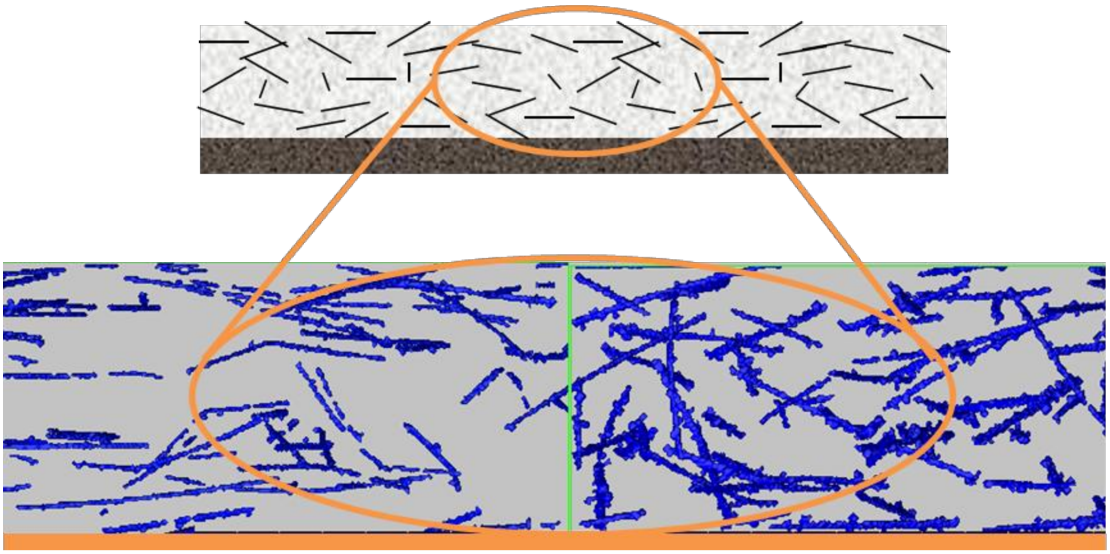

**Figure 4-2 Representation of a thin FFC and actual post-processed image showing the dispersion of synthetic fibers.**

## 4.2. Techniques to Identify Fibers in Concrete

Stereology has been a classic technique (Stroeven 1979) for verifying fiber density and estimating fiber orientation. The method of counting of fibers which extend across a cut or fractured plane, as illustrated in Figure 4-3, is still commonly performed (Soroushian and Lee 1990; Dupont and Vandewalle 2005; Torrijos et al. 2010; Ferrara et al. 2011). Through these stereology studies, the location of fibers, e.g. see the image in Figure 4-3, and number of fibers are used to estimate distribution and the local orientation of fibers as they cross a 2D sliced plane. Fibers which are parallel with a given slice plane are either not found or the entire fiber will be projected on the slice. Furthermore, any potential variation in the fibers geometry (in cross-section or length) can make orientation predictions difficult from stereological 2D slices. It is preferable to gather 3D information on the fibers spatial distribution and orientation.

The majority of research to detect fibers in three-dimensions from within concrete or cement has been performed using steel fibers. Primarily, rigid steel fibers have been

selected in analysis of FRC mixtures because of the greater contrast with x-rays (Stroeven 1985; Redon et al. 1998; Redon et al. 1999), electrical resistivity (Lataste et al. 2008), electrical impedance (Ozyurt et al. 2006), or visual contrast through scanning electron or optical microscopes (Chermant et al. 2001; Gettu et al. 2005; Shen et al. 2008; Torrijos et al. 2010). X-ray computed tomography (CT) was useful for not only detecting steel fibers, but also can be used in quantifying fiber orientation (Stähli et al. 2008; Krause et al. 2010).

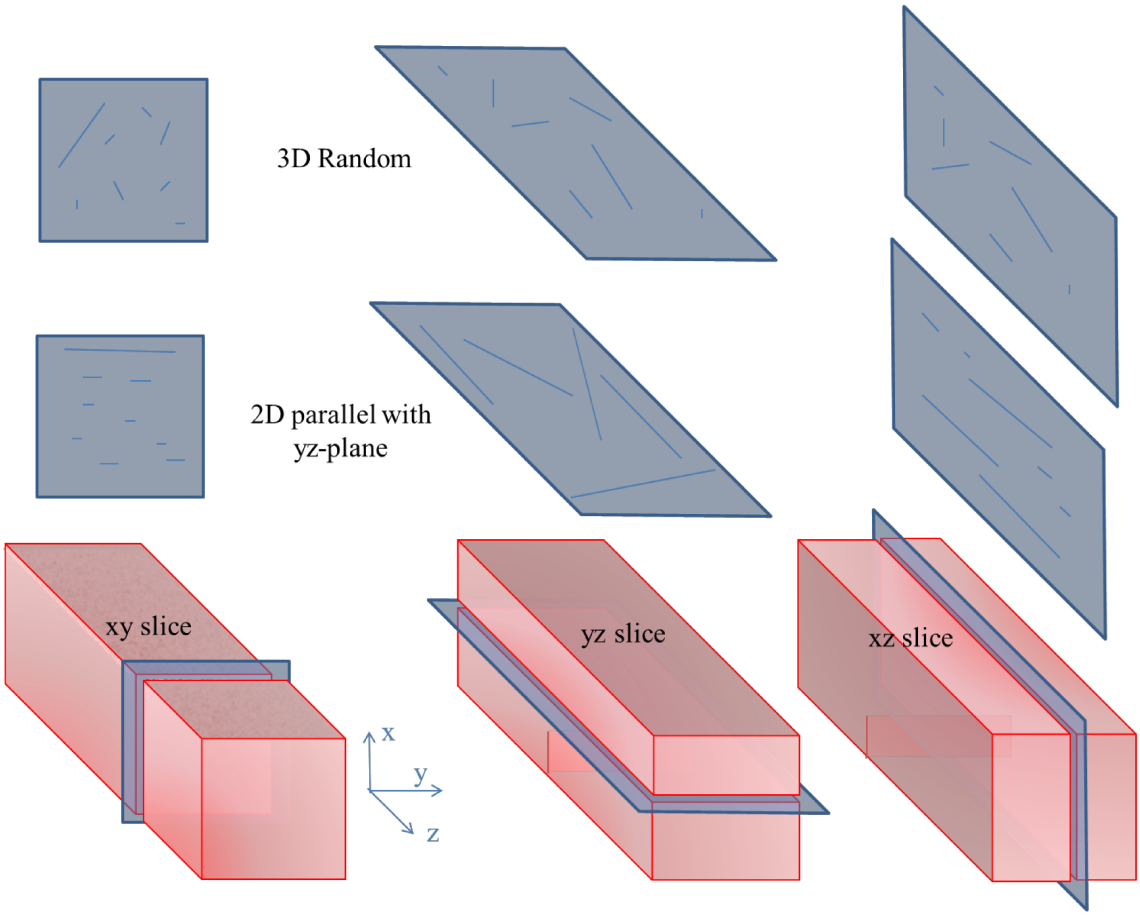


**Figure 4-3 Stereology schematic showing estimated projections found on orthogonal slices for rigid fibers with either 3D random or 2D planar (yz) dispersion.**

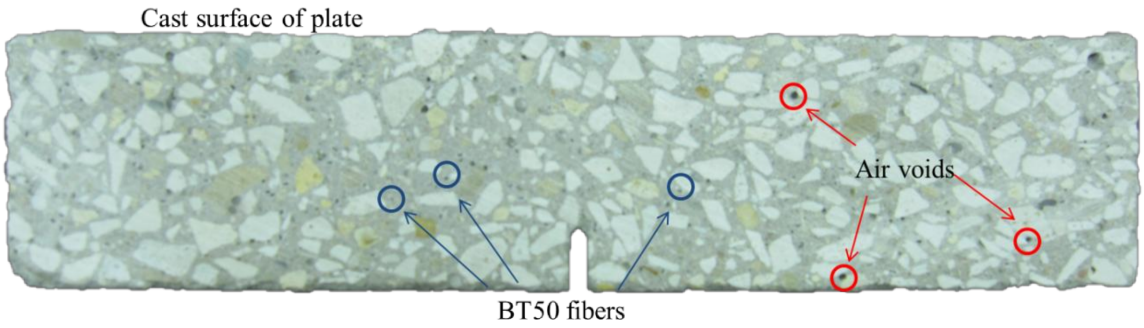


**Figure 4-4 Photograph image of the side of a plate specimen containing BT50 fibers.**

The significant challenge addressed in this research was the detection of polymer fibers in the concrete, which are flexible, non-magnetic, and non-conductive, eliminating the application of several common detection techniques. A stereology technique has been used for identifying cellulose fibers dyed in a florescence whitening agent and then their distribution examined under optical microscopes with ultra-violet light (Rapoport and Shah 2005). The x-ray CT technique has been performed previously on concrete containing glass microfibers, but only as a quality control to look for fiber clumping determined from the average grayscale intensity of low resolution images (Shen et al. 2004). Of the current published procedures for detecting synthetic fibers, none of these methods have been proven useful to determine each fiber's orientation and the distribution within the concrete. Thus the research presented herein describes a technique of using x-ray CT with a finer image resolution combined with computer software post-processing to successfully locate and identify individual synthetic fibers in the FFC.

## 4.3. X-ray CT Scanning Technique

X-ray CT is a non-destructive evaluation method that can be applied to generate a 3D image representation of the internal structure within the concrete. With x-ray CT, variations in attenuation, similar to density, can be identified in the reconstructed 3D

image (Stock 2009). A stereological analysis can be still be performed by viewing 2D slices at any angle or plane within the reconstructed tomographic image. However, a benefit of performing x-ray CT over other stereological techniques is the entire internal structure can be determined without destroying the specimen (i.e. without cutting and preparing slices). For this research, 52x52x229 mm notched beam specimens were tested in fracture, then each half of the beam was scanned in the x-ray CT.

### 4.3.1. X-ray Scanning Procedure

The x-ray CT scanning (see Figure 4-5) consisted of three main components: a cone beam of x-rays were sent through the concrete specimen on a rotating stage, x-rays were collected as radiographs through a flat-panel scintillator detector for each stage rotation angle, and computer software was used to reconstruct a 3D image of the sample's interior. The quality of the image, i.e. intensity contrast and spatial resolution, was dependent on the variation in attenuation of the material (the absorbance of x-rays by the material which is related to material density), the power magnitude of the x-ray source, the time of exposure/collection, the size of the sample, the type of detector, and the image reconstruction software.

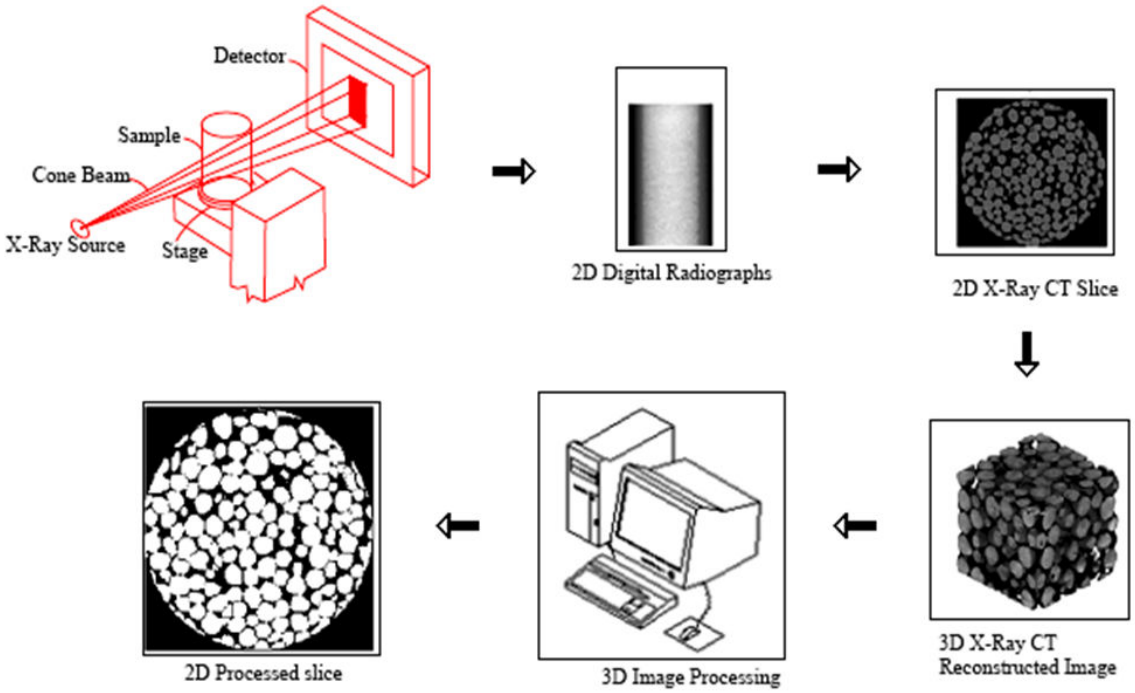


**Figure 4-5 Diagram of the x-ray computed tomographic scanning of a cylindrical sample (Nega and Balasingam 2010).**

Based on the materials of interest listed in Table 4-1 within the FRC, a required image spatial resolution was estimated at most to be 0.5 mm. This resolution was needed to distinguish the synthetic macro-fiber particles in at least one orthogonal plane. Placing the sample stage closest to the source would result in the best image pixel spatial resolution. A square or cylindrical cross-section was considered optimal to minimize the computer reconstructed image artifacts produced from any non-uniform specimen thickness (Benson et al. 2005; Stock 2009). No sample preparation was required prior to x-ray CT scanning.

**Table 4-1 Particle Sizes in Concrete**

| Material | Size Range (mm) | Reference |
|---|---|---|
| Cement/Fly Ash | 0.001 to 0.1 diameter | (Mindess et al. 2003) |
| CSH; Ettringite; CH (smallest estimated crystal size) | 0.0001; 0.0005; 0.01 | (Mindess et al. 2003) |
| Air voids in paste (based on Mercury Intrusion Porosimetry) | 0.00001 to .01 diameter | (Mindess et al. 2003) |
| Fibromac 6 Micro-fibers | 0.018 diameter, 6 long | Maccaferri |
| Strux 90/40 Macro-fibers | 0.11 thick, 1.4 wide, 40 long | W.R. Grace |
| "BT50" Macro-fibers | 0.4 thick, 1.2 wide, 48 long | measured |
| Limestone Coarse Aggregate | 0.075 to 9.5 diameter | Sieve analysis in lab |
| Sand Fine Aggregate | 0.075 to 4.75 diameter | Sieve analysis in lab |

For detecting synthetic fibers in concrete, a higher power x-ray tube source was needed to penetrate through concrete, particularly for thick samples (Masad et al. 2002), and still display enough grayscale resolution to differentiate slight variations in densities. For example, the density and attenuation difference between limestone aggregates and hardened cement are similar, and thus enhanced contrast resolution is needed. The x-ray attenuation of the polymeric fibers was found to be similar in magnitude to the air voids, despite different densities. X-ray CT energy settings (voltage, time, and amperes) were determined through trial and error such that there was enough energy for distinguishing fibers and voids in the concrete matrix without oversaturating the detector in absorbed x-ray energy.

4.3.2. X-ray CT Laboratories

Various laboratories listed in Table 4-2 across the United States were contacted and considered for x-ray CT scanning of FFC samples. Initial testing used a micro CT machine at Beckman Institute, but due to its lower power x-ray source, smaller concrete samples could only be scanned at a time. As it was deemed a higher x-ray source would

provide good image resolution for larger concrete sample sizes, the 5 cm thick samples were sent to three laboratories with higher power x-ray sources: Texas A&M University, Washington State University, and North Star Imaging. Specific images of samples sent to these laboratories can be seen in Appendix C. The Washington State X-ray CT (WAX-CT) machine was selected for its finer spatial resolution and capability to provide contrast resolution for a 5 cm concrete thickness with a 420 kV x-ray tube (Nega and Muhunthan 2010).

**Table 4-2 X-Ray CT Scanning Locations and Capacity Details**

| Machine/Location | X-ray Source (kV) | Maximum Concrete Sample (mm) | 3D Reconstruction Resolution (mm/pixel) | Estimated Time (Scan + Reconstruct) |
|---|---|---|---|---|
| Xradia Bio MicroXCT-400 (Beckman Institute, Urbana, IL) | 90 | 6 x 25 x 25 | 0.032 | 2.5 hr |
| Micro- and Mini-focus X-ray CT (Texas A&M University, College Station, TX) | 225 or 350 | 150 x 150 x 250 | 0.170* | 2 min/image |
| Washington State High-Resolution X-Ray CT (Washington State University, Pullman, WA) | 225 or 420 | Up to 200 | 0.127 | ~2 hr |
| North Star Imaging X-View X500-CT (Rogers, MN) | 225 or 450 | 400 x 400 x 400 | 0.150* | NA |

*Image resolution is estimated by manufacturer.
NA = information is not available.

## 4.4. Image Analysis

Image processing through grayscale or contrast filters are typically performed to segment an image for locating components with unique x-ray attenuations. These techniques were performed originally on 2D sliced images using MATLAB® Image Analysis Toolbox (Mathworks 2009) or ImageJ® (National Institutes of Health 2010). As shown in Figure 4-6, the MATLAB® software code (provided in Appendix C) clearly could be used to

locate the combination of air voids and fiber objects within the concrete. However, most image processing analyses were incapable to threshold images in locating specific fibers particularly in three dimensions. The main key in image analysis was to identify fibers by their shape in 3D, as the fiber dimensions and pixel intensities were similar magnitudes as potential air voids. Image analysis by way of density, size and shape identification was needed to distinguish separate fiber particles before a quantitative analysis on the fiber location and orientation could be made.

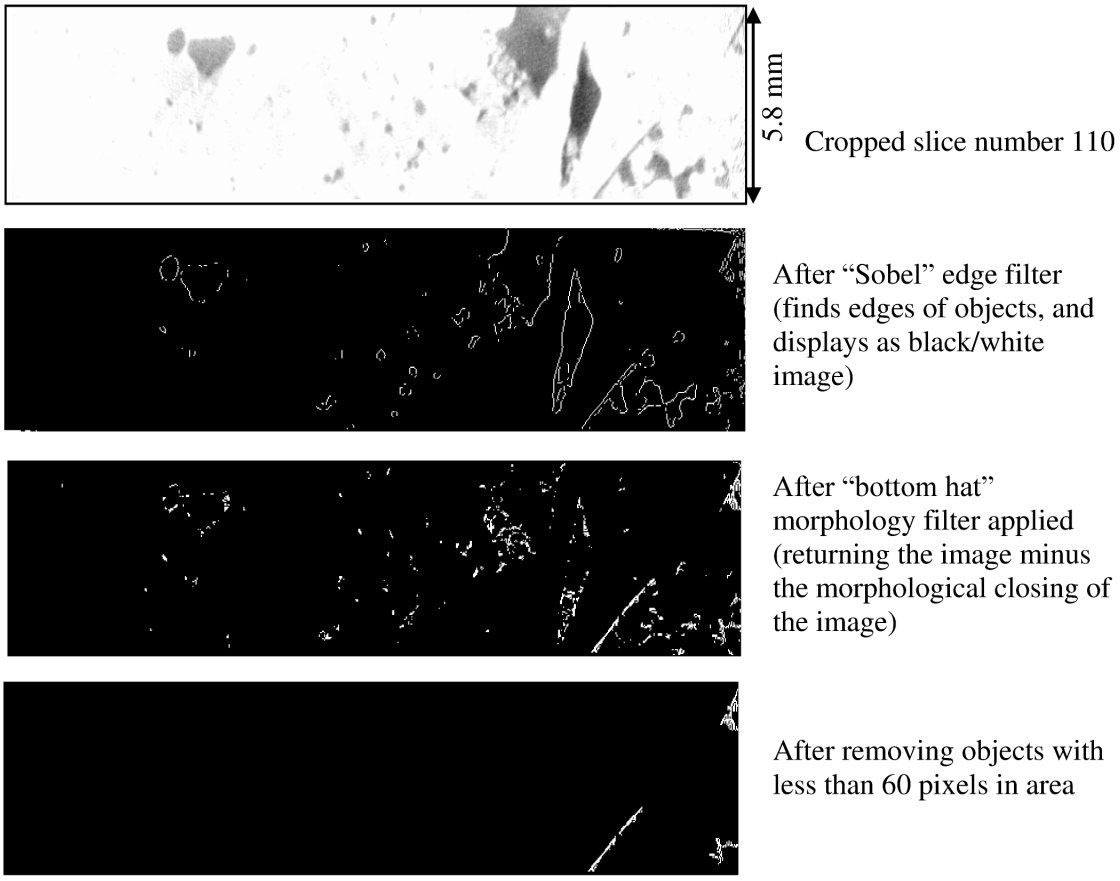


**Figure 4-6 Two-Dimensional Image Analysis using MATLAB® (Mathworks 2009) of the Beckman sample.**

### 4.4.1. Imaging Procedure with IMARIS®

A variety of software has been developed for biological imaging to view x-ray CT components in three dimensions. The IMARIS® software (Bitplane 2009) was selected over other 3D imaging programs as it provided the ability to filter based on shape (ellipsoid) as well as individual selection of objects once a grayscale threshold was applied. The image post-processing steps taken (the program screen images can be viewed in Appendix C) to identify the synthetic fibers were as follows:

- Rotate, crop, and scale image
- Invert image to make hardened concrete as dark objects
- Threshold using a background subtraction to only view fibers and air voids
- Filter by shape to identify fibers

### 4.4.2. Contrast Threshold

The program background contrast subtraction threshold compared intensities of neighboring pixels, averaged over a specified spherical diameter. In this case, the smallest fiber dimension of 0.4 mm was selected. The background subtraction threshold value was manually selected (with final selected values shown in Table 4-3) to negate the concrete and aggregates objects, leaving only the fibers and air void structure remaining.

The initially scanned 8-bit images had a smaller range in image intensity values, thus a background subtraction threshold value near 13 was used instead of around 1000 for the later scanned 16-bit images. A higher background contrast threshold value in the software meant a higher intensity gradient between neighboring voxels. In the software, the number of objects found typically decreased with a higher background contrast threshold.

**Table 4-3 Dimensions, Thresholds and Filter Values for CT Sample Images**

| Specimen | Data Format | Crop Dimensions | | | | | | Scaled Dimensions (mm) | | | Dia. Sphere (mm) | Contrast Threshold | Ellipsoid C-axis Length | | Maximum Sphericity |
|---|---|---|---|---|---|---|---|---|---|---|---|---|---|---|---|
| | | x | | y | | z | | x | y | z | | | min | max | |
| XY1 | 8-bit | 59 | 218 | 55 | 216 | 1 | 356 | 51.84 | 52.49 | 115.34 | 0.4 | 13.6 | 2 | - | 0.624 |
| XY2 | 8-bit | 57 | 218 | 55 | 218 | 1 | 353 | 52.49 | 53.14 | 114.37 | 0.4 | 12.5 | 2 | - | 0.624 |
| BT14a | 16-bit | 8 | 173 | 6 | 175 | 1 | 370 | 53.78 | 55.08 | 119.88 | 0.4 | 1051.4 | 2 | - | - |
| BT14b | 16-bit | 11 | 176 | 9 | 172 | 1 | 370 | 53.78 | 53.14 | 119.88 | 0.4 | 1003.9 | 2 | - | - |
| BT13a | 16-bit | 8 | 178 | 6 | 178 | 1 | 366 | 55.40 | 56.05 | 118.58 | 0.4 | 1000.0 | 2 | - | 0.620 |
| BT13b | 16-bit | 6 | 175 | 3 | 175 | 1 | 370 | 55.08 | 56.05 | 119.88 | 0.4 | 837.8 | 4 | - | - |
| BT9a | 16-bit | 8 | 173 | 5 | 178 | 1 | 370 | 53.78 | 56.38 | 119.88 | 0.4 | 1000.0 | 2 | 30 | 0.586 |
| BT9b | 16-bit | 8 | 175 | 5 | 180 | 1 | 370 | 54.53 | 57.02 | 116.96 | 0.4 | 1000.0 | 2 | - | |

4.4.3. Shape Filtering

The key to separating the fibers from air voids was by applying a filter which searched for an ellipsoid-like object. The IMARIS® software automatically computes sphericity, and ellipsoidal (prolate and oblate) properties described in Figure 4-7 for each object located in the 3D image. The difference between a spheroid and ellipsoid is defined by at least one axes being significantly longer than the other(s). An elongated fibril particle would have a "C" axis length which was larger than the "A" and "B" axes. Two shape-based filters were used successfully to retain the elongated fiber (or fibril) components instead of more spherical air voids. These filters were a minimal C-axis length and a maximum sphericity. The specific values utilized are listed in Table 4-3. The minimum length of 2 mm along the C-axis was found to remove small air voids. Maximizing the sphericity value removed purely spherical voids, or those possibly shaped due to the air-entraining admixture. Although using specific fiber dimensions for filtering would be ideal for identifying the synthetic fibers, some of these fibers were found to have a

curvature to them. Additionally, from reconstruction image resolution and thresholds of the 3D image, many of the fibril objects were found as short disconnected segments.

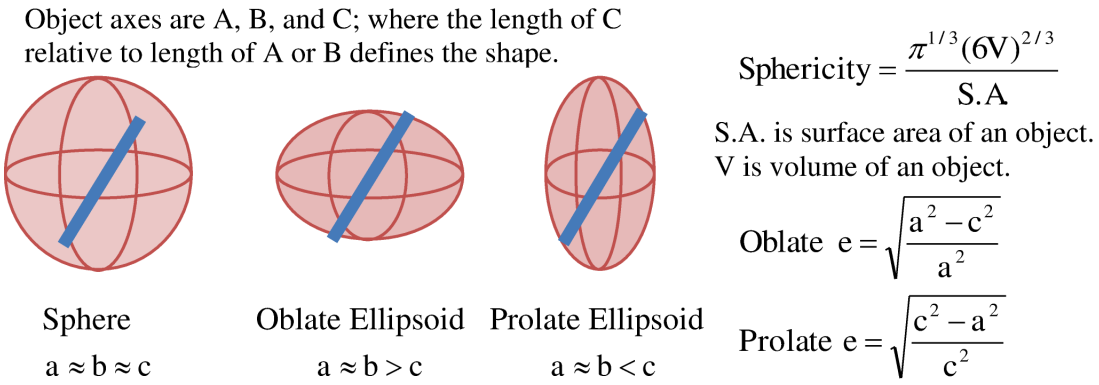


**Figure 4-7 Description of Sphericity versus Oblate and Prolate Ellipticities e.**

4.4.4. Manual Adjustment and Selection

The additional advantage with using the IMARIS® software was the ability for manual selection of individual objects and the ability to selectively group these individual fibril segments as one fiber. In some occasions during the background contrast thresholding, portions along the fiber length were removed, thus producing small fibril segments which appeared in three-dimensions to be part of one continuous fiber. These short segments were manually grouped in the software. Additionally through visualization of the post-filtered objects, some of these small short segments were selectively determined to be air voids instead of fibers, as illustrated in Figure 4-8. Some artifacts existed as marked in red in Figure 4-8, and appeared as dark rings in the original 2D slices of each scanned half beam sample. These artifacts were a result of bad pixels on the flat panel detector.

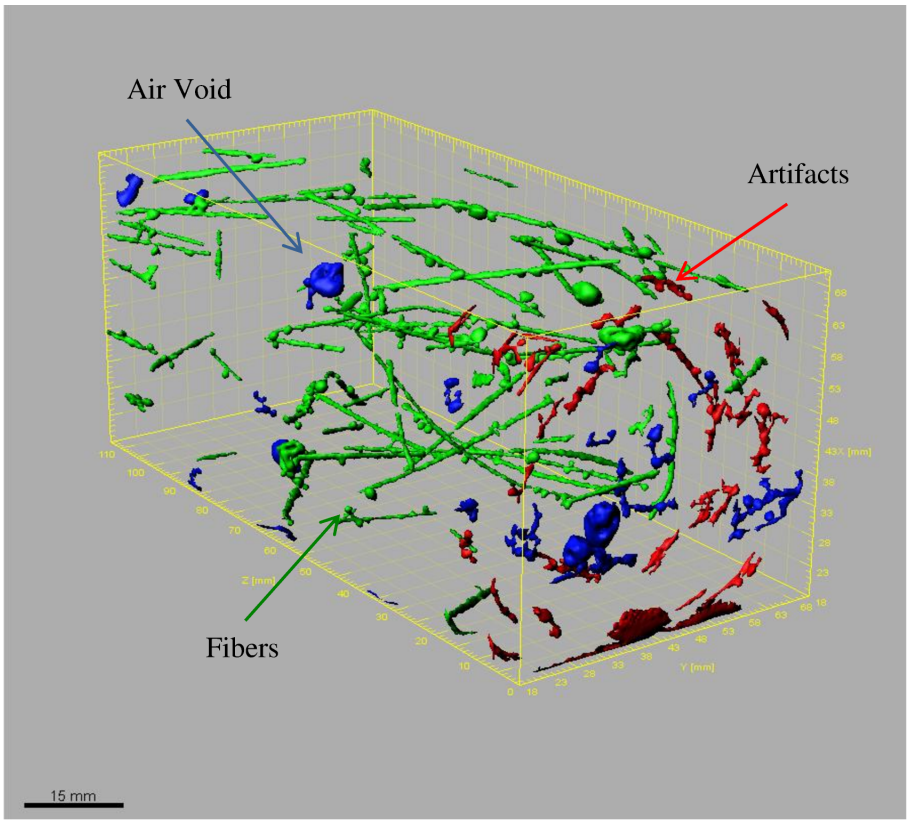


**Figure 4-8 Isometric view of CT sample shows manual identification of thesholded objects into fibers, air voids and artifacts.**

Several air voids remained attached to the fibril objects after the threshold as their grayscale intensity was similar in magnitude to the fiber. Further manipulation using a cut tool was used to manually chop off any significant air voids found along the fiber axis. This cut tool was also utilized to separate individual fibers in situations where multiple fibers were "clumped" together or close enough that the size and contrast threshold was not able to differentiate between.

### 4.4.5. Computed Statistics on Fibers Properties

Of the fiber object properties computed with the IMARIS® software (an example is shown in Figure 4-9 and Table 4-4 for a single whole fiber object), the centroid and ellipsoid C-axis were used to determine the fiber distribution and orientation,

respectively. These properties were output to files for individual full length fibers and groups of fibril segments associated with single individual fibers. Further calculation on statistics on fiber distribution and orientation are described later in this chapter and in Chapter 5, respectively.

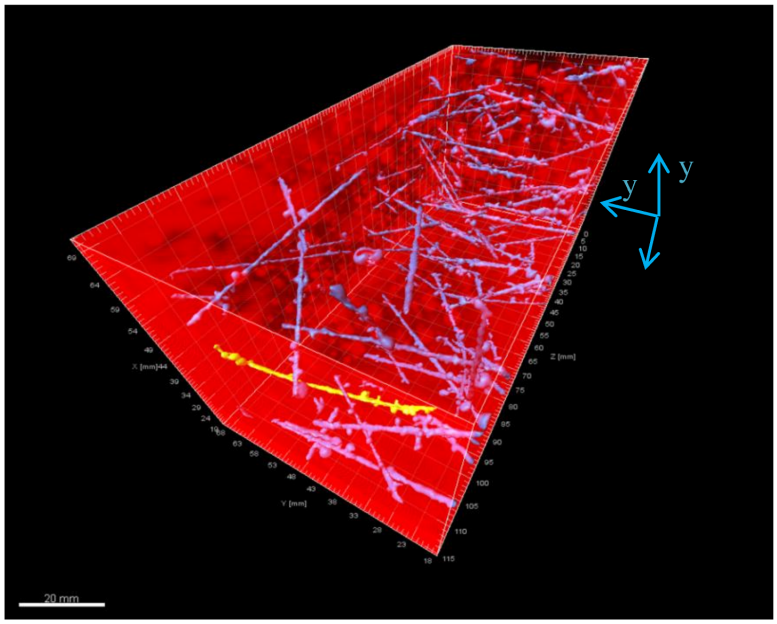


**Figure 4-9 Selected single fiber shown in yellow for 3D rendered and thresholded image.**

**Table 4-4 Properties of Selected Single Fiber**

| Properties | Unit | Example (Selected Fiber) |
|---|---|---|
| Area | $mm^2$ | 210.06 |
| Centroid | mm | x=36.40, y=50.39, z=103.94 |
| Ellipsoid A,B,C projections and length | vector, mm | A Axis 0.29, 0.29, -0.94 Length 1.14<br>B Axis 0.96, -0.03, 0.29 Length 2.91<br>C Axis 0.02, -0.99, -0.17 Length 31.86 |
| Ellipticity (oblate and prolate) | | 0.02 and 0.26 |
| Intensity Properties | | Minimum 100; Mean 161; Median 160;<br>Maximum 222; Standard Deviation 19; Sum 228,468 |
| Number Vertices | | 2964 |
| Number Voxels | | 1417 |
| Sphericity | | 0.28 |
| Volume | $mm^3$ | 42.67 |

## 4.5. X-ray CT Sample Selection

Four fracture beam specimens, as illustrated in Figure 4-10, were selected to be scanned and imaged. The x-ray CT samples all consist of the same laboratory FFC mixture (Table 2-1) at 0.46% volume fraction of BT fibers. The goals of selecting specific samples were to cover the entire range in fracture resistance, as summarized in Figure 4-11, and to provide insight on the cracking resistance based on the number of fibers at the fracture plane, fiber spatial distribution, and net orientation of these fibers. The fracture performances for different fiber types (Strux 90/40 and BT50) and placement techniques (randomly or under directional flow as shown in Figure 4-12) are described further in the next sections. The selected 5 cm fracture beam specimens were scanned in the WAX-CT as two half sections after the fracture testing was performed.

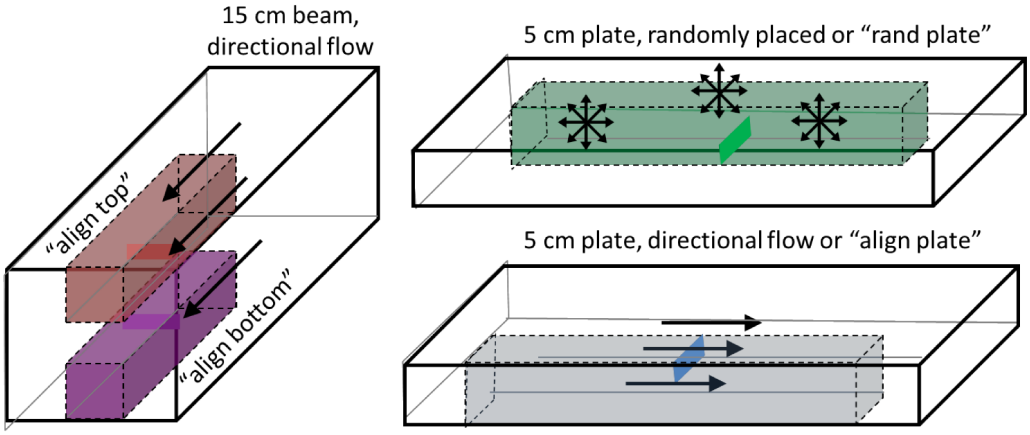


**Figure 4-10 Schematic of specimens extracted and scanned in the x-ray CT.**

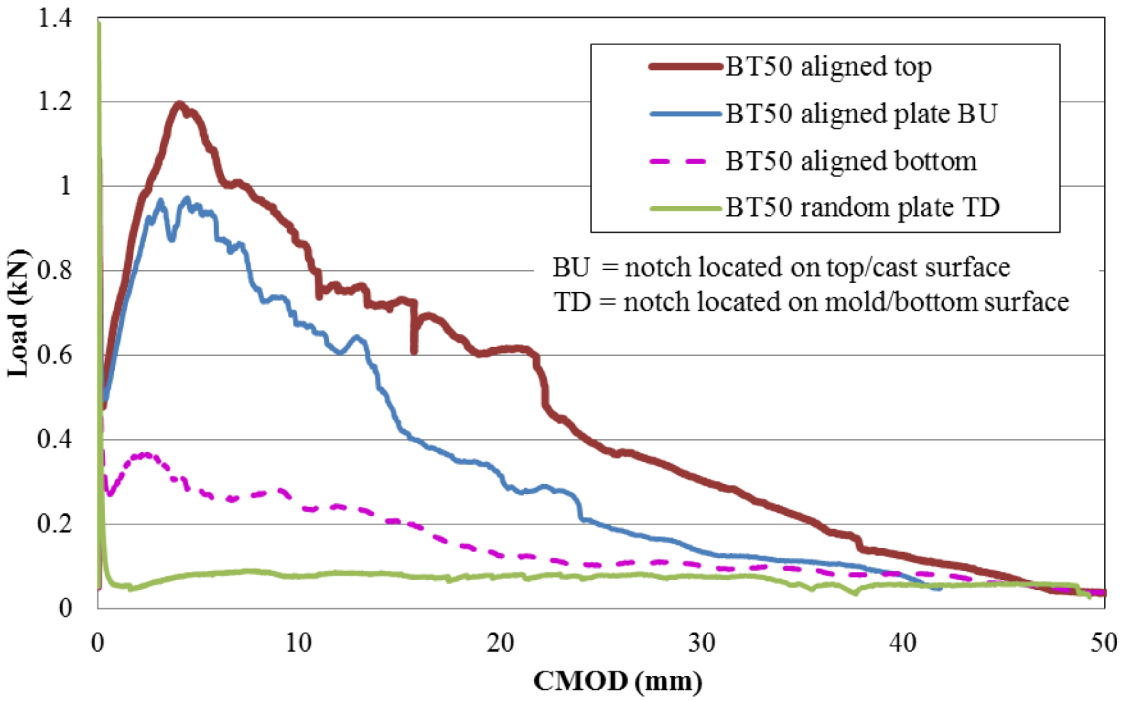


**Figure 4-11 Summary of fracture load versus CMOD curves of the x-ray CT beam specimens.**

Placement of FFC from end of specimen

External consolidation of FFC with mallet

**Figure 4-12 Photographs showing the directional flow or "aligned" placement technique for the FFC specimens.**

4.5.1. Synthetic Fiber Type

Synthetic fibers were expected to sometimes bend around aggregates when mixed within the concrete, making identification of these flexible fibers difficult for the post-processing image software. X-ray CT imaging of the lower stiffness Strux 90/40 fibers was attempted, but the fibers were too flexible to be distinguished by shape, and thus

could not be post-processed using the available imaging and software. The stiffer synthetic fiber, BT50, was chosen for their ability to remain relatively straight within the concrete compared to the Strux 90/40 fiber. Still, detection of the BT fibers in the FFC required the combination of the high power x-ray source scanning and image post-processing based on the contrast threshold and shape filtering.

### 4.5.2. Strux90/40 FFC Fracture Performance

The Strux 90/40 fibers in FFC were compared against the BT50 fibers in the FFC by the measured fracture responses of SEN[B] specimens. The fracture properties and variability are listed in Table 4-5 for all of the 5 cm beams cast randomly ("rand") or with directional flow ("align") (as illustrated in Figure 4-12) as either a plate or a 15 cm beam. The randomly constructed Strux FFC mixture was implemented in the field project described in Chapter 2. In the 5 cm beams randomly cast as 15 cm beams, the Strux FFC mixture actually performed slightly higher in fracture energy (listed in Table 4-5 and displayed in Figure 3-7) than when placed under directional flow (displayed in Figure 4-13). Based on these findings, it was determined that because these randomly cast specimens were cut from near the top and bottom surfaces of the 15 cm beam, a potential boundary wall fiber alignment condition or a locally higher volume fracture of fibers likely dominated the fracture response.

**Table 4-5 Fracture Results for 5 cm Beams With Different Placement Techniques**

| Fiber Type | Construction Method | Original Cast Specimen | Number of replicates | $1.5P_{max}S/(b(d-a_0)^2)$ (MPa) | $K_{Ic}$ (MPa-$m^{1/2}$) | $CTOD_c$ (mm) | $G_{Ic}$ (N/m) | $G_{FRC}$ (N/m) |
|---|---|---|---|---|---|---|---|---|
| Strux 90/40 Fiber | Rand | 15cm beam | 8 | 5.10 (9%) | 0.78 (12%) | 0.010 (13%) | 28 (19%) | 5862 (33%) |
| | Align | 5cm plate | 6 | 5.52 (9%) | 0.81 (13%) | 0.009 (28%) | 30 (31%) | 6345 (33%) |
| | | 15cm beam | 2 | 4.85 (39%) | 0.79 (10%) | 0.011 (31%) | 28 (38%) | 4508 (15%) |
| BT50 Fiber | Rand | 5cm plate | 5 | 4.47 (5%) | 0.75 (11%) | 0.012 (40%) | 29 (26%) | 1105 (86%) |
| | | 15cm beam | 8 | 5.03 (9%) | 0.81 (10%) | 0.011 (23%) | 29 (16%) | 3954 (60%) |
| | Align | 5cm plate | 3 | 4.77 (7%) | 0.76 (11%) | 0.012 (10%) | 30 (10%) | 5702 (51%) |
| | | 15cm beam | 8 | 4.68 (8%) | 0.73 (7%) | 0.010 (12%) | 26 (14%) | 6376 (56%) |

All specimens were 5cm beams tested at 7 days. Values are averages. Numbers in parentheses are the coefficients of variation.

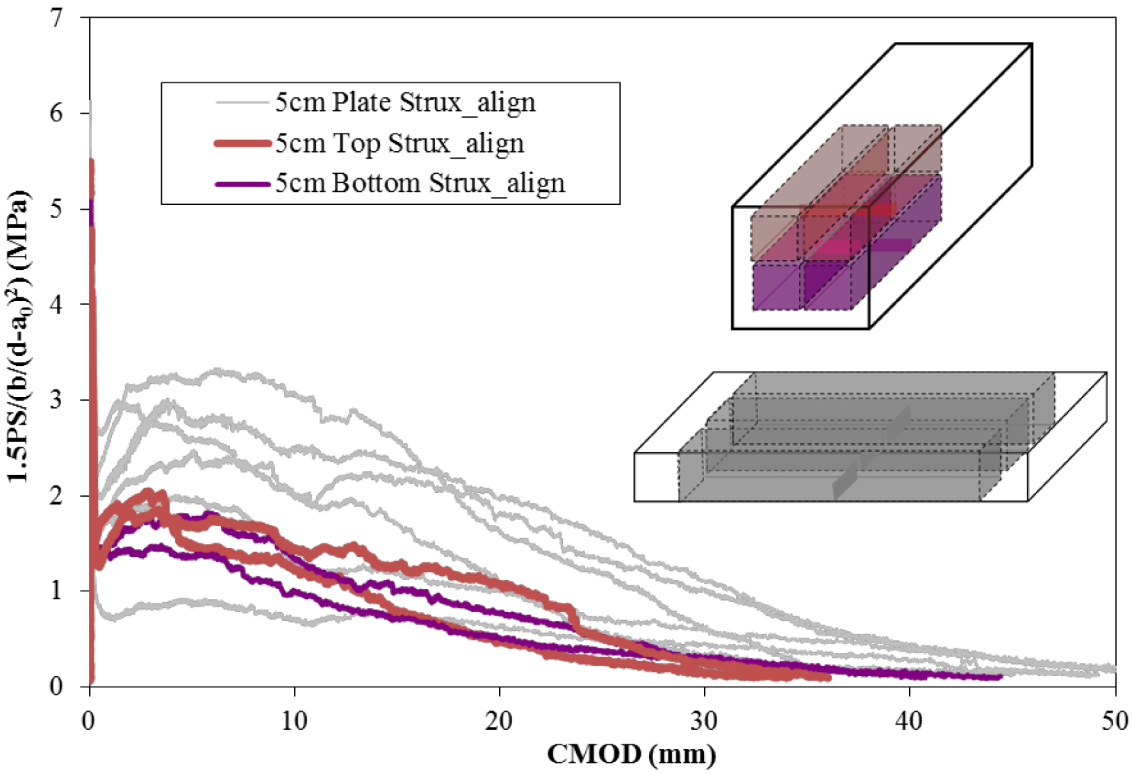


**Figure 4-13 Stress versus CMOD fracture curves are plotted for the FFC beams containing Strux fibers, placed with directional flow.**

The entire range of post-cracking fracture response curves for the 5 cm SEN[B] specimens (cut from a 15 cm beam or 5 cm plate) with Strux 90/40 FFC was not significantly altered by the placement technique (Figure 3-7 shows the random placement while Figure 4-13 shows the directional flow placement). The number of fibers counted at the fracture plane for Strux mixture was also consistent between all specimens, contributing to the lower variation of 15 to 33% in total fracture energy compared to that of the BT50 fiber mixtures. A close observation of the Strux specimens cut from the top half of 15 cm beams (Figure 4-14) revealed consistent flexural toughness performance curves regardless of the casting technique (random or directional flow). Thus, the top half of the 15 cm beams was assumed not to have been affected by the placement of the Strux FFC. The randomly placed 5 cm specimens in Figure 4-14 cut exactly from the

bottom mold surface of a 15 cm beam were distinctly higher in fracture energy than specimens cut from all other heights within a 15 cm cast beam. The fiber orientation of the Strux 90/40 was hypothesized to be more aligned for the fibers located in the 5 cm nearest to the mold wall.

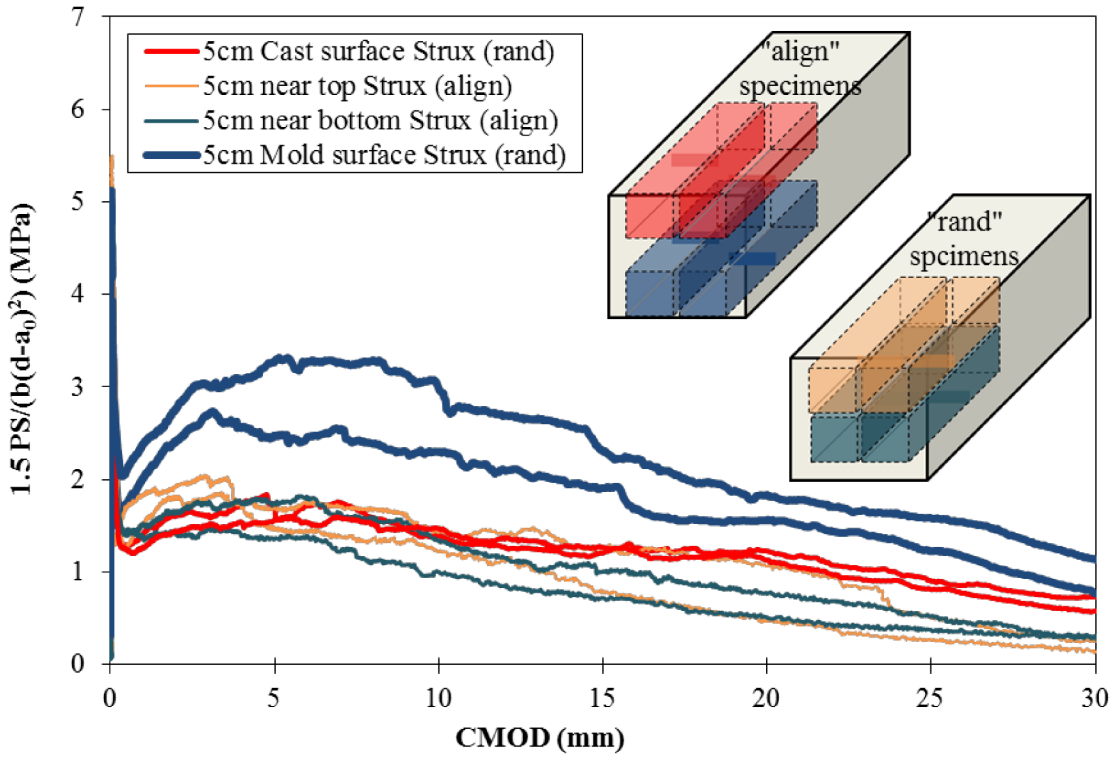


**Figure 4-14 Stress versus CMOD fracture curves comparing FFC SEN[B] beams containing Strux fibers, cut from different heights of a 15 cm cast beam and different placement techniques.**

4.5.3. BT50 FFC Fracture Performance

The BT fiber mixture fracture performance was significantly affected by the placement technique whether cast randomly (Figure 4-15) or under directional flow (Figure 4-16). The BT fiber mixture exhibited high coefficient of variation (see Table 4-5) of 51 or 86 percent for 5 cm plate specimens when cast under directional flow or placed randomly,

respectively. Even with the high variability, the BT plate specimens cast under directional flow had on average five times the fracture energy than those under random placement.

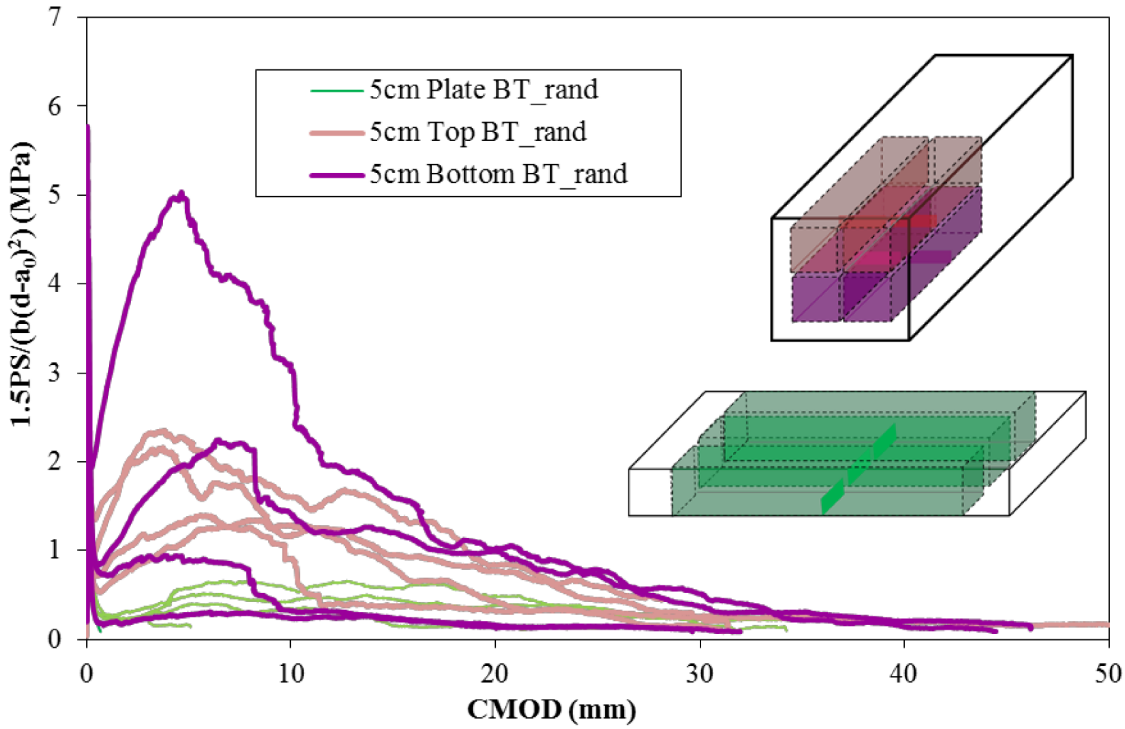


**Figure 4-15 Stress versus CMOD fracture curves are plotted for the beams containing bi-tapered (BT) fibers, placed randomly.**

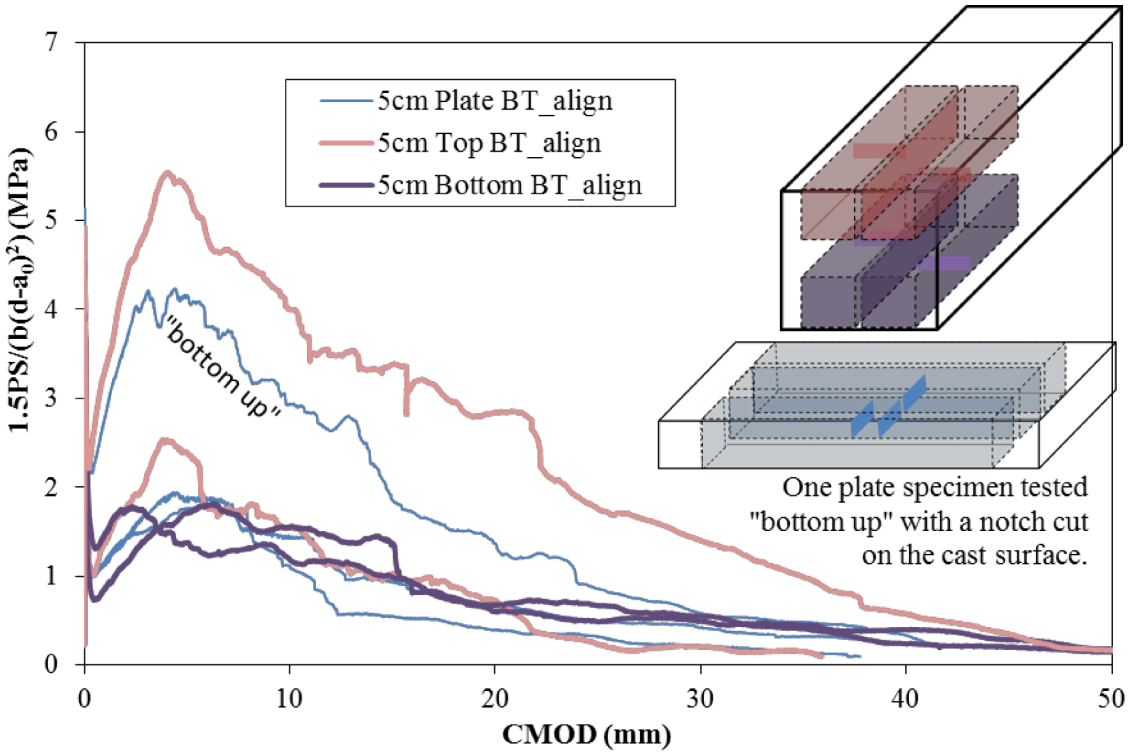


**Figure 4-16 Stress versus CMOD fracture curves area plotted for the beams containing bi-tapered (BT) fibers, placed with directional flow.**

Most of the BT specimens cast within a 15 cm beam had a higher variation in fracture energy, but the range of fracture response was similar regardless of whether a random or aligned placement technique was used (see Figure 4-15 and Figure 4-16). There were some extreme fracture responses measured from the 5 cm SEN[B] specimens cut from a 15 cm beam, such as that near the top surface with a directional flow ($G_{FRC}$ = 13,458 N/m) in Figure 4-16 or from the bottom half with random placement ($G_{FRC}$ = 990 N/m) in Figure 4-15. The specimens cut within 5cm of cast or molded surfaces of the 15 cm beam demonstrated some of the highest fracture curves, which were hypothesized to be related to a boundary wall effect or a non-uniform distribution of fibers. One of these BT plate fracture specimens cast under directional flow was tested with the notch on the cast surface. This specimen, referred to as “bottom up”, performed with a much higher post-cracking stress and was comparable with the superior fracture energy of the specimen cut

from the top of the 15 cm beam (with a notch cut from the internal portion of the 15 cm beam). It would appear that the BT fibers cast under directional flow either segregated to the top cast surface or became more aligned near this cast surface in order to produce such high fracture energy.

### 4.5.4. Placement Technique Effects

A summary of the combined fracture SEN[B] results for 5 cm specimens cut from a 5 cm plate or cut from a 15 cm beam with FFC containing either BT50 or Strux 90/40 fibers is illustrated in Figure 4-17. On average, the measured fracture energy of these mixtures was similar, near 6,000 N/m, when cast under directional flow. However, there was a large coefficient of variation (86%) in post-cracking performance among the BT fiber mixture compared to the Strux fiber mixture (33%). The placement technique clearly altered the post-cracking response of the FFC containing BT fibers, whereas the placement technique appeared to have negligible impact on the overall post-cracking performance for the FFC mixture containing Strux 90/40. Fracture test results suggest the Strux fiber with the lower flexural stiffness can provide the same fracture energy with lower variation and may be more ideal for utilization in thin FFC inlays to achieve the desired pavement service life. The higher flexural stiffness of the BT fibers enabled the BT fibers to be rotated parallel to the direction of the flow, but resulted in lower fracture energies when the FFC material was placed randomly.

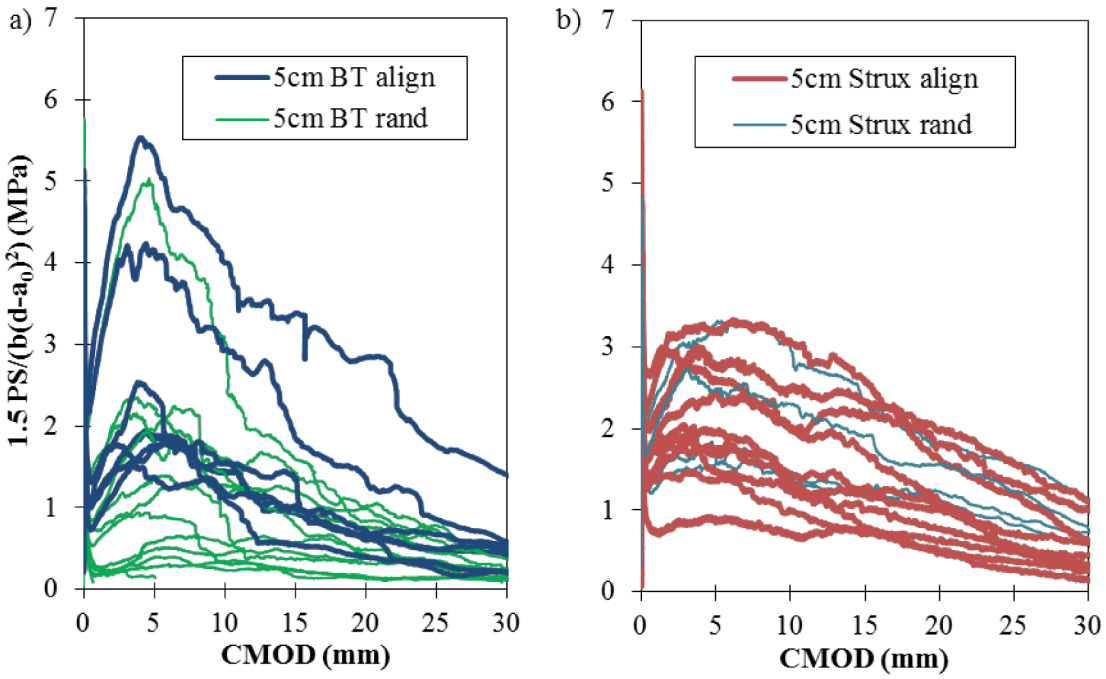


**Figure 4-17 Fracture curves for all 5 cm SEN[B] specimens (cut from 5 cm plates or 15 cm beams) comparing directional versus random placement with (a) BT fibers in FFC and b) Strux 90/40 fibers in FFC.**

The analysis of the BT fiber mixture's net orientation based on the x-ray CT imaging can be studied to test the hypothesis that directional flow enabled more parallel fiber alignment and thus contributed to higher fracture responses. The goal of x-ray CT imaging was therefore to understand whether these BT fibers had significantly different distribution or orientation near the cast surfaces, which could contribute to an increase in fracture energy and variability between specimens. Thus the samples selected (shown in Figure 4-10) represent either the constructed plate sample or the top and bottom surface of a 15 cm constructed beam. A sample from the 5 cm plate specimen cast randomly was also scanned to gain insight as to why these particular plate specimens exhibited low fracture performances.

## 4.6. X-ray CT Sample Images

After thresholding and filtering the x-ray images, the BT fibers can be visualized. The post-processed images for all eight half fracture beam specimens can be viewed in Figure 4-18a through d. The notch location, cast surface, and end mold surfaces have been superimposed on the figures to aid in visualization of fiber location. These 5 cm beam specimens were either cut from either 5 cm plate specimens cast randomly (Figure 4-18c), cast with a directional flow (Figure 4-18d), or were cut from within the top (Figure 4-18a) or bottom (Figure 4-18b) of a 15 cm cast beam placed under directional flow.

The number of BT fibers seen through visual inspection in the randomly cast plate (Figure 4-18c) and the bottom mold (Figure 4-18d) appear to be lower than in specimens either under directional flow or at the cast surface. The images suggest a dominant mold surface boundary effect on fiber alignment even under directional flow. This mold boundary impact on fiber alignment, to be discussed in Chapter 5, has been noted by other researchers (Stähli et al. 2008; Zerbino et al. 2011). The BT fibers appeared to have an angle of orientation more parallel with the direction of flow, which resulted from friction between fibers and the flowable concrete mixture during placement. The more aligned fibers closer to the cast surface appeared, in particular, to have exhibited shear friction as a result from the striking off and finishing of the specimens after FFC placement. Only a few vertical fibers or fibril segments were seen in the specimens, typically located within 5 mm of an edge mold boundary, as illustrated the end view of the plate specimen in Figure 4-18e.

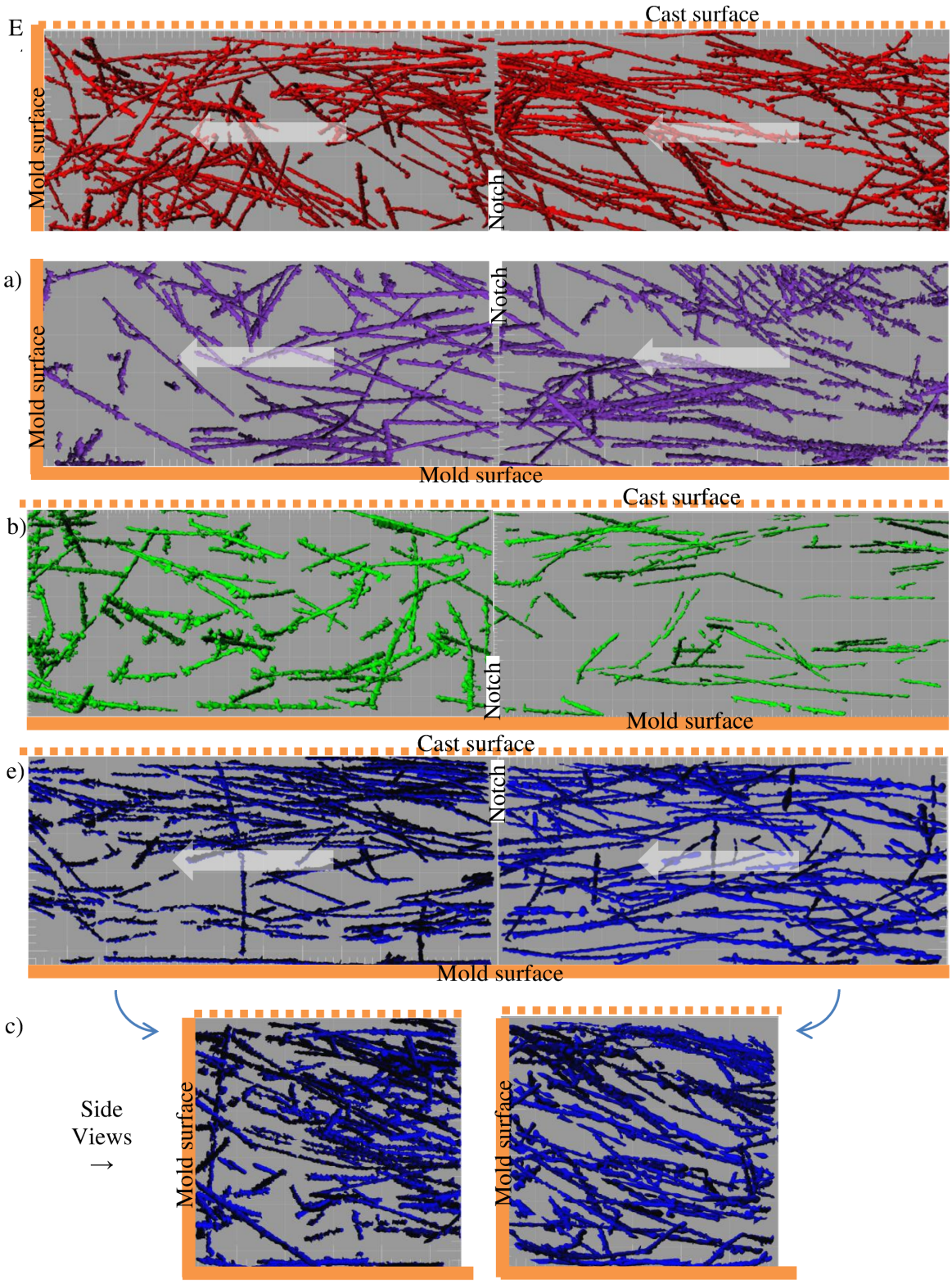


**Figure 4-18 Images show BT fibers within the 5 cm beams: a) cut from the top or b) cut from the bottom of a 15 cm beam; c) cast randomly or d) cast with directional flow as a plate; e) side view of the ends of the align plate beam.**

## 4.7. Accuracy of X-ray CT Imaging

It was important to understand the limitations and repeatability of the x-ray CT imaging and post-processing in order to have an accurate estimation on the number of fibers found in the concrete and their respective orientations. With very few specimens (eight half-beam samples) scanned in the x-ray study, verification was needed that the imaging was accurate in order to be sure that the measured fiber distributions and orientations are valid. Two replicates (each half of the original beam) were scanned with the x-ray CT for two placement techniques (random and directional) of a thin 5 cm plate and two 5cm specimens cut from the boundaries of a 15 cm beam. The accuracy of locating fibers between the two replicate samples was verified by manually counting the fibers present at the cracked beam face and comparing them with the fibril lines from the imaging as seen in Figure 4-18a through d.

### 4.7.1. Volume Fraction Estimation

An accurate estimate of $V_f$ is important since it is utilized in many micromechanical models to predict FRC toughness performance (Li et al. 1991; Balaguru and Shah 1992; Li et al. 1993). By selecting the contrast threshold resolution size to 0.4 mm, which was the same as the smallest fiber dimension, it was anticipated that a close match in estimating the true volume of each fiber would be made. The estimated volume for each fibril object based on IMARIS® was on average (19.24 $mm^3$) slightly lower than the theoretical BT50 fiber volume (23.04 $mm^3$). Some variation in the volume estimation of individual fibril objects was to be expected. An increase in the fiber volume estimation exists for any attached air voids on the fiber surface. There was also an expected

reduction in the estimated volume for fibers which were broken into short fibril segments, during contrast thresholding.

The number of fibers found within the specimen is directly linked with the estimated fiber volume fraction $V_f$ (Hannant 1978; Bentur and Mindess 1990). The estimated volume fraction can be computed one of two ways: based on the number of fibril objects $N_{obj}$ counted times the theoretical volume of a single fiber ($V_{f1}$), or based on the total volume of fibril objects divided by the overall concrete volume ($V_{f2}$). All of the x-ray CT beam specimens were batched with 0.46 percent volume fraction of BT fibers in the same FFC mixture. The computed volume fraction estimation for each of the fracture beam specimens based on their x-ray CT post-processed images can be seen in Table 4-6. The calculation of $V_{f1}$ based on the number of fiber objects was anticipated to be greater than $V_{f2}$ (calculated total fiber volume) in Table 4-6 because $V_{f1}$ assumes all identified objects are whole fibers, while in reality many fibers have been sliced during the cutting of the fracture beam samples. The volume of fibril objects $V_{obj}$ estimation based on the software was foreseen to be slightly higher due to air voids existing along the surface of the fiber which would have been included in the volume estimation. To avoid the error brought on by these attached air voids, any significant air voids were manually removed using the software's cutting tool.

**Table 4-6 Fiber Volume Fraction Estimations**

| | | | BT align top | | | BT align plate | | | BT align bottom | | | BT rand plate | | |
|---|---|---|---|---|---|---|---|---|---|---|---|---|---|---|
| | Beam half: | | a | b | total | a | b | total | a | b | total | a | b | total |
| Volume of single fiber | $V_{sf}$ | ($mm^3$) | 23.04 | | | | | | | | | | | |
| Number of objects | $N_{obj}$ | (-) | 164 | 125 | 289 | 141 | 131 | 272 | 124 | 82 | 206 | 95 | 66 | 161 |
| Total object volume | $V_{obj}$ | ($cm^3$) | 3.1 | 2.9 | 6.0 | 2.3 | 3.2 | 5.4 | 2.2 | 1.8 | 3.9 | 2.2 | 0.6 | 2.9 |
| Reconstructed image volume | $V_{tot}$ | ($cm^3$) | 355 | 343 | 698 | 363 | 364 | 727 | 368 | 370 | 738 | 314 | 319 | 633 |
| $N_{obj}*V_{sf}/V_{tot}$ | $V_{f1}$ | (%) | 1.06 | 0.84 | 0.95 | 0.89 | 0.83 | 0.86 | 0.78 | 0.51 | 0.64 | 0.70 | 0.48 | 0.59 |
| $V_{obj}/V_{tot}$ | $V_{f2}$ | (%) | 0.86 | 0.85 | **0.86** | 0.63 | 0.87 | **0.75** | 0.60 | 0.47 | **0.53** | 0.71 | 0.19 | **0.45** |

All fibril objects were manually confirmed by using the imaging software. However, further verification of the imaging accuracy for identifying fibers was made by breaking the concrete samples apart and manually counting the fibers inside. The number of fibril objects $N_{obj}$ based on imaging was found to be anywhere from 0.8 to 10% lower than actual number of fibril objects (determined by breaking the samples apart and manually counting the fibers). The specimen containing 10% less identified fibers (by imaging) was from the top of the 15 cm beam and was confirmed to contain a large amount of fiber clumping (clumped fibers had to be manually separated using the imaging software cutting tool). $V_{f2}$ was expected to represent the realistic volume fraction estimation within each specimen. From Table 4-6, the variation in volume fraction between each analyzed specimen was assumed to be the result of placement techniques during casting. Because each of these analyzed specimens were cut from a larger casting, it was very possible that the volume of fibers calculated only represents the local fiber amount and not the volume fraction or distribution of fibers throughout the entire cast specimen.

4.7.2. Placement Technique Effect

The specimens from the top 5 cm of the cast surface (either from a 15 cm beam or cast as a 5 cm plate) were found to contain almost double the amount of fibers (see $V_{f2}$ in Table 4-6) than the 0.46% volume batched in the FFC mixtures. However, the randomly placed FFC mixture had a similar volume fraction on average (for both half-beam samples) as was originally batched FFC mixture. There was also a high variation (0.71% versus 0.19%) between the computed volume fractions between each half-beam specimen for the randomly placed FFC. This was in contrast to the half-beam plate samples which were placed with directional flow ("align") (shown in Figure 4-12) and had a much smaller variation among the two half-beam samples. The x-ray CT specimens cast under directional flow exhibited on average higher volume fraction estimations by 1.2 to 1.8 times above the batched $V_f$. Based on the volume fraction findings, it is hypothesized that portions of the same 15 cm cast beam or 5 cm cast plate must have lower concentrations of the BT fibers, while the portions cut out and scanned for this study may have contained fiber clumps and a high concentration of fibers. As anticipated, the increasing volume fraction directly correlated with the beam ranking in fracture performance, illustrated in Figure 4-11).

## 4.8. Expected Toughness with Thin FFC Pavements

4.8.1. Fiber Distribution along Specimen

Based on fracture testing listed in Table 4-5, the randomly cast BT fiber FFC specimens revealed high variability (86%) in measured fracture energy and visually in the number of fibers at the fracture plane, as shown in Figure 4-19. This high variation was also

exhibited among the volume fraction estimation (see Table 4-6) for each half-beam (from 0.19% to 0.71 % volume fraction for the randomly placed plate half beam samples a and b, respectively). With field construction, this type of random placement technique was likely to occur by practitioners rather than placing the FFC with directional flow or extrusion methods. The problem with this high variation in the number of BT fibers with randomly cast FFC was that the prediction of toughness performance was similarly highly variable.

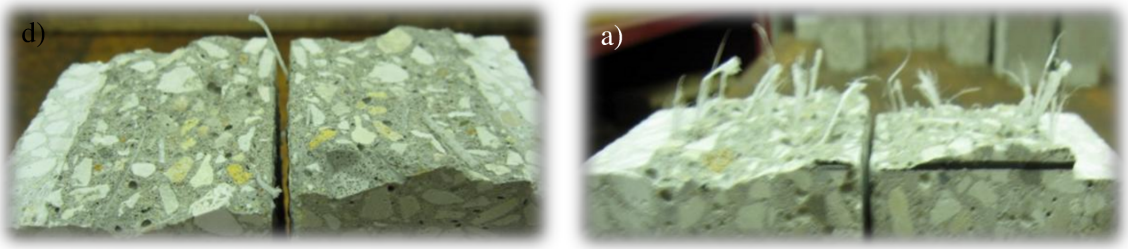


**Figure 4-19 Photographs showing fractured surfaces of a) plate specimen and b) a specimen from the bottom of a 15 cm beam for the BT randomly placed beams.**

The distribution of the BT fibers along the specimen, shown in Figure 4-20, was calculated based on two methods: the fiber centroid location and use of an orthogonal (vertical) slice at various positions along the beam. The number of fibers were manually counted after using the orthogonal plane slicing tool (illustrated in Figure 4-21), available within the IMARIS® software, which provided a realistic estimation of the expected number of fibers intersecting any plane along the beam. A distribution based on the fiber centroid location relative to a stereology-based distribution, will always underestimate the total number of fibers across any given orthogonal plane, since each fiber is only counted once with the centroid method. Using the orthogonal slice at roughly every 5 mm, any fibers which are perpendicular to cast surface would not likely be represented in the vertical orthogonal slice counting, while aligned fibers would be counted across

multiple orthogonal slices. A high concentration of fibers at a specific location was typically a clump of BT fibers. In particular, clumped fibers aligned parallel to casting would appear as a hump spanning approximately 48 mm (the fiber length). Visualization of the images in Figure 4-18 verifies that fiber clumps were more commonly exhibited in the specimens cast under directional flow.

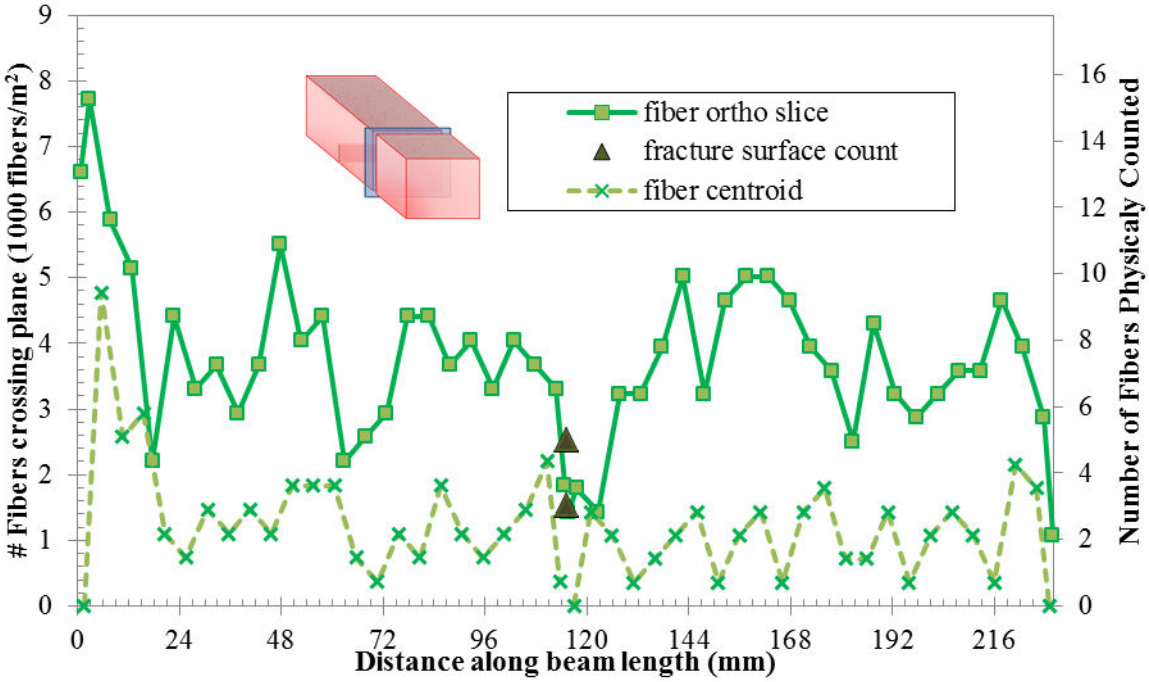


**Figure 4-20 Example of the number of fibers in the randomly placed BT50 plate specimen determined from an orthogonal xy plane slice or centroid.**

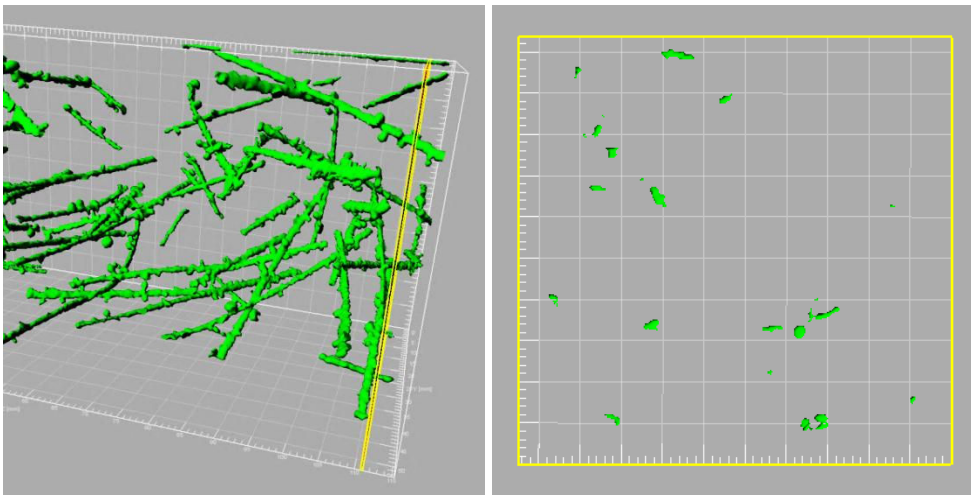

**Figure 4-21 Screen captures showing orthogonal slicing tool used for manually counting fibers in the vertical xy plane.**

The two specimens with the greatest fracture energy that were x-rayed (BT align top and BT align plate) had approximately double the amount of fibers located at the fracture plane relative to the other two specimens (BT align bottom and BT rand plate), as illustrated in Figure 4-22. The distributions of fibers using orthogonal slices for all of the x-ray CT specimens (shown in Figure 4-22) were compared against the number of fibers physically counted at the fracture plane for each half-beam in order to verify the accuracy of x-ray imaging to identify fiber objects.

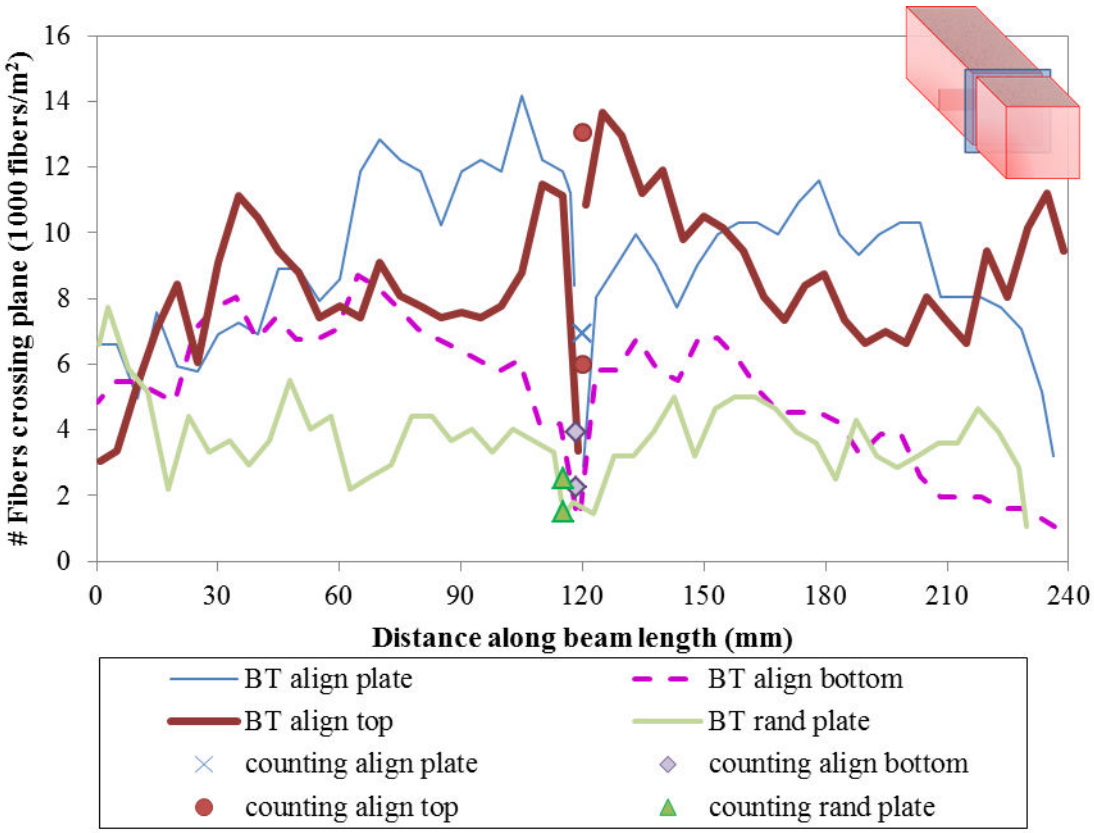


**Figure 4-22 The number of fibers using the orthogonal slice tool crossing potential fracture planes for the x-ray CT specimens.**

4.8.2. Expected Number of Fibers

Most micromechanical models described in the literature include either the volume fraction or utilize the number of fibers to predict the FRC toughness performance (Krenchel 1975; Gopalaratnam and Shah 1987; Li et al. 1991; Li et al. 1993; Dupont and Vandewalle 2005). Several of these models also incorporate the expected values of fiber orientation (Li et al. 1991; Geng and Leung 1997) or expected embedment length (Lange-Kornbak and Karihaloo 1997). All of these models assume a uniform distribution of fibers across the entire concrete specimen.

The calculation of expected number of fibers per unit area was presented by Krenchel (1975) as $n = \alpha V_f/A_f$, where $\alpha$ was an orientation factor and $A_f$ was the fiber cross-

sectional area. The orientation factor for randomly distributed fibers in a 3D space has been published to be 0.5 (Li et al. 1991; Dupont and Vandewalle 2005; Stroeven and Hu 2006), making the expected number of BT fibers to be 3750 per $m^2$ in the FFC specimens. A standard normal distribution (shown in Figure 4-23) was found to be sufficient for estimating the number of fibers when the FFC mixture containing the BT fibers was placed randomly. The actual average number of fibers from the random placement FFC based on the x-ray imaging was 3720 fibers per $m^2$ which was similar to the theoretical expected value (3750 fibers per $m^2$).

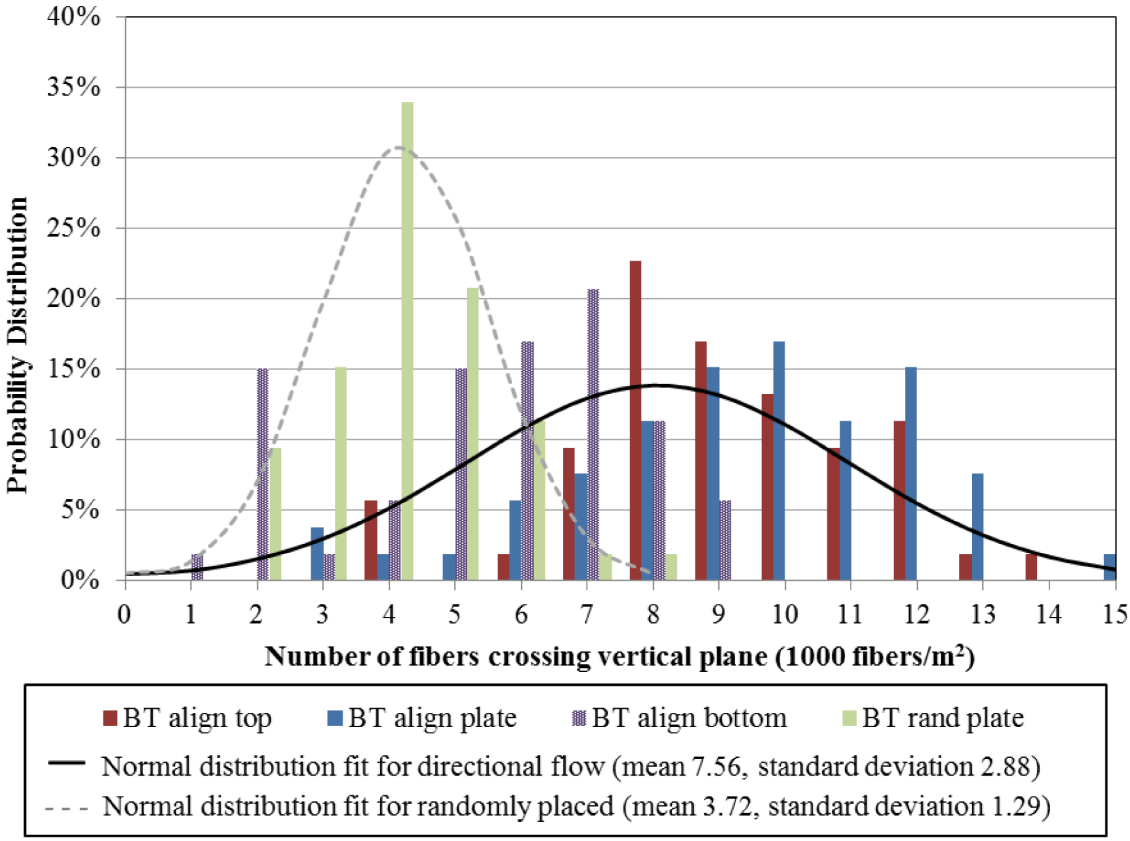


**Figure 4-23 Distribution of fibers crossing a vertical xy plane at any horizontal position within the sample.**

A 2D distribution (parallel with yz plane shown in Figure 4-3) was assumed to occur for fibers cast under directional flow with close proximity to boundary surfaces. A 2D planar

fiber orientation factor was anticipated to be either 0.57 (Soroushian and Lee 1990), 0.60 (Dupont and Vandewalle 2005), or 0.636 (Li et al. 1991; Geng and Leung 1997; Stroeven and Hu 2006), and thus have an expected number of fibers on the fracture plane should be anywhere from 5460 to 6100 per $m^2$, respectively, for 0.46 percent volume fraction. At an estimated fiber volume fraction of 0.75 percent (found in the align plate sample), the number of fibers crossing the vertical fracture plane was expected to be 8910 to 9950 per $m^2$ for 2D alignment or 7810 per $m^2$ for 3D random. Since the average number of fibers found in a cross section for the aligned plate sample was at 8970 fibers per $m^2$, the distribution of fiber in the thin FFC plate was verified to fall within the expected theoretical 2D fiber distribution.

An understanding of the absolute expected range of fibers at any given vertical plane (listed in Table 4-7) was useful for predicting the best- and worst-case fracture performances. The estimated fracture energy was calculated using the correlation equation $G_{FRC} = 1299.1*N_f - 61.335$ (from Figure 2-8) with the minimum or maximum number of BT fibers found in each cross-sectional image plane. The average number of fibers at any vertical cross-section was correlated to the volume fraction estimation listed in Table 4-7.

**Table 4-7 Number of Fibers and Estimated Fracture Energy of X-ray CT Samples**

| | Units | BT align top | BT align plate | BT align bottom | BT rand plate |
|---|---|---|---|---|---|
| Minimum $N_f$ | (1000 fibers/$m^2$) | 3.0 | 2.6 | 1.0 | 1.1 |
| Maximum $N_f$ | (1000 fibers/$m^2$) | 13.6 | 14.2 | 6.8 | 7.7 |
| Average $N_f$ | (1000 fibers/$m^2$) | 8.5 | 9.0 | 4.0 | 3.7 |
| $N_f$ (actual) | (1000 fibers/$m^2$) | 10 | 7 | 3 | 2 |
| Est. min $G_{FRC}$ | (N/m) | 3,885 | 3,281 | 1,201 | 1,336 |

| | | | | | |
|---|---|---|---|---|---|
| Est. max $G_{FRC}$ | (N/m) | 17,667 | 18,362 | 8,775 | 9,965 |
| Actual $G_{FRC}$ | (N/m) | 13,458 | 8,897 | 4,759 | 2,017 |

The number of fibers found in the top of a 15 cm beam was significantly higher than those found in the bottom of the 15 cm beam (as listed in Table 4-7). It was hypothesized that a segregation of the BT fibers may have occurred in the 15 cm beam as a result of having both a lower specific gravity for the BT fibers and use of the flowable concrete mixture. Therefore, it appears there was a gradient in $N_f$ within the 15 cm beam, which may also occur as a spatial distribution of fibers in the cast 5 cm plate specimens.

It is useful to be able to predict the number of fibers distributed in the FFC in order to improve modeling and designs of the thin concrete inlay. The number of fibers crossing any given vertical plane was lower when FFC with BT fibers was placed randomly into a 5 cm thin plate. Still, a normal distribution with found to be sufficient in describing the variation of $N_f$ along a beam with the random placement of FFC as a thin plate. When cast under directional flow, the FFC containing BT fibers appeared not to follow a normal distribution (see Figure 4-23), and was likely skewed by the local volume fraction differences or fiber clumping. Although the expected fracture energy was higher on average with directional flow, the FFC with BT fibers demonstrated a high variability in the volume fraction, number of fibers, and as a result high variability in expected fracture energy response. For example, the plate specimen cast under directional flow had a range of expected fracture energy based on the number of BT fibers crossing a given fracture plane between 3,300 and 18,400 N/m (Table 4-7).

## 4.9. Summary

Past imaging techniques have been used to locate steel fibers within concrete. This is the first attempt to locate synthetic macro-fibers in three-dimensions within concrete. X-ray computed tomography was selected for the technique to identify the synthetic fibers within the concrete, with a high power source x-ray machine needed to produce a good contrast and spatial resolution. Image processing software was utilized for thresholding and filtering based on an ellipsoidal shape assumption. Two types of synthetic fibers were tested with the x-ray CT machine; one with a higher flexural stiffness (BT50) and another with a lower flexural stiffness (Strux 90/40). The Strux 90/40 fibers could not be successfully located within the concrete using the image analysis software due to difficulties in detecting the shape of the bent or curved fibers in the concrete matrix. Imaging of the BT50 fibers verified that a higher concentration of fibers, 1.8 times the batched volume fraction, was found in the top 5 cm of a 15 cm cast beam. The imaging process was verified to be accurate for identifying 90 to 99.2% the BT50 fibers in concrete.

Fracture test results for the BT50 fiber in the FFC mixture illustrated the number of fibers and total fracture energy can be increased by a magnitude of 5 when the FFC is placed under a directional flow. With BT50 fibers cast randomly as a 5 cm plate, the specimens produced a significant variability up to 86% in total fracture energy. The Strux 90/40 FFC placed either randomly or under directional flow produced similar average fracture energies near 6000 N/m, which were also comparable with the average fracture energy of the FFC with BT50 fibers cast as a 5 cm plate under directional flow. Fiber distribution along the x-rayed FFC specimens was assessed by using an orthogonal slice tool and manual counting of fibers at a given vertical plane. For the cast 5 cm plate specimens

scanned, the fiber distribution correlated well with the theoretical 3D random dispersion of fibers for the randomly placed FFC specimen and with the theoretical 2D planar dispersion of fibers for the FFC placed with directional flow. The number of fibers at a given vertical plane found from the x-ray CT of a SEN[B] sample can be used to predict the projected total fracture energy for the FFC.

# CHAPTER 5. FIBER ALIGNMENT NEAR SURFACE BOUNDARIES

## 5.1. Motivation

Test results have shown FFC samples cut from a 5 cm thick plate achieved higher fracture energy including a deflection hardening response, compared to the 15 cm thick standard beam. In the thin FFC specimens, the enhanced fracture toughness or deflection hardening response was supposedly due to fiber alignment. Fiber alignment in FFC could be achieved in two ways: by casting with a directional flow or casting thin specimens which exhibit significant boundary wall effects. Extrusion techniques have been utilized to purposefully align fibers for improving fracture performance (Takashima et al. 2003; Shen et al. 2008). However, with FFC, the intent was to place the concrete at one end of a plate to produce a directional flow (as shown in Figure 4-12) which should sufficiently align the fibers and improve fracture performance. Boundary wall effects are described to be material particle packing limited to a finite size next to a boundary mold or cast surface (Bažant and Planas 1998). Because the thin plate specimens were cast of the same height as the fiber length, the boundary surfaces were always in close proximity to any point in the FFC specimen. The fibers near the boundary (cast or mold) surfaces would be more aligned. This chapter discusses the following: the increase in fiber alignment due to a directional flow rather than random placement, determining an estimated boundary-affected size on fiber orientation and fiber distribution near cast and mold surfaces, and the combined influence of fiber alignment and number of fibers ahead of a fracture plane on the measured fracture response.

### 5.1.1. Fiber Orientation

Fibers oriented vertically in the thin plate do not contribute to the measured fracture performance, while those fibers oriented with some projected angle in the 2D horizontal plane would contribute to the pull-out fracture resistance. A perfectly "aligned" system of fibers in the thin plate would result in fibers oriented anywhere within the yz-plane. This in-plane 2D fiber dispersion follows a delta-dirac function of probability, where all fibers must have a polar angle of 90 degrees from the x-axis (Jain and Wetherhold 1992). The probability of a fiber being randomly oriented in a 3D space follows a sinusoidal function as shown in Figure 5-1a (Li et al. 1990; Li et al. 1991; Jain and Wetherhold 1992; Dupont and Vandewalle 2005; Stroeven and Hu 2006). The computed expected mean value of a 3D random orientation (shown in Figure 5-1b) of fibers was 57.3 degrees from the vertical polar axis. Dispersion of fibers in the other 2D planes (xz or xy) would be considered out-of-plane (see Figure 5-1a) and would be used to describe an edge boundary wall distribution. But for the thin inlay pavements, the edge wall is considered negligible to the overall slab fracture resistance. Fibers in the FFC specimens cast as thin plates were anticipated to be closer to the 2D in-plane dispersion, having a polar angle closer to 90 degrees, while larger 15 cm cast beams were expected to have a 3D random dispersion of fibers with a polar angle closer to 57.3 degrees.

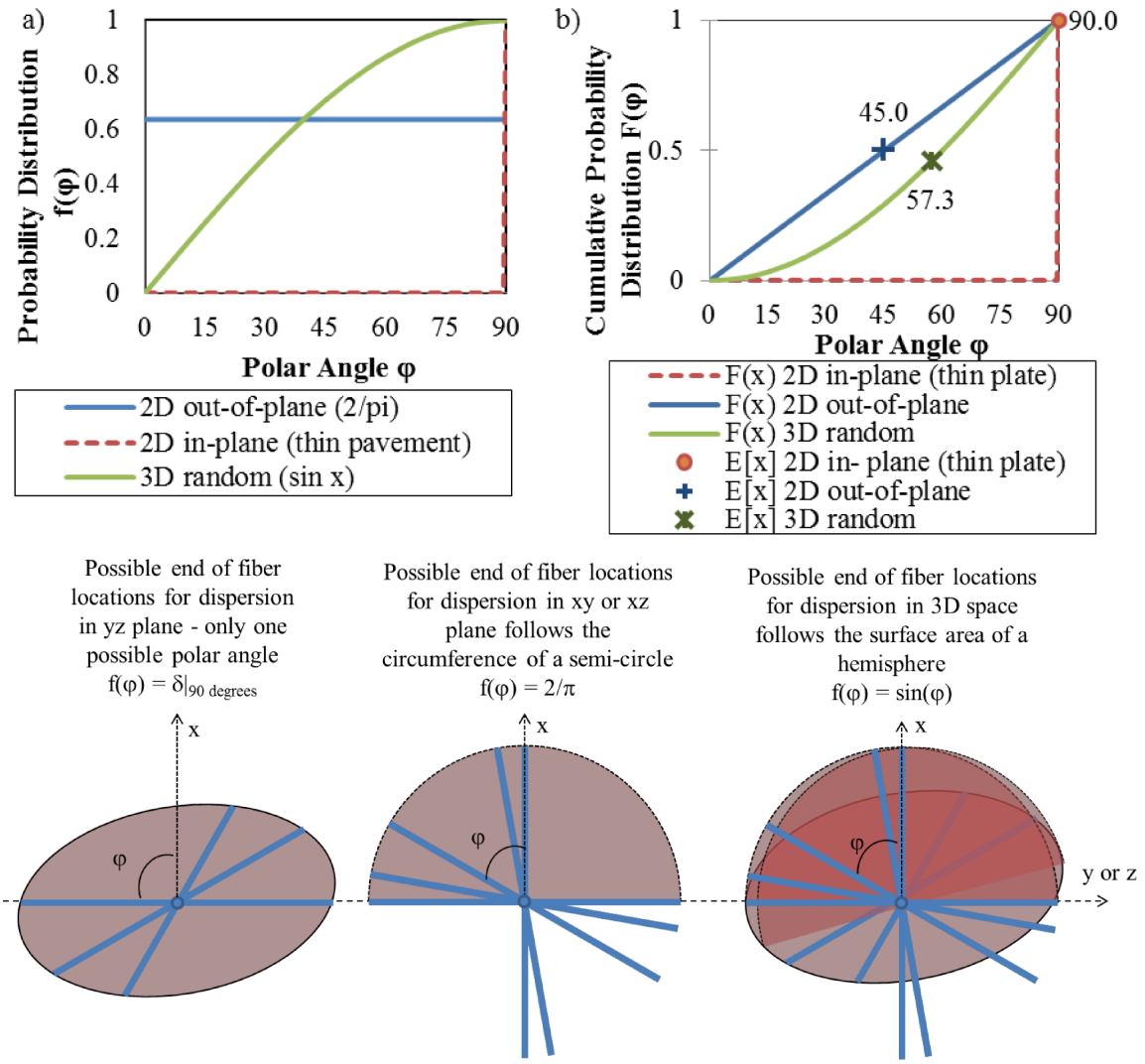


**Figure 5-1 The a) probability density, b) cumulative distribution functions with expected mean values, and c) schematic drawing are shown for 2D in-plane, 2D out-of-plane, and 3D analyses.**

5.1.2. Casting Technique

It was desired to have a 2D planar alignment (with fibers oriented anywhere in the yz plane shown in Figure 4-3 and Figure 5-1c) for optimal pull-out resistance to cracking at the joints or any cracking within a slab panel. By having fibers oriented perpendicular to cracking, the measured fracture performance will increase. This orientation of fibers in concrete can be influenced by the casting technique utilized. Past research has indicated

that steel fibers in SCC mixtures cast into plates, long beams, or vertical walls can have a large variation in the tested toughness performance (unnotched beam specimens cut from the cast samples) at different orientations relative to the flow direction (Ferrara et al. 2007; Barnett et al. 2010; Torrijos et al. 2010). Toughness test specimens cast as a beam or round plate to a thickness of three to four times the fiber length were found to have fibers oriented parallel with the direction of flow (Ferrara et al. 2007; Torrijos et al. 2010; Zerbino et al. 2011). Other researchers reported that steel fibers were oriented perpendicular to flow, based on visual inspection, x-ray CT imaging, and electrical impedance testing of FRC in thin round plates of height two to three times the fiber length (Lataste et al. 2008; Barnett et al. 2010). For a thin inlay pavement, the orientation of fibers either parallel with the flow or perpendicular to flow is not a crucial concern because slab joints are cut in both longitudinal and transverse directions. It is important to gain an understanding of casting placement technique effects on the expected net fiber orientation with regards to this 2D plane in order to predict the thin FFC fracture performance.

### 5.1.3. Boundary Wall Effect

Boundary effects are typically negated in the design of concrete structures, because most structural concrete dimensions are much larger in comparison to the size of these material components. However, the benefit of having fibers more aligned by their location near a boundary surfaces is implemented with the thin FFC inlay pavement for enhancing the fracture performance of the concrete slabs. In addition to directional casting techniques, fibers located close to a mold surface have been discovered to rotate and become more aligned parallel with that mold surface (Moses et al. 2001; Stähli et al. 2008), as

illustrated schematically in Figure 5-2a. The combination of directional flow and boundary wall effects was observed with steel FRC through sliced x-ray images (Stähli et al. 2008). Even along the wall surface shown in Figure 5-2b, fibers were oriented in the 2D plane parallel to the wall with some preferential orientation in the direction of the flow. The work by Stähli et al (2008) did not quantify the boundary effects on fiber orientation or distribution; however, with the research presented here, the quantification of fiber distribution and fiber orientation within the specimen height were computed using the x-ray CT imaging results from Chapter 4 of the BT50 fibers in FFC.

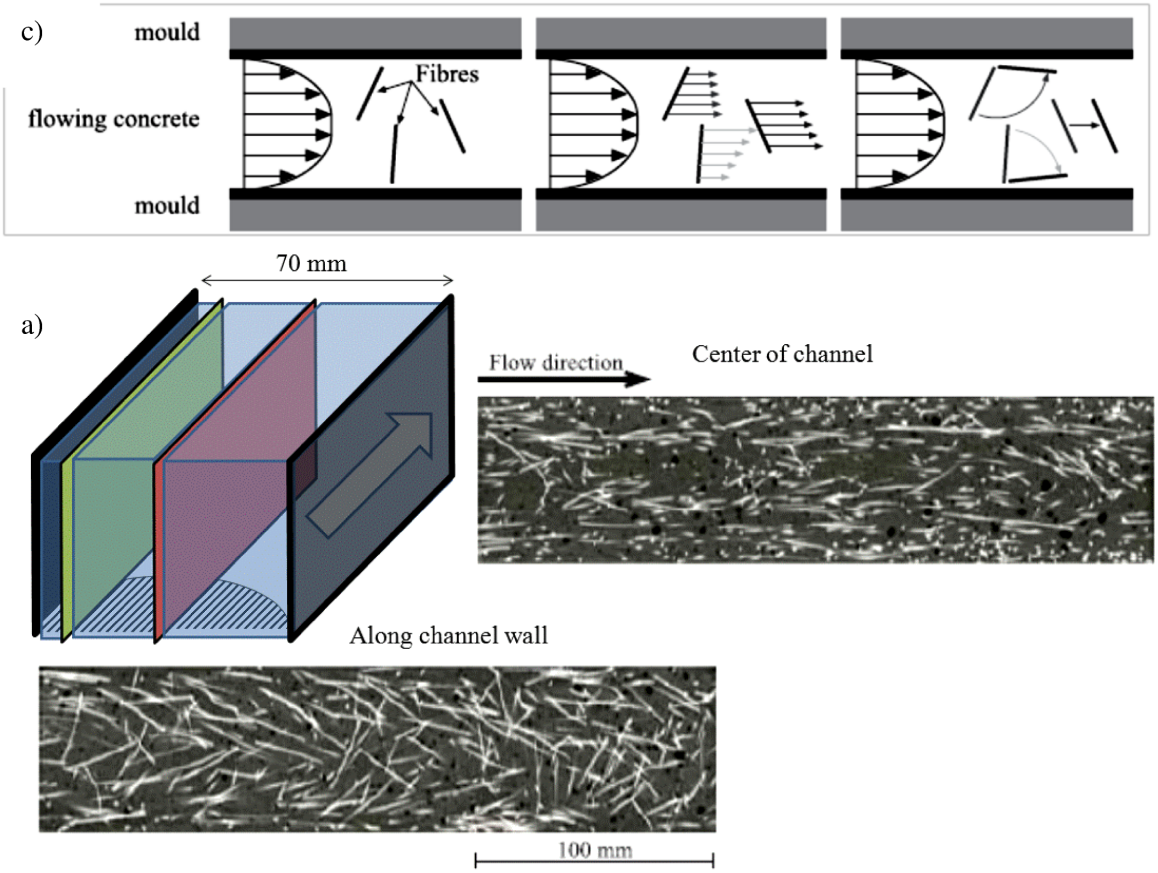


**Figure 5-2 a) Schematic top-down view and b) x-ray profile images (parallel to wall) results show fiber movement through a narrow channel (Stähli et al. 2008).**

The size of a boundary-affected zone is important for designing the thickness of the FFC inlay in order to have improved fiber alignment from the close proximity of cast and

mold surfaces. FRC stereology publications (Soroushian and Lee 1990; Dupont and Vandewalle 2005; Stroeven and Hu 2006) have assumed a boundary zone size of $L_f/2$ due to spatial and time limitations in cutting frequent cross-sectional slices at given distances from a boundary surface. However, the study by Moses et al. (2001) found in the presence of a flow a logarithmic relation described how much fibers rotated, to become parallel with the mold wall, with respect to the fiber's proximity to the wall. The magnitude of the boundary-affected distance of fiber alignment was anticipated to be between the diameter of the fiber $d_f$ and the length of the fiber $L_f$ from a mold surface (Moses et al. 2001). For the FFC cast plate specimens of a thickness proportional to the fiber length, the entire specimen height was anticipated to be dominated by the boundary-wall effects. Therefore, by studying the two x-ray CT specimens cut from the cast and mold surfaces of a 15 cm cast beam, differences in the number of fibers and orientation of the fibers with respect to a boundary surface can be used to estimate the boundary-affected size.

## 5.2. Cast versus Mold Surface Fracture Behavior

FFC specimens cut from near the cast surface of a 15 cm beam demonstrated a higher fracture performance than specimens cut from the bottom mold surface, as represented in Figure 5-3a. Visually, it appears that the number of BT50 fibers was greater near the cast surface, based on the x-ray imaging presented Figure 4-18a and d. The fracture test results are anticipated only to reflect the post-cracking performance influenced by fibers located ahead of the saw-cut notch. For the SEN[B] specimens (notch is 1/3 of the beam height), this means that any boundary-affected fiber orientation or distribution within

roughly $L_f/3$ of the notched surface does not contribute to the fracture performance. Among the specimens cut from the top of a 15 cm cast beam, those with a notch on the interior (leaving the entire boundary surface intact) exhibited the highest post-cracking responses, as illustrated in Figure 5-3b. Consequently, one may think the top cast surface always would provide a higher toughness performance. However, the fracture tests on a thin plate section indicated the best fracture response occurred when cracking initiated through the 2/3 height near the mold surface, as seen in Figure 5-4. Thus, with casting a 5 cm specimen, with a height close to the length of the fiber, a different fiber distribution and orientation within the plate specimen likely existed relative to a 15 cm beam specimen. A comparison will be presented later in the next sections of the determined fiber distributions and orientations for the four specimens scanned in the x-ray CT. The average number of fibers and net fiber orientation determined from fibers located ahead of the SEN[B] specimen notch were expected to contribute to the measured fracture energy of the beam.

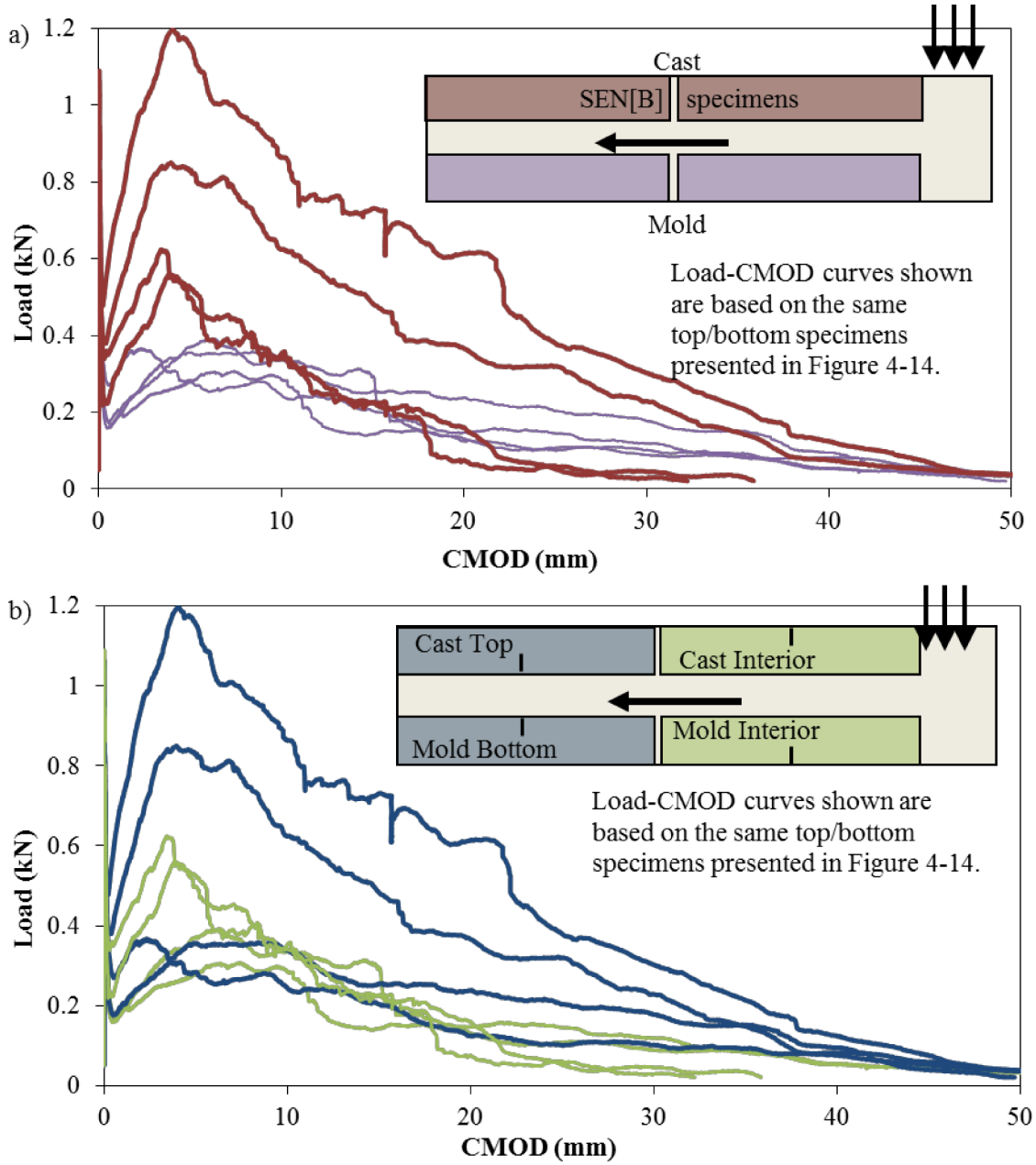


**Figure 5-3 Load versus CMOD results of 5 cm SEN[B] specimens cast as a 15 cm beam, comparing (a) the cast/mold boundary surfaces versus (b) notch location.**

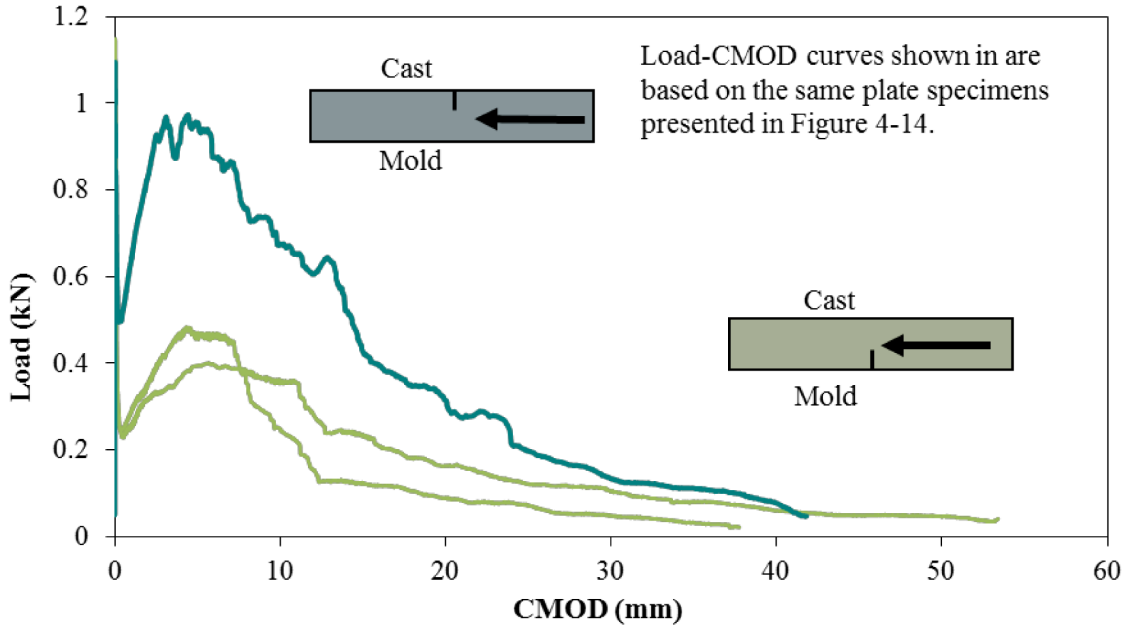


**Figure 5-4 Load versus CMOD results of 5 cm SEN[B] specimens cast as a 5 cm plate, comparing notch location.**

## 5.3. Fiber Distribution in Fracture Plane

The fibers crossing the fracture plane, perpendicular to the direction of casting in the case of the directional placement, influence the post-cracking performance. There are three factors associated with the post-cracking performance: the fiber orientation, the total number of fibers (related to volume fraction), and the spatial distribution in the number of fibers (altered by boundary surface effects or segregation) ahead of the notch. The total number of fibers crossing ahead of the fracture plane has been shown to be the primary factor contributing to the measured fracture energy (see Figure 2-8). However other factors, such as the fiber orientation and distribution of these fibers within the fracture plane, may also contribute to the overall fracture response. This section investigates the number of fibers distributed within the fracture plane.

### 5.3.1. Fibers near the Boundary Surface versus Interior

For a rigid fiber particle, the limited packing density of fibers against a solid mold wall can affect the orientation of the fiber, which also impacts the number of fibers counted through 2D stereology slices. The number of fibers was computed as the sum of all fibers crossing the horizontal yz plane (as shown in Figure 4-3) at given distances from a cast (Figure 5-5) or mold (Figure 5-6) surface. The orthogonal slice tool in IMARIS® was used for locating the sliced plane at roughly 3 mm increments, and fibers were manually counted at each plane for the eight half-beam x-ray image samples. The total number of fibers located within the fracture plane was greatest for the specimen cut from the top cast surface of a 15 cm beam. This higher fiber count was expected because the estimated volume fraction in this particular specimen (shown in Table 4-6) was roughly double the batched fiber amount. Subsequently, Figure 5-5 and Figure 5-6 were normalized by the estimated volume fraction $V_{f2}$ (based on the 3D volume of fibril objects) from Table 4-6 as well as normalized to a unit cross-sectional area, in order to only view the distribution of fibers throughout the specimen height. Fibers which are perfectly aligned in the yz plane (90° from vertical), as desired for a thin inlay pavement, would likely not exist at the exact sliced location and thus a reduction in the number of fibers was anticipated (see Figure 5-7) at the sliced height where fibers were more aligned.

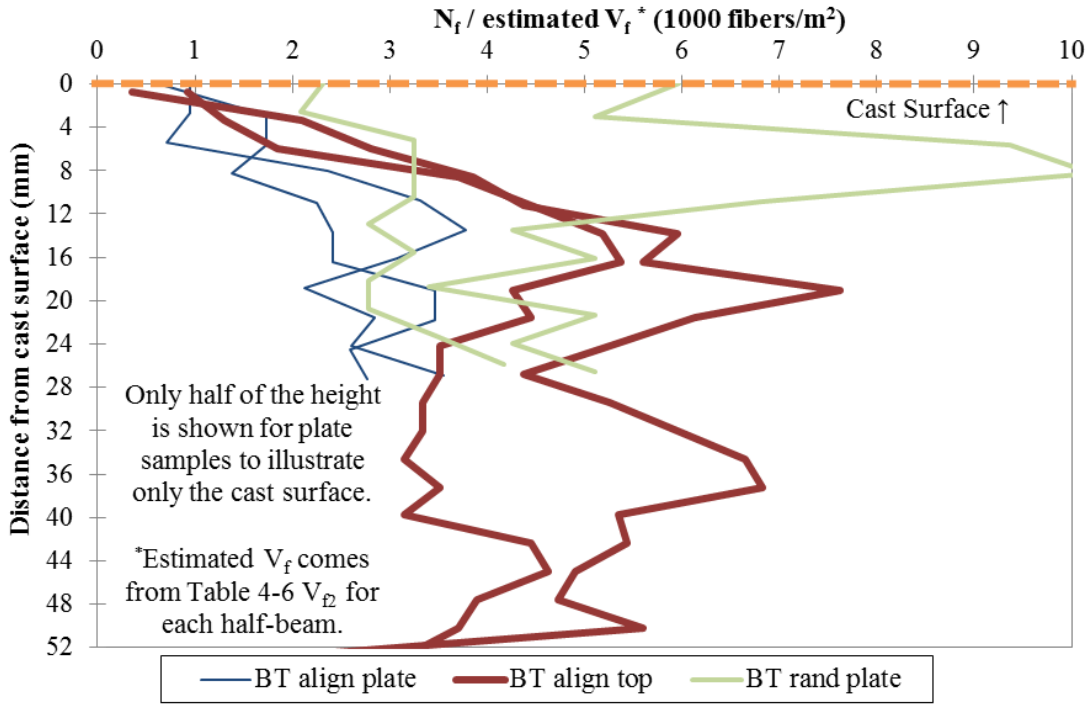


**Figure 5-5 The number of fibers crossing an orthogonal horizontal plane normalized by the specimen volume fraction at various distances from the cast surface.**

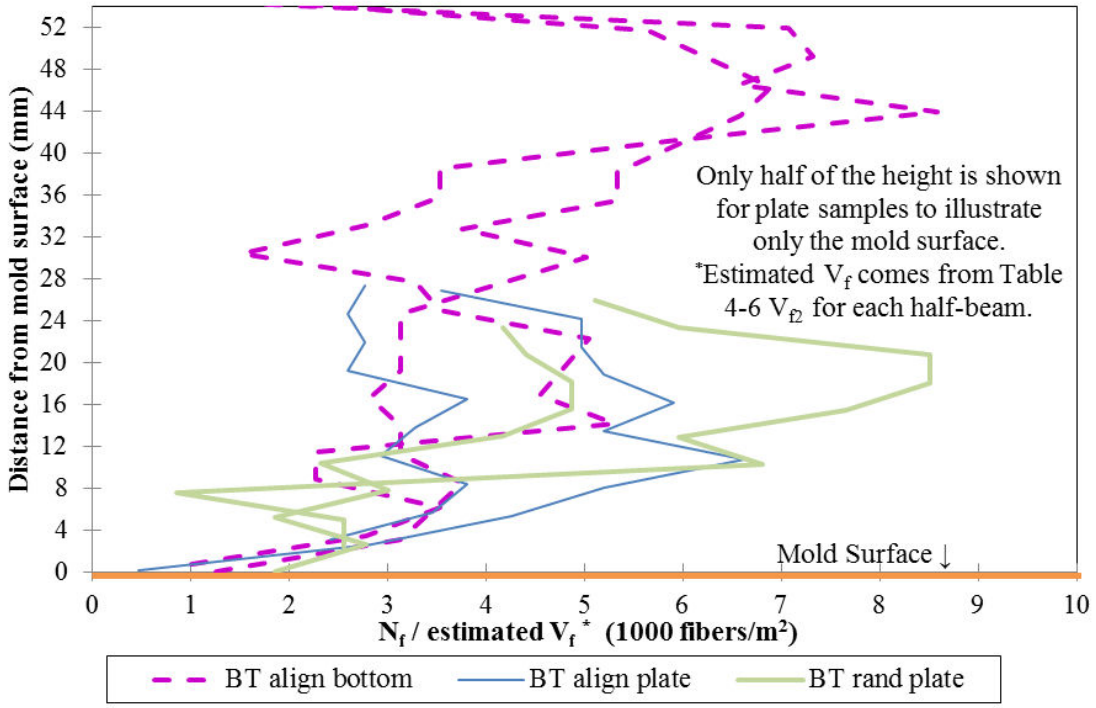


**Figure 5-6 The number of fibers crossing an orthogonal horizontal plane normalized by the specimen volume fraction at various distances from the mold surface.**

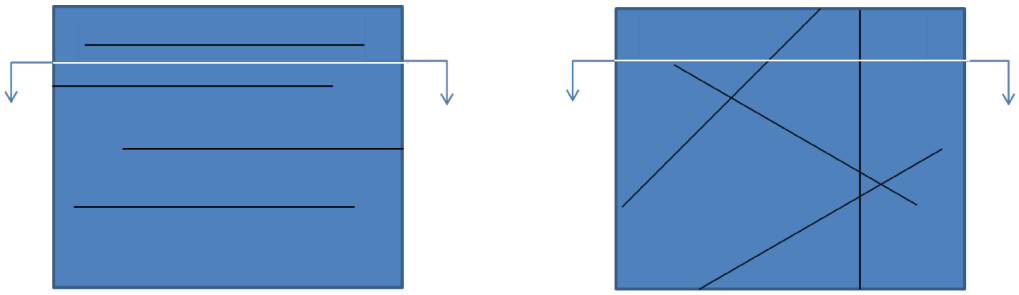

Horizontal (e.g. YZ) Slices

$N_f/V_f$ aligned fibers < **$N_f/V_f$ random fibers**

**Figure 5-7 Schematic showing the reduced number of fibers counted in a horizontal slice with perfect 2D (yz) planar fiber alignment versus with a 3D random orientation of fibers.**

The packing density of fibers at a boundary surface is presumed to induce alignment, which as a result reduces the number of fibers counted in planes parallel to the surface. A reduction of fibers within half of the fiber length of a mold surface (see Figure 5-6) was calculated to be 31% from the x-rayed CT images with BT50 fibers. This is comparable with the 39% reduction in the number of fibers found within half the fiber length from a mold surface with steel FRC (Stroeven and Hu 2006). An exception to this reduction in the number of fibers was found among the FFC specimens cast randomly as a 5 cm plate (see Figure 5-5), which had a higher number of fibers, relative to the volume fraction, near the cast surface. The fibers in this randomly-placed plate specimen were assumed to have exhibited less fiber alignment along the cast surface. In order to verify that fibers were more aligned near the boundary surface, the orientation of each fiber was to be calculated from the x-ray CT imaging.

Past stereology research suggested the size of the boundary zone was proportional to half the fiber length. The number of fibers did appear to be reduced for distances of $L_f/2$ from the mold surface (Figure 5-6). Although, by viewing the stereology slice results in Figure 5-5, there appeared to be a continuously decreasing number of fibers towards the cast

surface from 12 mm or $L_f/4$ from the cast surface in specimens placed with a directional flow. This means that the assumption for the boundary-affected zone size to be $L_f/2$ (or 24 mm) from a cast surface may not be appropriate. A reduced boundary-affected zone size was expected along the cast surface, as fiber particles would not have the same solid surface restricting the fiber orientation and packing. The estimated boundary affected-zone sizes, based on a reduction in the number of fibers crossing a horizontal plane, for the cast 15 cm beam with FFC was $L_f/4$ from the cast surface and approximately $L_f/2$ from a mold surface.

### 5.3.2. Fiber Spatial Segregation

It was anticipated, based on the measured fracture energy being higher for specimens near the cast surface of a 15 cm beam (Figure 5-3a), that there may be non-uniform vertical distribution of the BT fibers within the FFC. Past researchers have noticed steel fibers would segregate to the bottom of concrete beams (Stroeven 1979; Ferrara et al. 2007). As the polymeric fibers are less dense than water (specific gravity of 0.91), there may have been a tendency for these fibers to float or segregate towards the top of a specimen. Fiber segregation based on the estimated volume fraction of BT fibers in the FFC did appear to occur among the two imaged specimens from the 15 cm cast beam, with 0.86% volume fraction within the top 5 cm versus 0.53% within the bottom 5 cm (see Table 4-6). However, within the plate specimen under the directional flow, there was slightly higher amount of BT fibers in the bottom half of the plate height (Figure 5-5 and Figure 5-6). Based on the X-ray CT data collected, there appeared only to be segregation of the BT50 fibers for the 15 cm thick cast beams, as determined by a locally

gradient in the fiber volume fraction with specimen height (see Table 4-6), but there was no evidence of spatial fiber segregation within a single 5 cm height specimen.

### 5.3.3. Fiber Orientation

The orientation of each individual fiber within the FFC was determined based on the x-ray CT imaging. A polar angle of the fiber with respect to the vertical (x-axis) was utilized to understand the effectiveness of the fiber to contribute in a 2D planar system (90 degree polar angle from the vertical would be considered "aligned" in the preferred yz plane). Although computing the fiber's angle in each plane (e.g. the xy or xz planes) may provide insight into the fiber orientation (see Appendix C for an example calculation of fiber orientation), the polar angle from the x-axis was computed since it indicates the level of a fiber's contribution in improving toughness for the FFC inlay pavements. The orientation of the fiber was calculated based on the fit ellipsoidal axis orientation from the IMARIS® software. For each fibril object, the longest dimension, R, was determined to be the C-axis of the ellipsoid and the projection of the C-axis on the Cartesian coordinate x-axis, Cx, was used to compute a polar angle as shown in Figure 5-8. All of the BT fibers imaged were assumed to be straight when calculating their orientation.

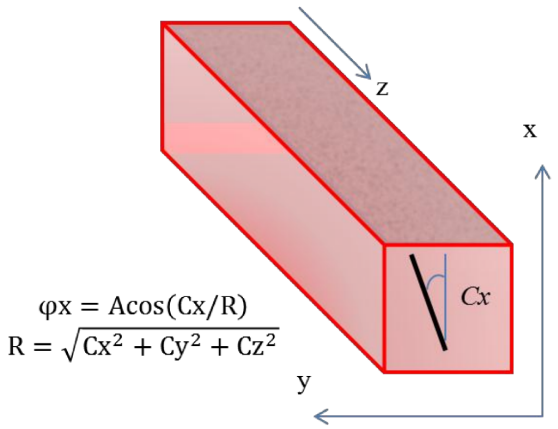


**Figure 5-8 Schematic for calculating the polar angle, φ.**

The centroids of these fibers have a finite packing distance limit from the cast or molded surface based on their orientation angle and uniform fiber length (i.e. 48 mm for the BT fibers) as illustrated in Figure 5-9. A fiber with a centroid located at the boundary surface would have to be oriented 90 degrees from the vertical, and at any 2D orientation within the yz plane. The centroid of a vertical fiber can only be located $L_f/2$ or greater from the boundary surface. Since these specimens were cut from larger plates and beams, some fibers near the edge of the specimen may have been sliced (with fibril lengths less than $L_f$), and thus their centroid value may show them to be closer to a cast or mold surface than a whole fiber. These shorter fibril segments outside the polar angle limits are shown in Figure 5-10. Moving averages of the fiber centroid distances with respect to the surface were made by either averaging the nearest 20 fibers or averaging the fibers which fall within a 2 mm distance bin, shown in Figure 5-10. The 2 mm size was selected to reduce the noise (2 mm was equivalent to roughly 6 pixels in the image) in the average fiber orientation through the specimen height.

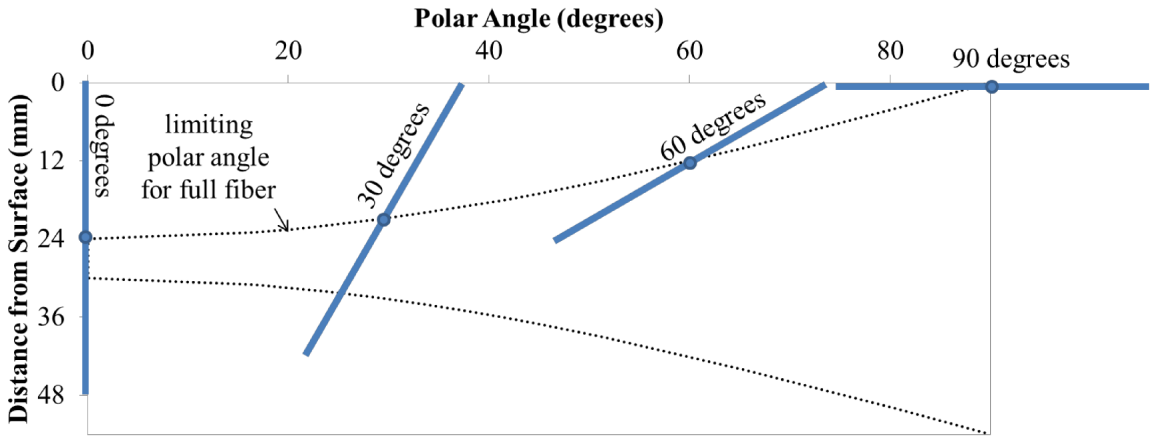


**Figure 5-9 Schematic showing the limiting polar angle of fibers near a boundary surface.**

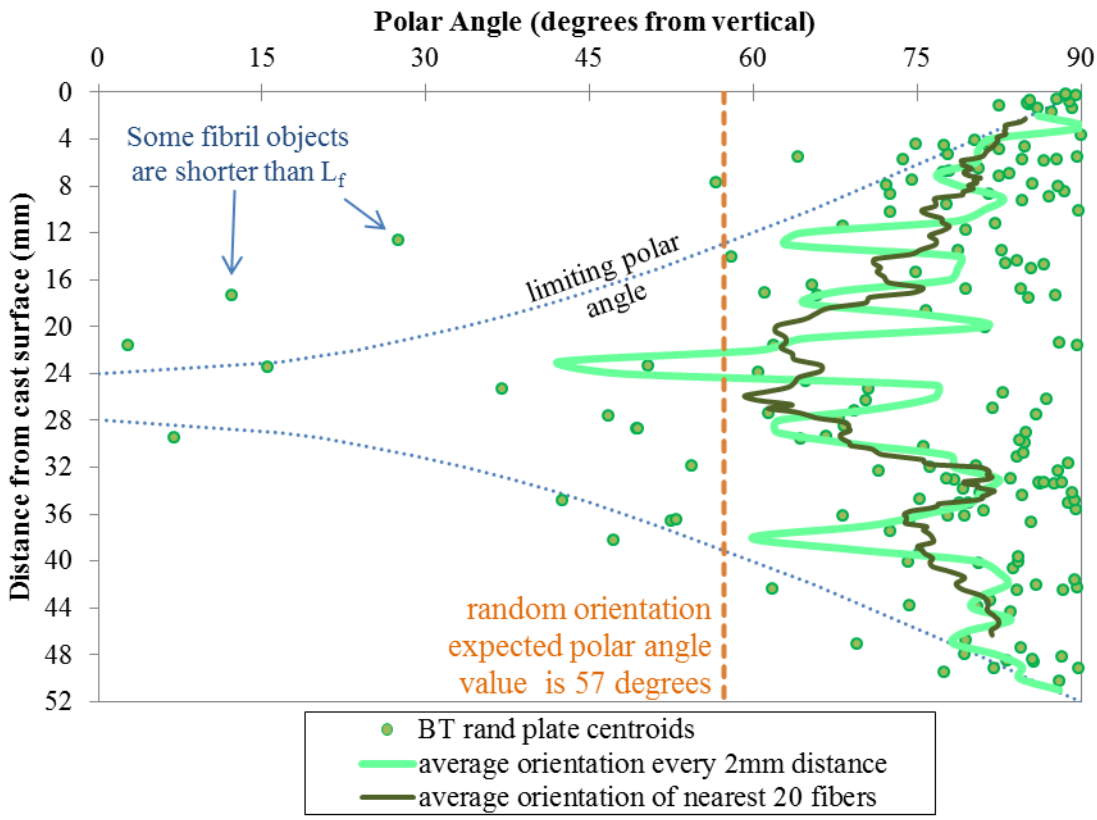


**Figure 5-10 Polar angles versus the fiber centroid distance from the cast surface of 5 cm plate with random placement.**

By viewing the centroids of BT fibers within a randomly-placed plate specimen, shown in Figure 5-10, fibers near the cast and mold surfaces approached 90 degree orientation due to the limitations shown in Figure 5-9. The average polar orientation angle for the randomly-placed plate specimen was 76.3 degrees, which was still greater than the expected mean polar angle value of 57 degrees for 3D random dispersion. It appeared that even without directional flow, more aligned fibers resulted in these thin plate FFC specimens. The BT fibers were hypothesized to be more aligned due to the boundary-affected zone packing density limitation and fiber alignment generated by using the flowable concrete with some external vibration (consolidated with a mallet).

The fiber orientations of all four x-ray imaged samples were recorded. A comparison of fiber polar angles from each x-ray CT specimen were averaged over a 2 mm height was plotted versus height to visualize the variation in fiber orientations exhibited by these four specimens. In comparing placement techniques of thin plates (shown in Figure 5-11), the randomly-placed concrete resulted in more random fiber orientations on average (at 76 degrees) than when cast under directional flow with 80 degrees on average (see average orientation summary in Table 5-1). There is still a greater amount of fibers aligned near the boundary surfaces of the plate for both casting techniques. However, there appears to be no significant difference in fiber distribution or orientation between the cast and mold surface for both plate specimens shown in Figure 5-11.

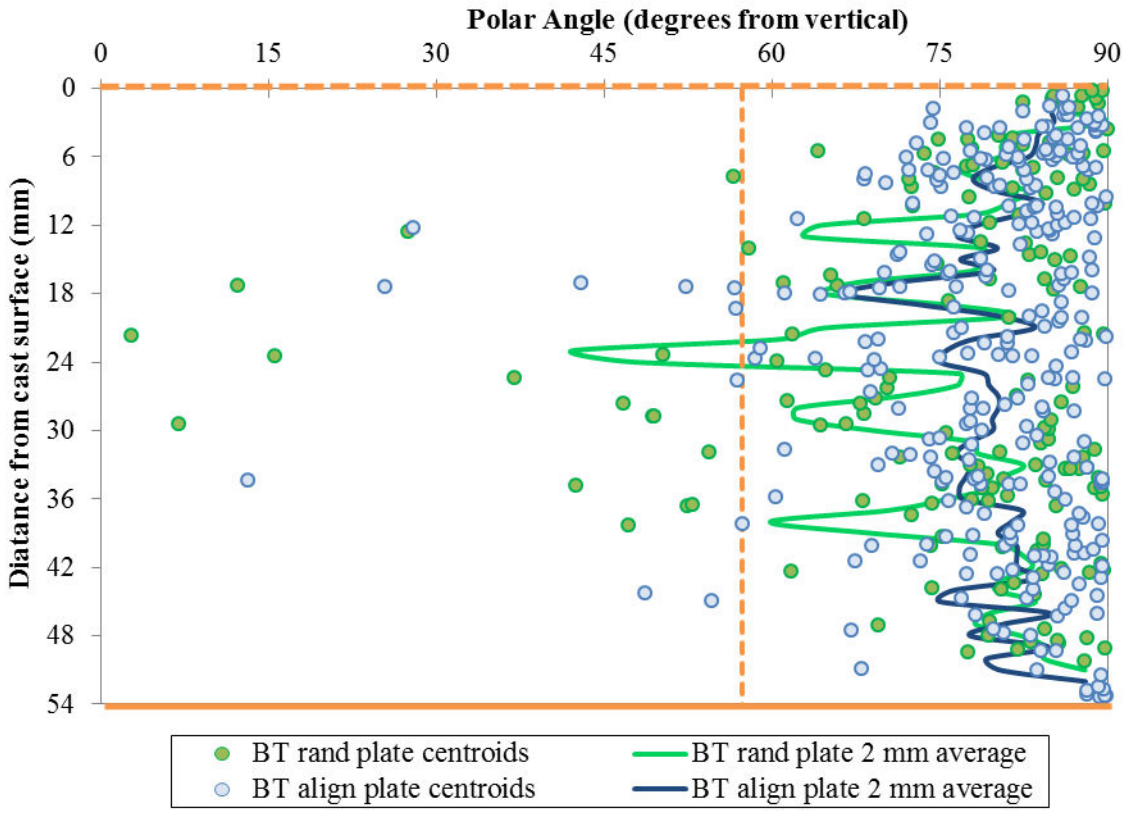


**Figure 5-11 Polar angles and average orientation for each 2 mm through the specimen height for the plate specimens.**

**Table 5-1 Average Fiber Orientation and Standard Deviation**

| | Aligned Top | Aligned Bottom | Aligned Plate | Random Plate |
|---|---|---|---|---|
| Average Polar Angle (degrees from vertical) | 73.6 | 69.1 | 79.6 | 76.3 |
| Standard Deviation (degrees) | 12.5 | 15.1 | 10.3 | 15.8 |
| Number of Fibril Objects | 289 | 206 | 272 | 161 |

For the 5 cm beams cut out of 15 cm cast beams, the fibers located close to cast surfaces were more aligned with polar angles closer to 90 degrees than the theoretical 3D random value of 57 degrees, as shown in Figure 5-12. An average orientation for interior fibers located more than $L_f/2$ (24 mm) from the cast or molded 15 cm beam surface was 68.8 or 64.7 degrees from the vertical, respectively. The fibers located within the interior of the beam were closer to the predicted 3D random orientation of 57 degrees (Dupont and Vandewalle 2005; Stroeven and Hu 2006) and can be seen visually with the moving average orientation approaching the 57 degree orientation line in Figure 5-12. The mold surface also produced a higher fiber alignment close to the surface boundary, with more aligned fibers located within roughly $L_f/2$ from the mold surface (see Figure 5-12). All four x-rayed specimens had an average polar angle being close to 70 to 80 degrees from the vertical axis (see Table 5-1), yet due to the high standard deviations of 10 to 16 degrees, the individual specimens could not significantly be compared.

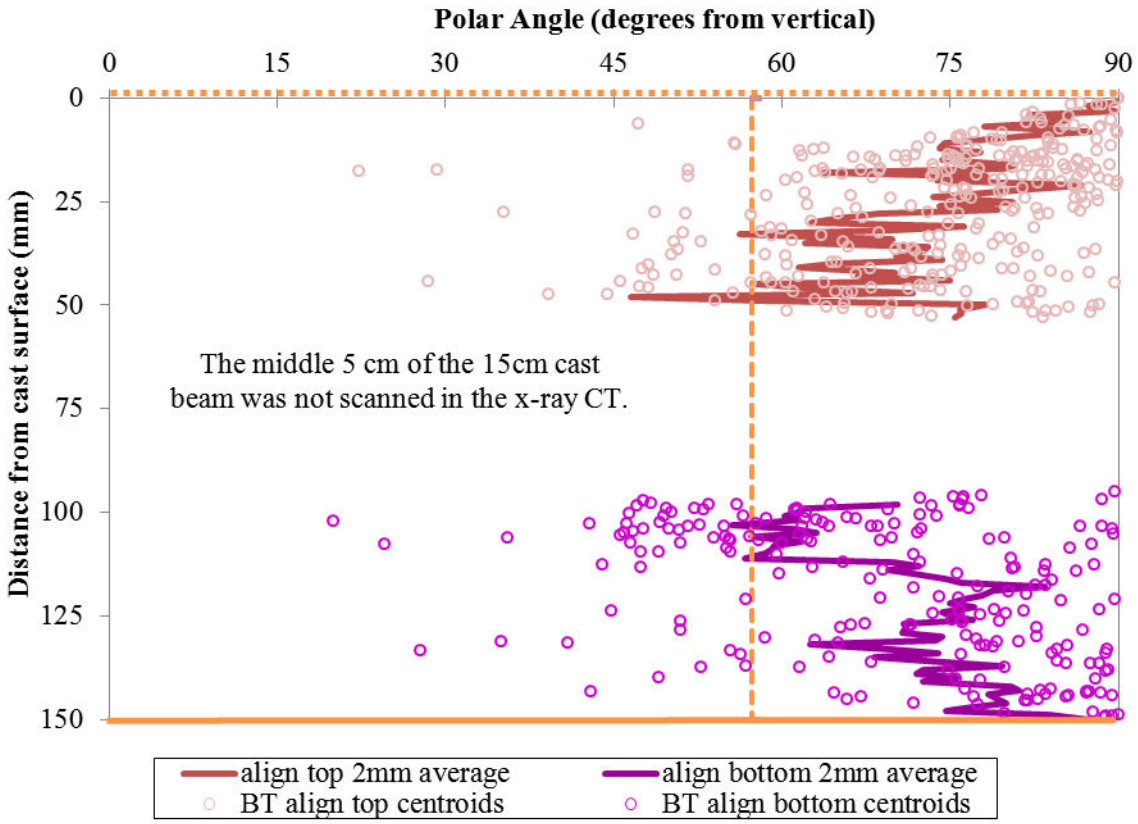


**Figure 5-12 Polar angles and average orientation for each 2 mm through the specimen height of a 15 cm cast beam (from the top 5 cm and bottom 5 cm specimens, both with directional flow).**

Since there appears to be a boundary effect for fiber orientation along both the cast and mold surfaces, the size of this with respect to the material was examined. Moses et al. (2001) studied the effect of shear rate on the rotation of a fiber in proximity to boundary surface and found a logarithmically-related relationship relating the shear rate, the fiber aspect ratio and the angular rotation of a fiber. Although shear rate was not known for the casting techniques used to construct the FFC specimens in this research, it was anticipated that a logarithmic function could be utilized for predicting the fiber orientation influenced by a boundary surface. As illustrated in Figure 5-13, the natural log function was used to describe the anticipated alignment of fibers from a cast or molded surface. It appears from the similar logarithmic functions in Figure 5-13 that the

boundary-affected zone based on fiber orientation was comparable for the cast and mold surfaces of a 15 cm beam cast with FFC under directional flow. Although the logarithmic function may not be a perfect fit of the fiber orientations from the x-ray CT imaged specimens, it is a good approximation of the fiber alignment within a distance from a boundary surface.

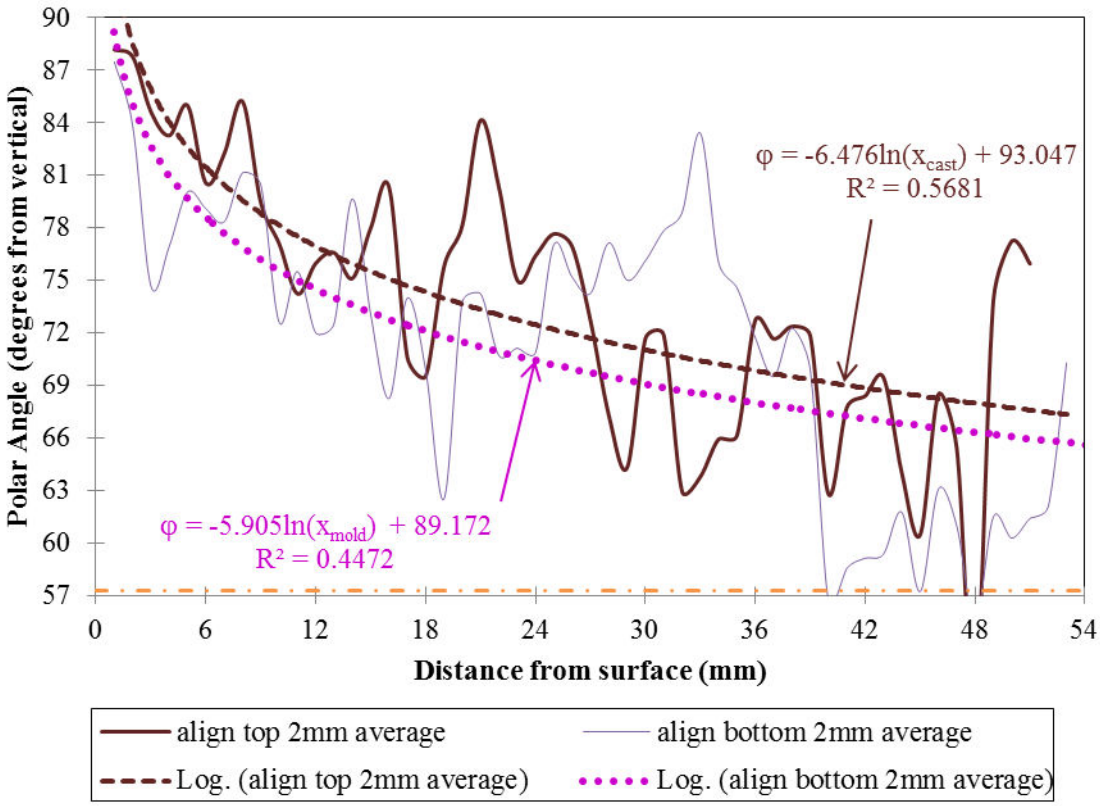


**Figure 5-13 Logarithmic functions of fiber polar angle plotted versus the distance to a cast or mold surface based on the two 5 cm specimens (top and bottom) cut from a 15 cm cast beam.**

## 5.4. Combined Distribution and Orientation Effect

The fracture performance of the specimens was expected not only to be based on the total volume fraction of fibers, but by the distribution of fibers and orientation of fibers which bridge across a cracked plane. When the boundary wall influence zone extends any

distance beyond the saw-cut notch length, the preferred alignment of fibers was anticipated to improve the fracture energy of the SEN[B] specimen. However, the alignment of fibers along an opposite boundary wall farther ahead of the crack tip has negligible effect on the overall tensile stress because the opposite boundary-affected zone falls within the compression of the SEN[B]. An improvement in post-cracking joint performance of the thin FFC inlay can only occur when the alignment of fibers is located immediately beyond the saw-cut notch. Cracks initiating and propagating within the slab surface would be arrested due to fiber alignment at the boundary surface. The advantage of the thin FFC inlay, with a slab thickness of the same magnitude as the fiber length, is that fibers are in close proximity to both the cast and molded surface. With a directional flow, the anticipated fiber alignment improves as found through the x-ray CT imaging (Figure 5-11).

The ranking from lowest to highest fracture energy measured from the SEN[B] fracture test results for each of the x-ray CT specimens (presented as Figure 4-11 and re-illustrated in Figure 5-14) was "rand plate" < "align bottom" < "align plate" < "align top". The actual number of fibers and their orientation, shown in Figure 5-14 and Figure 5-15 (Figure 5-15b is a zoomed in version of Figure 5-15a to specifically look at fiber orientation ahead of the notch), are anticipated to contribute to the measured fracture performance of the specimen. The highest number of fibers (due to highest specimen volume fraction) occurred with the "align top" specimen (see Figure 5-14). The fibers ahead of the crack tip of the "align top" specimen did not have a significantly higher alignment than the theoretical random distribution of 57 degrees (see Figure 5-15b). Thus the number of fibers ahead of the notch dominated in the fracture response curve of

the SEN[B] specimen. For specimens with similar numbers of fibers seen in Figure 5-14, such as the "aligned plate" and "aligned bottom", the net orientation in the "aligned plate" was greater (averaged at 76.6 degrees ahead of the notch) which was assumed to contribute to the greater fracture response than the "aligned bottom" (polar angle average of 73.0 degrees ahead of the notch). Thus the net fiber orientation of the FFC, as improved with directional flow and boundary wall effects, also can improve the measured fracture response of a SEN[B].

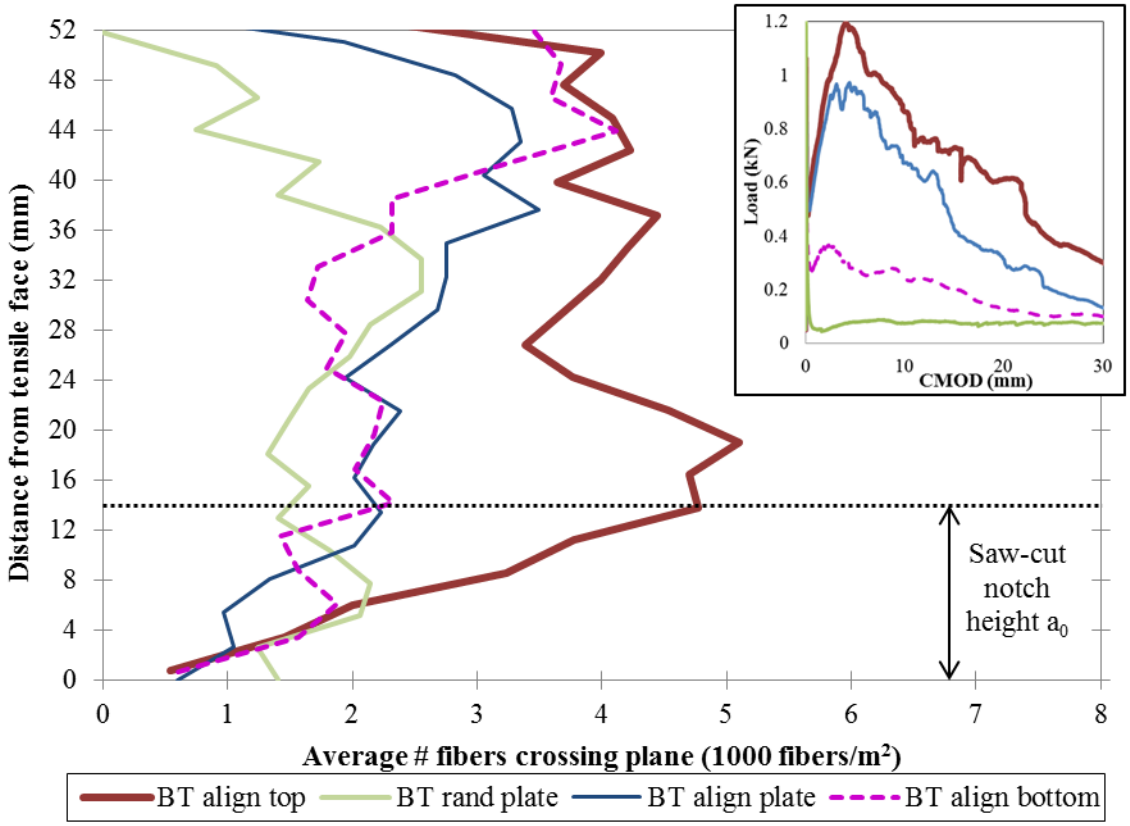


**Figure 5-14 Average number of fibers found ahead of crack front for each x-ray CT specimen, with superimposed SEN[B] load versus CMOD curves.**

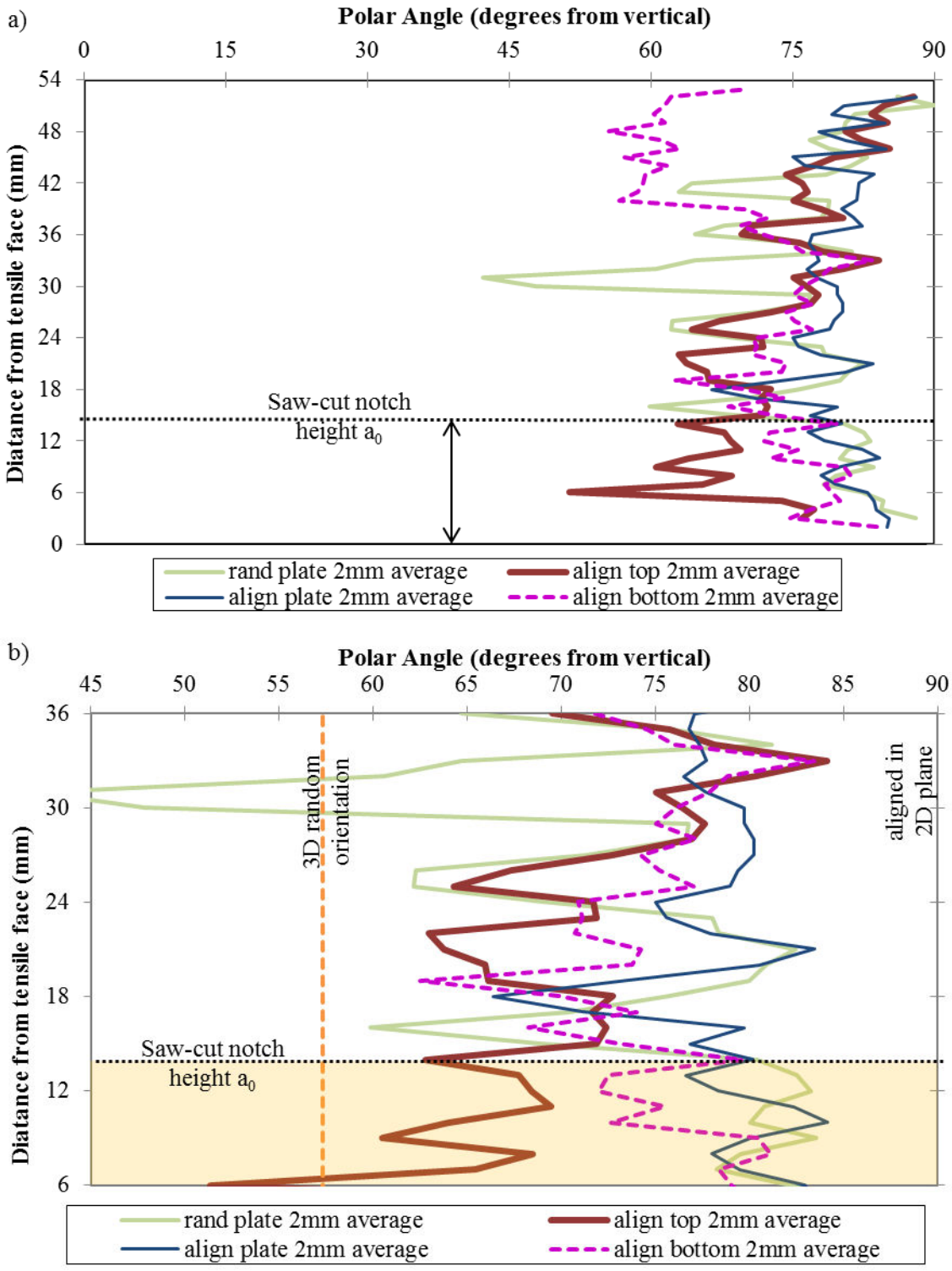


**Figure 5-15 Average polar angle of fibers a) displayed across the entire height of the tested 5 cm SEN[B] and b) a zoomed in view of the orientation ahead the crack tip.**

## 5.5. Summary

The combined effect of fiber volume fraction, fiber distribution in a fracture plane, and orientation of fibers all contributed to the fracture response of FFC specimens. These were verified through x-ray CT imaging of SEN[B] specimens of the FFC containing BT fibers. The number of fibers counted through stereology slices in proximity to a surface boundary was verified to be reduced due to the packing and alignment of fibers. The boundary-affected size based on stereology of the x-ray CT imaging was estimated to be roughly a distance of $L_f/4$ from a cast surface, rather than the past researchers' assumption of $L_f/2$ for a boundary effect on a mold surface. A logarithmic function relating the fiber's proximity to a surface and the expected fiber alignment was determined in order to predict the orientation of fibers at any specimen depth from a cast or molded boundary.

The measured fracture response was related to the local volume fraction of fibers in a tested SEN[B] specimen, and particularly with the number of fibers directly ahead of the notch. The net fiber alignment also ahead of the notch was projected to further increase the post-cracking fracture response curve. All x-ray CT imaged specimens of the FFC containing BT50 fibers had an average polar angle of 69 degrees or greater from a vertical axis, which is more aligned than the theoretical 3D random distribution with an expected polar angle of 57 degrees. BT50 fibers throughout a 5 cm plate thickness were verified to be more aligned with directional flow placement, rather than with random placement. Fibers alignment within the boundary-affected zone and located within a distance less than the saw-cut notch have negligible effect on the overall fracture energy performance. Therefore, in thin FFC inlays with saw-cut joints on the cast surface, an

improvement in fracture performance was expected only for fiber alignment occurring beyond the notch depth. By having the FFC inlay thickness of the same magnitude as the fiber length, the fibers were all affected by the boundary surface packing and become more aligned near the surface. Thus higher toughness performances could be expected when construction these thin FFC pavements, compared to pavements which are considerably thicker than the fiber length. Although some non-uniform spatial distribution was seen among the FFC specimens, the only evidence of segregation was exhibited by the volume of BT50 fibers in the FFC cast as a 15 cm beam.

# CHAPTER 6. CONCLUSIONS AND RECOMMENDATIONS

This research investigated the effect of synthetic, macro-fiber spatial distribution and orientation on the measured beam fracture performance for a flowable fibrous concrete (FFC) mixture. The identification of these synthetic macro-fibers within the concrete was made using contrast and shape-based filtering of x-ray computed tomography (CT) images of various FFC beam samples. The effect of specimen size, casting technique, and presence of a boundary surface were analyzed with the CT images. Although, the alignment of fibers were influenced by the construction technique of the FFC specimen, the measured FFC fracture energy was dominated by the number of fibers distributed at the fracture plane within a specimen. Additional findings were made related to the FFC mixture design, test specimen selection for the measured post-cracking performance, and modeling the of FFC fracture response.

## 6.1. Findings

The FFC mixture was designed for the purpose of rapidly constructing a thin concrete inlay over an existing asphalt pavement, with enhanced fracture toughness performance for reduced crack widths and a longer pavement service life. This FFC was an adaptation based on the existing technologies of self-consolidating concrete (SCC), fiber-reinforced concrete (FRC), and ultra-thin whitetopping (UTW). Compared to typical paving mixtures, the FFC utilized higher cementitious contents, smaller aggregate sizes, and higher percentage of sand to achieve a desired 380 mm diameter slump flow spread. The higher cementitious content was required to coat fibers in the FFC, not only to improve the concrete workability, but to provide an adequate cement-fiber bond for optimal pull-

out resistance, and ultimately higher FFC total fracture energy. Micro-fibers were added to the FFC mixture design to assist in achieving a flowable consistency which is stiffer than the typical SCC mixtures. Based on standard toughness tests, the FFC mixture containing roughly 0.5% volume fraction of synthetic macro-fiber reinforcement achieved two times the measured residual strength ratio (post-cracking strength relative to the peak flexural strength) of that recommended for a concrete used for a 7.5 cm or greater UTW thickness design.

The measured toughness performance of FRC has been known to contribute to the improved load carrying capacity of FRC slabs. However, a standard 15 cm flexural beam (ASTM C1609) was found to underestimate the toughness performance of the 5 cm thick FFC inlay. Smaller 5 cm beams were tested to determine the toughness performance of the FFC inlay. The geometrically-similar 5 cm beam size produced 59% greater nominal (peak) strength and higher residual strength ratios compared to 15 cm beams. It was recommended future test samples be constructed similar to the field in terms of geometry, placement, and consolidation techniques. A 5 cm cast plate can be cut into the 5 cm beams to determine the measured post-cracking performance, either through flexural unnotched tests or single-edge notched beam (SEN[B]) tests. Due to higher variability in measured properties between thinner specimens, it is recommended that multiple 5 cm beam specimen replicates be tested.

Several fracture properties of FFC were similar to conventional FRC paving materials except that the total fracture energy for FFC was significantly higher. The computed FFC fracture properties, based on 15 cm single edge notched beam (SEN[B]) specimens, can be used in finite element modeling to predict the load versus crack opening response

of the material. A tri-linear cohesive zone softening model, which had also been implemented for FRC beams and slabs containing a volume fraction of macro-fibers up to 0.78%, was successfully implemented to describe the FFC fracture response for a 15 cm SEN[B]. However, due to the deflection hardening response found in some of the 5 cm SEN[B] specimens, the cohesive zone damage model was not able to accurately represent the fracture response of the beam especially at higher displacement levels and higher fiber contents.

For FFC, a higher toughness and deflection hardening response was expected to be the result of more fiber alignment or non-uniform fiber distribution within the cast 5 cm plate specimens. A technique to verify the spatial distribution and orientation of synthetic fibers within the concrete in three-dimensions was needed to improve the fracture performance predictions. Although many techniques exist for steel fibers, this is the first attempt to locate synthetic fibers in concrete. A high powered x-ray CT was utilized for image contrast and spatial resolution in order to identify material components in the FFC. A shape-based filter with a threshold by contrast and size were used to separate fibers from air voids in the concrete images. Only synthetic fibers which had a higher flexural stiffness, and thus remained straight after placement with the FFC, could be confidently identified with the current non-destructive x-ray CT technique.

Analysis of the fiber distribution from the imaging found a higher concentration of synthetic fibers near the top of the 15 cm cast beam. There was a large range in the number of stiffer synthetic fibers (0.1 to 1.4 fibers/cm$^2$) found at any vertical plane in the imaged FFC specimens. An 86% coefficient of variability in total fracture energy was measured corresponding to the randomly-cast plate FFC specimens containing the stiffer

synthetic fibers. Conversely, a FFC containing flexible synthetic fibers had a lower coefficient of variability (33%), but with the same average total fracture energy of 6000 N/m when cast as a 5 cm thick plate.

Fiber orientation was computed as a polar angle, relative to being aligned within the 2D thin slab, where 90° from the vertical represented the desired alignment, while 57° represented the statistical mean for 3D random fiber dispersion in the concrete. Fibers near a cast or mold boundary surface were expected to be more aligned due to the fiber particle packing along the surface. In addition, the flow during construction of the FFC was found to further induce alignment of fibers in the thin plate. The number of fibers located ahead of the notch for the SEN[B] specimens were found to directly be correlated with the total fracture energy of the specimen. The net orientation of fibers also contributed to the post-cracking performance for specimens with a similar number of fibers ahead of the notch. By using the thin 5 cm inlay with the FFC material, fibers were more aligned due to proximity of boundary surfaces and with the flow of the material at casting and therefore the necessary toughness and deflection hardening response can be achieved to meet the desired service life.

## 6.2. Recommendations for Future Research

As many synthetic fibers are flexible and can bend during placement in the concrete, this straight shape-based image processing procedure was not able to identify these fibers. The x-ray CT technique was successful in combination with image post-processing for identifying the stiffer synthetic fibers, yet further studies are needed in order to identify more flexible synthetic fibers. Some suggested ideas are:

- Improve the image contrast through alternative the x-ray scanning procedures or equipment
- Use synthetic fibers which have a higher x-ray absorbance such that they are easily identified in the concrete
- Develop a computer algorithm to identify and track the flexible synthetic fibers

There is a gap between using micro-mechanical models and test-specimen scale finite element models in predicting the fracture performance of fiber-reinforced concrete. In addition, many of these models overlook boundary-wall effects and the physical specimen geometry on fiber packing orientation and distribution near these surface boundaries. There is a need to derive a model which includes the details of fiber-matrix bonding and fiber orientation along with geometric constraints and loading to improve prediction of FRC specimen tests, especially for predicting a deflection hardening response.

Lastly, there is a need to determine the minimum requirements of toughness performance for a thin FFC inlay to have a 10 to 15 year service life. Many factors involved in pavement design, such as the existing pavement condition, and interfacial bonding condition expected between concrete and the underlying asphalt, and pavement service loading, all can impact the service life of the thin inlay. It is suggested that understanding the expected distresses of the FFC inlay through accelerated load testing, can provide insight into the anticipated pavement service life.

# REFERENCES


Altoubat, S. A., Roesler, J. R., and Rieder, K. A. (2004). "Flexural Capacity of Synthetic Fiber Reinforced Concrete Slabs on Ground Based on Beam Toughness Results." Sixth International RILEM Symposium on Fibre Reinforced Concretes (BEFIB 2004), Rilem Publications SARL, Varenna, Italy, 1063-1072.

Altoubat, S. A., Roesler, J. R., Lange, D. A., and Rieder, K. A. (2008). "Simplified method for concrete pavement design with discrete structural fibers." Construction and Building Materials, 22(3), 384-393.

American Concrete Pavement Association. (1998). Whitetopping - State of the Practice. American Concrete Pavement Association, Skokie, IL.

Anderson, T. L. (2005). Fracture Mechanics: Fundamentals and Applications. Taylor & Francis Group, Boca Raton, FL.

Assaad, J., Khayat, K. H., and Mesbah, H. (2003). "Assessment of thixotropy of flowable and self-consolidating concrete." ACI Materials Journal, 100(2), 99-107.

ASTM Standard C1018. (1997). Standard Test Method for Flexural Toughness and First-Crack Strength of Fiber-Reinforced Concrete (Using Beam With Third-Point Loading) (Withdrawn 2006). ASTM International, West Conshohocken, PA.

ASTM Standard C138. (2009). Standard Test Method for Density (Unit Weight), Yield, and Air Content (Gravimetric) of Concrete. ASTM International, West Conshohocken, PA.

ASTM Standard C1399a. (2007). Standard Test Method for Obtaining Average Residual-Strength of Fiber-Reinforced Concrete. ASTM International, West Conshohocken, PA.

ASTM Standard C143/C143M. (2008). Standard Test Method for Slump of Hydraulic-Cement Concrete. ASTM International, West Conshohocken, PA.

ASTM Standard C1550. (2008). Standard Test Method for Flexural Toughness of Fiber Reinforced Concrete (Using Centrally Loaded Round Panel). ASTM International, West Conshohocken, PA.

ASTM Standard C1609. (2007). Standard Test Method for Flexural Performance of Fiber-Reinforced Concrete (Using Beam With Third-Point Loading). ASTM International, West Conshohocken, PA.

ASTM Standard C1611b. (2009). Standard Test Method for Slump Flow of Self-Consolidating Concrete. ASTM International, West Conshohocken, PA.

ASTM Standard C231a. (2009). Standard Test Method for Air Content of Freshly Mixed Concrete by the Pressure Method. ASTM International, West Conshohocken, PA.

Balaguru, P. N., and Shah, S. P. (1992). Fiber-reinforced cement composites. McGraw-Hill, New York.

Banfill, P. F. G., Starrs, G., Derruau, G., McCarter, W. J., and Chrisp, T. M. (2006). "Rheology of low carbon fibre content reinforced cement mortar." Cement and Concrete Composites, 28(9), 773-780.

Barnett, S. J., Lataste, J. -., Parry, T., Millard, S. G., and Soutsos, M. N. (2010). "Assessment of fibre orientation in ultra high performance fibre reinforced concrete and its effect on flexural strength." Materials and Structures/Materiaux Et Constructions, 43(7), 1009-1023.

Bažant, Z. P., and Gopalaratnam, V. S. (1991). "Fracture Mechanics of Concrete: Concepts, Models and Determination of Material Properties." Rep. No. ACI 446.1 R-91, ACI Committee 446, Fracture Mechanics, Farmington Hills, MI.

Bažant, Z. P., and Planas, J. (1998). Fracture and size effect in concrete and other quasibrittle materials. CRC Press, Boca Raton, FL.

Benson, S. D. P., Nicolaides, D., and Karihaloo, B. L. (2005). "CARDIFRC® - Development and mechanical properties. Part II: Fibre distribution." Magazine of Concrete Research, 57(7), 421-432.

Bentur, A., and Mindess, S. (1990). Fibre reinforced cementitious composites. Elsevier Applied Science, New York.

Bitplane. (2009). "IMARIS." 6.3.1.

Bordelon, A. C., and Roesler, J. R. (2011). "Design with Fiber-Reinforcement for Thin Concrete Overlays Bonded to Asphalt." ASCE Journal of Transportation Engineering, InPress.

Bordelon, A., Cervantes, V., and Roesler, J. R. (2009). "Fracture properties of concrete containing recycled concrete aggregates." Magazine of Concrete Research, 61(9), 665-670.

Bordelon, A., and Roesler, J. (2009). "Fiber-Reinforced Concrete Pavement Design and Material Requirements." Eighth International Conference on the Bearing Capacity of Roads, Railways and Airfields, Taylor and Francis Group, London, 717-727.

Bordelon, A. C. (2007). "Fracture Behavior of Concrete Materials for Rigid Pavement Systems." PhD thesis, University of Illinois at Urbana-Champaign, Urbana, IL.

Carlswärd, J. (2006). "Shrinkage cracking of steel fibre reinforced self compacting concrete overlays: test methods and theoretical modelling." PhD thesis, Lulea University of Technology, Lulea, Sweden.

Cervantes, V., and Roesler, J. (2009). "Performance of Concrete Pavements with Optimized Slab Geometry." University of Illinois at Urbana-Champaign, Department of Civil and Environmental Engineering, Urbana, IL.

Chermant, J., Chermant, L., Coster, M., Dequiedt, A., and Redon, C. (2001). "Some fields of applications of automatic image analysis in civil engineering." Cement and Concrete Composites, 23(2-3), 157-169.

De Schutter, G., Bartos, P. J. M., Domone, P., and Gibbs, J. (2008). Self-Compacting Concrete. Whittles.

Dupont, D., and Vandewalle, L. (2005). "Distribution of steel fibres in rectangular sections." Cement and Concrete Composites, 27(3), 391-398.

Elices, M., Guinea, G., and Planas, J. (1992). "Measurement of the fracture energy using three-point bend tests: Part 3—influence of cutting the P-δ tail." Materials and Structures, 25(6), 327-334.

European Standard EN 14651. (2005). Test method for Metallic Fibre Concrete - Measuring teh Flexural Tensile Strength (Limit of Proportionality (LOP), Residual). BSI:British Standards Institution, London.

Ferrara, L., Ozyurt, N., and Di Prisco, M. (2011). "High mechanical performance of fibre reinforced cementitious composites: The role of "casting-flow induced" fibre orientation." Materials and Structures/Materiaux Et Constructions, 44(1), 109-128.

Ferrara, L., Park, Y. D., and Shah, S. P. (2007). "Toughness properties and fiber dispersion in vibrated and self-consolidating fiber reinforced concrete." Proceedings of the 6th International Conference on Fracture Mechanics of Concrete and Concrete Structures, Taylor & Francis, London, 1341-1349.

Gaedicke, C. (2009). "Fracture-based Method to Determine the Flexural Load Capacity of Concrete Slabs." PhD thesis, University of Illinois at Urbana-Champaign, Urbana, IL.

Gaedicke, C., Roesler, J., and Shah, S. (2009). "Fatigue crack growth prediction in concrete slabs." International Journal of Fatigue, 31(8-9), 1309-1317.

Geng, Y. P., and Leung, C. K. Y. (1997). "Micromechanics-based FEM simulation of fiber-reinforced cementitious composite components." Computers and Structures, 64(5-6), 973-982.

Gettu, R., Gardner, D. R., Saldívar, H., and Barragán, B. E. (2005). "Study of the distribution and orientation of fibers in SFRC specimens." Materials and Structures/Materiaux Et Constructions, 38(275), 31-37.

Giaccio, G., Tobes, J. M., and Zerbino, R. (2008). "Use of small beams to obtain design parameters of fibre reinforced concrete." Cement and Concrete Composites, 30(4), 297-306.

Gopalaratnam, V. S., and Gettu, R. (1995). "On the characterization of flexural toughness in fiber reinforced concretes." Cement and Concrete Composites, 17(3), 239-254.

Gopalaratnam, V. S., and Shah, S. P. (1987). "Tensile Failure of Steel Fiber-Reinforced Mortar." Journal of Engineering Mechanics, 113(5), 635-652.

Gucunski, N. (1998). "Development of a Design Guide for Ultra Thin Whitetopping (UTW)." Rep. No. FHWA 2001 - 018, New Jersey Department of Transportation, Trenton, NJ.

Hannant, D. J. (1978). Fibre cements and fibre concretes. Wiley, New York.

Harrington, D. (2008). Guide to Concrete Overlays. American Concrete Pavement Association, Skokie, IL.

Highway Research Board. (1961). "The AASHO Road Test: Report I, History and Description of the Project." Rep. No. Special Report 61A, Highway Research Board, National Academy of Sciences, Washington, D.C.

Hillerborg, A. (1985). "The theoretical basis of a method to determine the fracture energy G F of concrete." Materials and Structures, 18(4), 291-296.

Hu, J. (2005). "A study of effects of aggregate on concrete rheology." PhD thesis, Iowa State University, Ames, Iowa.

Illinois Department of Transportation. (2008). "Portland Cement Concrete Inlay / Overlay Thickness Design." http://www.dot.state.il.us/desenv/PCC_Inlay-OverlayDesignSprdsht.xls (August 1, 2008).

Jain, L. K., and Wetherhold, R. C. (1992). "Effect of fiber orientation on the fracture toughness of brittle matrix composites." Acta Metallurgica Et Materialia, 40(6), 1135-1143.

Japan Concrete Institute. (1984). "JCI Standards for Test Methods of Fiber Reinforced Concrete." JCI, JCI-SF 4 45-51.

Jenq, Y. S., and Shah, S. P. (1985). "TWO PARAMETER FRACTURE MODEL FOR CONCRETE." Journal of Engineering Mechanics, 111(10), 1227-1241.

Jiang, Z., and Banthia, N. (2010). "Size effects in flexural toughness of fiber reinforced concrete." Journal of Testing and Evaluation, 38(3), 332-338.

Koehler, E. (2007). "Aggregates in self-consolidating concrete." PhD thesis, The University of Texas at Austin, Austin, Texas.

Kosaka, H., Higuchi, M., Takeuchi, H., and Nanni, A. (1996). "'Flowable' Concrete In Bridge Pier Caps." Concrete International, 18(2), 56-61.

Krause, M., Hausherr, J. M., Burgeth, B., Herrmann, C., and Krenkel, W. (2010). "Determination of the fibre orientation in composites using the structure tensor and local X-ray transform." Journal of Materials Science, 45(4), 888-896.

Krenchel, H. (1975). "FIBRE SPACING AND SPECIFIC FIBRE SURFACE." RILEM Symp, Fibre Reinf Cem and Concr, 69-79.

Kunieda, M., and Rokugo, K. (2006). "Recent Progress on HPFRCC in Japan: Required Performance and Applications." Journal of Advanced Concrete Technology, 4(1), 19-33.

Lange, D. A., Struble, L. J., D'Ambrosia, M. D., Shen, L., Tejeda-Dominguez, F., Birch, B. F., and Brinks, A. J. (2008). "Performance and Acceptance of Self-Consolidating Concrete: Final Report." Illinois Center for Transportation, University of Illinois at Urbana-Champaign, Urbana, IL.

Lange-Kornbak, D., and Karihaloo, B. L. (1997). "Tension softening of fibre-reinforced cementitious composites." Cement and Concrete Composites, 19(4), 315-328.

Lataste, J. F., Behloul, M., and Breysse, D. (2008). "Characterisation of fibres distribution in a steel fibre reinforced concrete with electrical resistivity measurements." NDT and E International, 41(8), 638-647.

Leng, Z., Ozer, H., Al-Qadi, I. L., and Carpenter, S. H. (2008). "Interface bonding between hot-mix asphalt and various portland cement concrete surfaces laboratory assessment." Transportation Research Record, (2057), 46-53.

Leung, C. K. Y., and Li, V. C. (1990). "Applications of a two-way debonding theory to short fibre composites." Composites, 21(4), 305-317.

Li, V. C. (2003). "On Engineered Cementitious Composites (ECC): A Review of the Material and Its Applications." Journal of Advanced Concrete Technology, 1(3), 215-230.

Li, V. C., Stang, H., and Krenchel, H. (1993). "Micromechanics of crack bridging in fibre-reinforced concrete." Materials and Structures, 26(8), 486-494.

Li, V. C., Wang, Y., and Backer, S. (1991). "A micromechanical model of tension-softening and bridging toughening of short random fiber reinforced brittle matrix composites." Journal of the Mechanics and Physics of Solids, 39(5), 607-625.

Li, V. C., Wang, Y., and Backer, S. (1990). "Effect of inclining angle, bundling and surface treatment on synthetic fibre pull-out from a cement matrix." Composites, 21(2), 132-140.

Li, V. C. (1992). "Postcrack scaling relations for fiber reinforced cementitious composites." Journal of Materials in Civil Engineering, 4(1), 41-57.

Löfgren, I., Stang, H., and Olesen, J. F. (2008). "The WST method, a fracture mechanics test method for FRC." Materials and Structures/Materiaux Et Constructions, 41(1), 197-211.

Lomboy, G. R., Wang, K., Taylor, P., Shah, S. P., Grove, J., and Wiegand, P. (2011). "Economic and Environmental Benefits of Using Semi-Flowable Self-Consolidating Concrete for Slip-Form Paving." 90th Transportation Research Board Annual Meeting, 11-2690.

Mack, J. W., Hawbaker, L. D., and Cole, L. W. (1998). "Ultrathin whitetopping - State-of-the-practice for thin concrete overlays of asphalt." Transportation Research Record, 1610 39-43.

Mack, J. W., Wu, C. L., Tarr, S., and Refai, T. (1997). "Model Development and Interim Design Procedure Guidelines for Ultra-thin Whitetopping Pavements." Sixth International Conference on Concrete Pavement Design and Materials for High Performance, Purdue University, 231-256.

Martinie, L., Rossi, P., and Roussel, N. (2010). "Rheology of fiber reinforced cementitious materials: classification and prediction." Cement and Concrete Research, 40(2), 226-234.

Masad, E., Jandhyala, V. K., Dasgupta, N., Somadevan, N., and Shashidhar, N. (2002). "Characterization of Air Void Distribution in Asphalt Mixes using X-ray Computed Tomography." Journal of Materials in Civil Engineering, 14(2), 122-129.

Mathworks. (2009). "MATLAB." 7.9.0.529 (R2009b).

Mindess, S., Young, J. F., and Darwin, D. (2003). Concrete. Prentice Hall, Upper Saddle River, NJ.

Moses, K. B., Advani, S. G., and Reinhardt, A. (2001). "Investigation of fiber motion near solid boundaries in simple shear flow." Rheologica Acta, 40(3), 296-306.

Naaman, A. E., and Reinhardt, H. W. (2006). "Proposed classification of HPFRC composites based on their tensile response." Materials and Structures/Materiaux Et Constructions, 39(289), 547-555.

National Institutes of Health. (2010). "ImageJ." 1.43u.

Nega, K., and Muhunthan, B. (2010). "Report on Visualizing the Statistical Distribution of Fibers by X-ray CT scanning of Fiber-Reinforced Concrete." Washington State High-Resolution X-Ray Computed Tomography (WAX-CT).

Nehdi, M., and Ladanchuk, J. D. (2004). "Fiber synergy in fiber-reinforced self-consolidating concrete." ACI Materials Journal, 101(6), 508-517.

Olesen, J. F. (2001). "Fictitious crack propagation in fiber-reinforced concrete beams." Journal of Engineering Mechanics, 127(3), 272-280.

Østergaard, L., Lange, D., and Stang, H. (2004). "Early-age stress-crack opening relationships for high performance concrete." Cement and Concrete Composites, 26(5), 563-572.

Ozyurt, N., Woo, L. Y., Mason, T. O., and Shah, S. P. (2006). "Monitoring fiber dispersion in fiber-reinforced cementitious materials: Comparison of AC-impedance spectroscopy and image analysis." ACI Materials Journal, 103(5), 340-347.

Park, K., Paulino, G. H., and Roesler, J. R. (2010). "Cohesive fracture model for functionally graded fiber reinforced concrete." Cement and Concrete Research, 40(6), 956-965.

Park, K., Paulino, G., and Roesler, J. (2008). "Determination of the kink point in the bilinear softening model for concrete." Engineering Fracture Mechanics, 75(13), 3806-3818.

Planas, J., Guinea, G. V., and Elices, M. (1997). "Generalized Size Effect Equation for Quasibrittle Materials." Fatigue & Fracture of Engineering Materials & Structures, 20(5), 671-687.

Rapoport, J. R., and Shah, S. P. (2005). "Cast-in-place cellulose fiber-reinforced cement paste, mortar, and concrete." ACI Materials Journal, 102(5), 299-306.

Redon, C., Chermant, L., Chermant, J., and Coster, M. (1998). "Assessment of fibre orientation in reinforced concrete using Fourier image transform." Journal of Microscopy, 191(3), 258-265.

Redon, C., Chermant, L., Chermant, J., and Coster, M. (1999). "Automatic image analysis and morphology of fibre reinforced concrete." Cement and Concrete Composites, 21(5-6), 403-412.

Riley, R. (2005). "SCC Quick Base and Patching Material 2005." Illinois Chapter of the American Concrete Pavement Association Presentation.

Roesler, J., Bordelon, A., Gaedicke, C., Park, K., and Paulino, G. (2008a). "Fracture behavior and properties of functionally graded fiber-reinforced concrete." 9th International Conference on Multiscale and Functionally Graded Materials, FGM IX, 513-518.

Roesler, J., Bordelon, A., Ioannides, A., Beyer, M., and Wang, D. (2008b). "Design and Concrete Material Requirements for Ultra-Thin Whitetopping." Rep. No. FHWA-ICT-08-016, Research Report for the Illinois Center of Transportation R27-3A, Urbana, IL.

Roesler, J., Paulino, G., Gaedicke, C., Bordelon, A., and Park, K. (2007). "Fracture behavior of functionally graded concrete materials for rigid pavements." Transportation Research Record, (2037), 40-49.

Roesler, J. R., Altoubat, S. A., Lange, D. A., Rieder, K. A., and Ulreich, G. R. (2006). "Effect of synthetic fibers on structural behavior of concrete slabs-on-ground." ACI Materials Journal, 103(1), 3-10.

Roesler, J., Paulino, G., Park, K., and Gaedicke, C. (2007). "Concrete fracture prediction using bilinear softening." Cement and Concrete Composites, 29(4), 300-312.

Rossi, P. (1997). "High Performance Multimodal Fiber Reinforced Cement Composites (HPMFRCC): the LCPC Experience." ACI Materials Journal, 94(6), 478-783.

Self-Compacting Concrete European Project Group. (2005). "The European Guidelines for Self Compacting Concrete: Specification, Production and Use." Rep. No. SCC 028, European Association for Producers and Applications of Specialist Building Products (EFNARC), Brussels.

Shah, S. P. (1990). "Determination of fracture parameters ( $K_{Ic}^{s}$ and $CTOD_c$) of plain concrete using three-point bend tests." Materials and Structures, 23(6), 457-460.

Shen, B., Hubler, M., Paulino, G. H., and Struble, L. J. (2008). "Functionally-graded fiber-reinforced cement composite: Processing, microstructure, and properties." Cement and Concrete Composites, 30(8), 663-673.

Shen, H., Nutt, S., and Hull, D. (2004). "Direct observation and measurement of fiber architecture in short fiber-polymer composite foam through micro-CT imaging." Composites Science and Technology, 64(13-14), 2113-2120.

Shen, L. (2007). "Role of aggregate packing in segregation resistance and flow behavior of self-consolidating concrete." PhD thesis, University of Illinois at Urbana-Champaign, Urbana, IL.

Silfwerbrand, J., and Paulsson, J. (1998). "Better bonding of bridge deck overlays." Concrete International, 20(10), 56-61.

Soroushian, P., and Lee, C. (1990). "Distribution and orientation of fibers in steel fiber reinforced concrete." ACI Materials Journal, 87(5), 433-439.

Stähli, P., Custer, R., and Van Mier, J. G. M. (2008). "On flow properties, fibre distribution, fibre orientation and flexural behaviour of FRC." Materials and Structures/Materiaux Et Constructions, 41(1), 189-196.

Stähli, P., and van Mier, J. G. M. (2007). "Manufacturing, fibre anisotropy and fracture of hybrid fibre concrete." Engineering Fracture Mechanics, 74(1-2), 223-242.

Stang, H., Li, Z., and Shah, S. P. (1990). "Pullout problem. Stress versus fracture mechanical approach." Journal of Engineering Mechanics, 116(10), 2136-2150.

Stang, H., and Shah, S. P. (1986). "Failure of fibre-reinforced composites by pull-out fracture." Journal of Materials Science, 21(3), 953-957.

Stock, S. R. (2009). MicroComputed Tomography: Methodology and Applications. CRC Press, Boca Raton, FL.

Stroeven, P. (1985). "Stereology of Concrete Reinforced with Short Steel Fibers." Heron, 31(2), 15-28.

Stroeven, P. (1979). "Morphometry of fibre reinforced cementitious materials - Part II: Inhomogeneity, segregation and anisometry of partially oriented fibre structures." Matériaux Et Constructions, 12(1), 9-20.

Stroeven, P., and Hu, J. (2006). "Effectiveness near boundaries of fibre reinforcement in concrete." Materials and Structures/Materiaux Et Constructions, 39(294), 1001-1013.

Struble, L. J., and Lange, D. (1997). "Do We Need a Standard Concrete Fracture Mechanics Test?" Cement, Concrete and Aggregates, 19(2), 112-115.

Takashima, H., Miyagai, K., Hashida, T., and Li, V. C. (2003). "A design approach for the mechanical properties of polypropylene discontinuous fiber reinforced cementitious composites by extrusion molding." Engineering Fracture Mechanics, 70(7-8), 853-870.

Tashman, L., Nam, K., and Papagiannakis, T. (2006). "Evaluation of the Influence of Tack Coat Construction Factors on the Bond Strength between Pavement Layers." Rep. No. WA-RD 645.1, Washington State University, Washington Center for Asphalt Technology, Pullman, WA.

The Concrete Society. (2003). "Concrete Industrial Ground Floors - A guide to their design and construction." Rep. No. Technical Report 34, Concrete Society, Crowthorne.

Torrijos, M. C., Barragán, B. E., and Zerbino, R. L. (2010). "Placing conditions, mesostructural characteristics and post-cracking response of fibre reinforced self-compacting concretes." Construction and Building Materials, 24(6), 1078-1085.

Voigt, T., Mbele, J., Wang, K., and Shah, S. P. (2010). "Using Fly Ash, Clay, and Fibers for Simultaneous Improvement of Concrete Green Strength and Consolidatability for Slip-Form Pavement." Journal of Materials in Civil Engineering, 22(2), 196-206.

Wang, K., Shah, S. P., White, D. J., Gray, J., Voigt, T., Gang, L., Hu, J., Halverson, C., and Pekmuzci, B. Y. (2005). "Self-Consolidating Concrete Applications for Slip-Form Paving: Phase I (Feasibility Study)." Center for Portland Cement Concrete Pavement Technology, Iowa State University, Ames, IA.

Ward, R. J., and Li, V. C. (1990). "Dependence of Flexural Behavior of Fiber Reinforced Mortar on Material Fracture Resistance and Beam Size." ACI Materials Journal, 87(6), 627-637.

Wille, K., Kim, D. J., and Naaman, A. E. (2011). "Strain-hardening UHP-FRC with low fiber contents." Materials and Structures, 44(3), 583-598.

Zerbino, R., Tobes, J. M., Bossio, M. E., and Giaccio, G. (2011). "On the Orientation of Fibres in Structural Members Fabricated with Self Compacting Fibre Reinforced Concrete." Cement and Concrete Composites, InPress.

Zhang, J., and Li, V. C. (2002). "Monotonic and fatigue performance in bending of fiber-reinforced engineered cementitous composite in overlay system." Cement and Concrete Research, 32(3), 415-423.

Zollinger, D. G., Tang, T. X., and Yoo, R. H. (1993). "Fracture-Toughness of Concrete at Early Ages." ACI Materials Journal, 90(5), 463-471.

# APPENDIX A. FIELD DEMONSTRATION PROJECT DETAILS

## A.1. Field Project Plan

The demonstration section was cast on July 14, 2009 in Rantoul, Illinois at the Advanced Transportation Research and Engineering Laboratory (ATREL) as illustrated in Figure A-1. Since this is an inlay section, the existing hot-mixed asphalt (HMA) was milled 50 mm down and roughly 3.3 m wide (ideally leaving a 150 mm wide HMA lip on either side to give side support for the concrete inlay). The target slab thickness was 50 mm thick with three sections consisting of different slab size configurations described in Chapter 2. Early saw-cutting was emphasized to reduce timing-related durability issues (Raoufi et al. 2008).

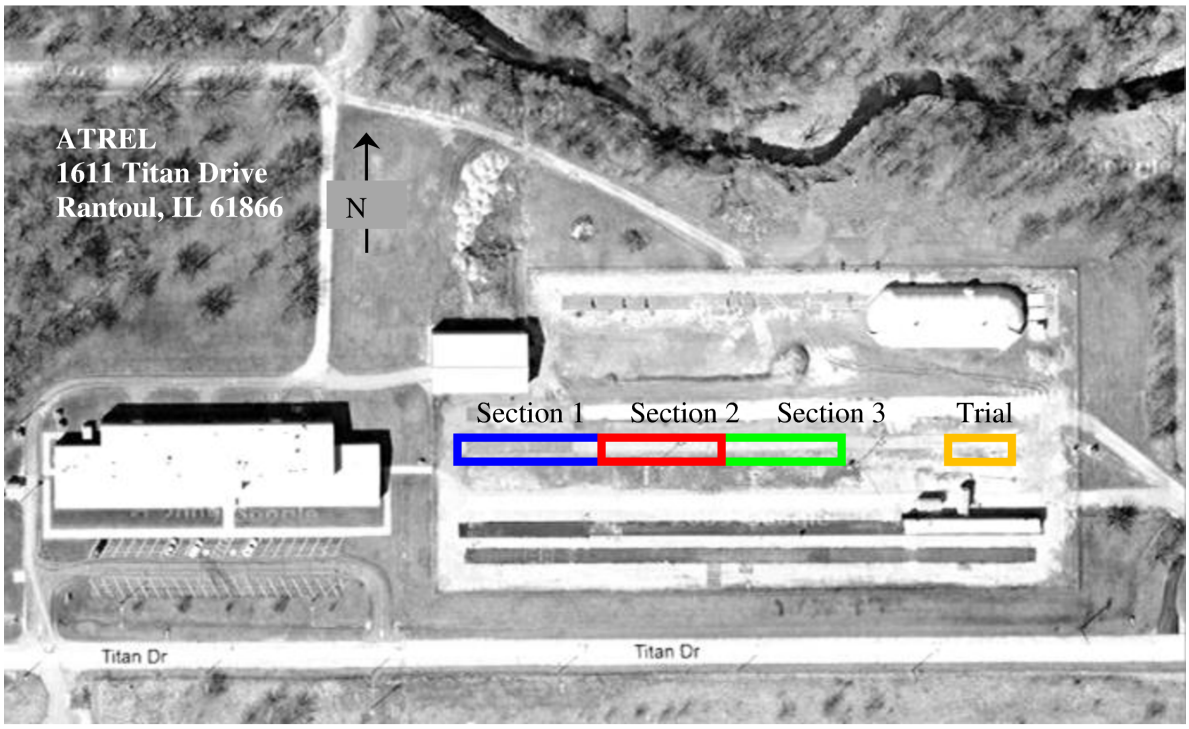


**Figure A-1 Location of full-scale concrete project demonstration.**

Testing with an Accelerated Transportation Loading System (ATLaS) was anticipated for the future of these sections to predict distresses, deterioration and fatigue cycles until failure of thin FFC wearing surface. Similar accelerated testing using ATLaS has been performed on other thin concrete overlay designs (Cervantes and Roesler 2009).

## A.2. Construction

### A.2.1. Milling

The pre-existing asphalt pavement ranged from 150 to 420 mm thick as detailed in Figure A-2 and was aged without visible distresses. The goal of the full-scale inlay demonstration was to achieve a bonded interface, thus the top 50 mm of the HMA was milled and cleaned using high pressurized water to remove any loose debris from the milled HMA. The pre-existing stone matrix asphalt layer seen in Figure A-3 still remained after milling and was difficult to remove. The final milled depth ranged from 13 to 76 mm (0.5 to 3.0 in.) with an average of 56 mm. Actual measurements of the milling are recorded as described in the detailed plan. The average width of the milled section ended up being 3.45 m, resulting in thinner support asphalt along the edges of the pavement.

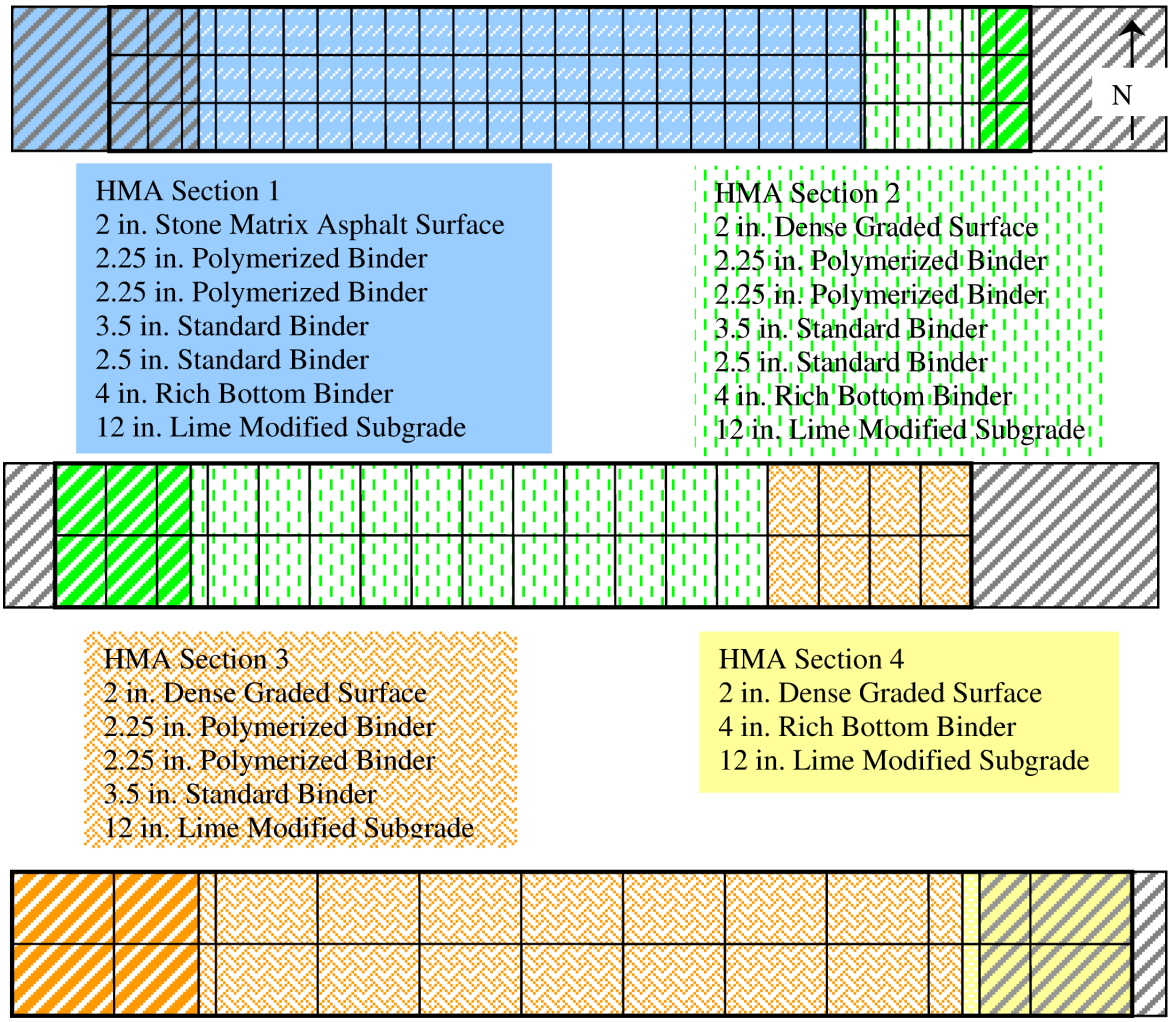


**Figure A-2 Pre-existing hot-mixed asphalt (HMA) sections and their location with respect to the full-scale concrete project. Hatched locations represent areas for future ATLAS supports.**

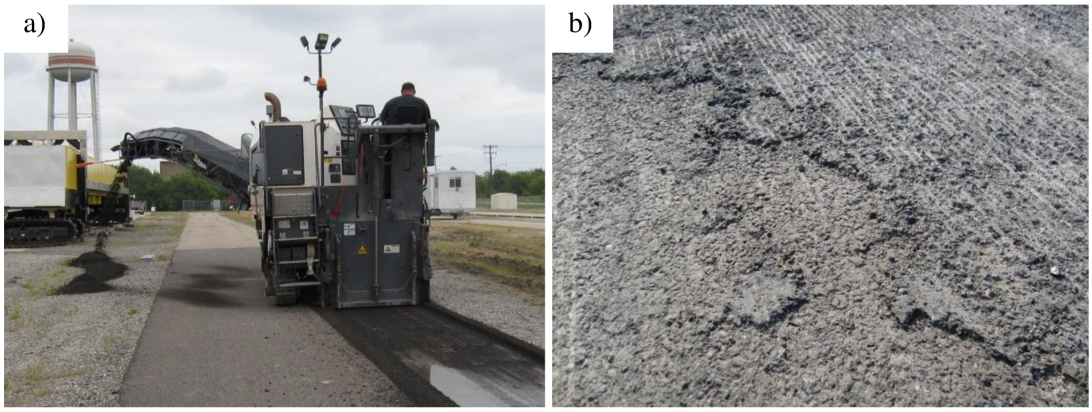


**Figure A-3 Photographs of the (a) milling and (b) surface texture prior to concrete placement in the stone-matrix asphalt section.**

### A.2.2. Trial Section

Prior to constructing the full-scale thin concrete inlay pavement section, a trial section was cast to verify that the FFC mixture design could be batched at a ready-mixed concrete plant, delivered in 40 minutes, and still be flowable enough for constructing the project. This trial section was cast as a 3.35 m wide x 12.01 m long x 0.38 m thick (11 ft x 39 ft-5 in. x 1.5 in.) overlay on the same existing asphalt as the HMA section 4 (shown in Figure A-3). Wood forms (2x4s placed on their side) were nailed to a pressure-washed HMA surface prior to casting. The FFC for the trial section was spread using rakes as seen in Figure A-4. The surface was leveled without external vibration using a 2x6 board as a screed.

The FFC mixture placement on the trial section was satisfactory since no visible segregation or compaction issues were prevalent despite the reduced amount of construction equipment. The manual labor of using a 2x6 board as a screed was difficult, thus a vibratory screed was selected for the full-scale demonstration. The hardened concrete surface of the FFC retained a rough texture, and thus would be useful as a wearing surface for providing vehicular friction. Intriguingly, the entire trial section exhibited no visible cracking or debonding well after a month of age despite the reduced thickness and un-milled surface. The combined asphalt-concrete pavement section appeared to shrink and curl at the ends of the slab.

**Figure A-4 Photograph of the construction of the trial section using rakes to spread the concrete and a wood screed for finishing.**

A.2.3. Full-scale Project

For the full-scale project, concrete was spread with shovels and rakes as shown in Figure A-5. A vibratory screed was used to strike-off and consolidate the pavement surface. Although some fiber clumping occurred primarily from several trucks, these visible fiber clumps were removed from the concrete before final finishing. Roughly 4 hours after casting, an early-entry saw was used to cut joints according to the plan shown in Chapter 2 at a depth of 13 mm (0.5 inch).


**Figure A-5 Photographs from construction showing (a) the vibratory screed and bull float, (b) pulling out fiber clumps from the surface, and (c) saw-cutting the concrete.**

## A.3. Ready-Mixed Concrete

The concrete mixture was delivered by four ready-mixed trucks totaling of 19 $m^3$ (25 cy). The FFC mixture for the demonstration project, described in Table A-1, contained the same proportions tested in the laboratory, namely of the 0.48 percent volume fraction of the 40 mm fibers combined with 0.06 percent of the 6 mm fibers and medium cementitious content (near 420 $kg/m^3$).

The ambient temperature was 20 degC during the morning the pour, with the concrete temperature measured at the concrete ready-mixed plant as 27.2 degC. The HRWR was

added at the site followed by 70 revolutions of the truck prior to casting. The truck delivery took roughly 43 minutes from the batch plant to the project location. The project casting began at 8:22 am and the entire 99.2 meters of the project was poured within 3 hours. Saw-cutting began around 1 pm, roughly 4.5 hours after construction began.

**Table A-1 Field Concrete Mixtures**

| Material | Unit | Trial | Truck 1 | Truck 2 | Truck 3 | Truck 4 | Lab Mixture |
|---|---|---|---|---|---|---|---|
| Sand | $kg/m^3$ | 898 | 890 | 887 | 887 | 887 | 857 |
| Limestone (9.5 mm) | $kg/m^3$ | 1072 | 1066 | 1068 | 1068 | 1068 | 1052 |
| Cement | $kg/m^3$ | 292 | 292 | 292 | 293 | 292 | 292 |
| Type C Fly Ash | $kg/m^3$ | 138 | 125 | 125 | 125 | 128 | 125 |
| AEA | $ml/m^3$ | 0.09 | 0.10 | 0.10 | 0.11 | 0.10 | 0.10 |
| Water | $kg/m^3$ | 168 | 168 | 168 | 168 | 169 | 167 |
| 40 mm Fiber | $kg/m^3$ | 4.4 | 4.4 | 4.4 | 4.4 | 4.4 | 4.4 |
| 6 mm Fiber | $kg/m^3$ | 0.8 | 0.6 | 0.6 | 0.6 | 0.6 | 0.5 |
| HRWR | $ml/m^3$ | 3.0 | 2.7 | 2.7 | 2.7 | 2.7 | 1.3 |
| Batch Amount | $m^3$ | 2.3 | 5.4 | 5.4 | 5.4 | 3.1 | 0.06 |
| Estimated w/cm | - | 0.39 | 0.40 | 0.40 | 0.40 | 0.40 | 0.40 |
| w/c | | 0.58 | 0.58 | 0.58 | 0.57 | 0.58 | 0.57 |

## A.4. Field Material Testing Results

Several samples were created in the field and tested in comparison to the laboratory mixture. Tests performed on were compression, split-tension, elastic modulus, modulus of rupture at 7 and 28 days after casting. In addition, fresh properties (slump flow, unit weight, and air content) were measured for each ready-mix truck batch. All of the measured sample properties for each truck batch are shown in Table A-2. The unnotched toughness and notched fracture beam test results are also illustrated in Figure A-6 and Figure A-7, respectively.

**Table A-2 Fresh and Hardened Properties of Field Batches**

| Test | Unit | Trial | Truck 1 | Truck 2 | Truck 3 | Truck 4 |
|---|---|---|---|---|---|---|
| Slump Flow Diameter | mm | 394 | 470 | 381 | 368 | 368 |
| Unit Weight | kg/m$^3$ | 2236 | 2275 | 2307 | 2371 | 2243 |
| Air Content | % uncorrected | 6.8 | 5.8 | 5.4 | 4.4 | 5.5 |
| 7 day Compressive | MPa | 33.6 | 36.4 | 35.9 | 35.5 | |
| 28 day Compressive | MPa | 46.2 | 45.2 | | 39.7 | |
| 7 day Split Tension | MPa | | | 2.91 | 5.23 | |
| 28 day Split Tension | MPa | | 4.13 | 4.19 | 4.54 | |
| 28 day Elastic Modulus | GPa | | | 32.3 | 31.4 | |

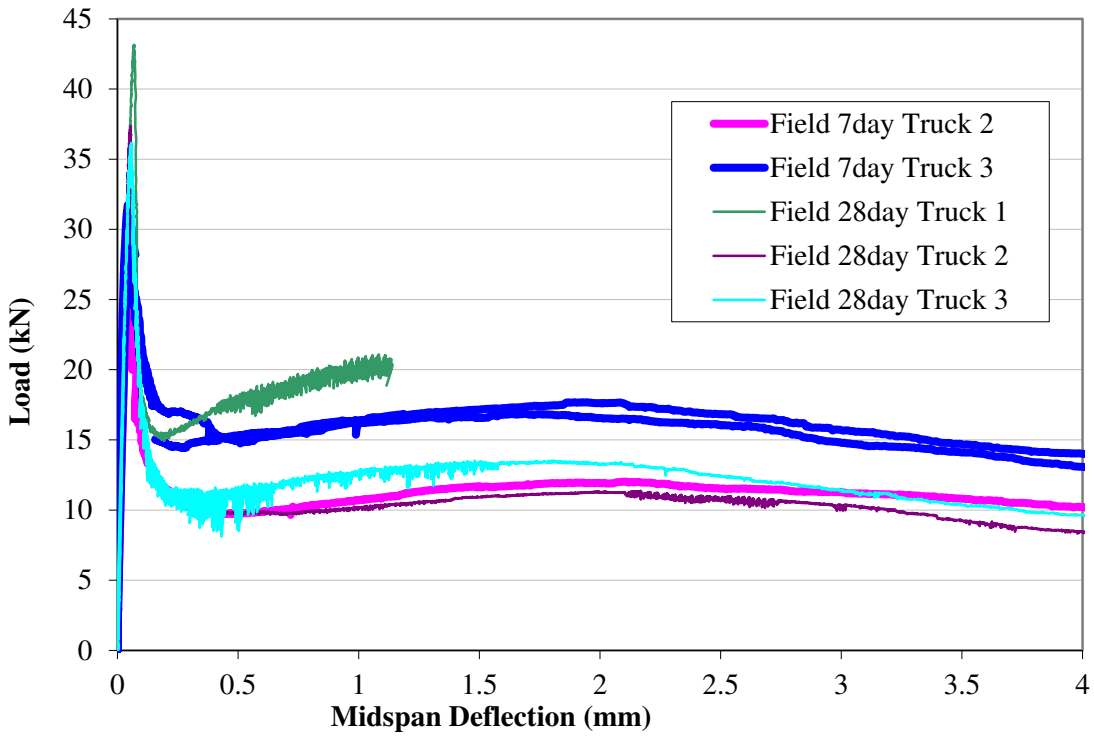


**Figure A-6 Load versus midspan deflection results of the standard unnotched flexural beam (15 x 15 x 53 cm) test.**

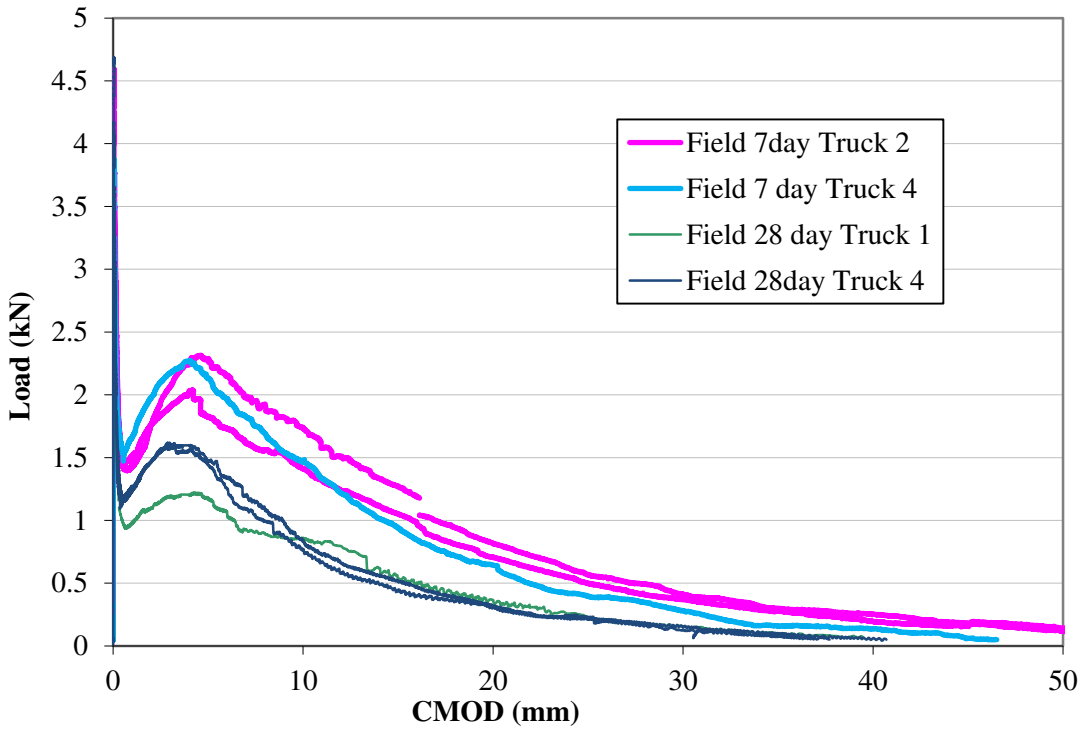


**Figure A-7 Load versus CMOD results of the standard fracture SEN[B] (15 x 15 x 70 cm) test.**

A.4.1. Shrinkage

Shrinkage beams were also cast from various truck batches in the field and tested as described in Appendix A. The resulting shrinkage values measured and mass loss values measured for these beams are shown in Figure A-8.

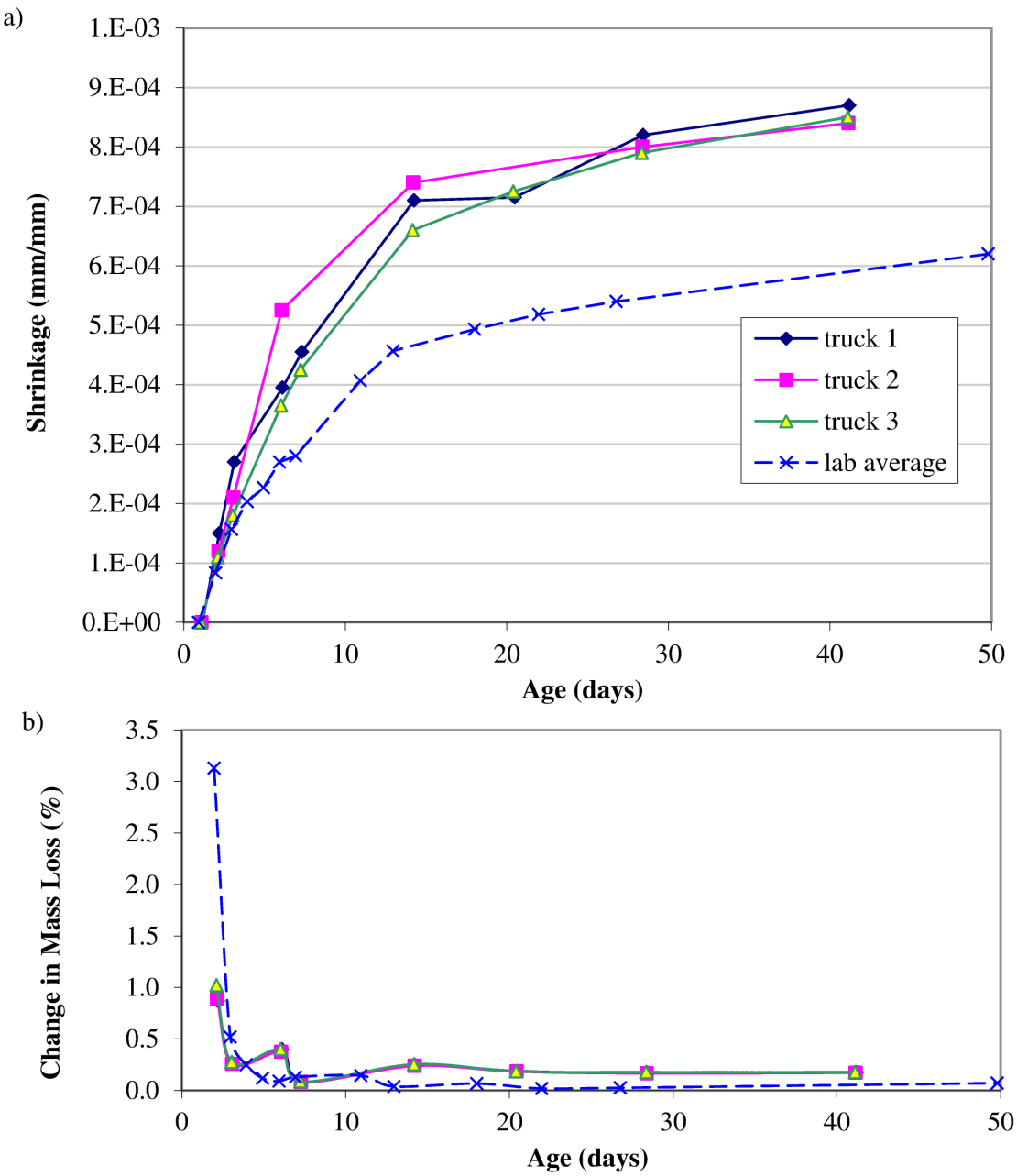


**Figure A-8 (a) Shrinkage and (b) mass loss results for ready-mixed concrete samples compared to a laboratory mixed sample.**

A.4.2. Temperature

Two trees of thermocouples, as shown in Figure A-9, were laid out to capture the temperature differences within the thin concrete layer and into the asphalt below. The west tree of thermocouples was located at the center of slab within section 2 (1.7 m panels) and the east tree of thermocouples was located at the center of slab within section 3 (1.7 x 3.4 m panels).

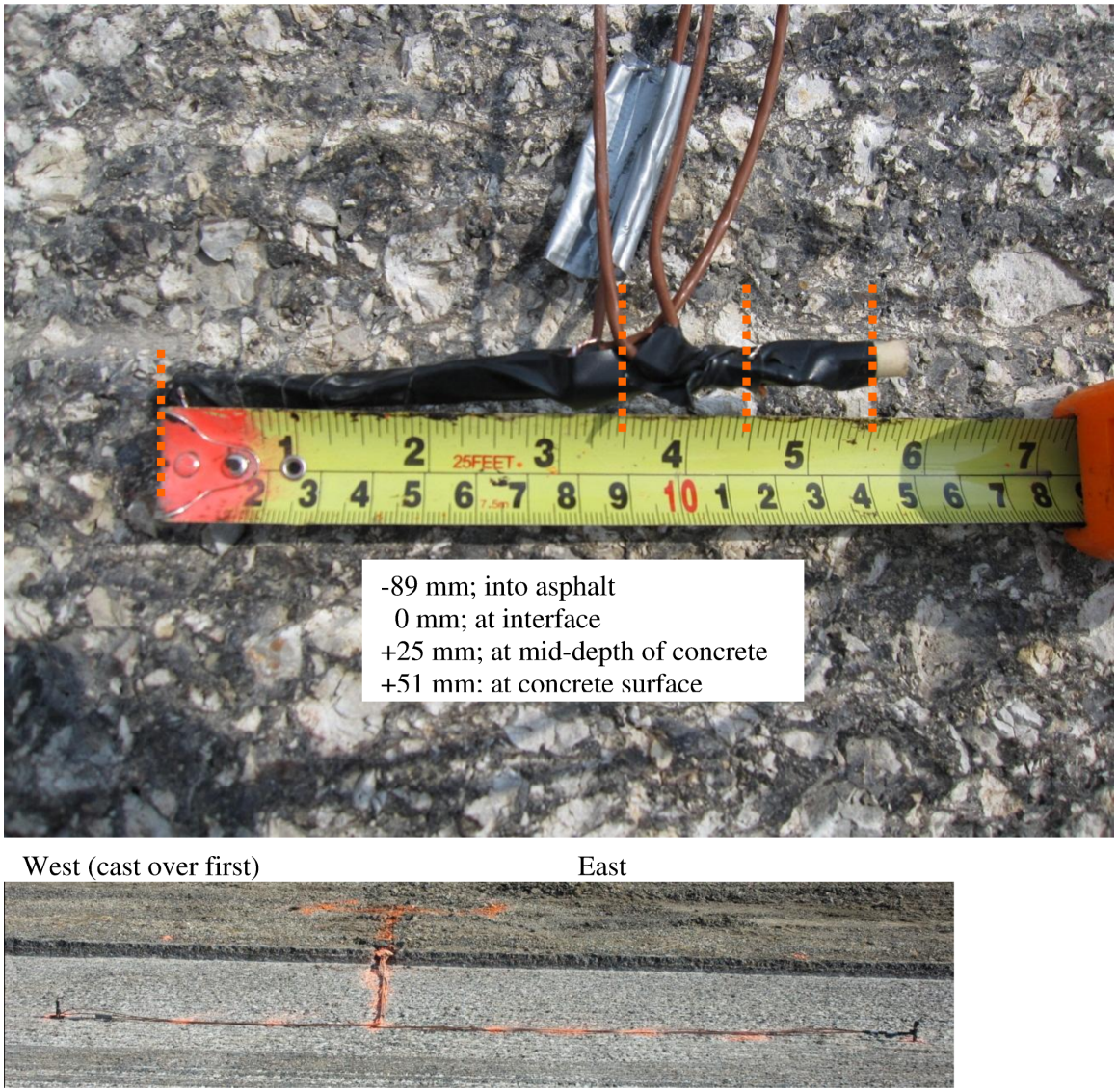


**Figure A-9 Thermocouple locations and depths.**

Due to a dead battery on the data acquisition system during the morning of casting, the temperature readings were not taken at the early hours of the concrete casting. Thus the heat of hydration curve was not captures at these early hours. However, temperature recordings were captured after roughly 7 hours from batching as shown in Figure A-10.

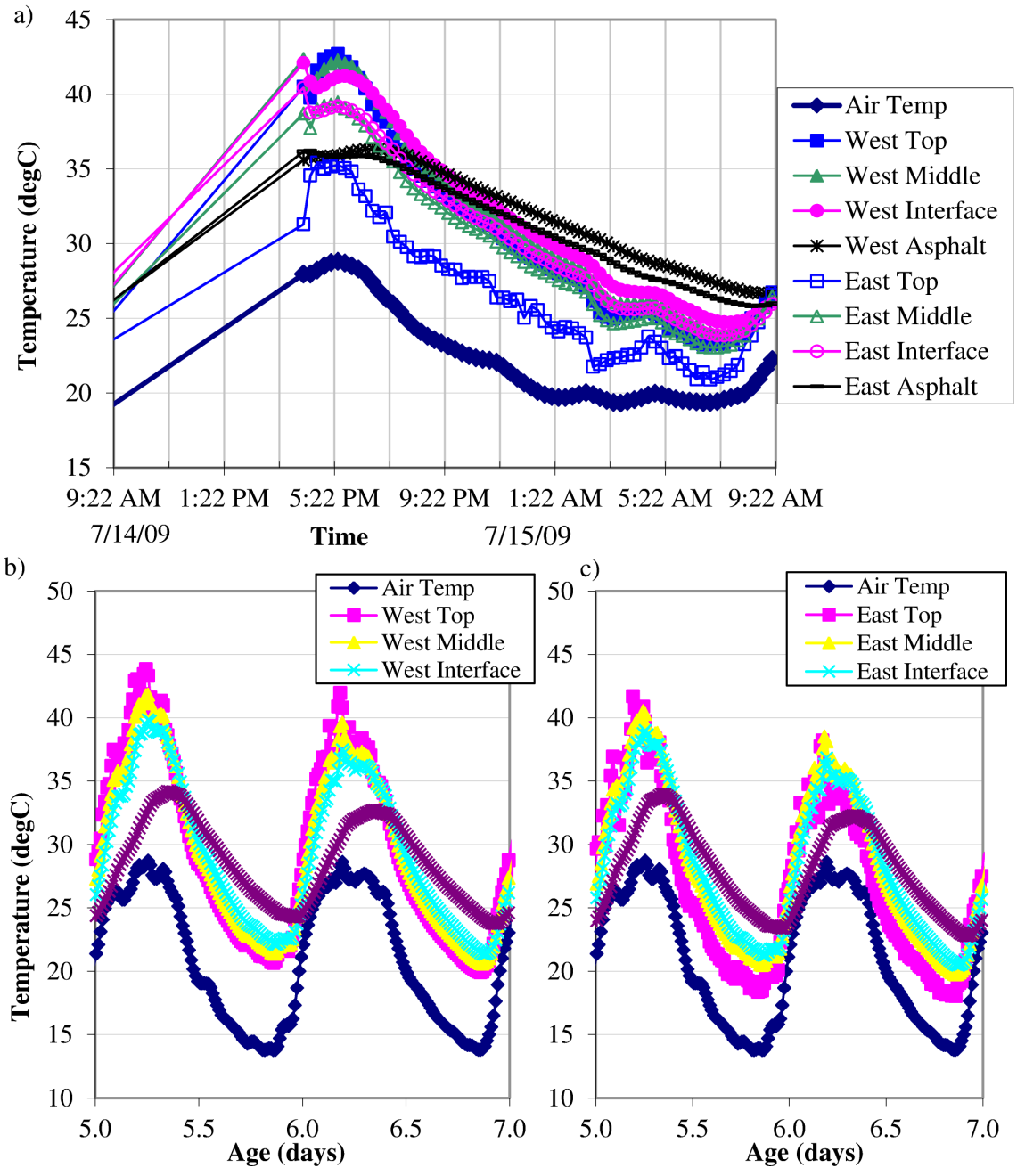


**Figure A-10 Thermocouple temperature readings after casting for (a) first 24 hours, (c) west sensor location and (c) east sensor location.**

## A.5. Cracking

The activation of joints was monitored at ages of 1, 3, 8, and 20 days by crack frequency and crack widths. The transverse contraction joints exhibited cracking as summarized in Figure A-11. The transverse joints in the largest slabs (section 3) exhibited the most percentage of joints cracked after one day, but joints within section 1 closely matched the crack frequency in section 3 at later ages.

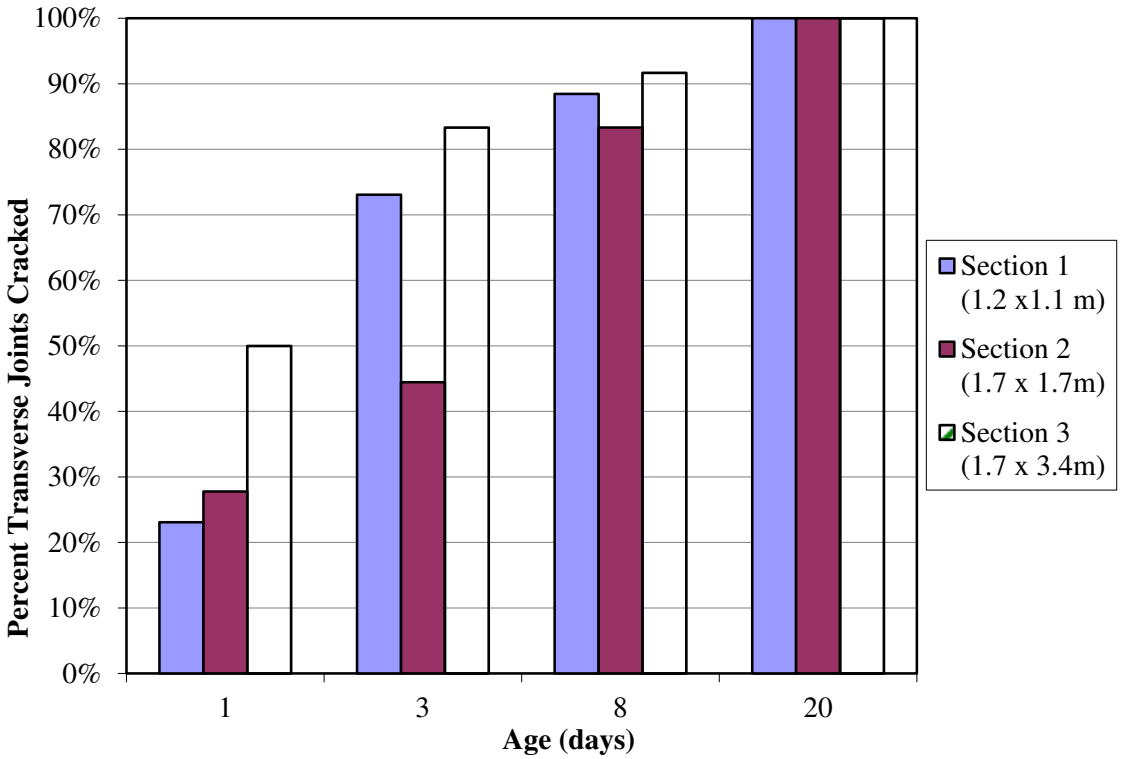


**Figure A-11 Percent of transverse joints cracked at different concrete ages.**

A plot of the crack width versus age for each section can be seen in Figure A-12. The larger slab sizes resulted in the greatest joint crack widths. Cracks measured at one day were investigated to determine whether any link between early age crack development and the crack widths at later ages exists, as previously discovered on UTW projects in Illinois (Bordelon 2007; Roesler et al. 2008b). As seen in Figure A-12, the data confirms

that cracks appearing by day one have a larger average crack width than the average crack width of all joints at day 20. This reinforces the desire to have contraction joints crack as early as possible as this would likely reduce the average crack widths at each joint at all ages and distribute the movement of each slab to avoid the potential for interface debonding.

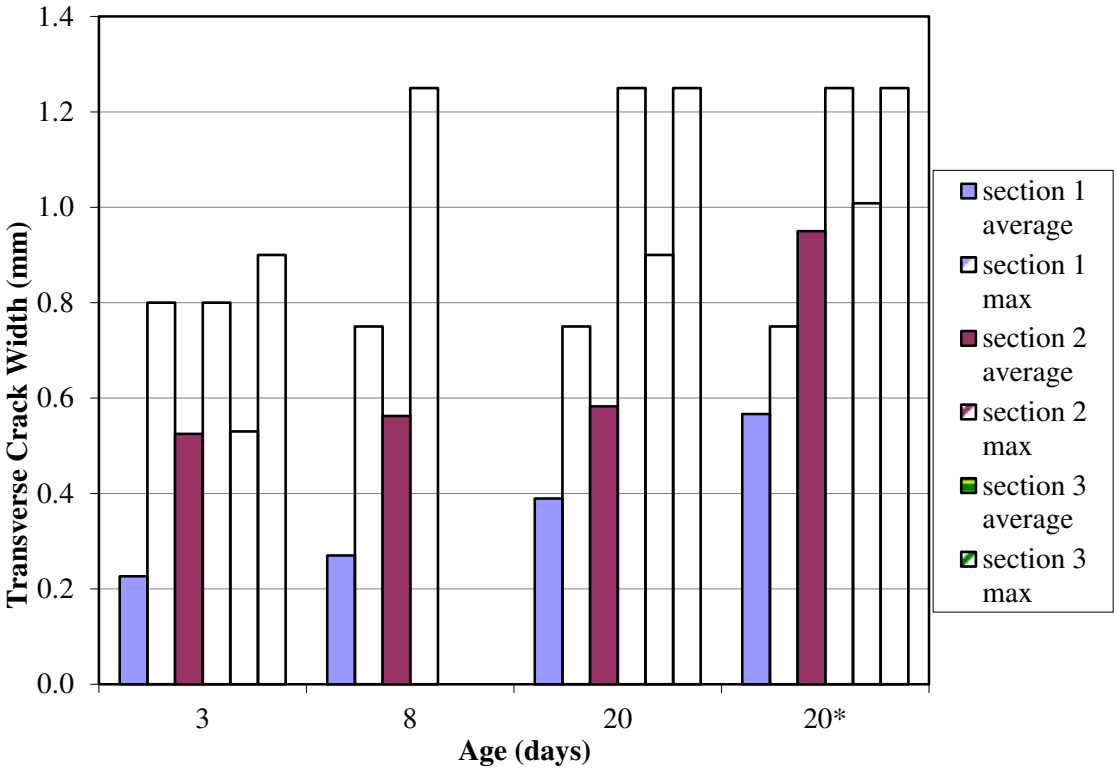


**Figure A-12 Average and maximum transverse crack widths at different concrete ages (20* denotes the average crack widths calculated using only joints cracked at 1 day).**

## A.6. Detailed Diagrams of Project Layout

Cracking within each section of the project was determined using visual inspection at 3, 8, 20 and 35 days after casting. A crack comparator was used to estimate the width of the cracks or joints and to estimate the depth of saw-cuts. The following diagrams show joints, cracked joints over time, and debonded zone locations and measurements of crack widths, saw cut depths and joint widths over time.

### A.6.1. Section 1

1.15 1.12 m (3' 9" wide x 3' 8"long) (typical for 4in UTW often cracking every 5-7 joints or 20 to 30 ft)

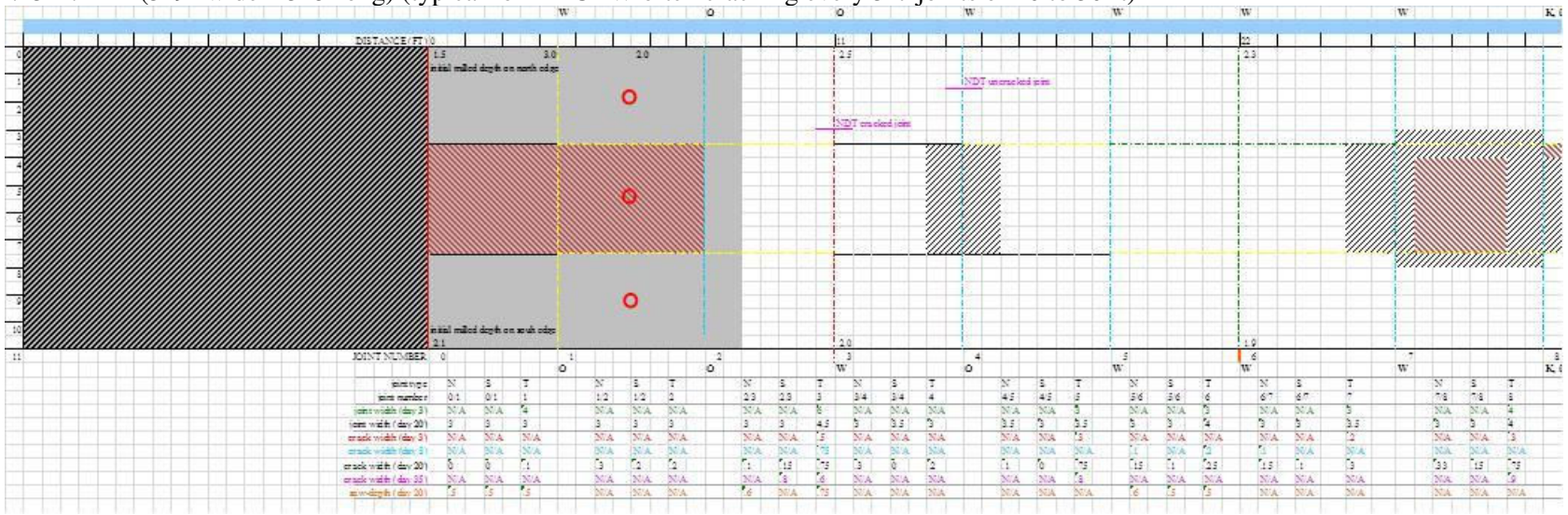

Legend

Joint Type

N = north longitudinal joint

S = south longitudinal joint

T = transverse joint

red lines are cracks seen on 7/15/09 (1 day)

blue lines are cracks seen by 7/17/09 (3 day)

green lines are cracks seen by 7/22/09 (8 day)

yellow lines are cracks seen by 8/3/09 (20 day)

HMA section1

HMA section2

HMA section3

HMA section4

estimated measurements for crack width (mm) on 7/17/09 (day 3)

estimated measurements for crack width (mm) on 7/22/09 (day 8)

estimated measurements for joint width (mm), crack width (mm) on 8/3/09 (day 20)

estimated measurements for crack width (mm) on 8/18/09 (day 35)

Estimated depth of saw-cut (mm) on 8/3/09 (day 20)

edge cracking determined on 8/18/09 (35 days)

A crack width (mm) determined in asphalt

C crack width (mm) determined in concrete

O no visible crack through asphalt at end of transverse saw-cut joint

W saw cut joint all the way through asphalt edge

K crack seen though asphalt edge at end of transverse joint

debonding determined from chain drag on 9/29/09

additional debonding determined from chain drag on 4/11/12

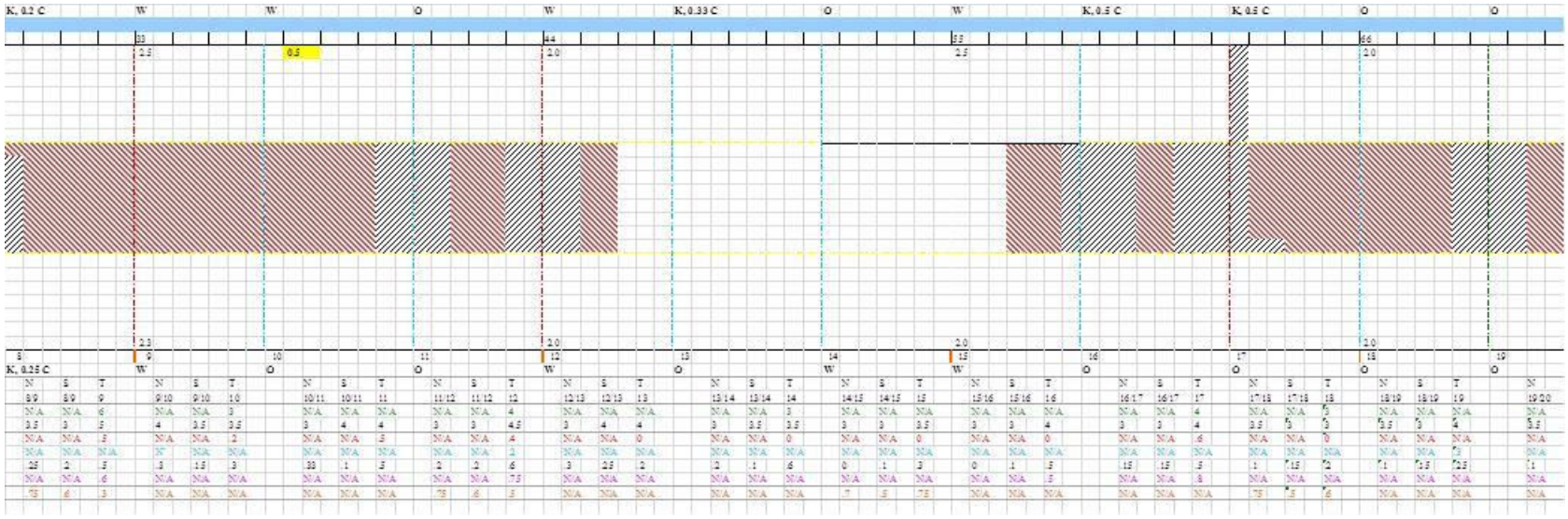

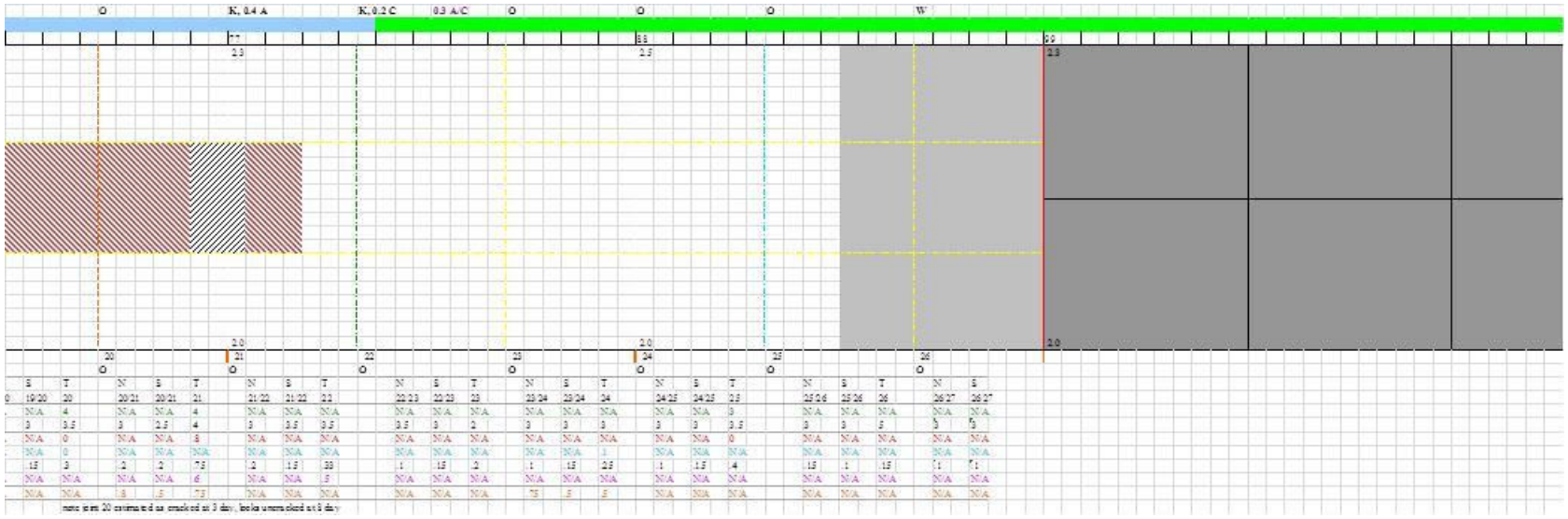

## A.6.2. Section 2

1.73 x 1.68 m (5' 8" wide x 5' 6" long)

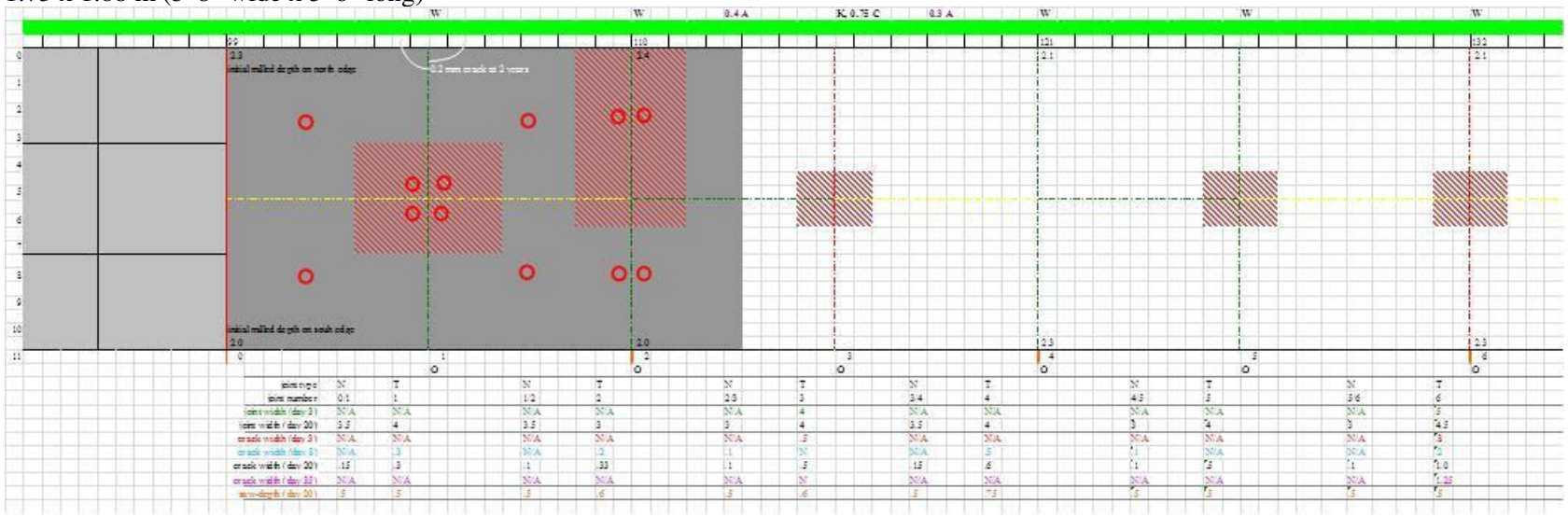

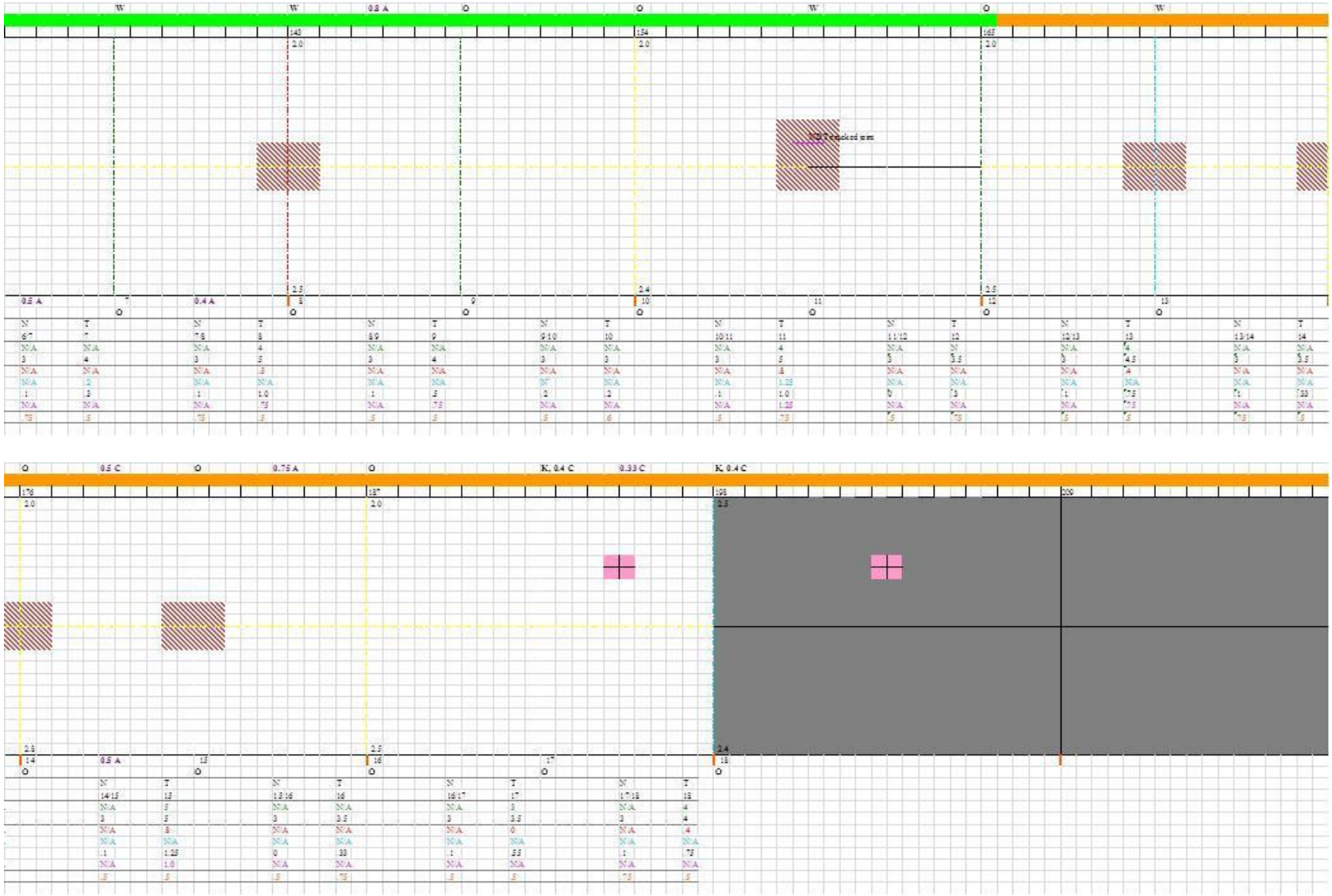

## A.6.3. Section 3

1.72 x 3.35 m (5' 7.5" wide x 11' long); (unjointed)

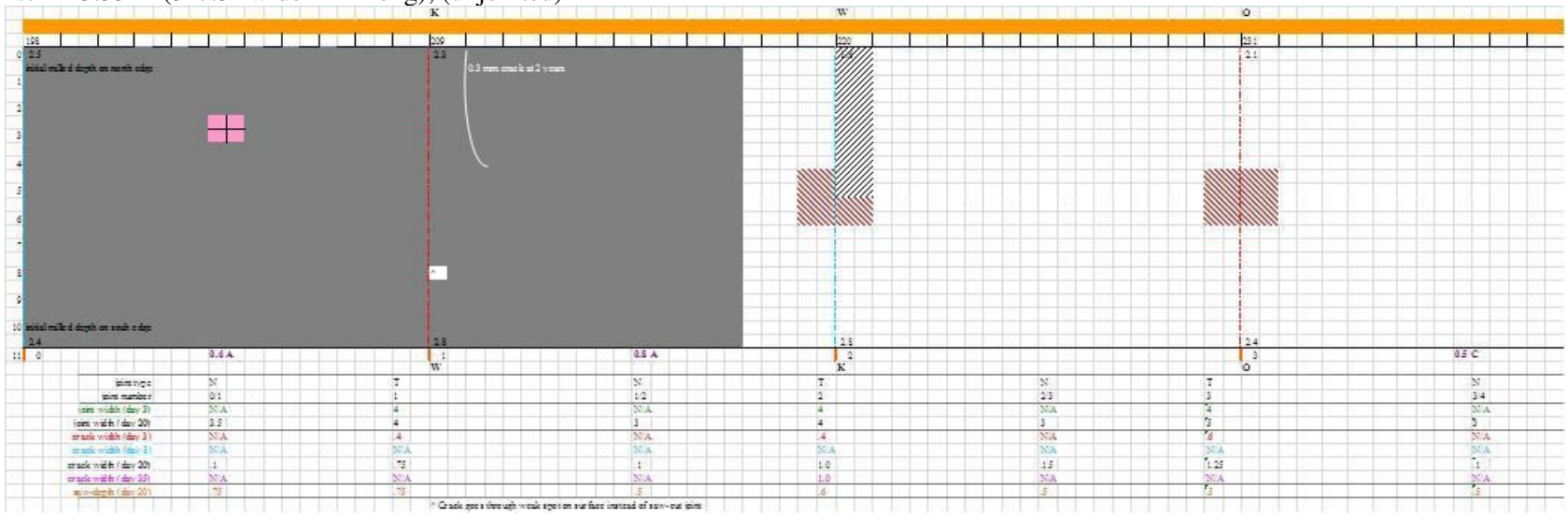

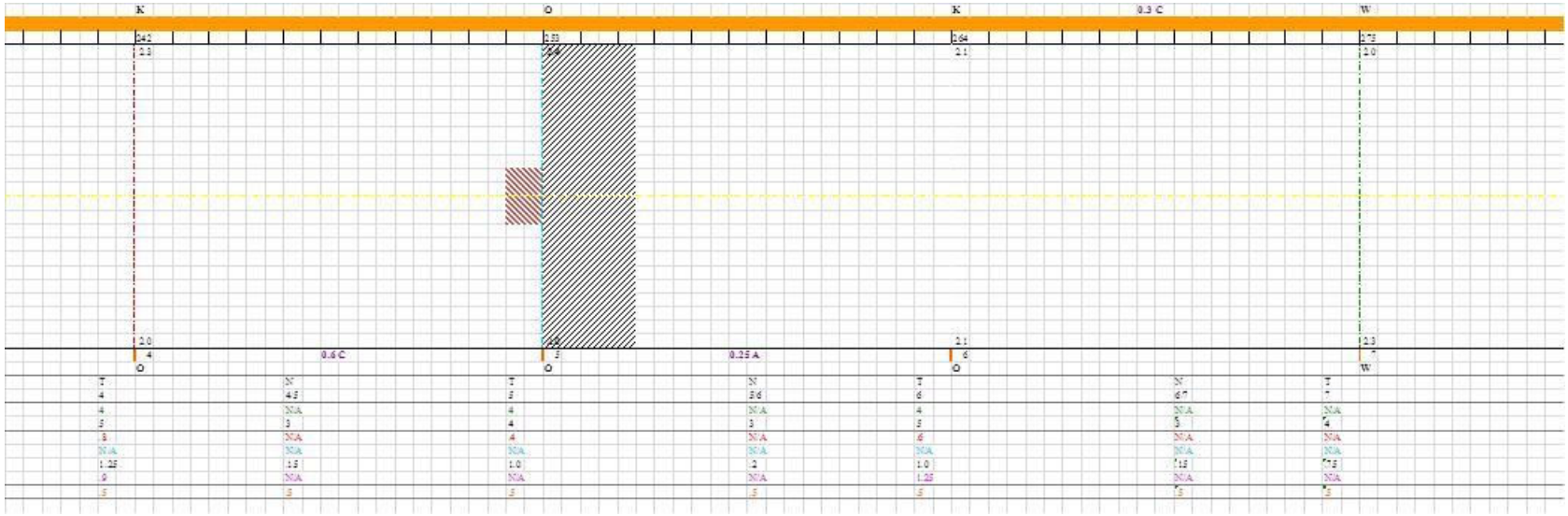

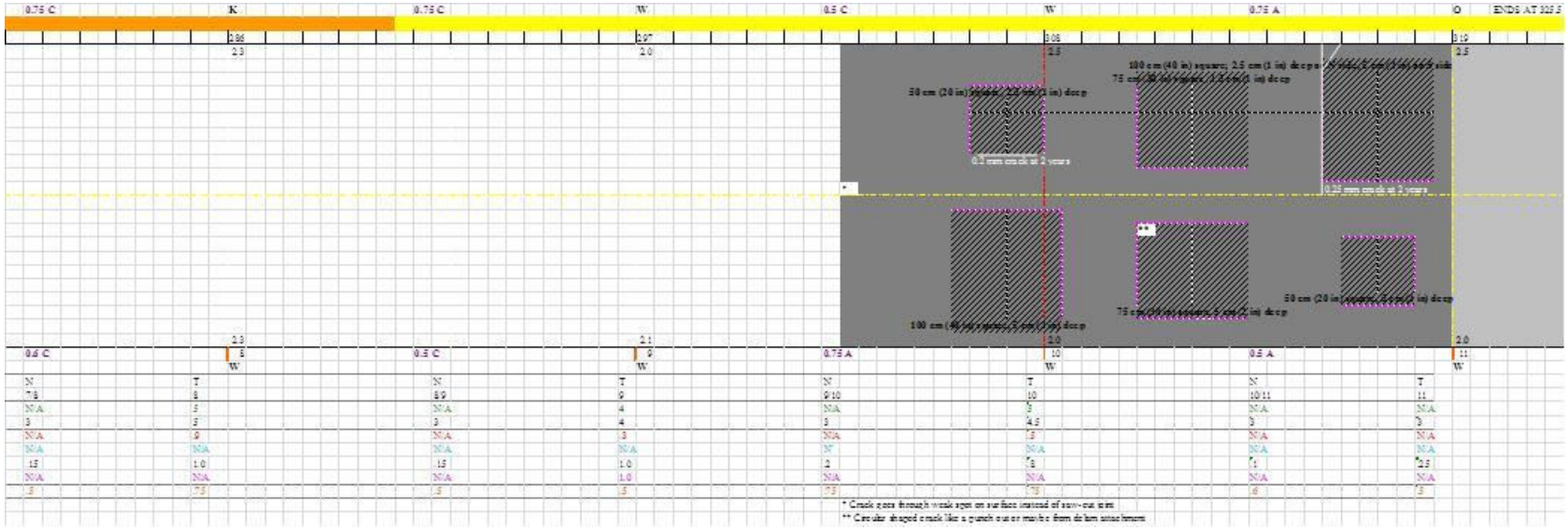
50 cm (20 in) square; 2.5 cm (1 in) deep
0.2 mm crack at 2 years
100 cm (40 in) square; 2.5 cm (1 in) deep
75 cm (30 in) square; 2.5 cm (1 in) deep
50 cm (20 in) square; 2.5 cm (1 in) deep
* Crack goes through weak spot on surface instead of saw-cut joint
** Circular shaped crack like a punch out or marks from debris removal

## A.6.4. End Section

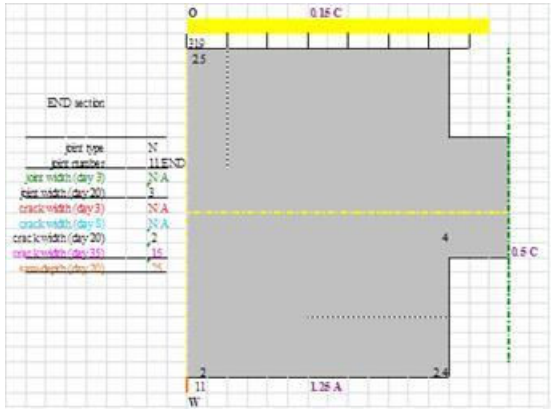


## A.6.5. Trial Section

11' wide x 39'5" long x 1.5" thick

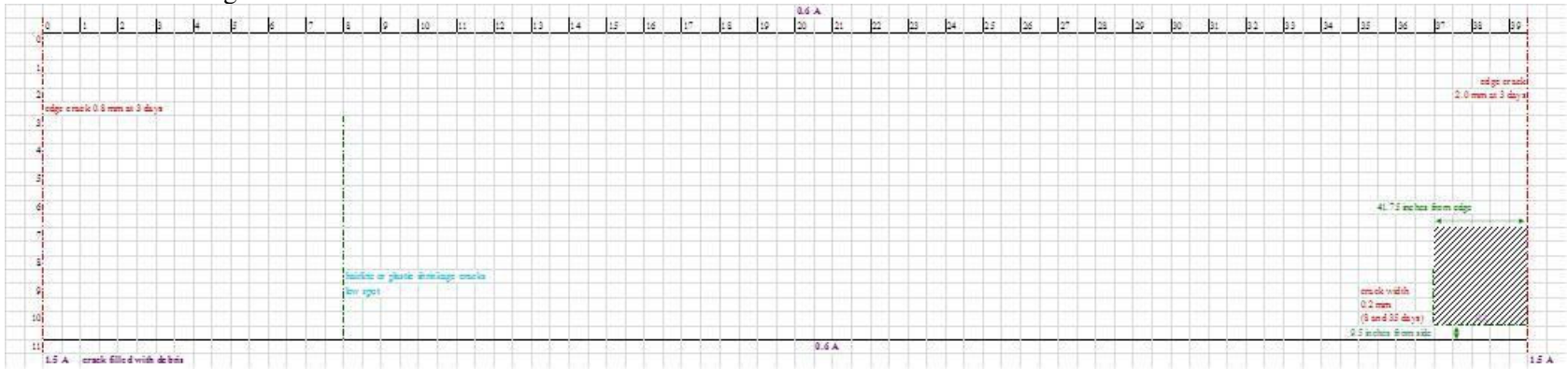

## A.7. Bond Strength

Each slab was checked for debonding by initially performing a chain drag across each slab and listening for a pitch change to determine a debonded zone. The pitch change heard over the placed delaminations on the east end of section 3 (as shown in the previous detailed diagram) to calibrate the chain drag. The areas of debonded are marked in Figure A-13 as dark shaded zones. The majority of bonding problems occurred in the center longitudinal row of slabs of section 1.

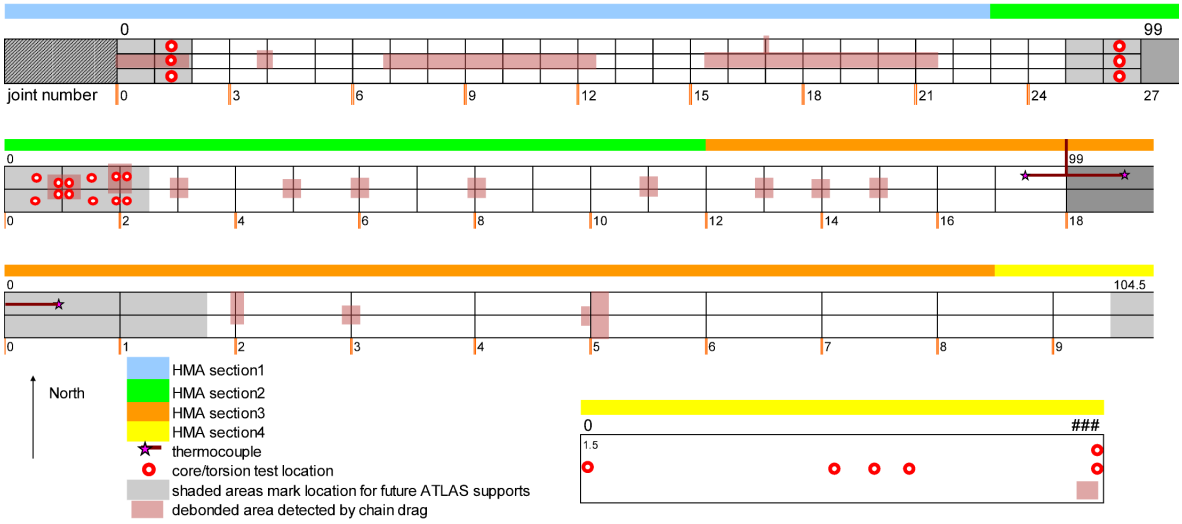


**Figure A-13 Locations of debonding (dark shaded regions) are shown and corresponding coring locations for bond testing.**

Cores were drilled to roughly 1 inch below the concrete-asphalt interface at the locations marked as red circles in Figure A-13. Using the in-situ torque wrench technique (Tashman et al. 2006; Leng et al. 2008), a plate was epoxied to the surface of the concrete and the maximum reading (as shown in Figure A-14) on the torque wrench indicated the strength of the interface. Although the torsional test was found to be highly variable, several of the tests exceeded the torque wrench meter (beyond 500 N-m). In addition

because measurements were made during a cold temperature day in October, the epoxy was quite brittle and many of tests broke at the epoxy-concrete surface.

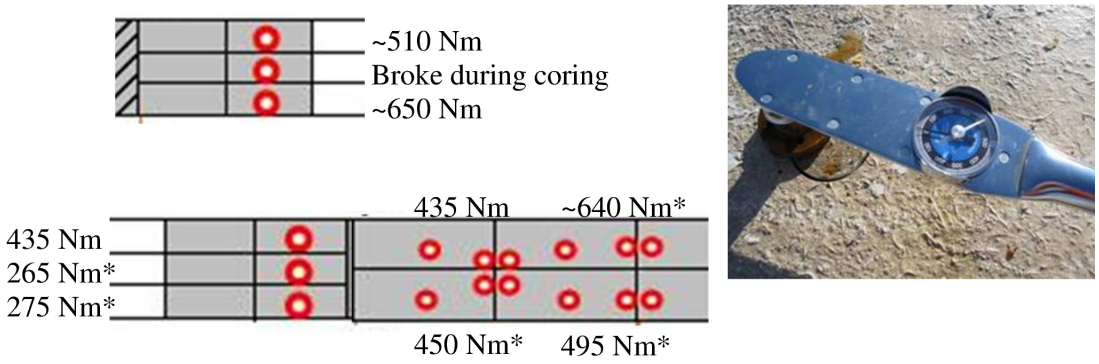


*Broke at Epoxy; concrete surface damaged from screws

**Figure A-14 Diagram shows the torque wrench readings on cored samples at various locations and a photograph of the torque wrench used.**

# APPENDIX B. FINITE ELEMENT ANALYSIS

## B.1. Mesh Generation

The finite element modeling (FEM) mesh nodes and elements were defined using MSC PATRAN® (2008). A 2D mesh of the single edge notched beam (SEN[B]) was modeled (Roesler et al. 2007; Park et al. 2008) as shown in Figure B-1. Nodes from one half of the beam were generated using a Fortran code (written to specifically create the trapezoidal element size reduction steps) and mirrored across the loading axis (at 0.5 or 1 mm spacing between nodes for a 5 or 15 cm beam height, respectively).

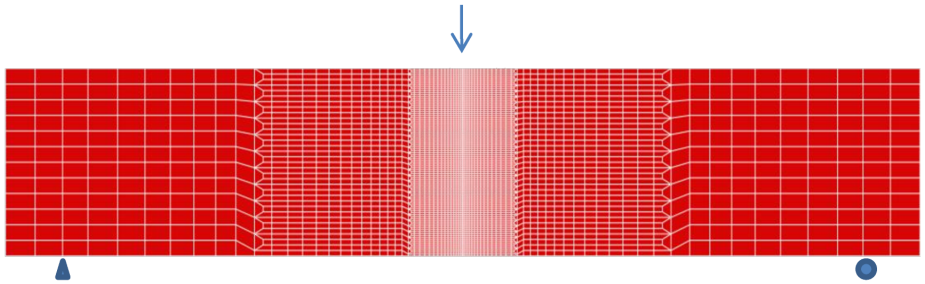

**Figure B-1 Finite element model mesh and boundary load conditions.**

Cohesive zone elements of zero width were manually defined for all the nodes ahead of the crack tip. The standard bulk elements were Q4 elements defined with PATRAN® and based on the concrete material assuming it has linear elastic and isotropic behavior. To prevent overlap of nodes in the crushing zone directly under the node, the top node and first cohesive element were removed as shown in Figure B-2 and Figure B-3.

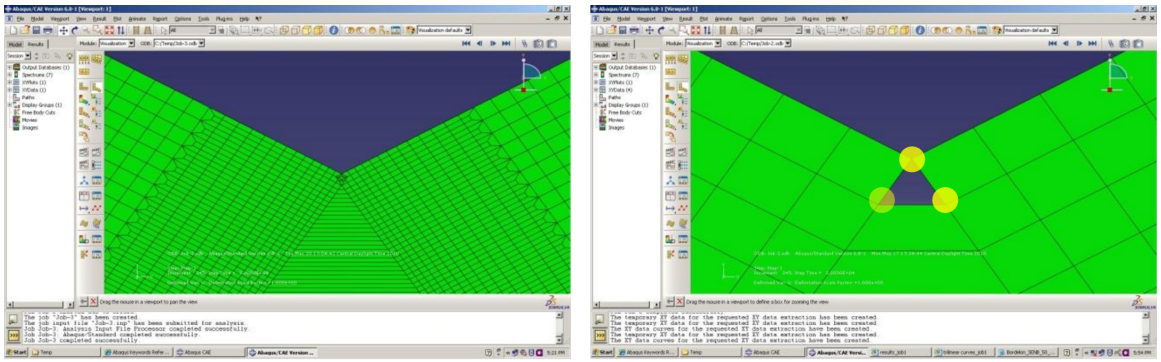

**Figure B-2 Screenshot of the FEM mesh (unpinned) with overlap and after pinning the top node.**

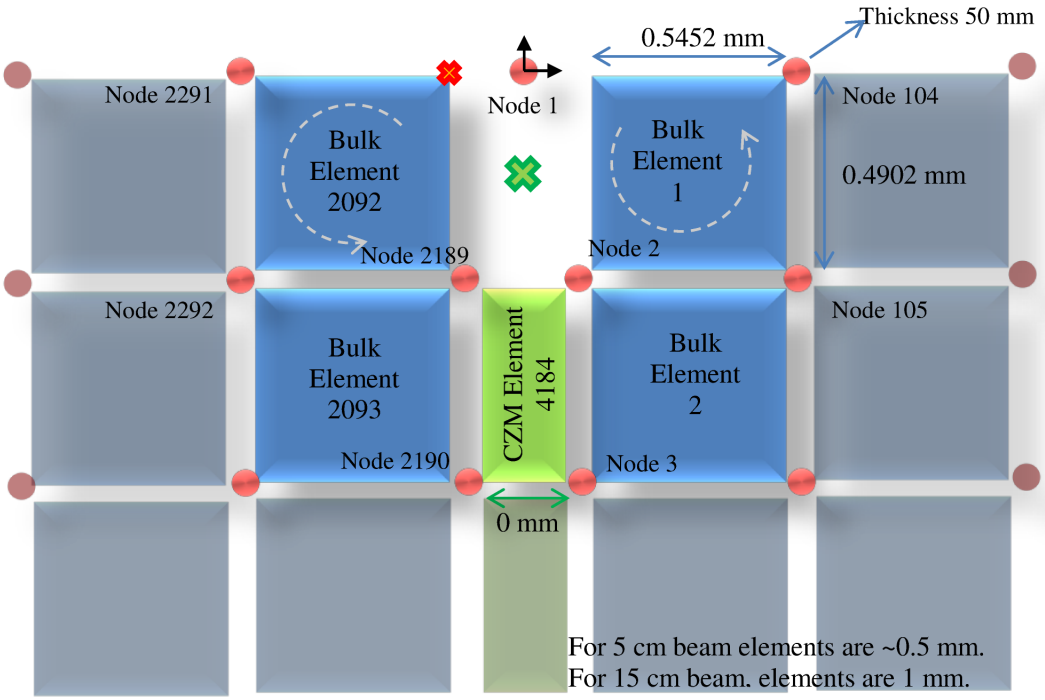


**Figure B-3 Top cohesive element removed to prevent overlap.**

## B.2. ABAQUS Input File

The analysis was run using ABAQUS ® Computer-Aided Engineering (CAE) software version 6.8-1. Points along the damage softening curve were defined for small crack openings $w_i$ every 0.001 to 0.1 mm. Equations for the damage curve are defined as follows with an example shown in Figure B-4.

B.2.1. Damage Softening Points

$$t'_i = K_{nn} w_i$$

$$\text{Relative Crack Opening } \delta_i = w_i - w_{cr}$$

$$\text{Damage } D = 1 - \frac{t'_i}{t'_s}$$

For $w < w_{cr}$:

$$t'_s = \frac{f_{sp}}{(w_1 - w_{cr})} \quad w_1 - w_i$$

For $w < w_{k1}$:

$$t'_s = \frac{\psi 1 f_{sp}}{(w_2 - w_{k1})} \quad w_2 - w_i$$

For $w < w_{k2}$:

$$t'_s = \frac{\psi 2 f_{sp}}{(w_f - w_{k2})} \quad w_f - w_i$$

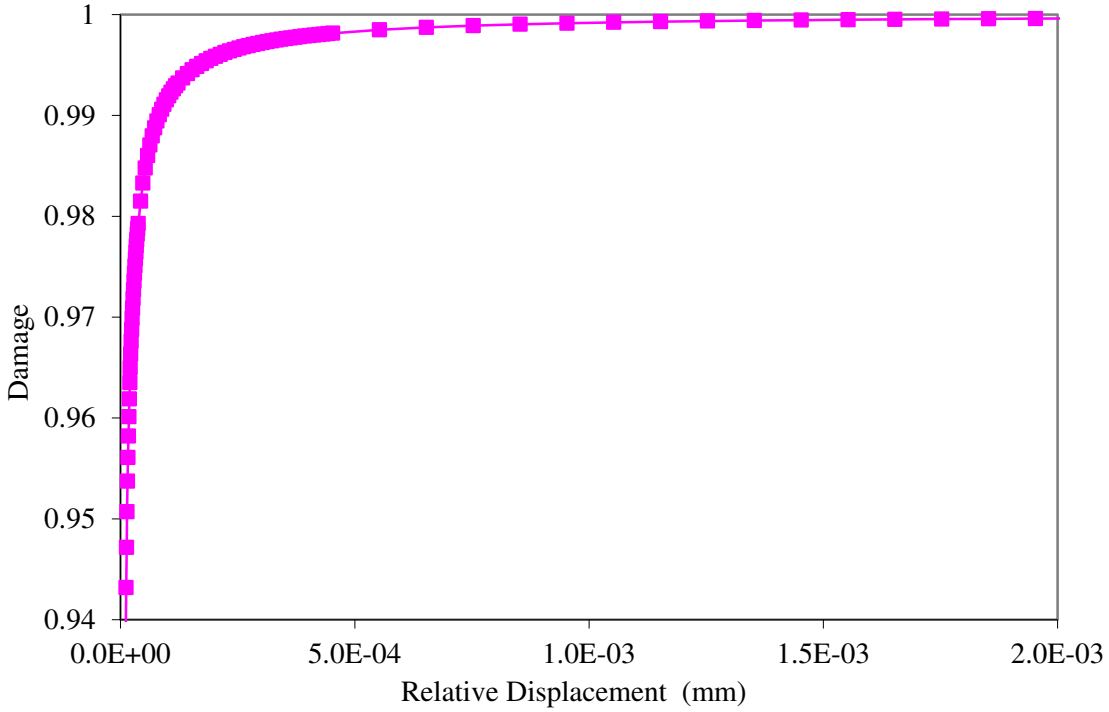


**Figure B-4 Example plot shows a damage response curve used (for BT rand with GFRC=8,677 N/m).**

### B.2.2. Node Definitions

```
*HEADING
*NODE, NSET=N1
1,0.35,0
2,0.35,0.001
3,0.35,0.002
…
**4373,0.35,0.149
**4374,0.35,0.15
4375,0.364,0
…
7445,0.7,0.128
7446,0.7,0.15
*NODE, NSET=N2
1,0.35,0
4224,0.35,0
```

### B.2.3. Element Definitions

```
*ELEMENT, TYPE=CPS4 , ELSET=Q4
   1001,   1003,   1004,   1016,   1015
   1002,   1004,   1005,   1017,   1016
...
   8092,   7444,   7445,   7435,   7434
   8093,   7445,   7446,   7436,   7435
*SOLID SECTION, ELSET=Q4, MATERIAL=con
0.08
*MATERIAL, NAME=con
*DENSITY
2313
*ELASTIC
26.45e9, 0.15
*ELEMENT, TYPE=COH2D4, ELSET=one
1,52,51,4274,4275
2,53,52,4275,4276
…
98,149,148,4371,4372
99,150,149,4372,150
```

### B.2.4. Material Definitions

```
*COHESIVE SECTION, elset=one, material=contrac,
thickness=specified, response=traction separation
1, 0.08
*MATERIAL, name=contrac
*ELASTIC, Type=traction
1e12, 4.35e11
*DAMAGE INITIATION, CRITERION=MAXS
```

```
3.052e6, 3.052e6
*DAMAGE EVOLUTION, Type=Displacement, Softening=Tabular
0, 0
0.288523201949046, 0.000001
0.46282502545429, 0.000002
0.579525453220854, 0.000003
…
0.998526454213592, 0.000114
0.999105075386038, 0.000124
1, 0.000146
```

### B.2.5. Step Function

```
*STEP, NLGEOM, inc=100
*STATIC
*BOUNDARY
4184, 1, 2
7407, 2, 2
*DLOAD
Q4, GRAV, 9.81, 0, -1, 0
*END STEP
*STEP, NLGEOM, INC=200
*STATIC
0.00002, 1.0, 0.0000001, 0.05
*BOUNDARY
 151, 2, 2, -0.001
*END STEP
```

Constant Deflection "Loading" from top of beam up to 1 mm

### B.2.6. Input Parameter Assumptions

Several of the assumptions, such as plane strain elements, zero gravity, and increment step size, used in the ABAQUS® input file were compared as shown in Figure B-5. There was no sensitivity between having the bulk elements be plane strain (CPE4) versus plane stress (CPS4) elements. No significant change was seen in the global response if gravity was left out of the input file or if the increment size was reduced to 0.005 instead of 0.05.

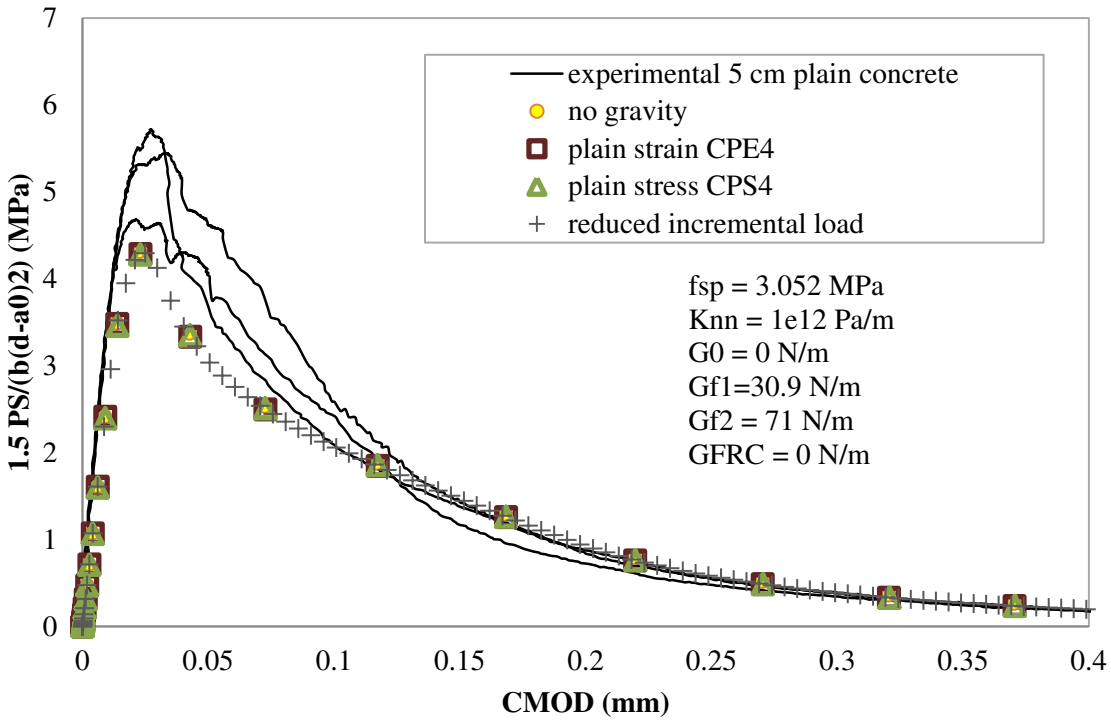


**Figure B-5 Sensitivity of settings for the plain concrete 5 cm beam in FEM.**

## B.3. Stress Results

The cohesive element stress distribution across the fracture plane and over the loading duration can be seen in Figure B-6 and Figure B-7, respectively. Similarly, the maximum principal stress was computed for the cohesive elements over the loading duration, as shown in Figure B-8.

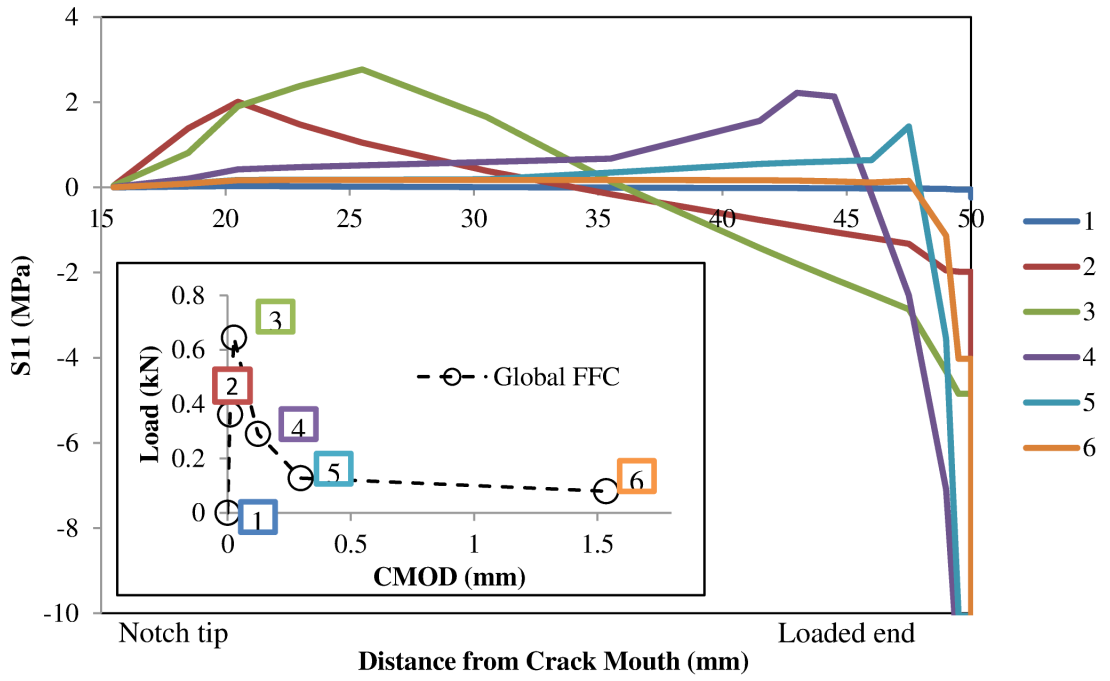


**Figure B-6 Tensile stresses along fracture plane at different opening displacements.**

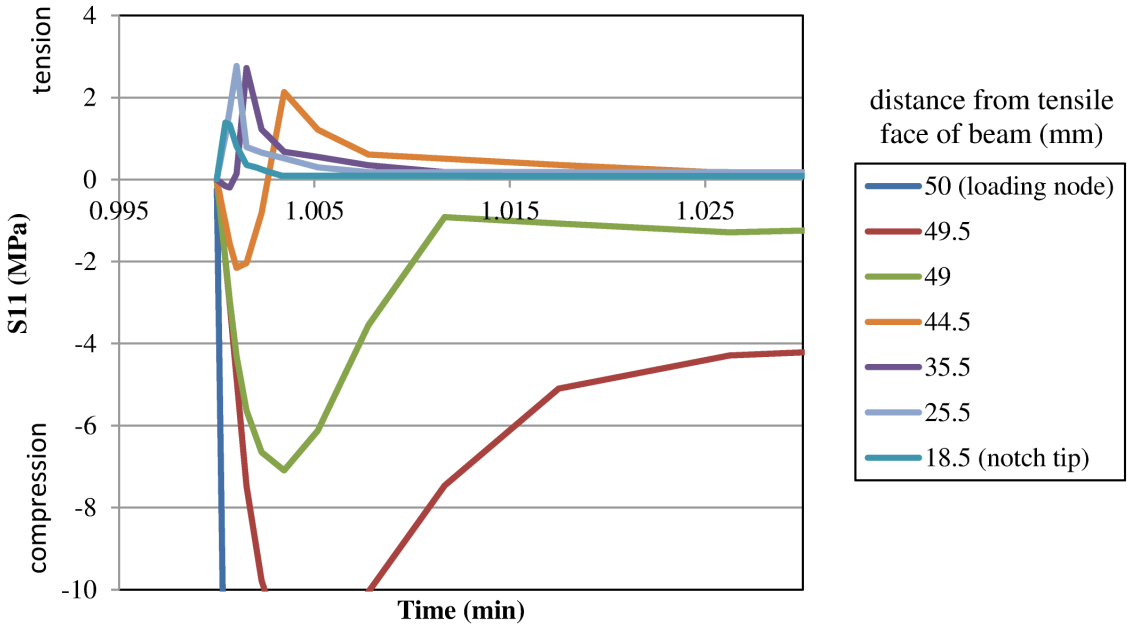


**Figure B-7 Tensile stresses along fracture plane at distances along fracture plane.**

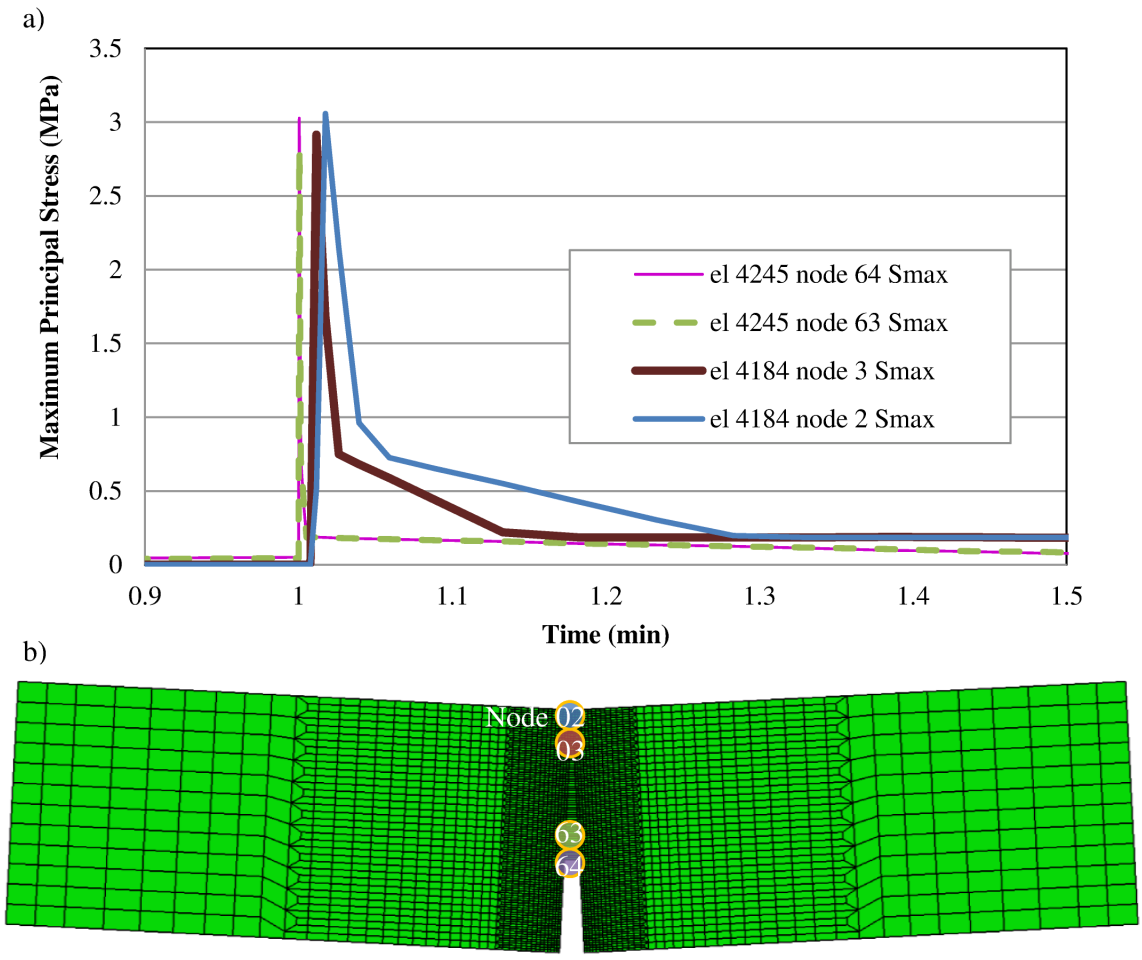


**Figure B-8 (a) Principal stresses changing with loading across (b) CZM elements along the fracture plane.**

# APPENDIX C. X-RAY CT IMAGING AND ANALYSIS

## C.1. X-ray CT Scanned Samples

### C.1.1. Beckman Institute Sample

Initially, a small piece of FFC (5.8 mm x 25.5 mm slice cut from the field-cast flowable fibrous concrete) was x-rayed and a 3D reconstructed image was created at the Beckman Institute Imaging Lab. These preliminary x-ray images demonstrated that fibers could be viewed but the contrast difference would make identification difficult, as illustrated in Figure C-1.

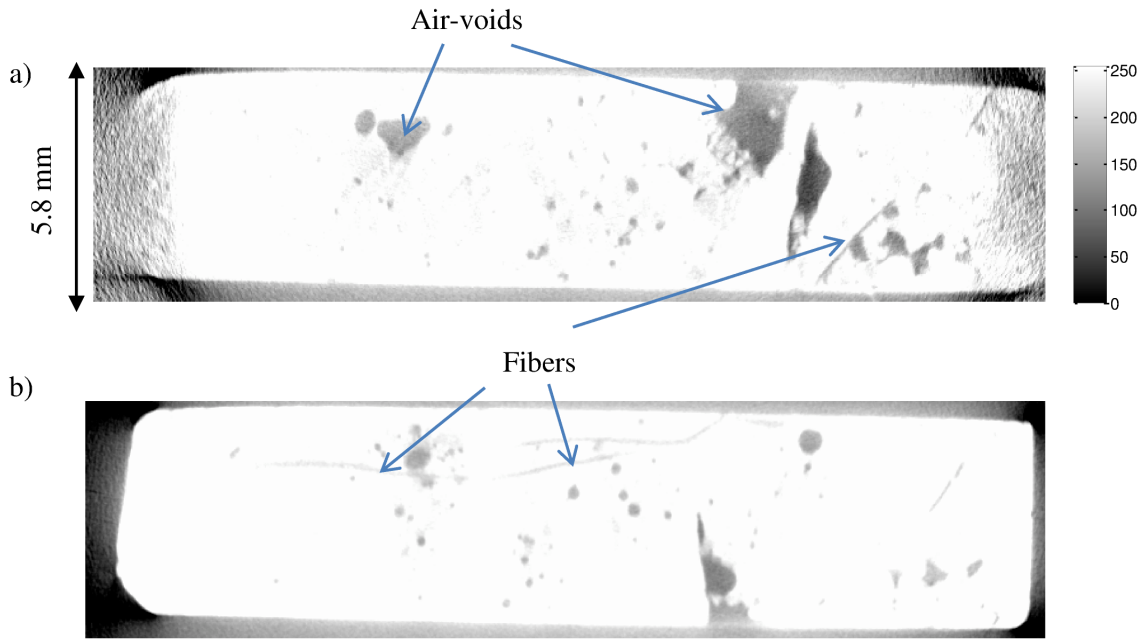


**Figure C-1 Images from Xradia Bio MicroXCT-400 of slice (a) 110 and (b) 200.**

### C.1.2. North Star Imaging Sample

The sample sent to North Star Imaging was a full (not tested in fracture) 50x50x197 mm beam specimen of FFC cut from the center of a 5 cm cast plate. Due to miscommunication on the cost for scanning at North Star Imaging, the results of this x-

ray sample were not returned. However screen-caps of the scanned image shown in Figure C-2 revealed an improved contrast to aid in identifying the synthetic fibers inside.

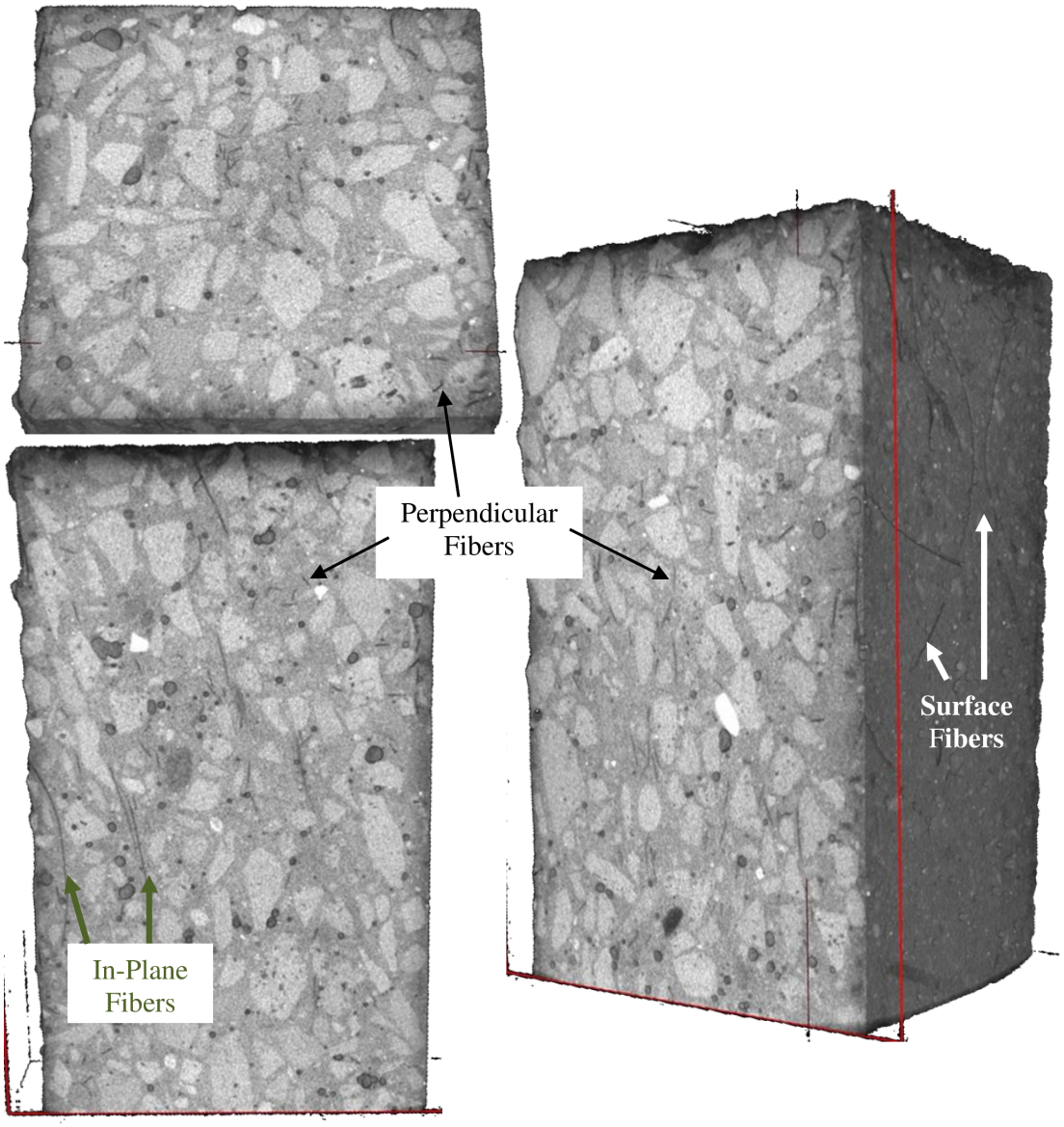


**Figure C-2 Screen-caps from North Star Imaging X-ray CT sample.**

C.1.3. Texas A&M University Sample

A 10 cm diameter field core sample (5 cm thickness), taken from the farthest west and center slab of the 1.1 m joint section in Figure A-14, was sent to the x-ray scanning laboratory at Texas A&M University as they typically scan similarly sized asphalt cores

(Masad et al. 2002). Images from the x-ray scanning may be ideal for identifying air void content, yet identification of any fibers inside the concrete was not plausible at this time, see Figure C-3.

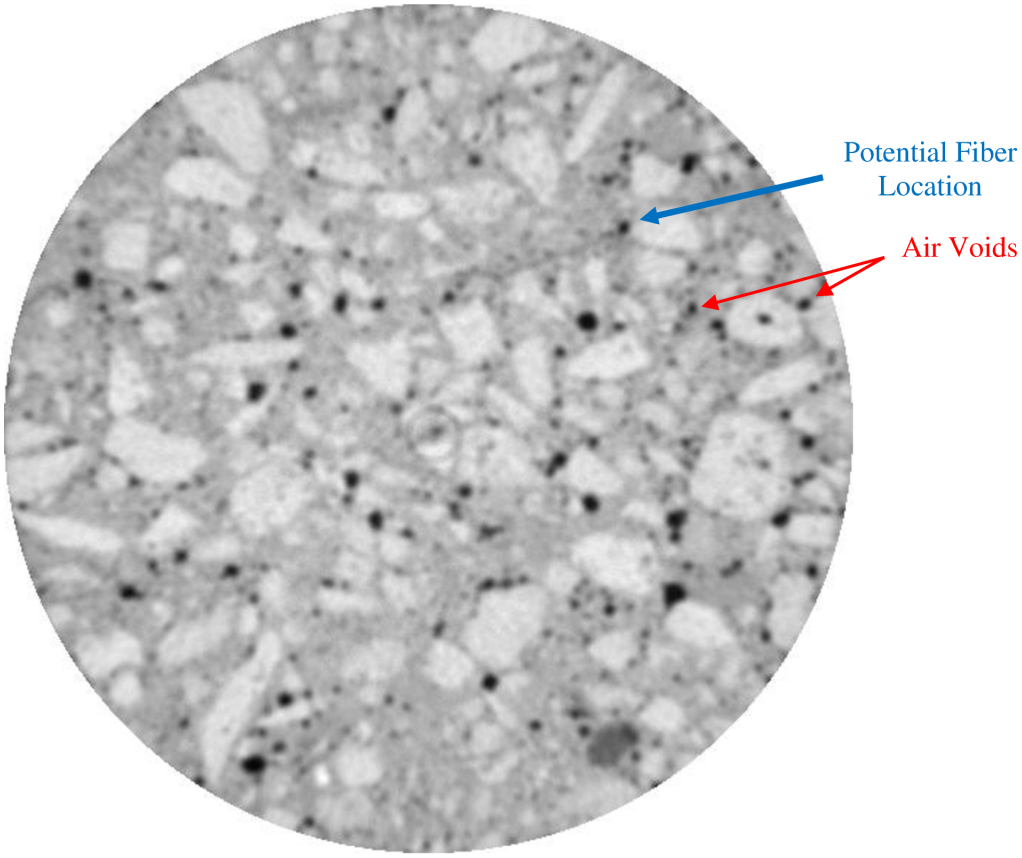


**Figure C-3 Slice 8 from Texas A&M x-ray scanned core sample.**

C.1.4. Washington State University sample

Finally, the x-ray scanning at Washington State University was selected as preliminary imaging showed the potential to identify fibers, similar to screen-caps from North Star Imaging. A total of 10 half-beams and 2 core samples were scanned at Washington State University (WSU). The settings utilized for the scanning machine (Nega and Muhunthan 2010) are listed in Table C-1 and adjustments on voltage and amperes were made to improve special resolution for each sample as listed in Table C-2. Examples of some of

the reconstructed sliced images from the WSU samples shown in Figure C-4 illustrate the range of brightness and contrast found.

**Table C-1 X-ray Settings for All WAX-CT Samples**

| | | | |
|---|---|---|---|
| Pixel Intensity | x-ray off | 623 | |
| | x-ray on | 3400 to 3600 | |
| Default Settings | direct beam to scatter ratio | 50 | |
| | ring removal value | 0.85 | |
| Image Resolution | detector size | 480 x 384 | pixels |
| | detector resolution | 0.508 | |
| | pixel spacing on detector | 127 | micrometers |
| | slice thickness | 324 | micrometers |
| Exposure Time | seconds/rotated position | 2.39 | |
| | minutes total time acquired | 17.3 | |
| | computed frames/sec | 0.0337 | |

**Table C-2 Specific X-Ray Settings Used for Each WAX-CT Sample**

| Scan Date | Sample ID | Voltage (kV) | Ampere (mA) | Spatial Resolution (micrometers) | Average Frames Acquired | Total Frames | Total Slices |
|---|---|---|---|---|---|---|---|
| July 2010 | XY1 | 380 | 1.5 | 79 | 15 | ND | 356 |
| July 2010 | XY2 | 380 | 1.5 | 79 | 15 | ND | 353 |
| 10/9/2010 | BT14a | 360 | 1.5 | 74 | 15 | 415 | 370 |
| 10/9/2010 | BT14b | 360 | 1.5 | 74 | 15 | 415 | 370 |
| 10/9/2010 | BT13a | 360 | 1.5 | 74 | 15 | 415 | 366 |
| 10/9/2010 | BT13b | 360 | 1.5 | 74 | 15 | 415 | 370 |
| 10/9/2010 | BT9a | 360 | 1.5 | 74 | 15 | 415 | 370 |
| 10/9/2010 | BT9b | 360 | 1.5 | 74 | 15 | 415 | 361 |
| 10/9/2010 | Strux6a | 360 | 1.5 | 74 | 15 | 435 | 366 |
| 10/9/2010 | Strux6b | 360 | 1.5 | 74 | 15 | 415 | 368 |
| July 2010 | Core1 | 390 | 1.5 | 55 | 15 | 751 | 179 |
| July 2010 | Core2 | 390 | 1.5 | 55 | 15 | 751 | 229 |

ND = not determined.

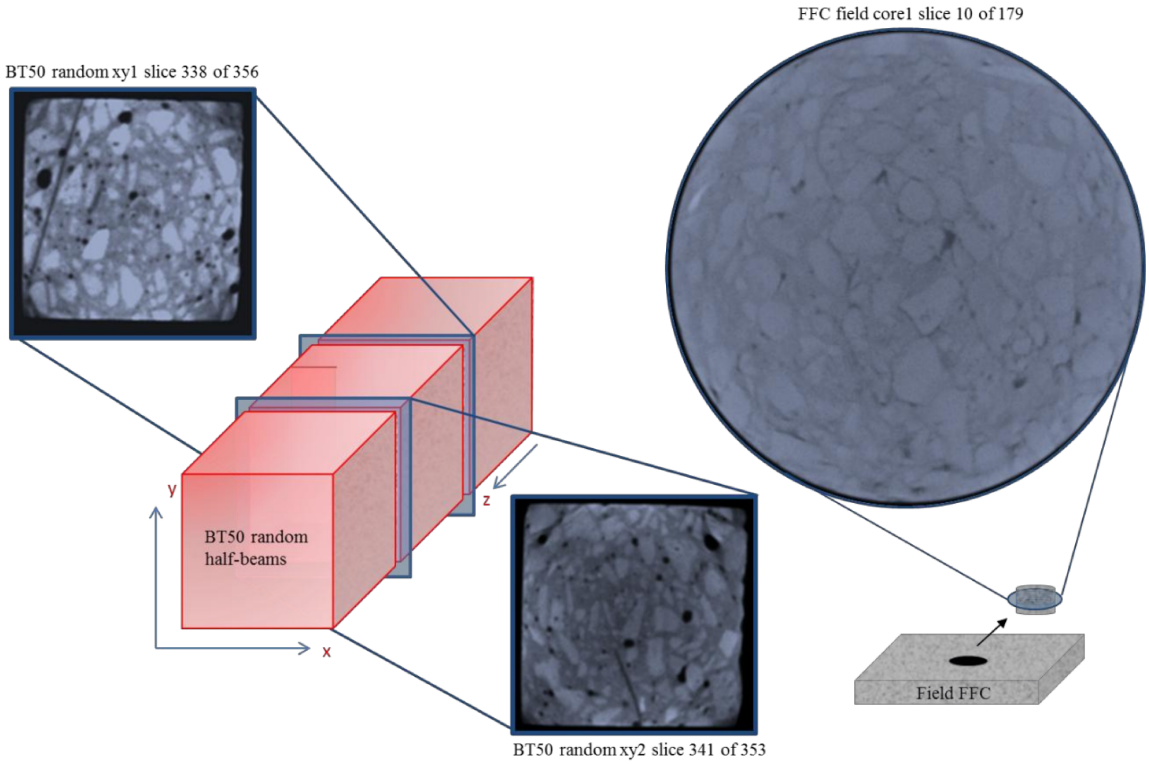


**Figure C-4 Example x-ray sliced (xy plane) images for the fracture specimen half-beams and field core.**

## C.2. Example Image Analyses

### C.2.1. 2D Stereology with MATLAB®

By using the Image Analysis Toolbox in MATLAB® on 2D sliced imaged from the CT scan, automatic threshold functions can also be applied to separate particles based on length, volume and connectivity. These tools are useful in identifying and separating the individual fibers within the concrete. Using raw image slices in the xy plane, the following program results in the image post-processing steps shown in Figure C-5.

```
%% Read Image
I = imread('xy0153.tif')
%% Inverted Image
I=imcomplement(I);
%% Rotate and Crop
Irot=imrotate(I,90.5);
Bpx=222;
Tpx=62;
```

```
Icr=imcrop(Irot,[54 Tpx 169 (Bpx-Tpx)]);
%% Otsu Grayscale Threshold
level=graythresh(Icr);
BWall = im2bw(Icr,level*1.1);
%% Remove Large Connected Objects & Edges
CC = bwconncomp(BWall);
[L, NUM] = bwlabel(BWall);
S=regionprops(CC,'Area');
large=find([S.Area]<100);
BWreg=ismember(L,large);
%% Eccentricity Threshold
CC2 = bwconncomp(BWreg);
[L2, NUM2] = bwlabel(BWreg);
S2=regionprops(CC2,'Eccentricity');
line=find([S2.Eccentricity]>=0.7);
BWln=ismember(L2,line);
%% Find Skeleton of Objects
BW2=bwmorph(BWln,'skel');
%% Remove Small Objects
BWmin=bwareaopen(BW2,15);
%% Run Hough Function
[H,T,R] = hough(BWmin);
P = houghpeaks(H,9,'threshold',ceil(0.3*max(H(:))));
%compute and plot hough lines
lines = houghlines(BWmin,T,R,P,'FillGap',1,'MinLength',15);
imshow(BWmin), hold on
max_len = 0;
for k = 1:length(lines)
  xy = [lines(k).point1; lines(k).point2];
  plot(xy(:,1),xy(:,2),'LineWidth',2,'Color','green');
  % Plot beginnings and ends of lines
  plot(xy(1,1),xy(1,2),'x','LineWidth',2,'Color','yellow');
  plot(xy(2,1),xy(2,2),'x','LineWidth',2,'Color','red');
  % Determine the endpoints of the longest line segment
  len = norm(lines(k).point1 - lines(k).point2);
  if ( len > max_len)
    max_len = len;
    xy_long = xy;
  end
end
hold off
```

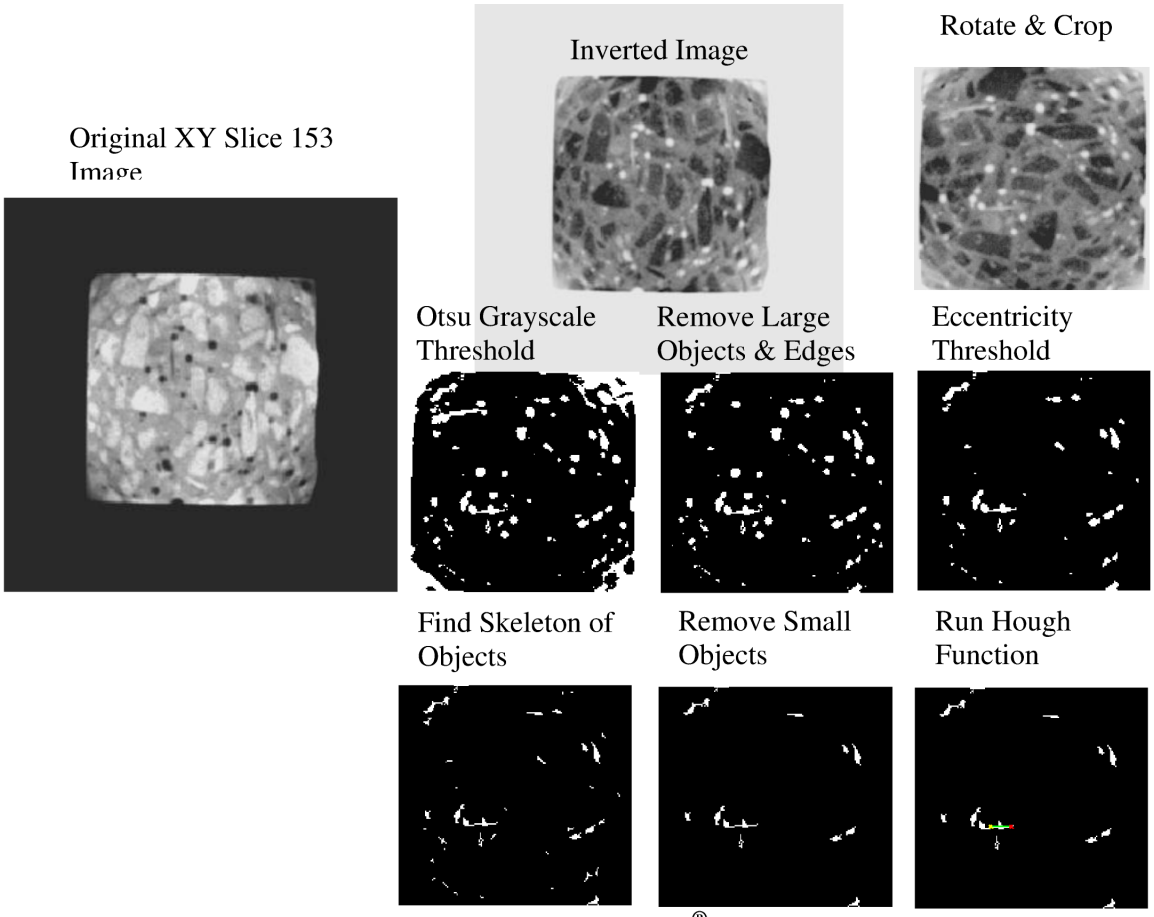


**Figure C-5 Image post-processing using MATLAB® on xy plane.**

C.2.2. Alternative 2D imaging post-processing function for Matlab®

Using slices in the xz plane, the following alternative program results in the image post-processing steps shown in Figure C-6.

```
%% read image and show image
I = imread('slice00084.bmp');
imshow(I)
axis on;
title('Original Image');
%% Rotate and Crop
Irot=imrotate(I,-0.4,'crop');
[m,n] = size(Irot);
Icr=imcrop(Irot,[60 6 165 m]);
%% Otsu Grayscale Treshold
level=graythresh(Icr);
BW = im2bw(Icr,level*0.8);
bw1=imextendedmax(Icr,110);
bw2=imextendedmax(Icr,140);
G=bw2-bw1;
```

```
%% Invert Image
BW2=imcomplement(BW);
%% Remove Large Connected Objects & Edges
open1 = imopen(G,strel('diamond',1));
open2 = imopen(G,strel('diamond',3));
rad2 = imsubtract(open1,open2);
CC = bwconncomp(BW2);
[L, NUM] = bwlabel(BW2);
S=regionprops(CC,'Area');
large=find([S.Area]<800);
BWreg=ismember(L,large);
%% Eccentricity
CC2 = bwconncomp(BWreg);
[L2, NUM2] = bwlabel(BWreg);
S2=regionprops(CC2,'Eccentricity');
line=find([S2.Eccentricity]>=0.8);
BWln=ismember(L2,line);
%% Skeleton
BWs=bwmorph(BWln,'skel');
%% Hough Transform
[H,T,R] = hough(BWs);
%subplot(2,1,2,'replace');
imshow(imadjust(mat2gray(H)),'XData',T,'YData',R, 'InitialMagnification','fit');
title('Hough Transform of Original Image');
xlabel('\theta'), ylabel('\rho');
colormap('jet');
axis on, axis normal, hold on;
P = houghpeaks(H,5,'threshold',ceil(0.7*max(H(:))));
x = T(P(:,2));
y = R(P(:,1));
plot(x,y,'s','color','white');
%% Run Hough Function
lines = houghlines(BWs,T,R,P,'FillGap',5,'MinLength',50);
figure; imshow(BWs), hold on
max_len = 0;
for k = 1:length(lines)
  xy = [lines(k).point1; lines(k).point2];
  plot(xy(:,1),xy(:,2),'LineWidth',2,'Color','green');
  % Plot beginnings and ends of lines
  plot(xy(1,1),xy(1,2),'x','LineWidth',2,'Color','yellow');
  plot(xy(2,1),xy(2,2),'x','LineWidth',2,'Color','red');
  % Determine the endpoints of the longest line segment
  len = norm(lines(k).point1 - lines(k).point2);
  if ( len > max_len)
    max_len = len;
    xy_long = xy;
  end
end
```

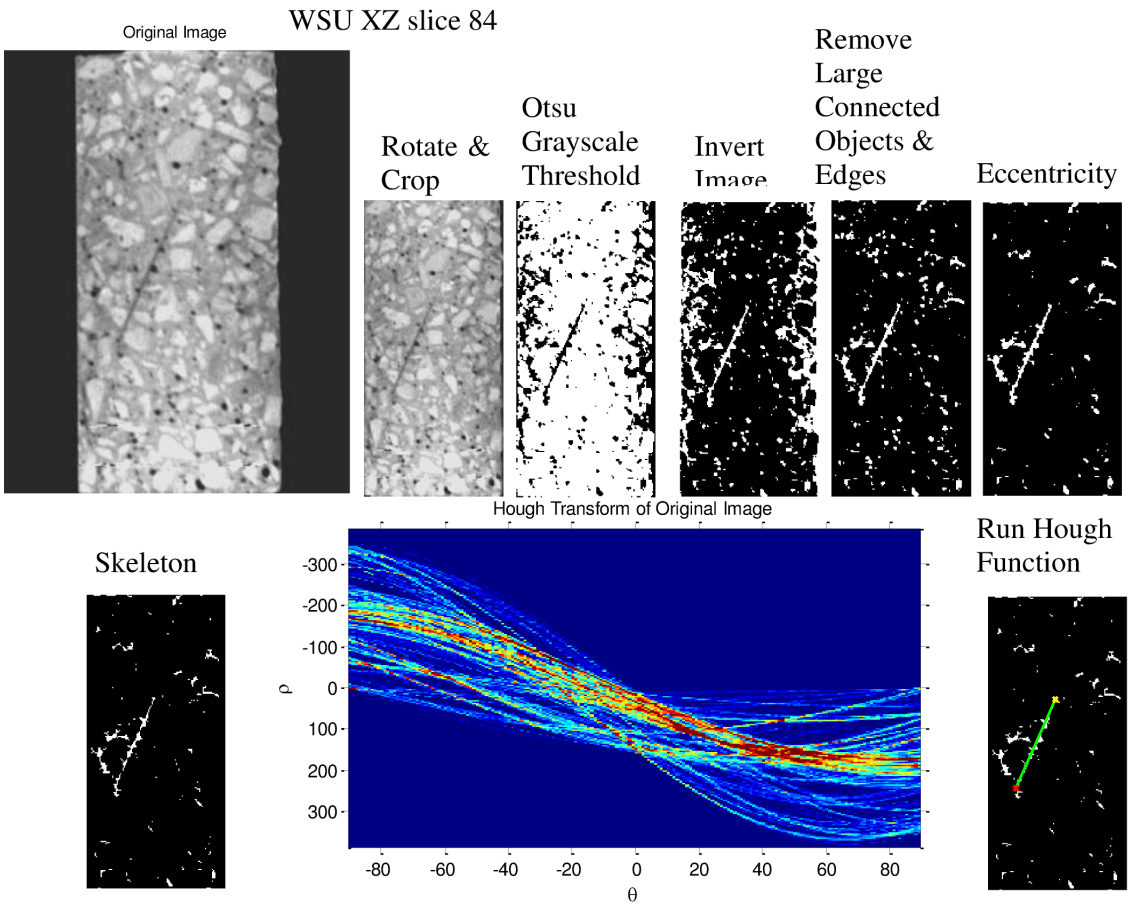


**Figure C-6 Image post-processing using MATLAB® on xz plane.**

C.2.3. Locating Fibers with IMARIS®

The Bitplane IMARIS® software was selected to image the FFC in three dimensions and provided the capability to filter based on shape (ellipsoid) as well as individual selection of objects once thresholded. The threshold and filter values were selected manually and the final selected values are shown in Table 4-3. The steps for locating the fibers inside the FFC sample labeled BT14a were:

- Upload stacked .tiff files (Figure C-7), in this case a 16-bit image
- Crop image voxels in 3 planes (Figure C-8)
- Scale image volume for 0.324 µm square voxel size (Figure C-9)
- Invert reconstructed image volume (Figure C-10)
- Use background contrast threshold to create object surfaces (Figure C-11)

- Additional filtering can be performed based on prolate ellipsoid, sphericity, object volume, or ellipsoid C-axis length.
- Further manipulation of fiber objects can be made by manually cropping away any attached air voids and grouping of multiple fiber segments to make one continuous fiber object.

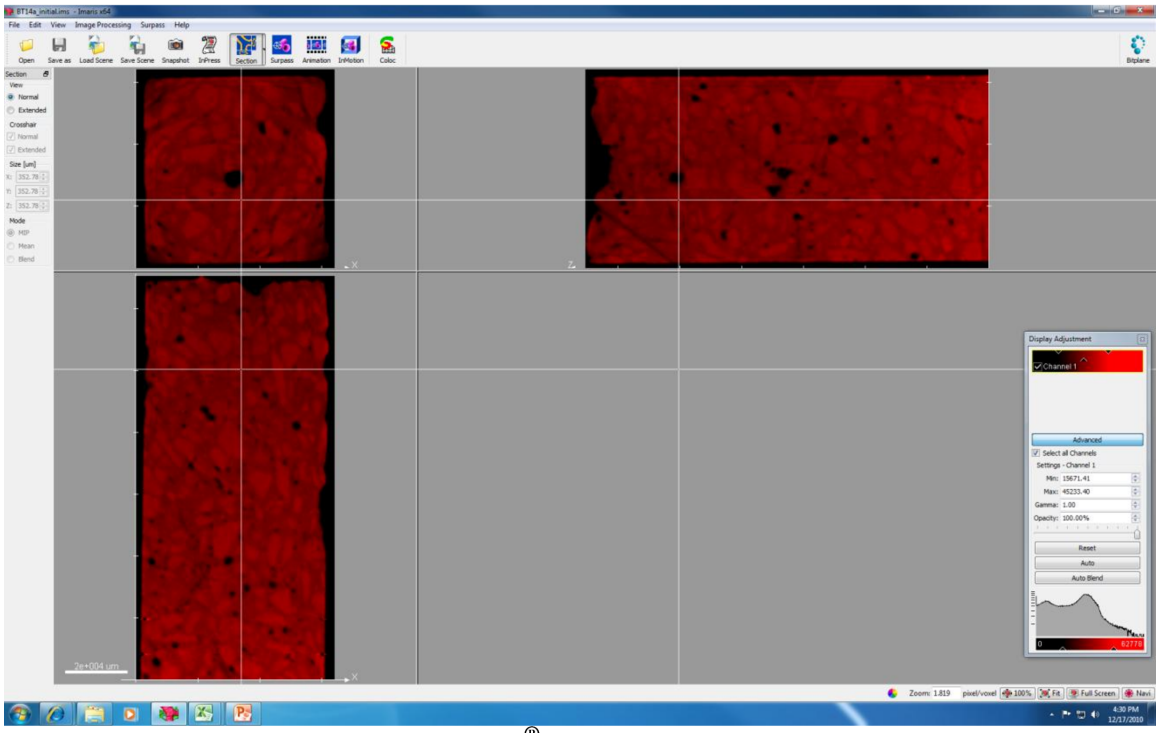

**Figure C-7 Slices loaded into IMARIS® and viewed in all three planes.**

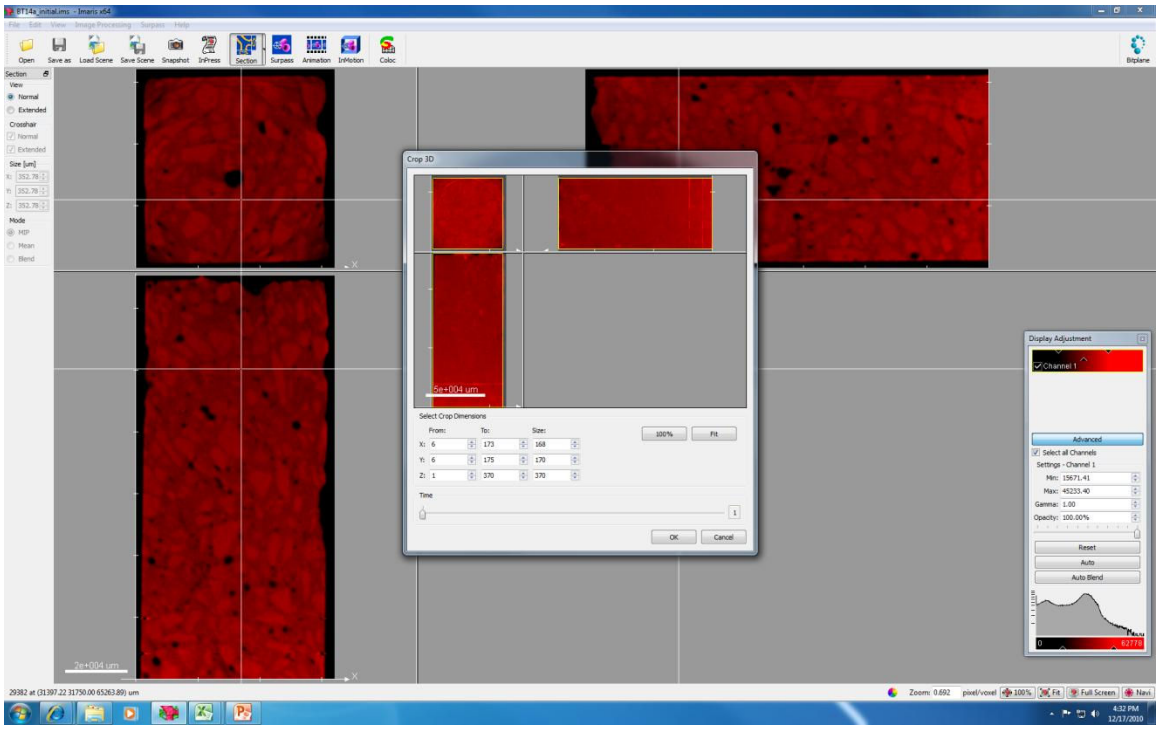

**Figure C-8 3D crop of images.**

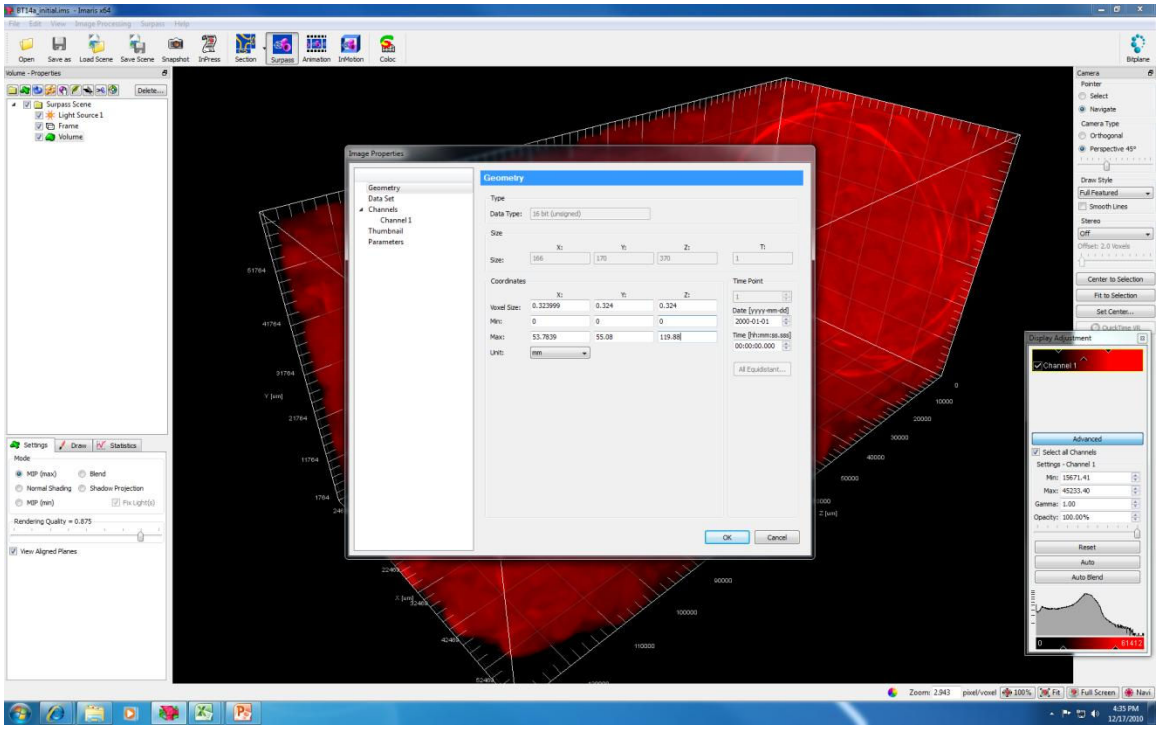

**Figure C-9 Scaling of images to 0.324 µm square voxel size.**

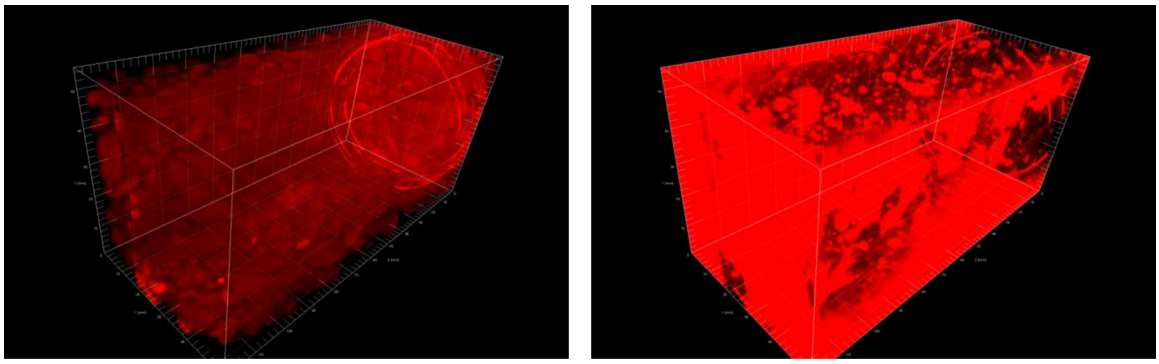

**Figure C-10 Image of BT14a rendered in 3d perspective view and then after inverting.**

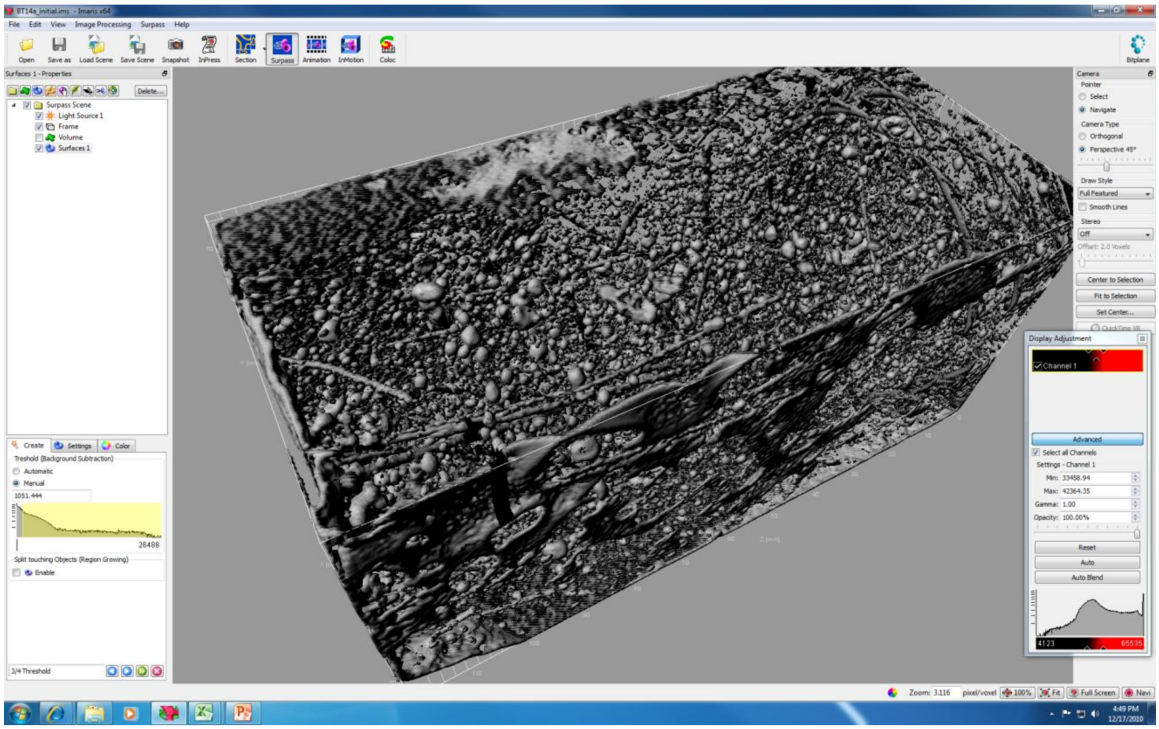

**Figure C-11 Surface created using the IMARIS® software after background contrast threshold 1051.44.**

For the fit ellipsoidal object shapes, filtering shown in Figure C-12 first was made to the background threshold objects based on the minimum length of the longest axis (C-axis), set to 2 mm to remove small air voids or other objects from Figure C-11.

Further manipulation was performed by manually cropping away any attached air voids using the “cut” tool. Also several short fibril objects which visually appeared in all 3

dimensions to be part of a larger whole fiber were copied as a grouped surface. The statistical information from the program was saved for each individual whole fiber object or grouped fiber components.

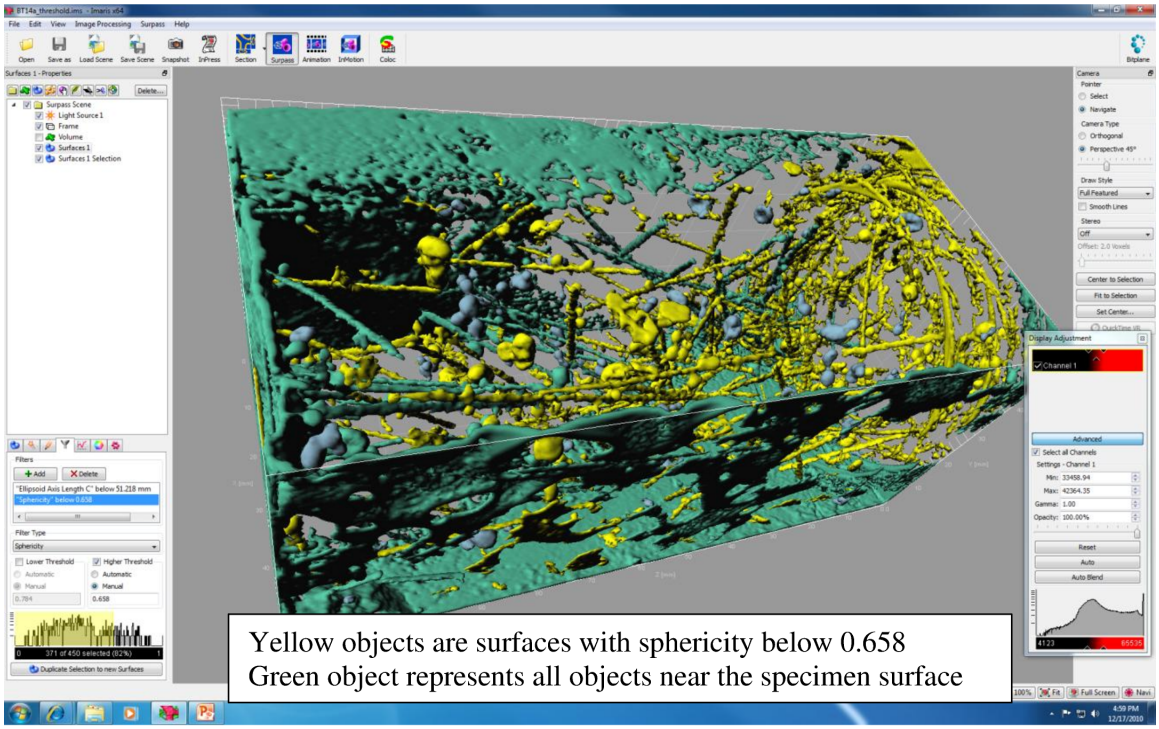


**Figure C-12 Image of object surfaces after applying a filter on the ellipsoid axis C length to be between 2 and 30 mm.**

## C.3. Computing Statistics on Fibers Properties

### C.3.1. 2D Orientation

The fiber's orientation projected on different 2D planes (e.g. xy, xz, and yz) can be computed. The following example of fiber orientation in each 2D plane was made using the BT50 sample cut from the top of a cast 15 cm beam placed with directional flow.

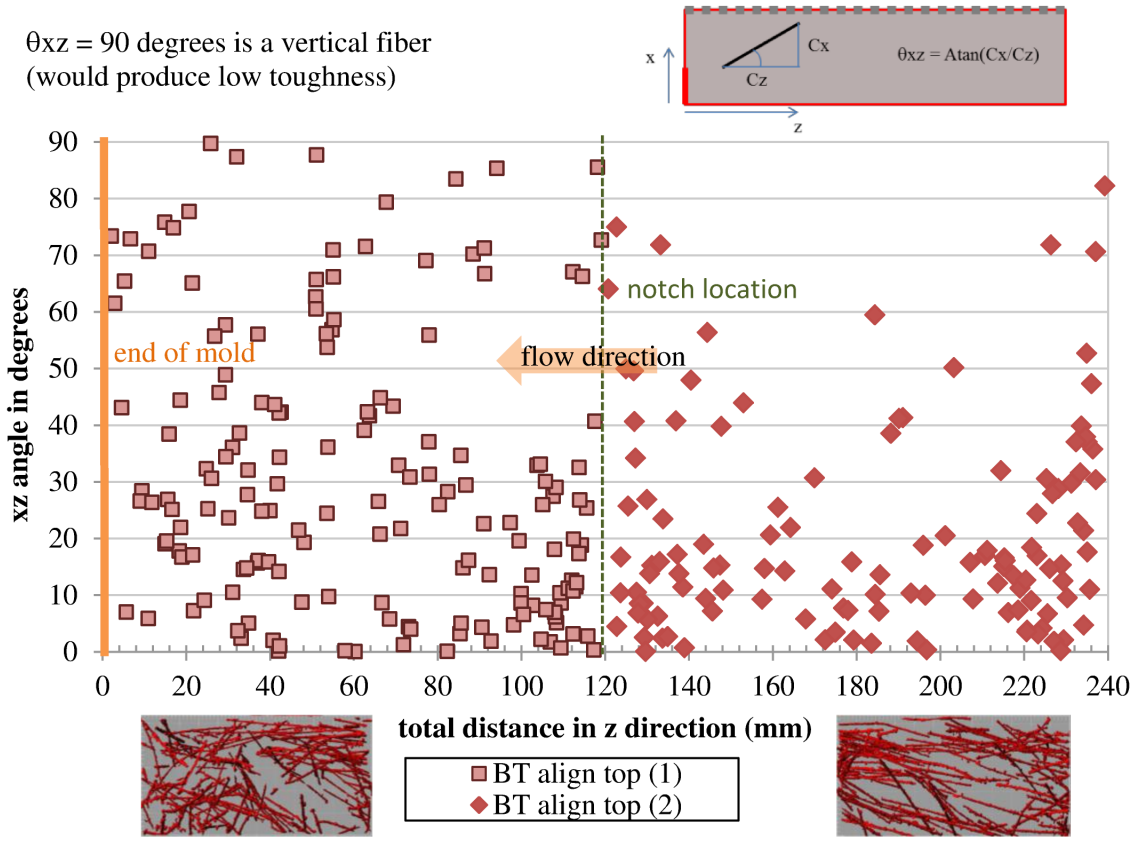


**Figure C-13 Example of the fiber orientation and centroid location within the xz plane.**

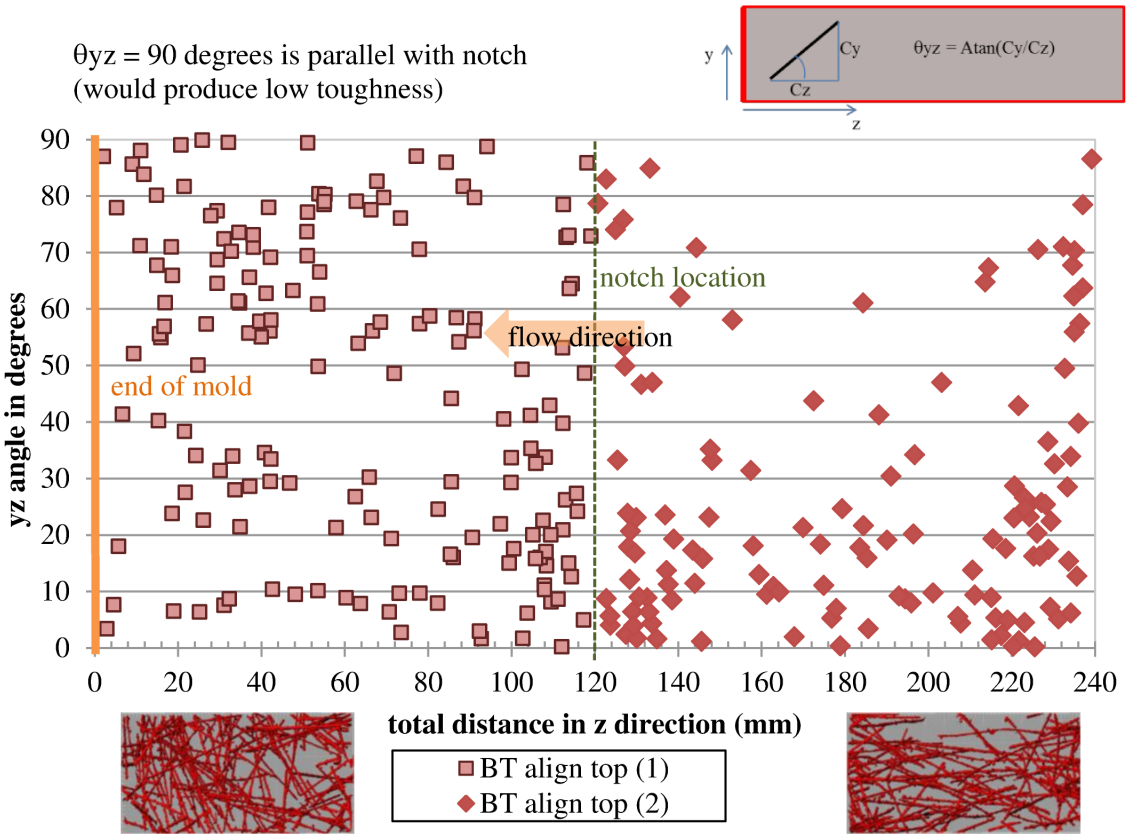


**Figure C-14 Example of the fiber orientation and centroid location within the yz plane.**

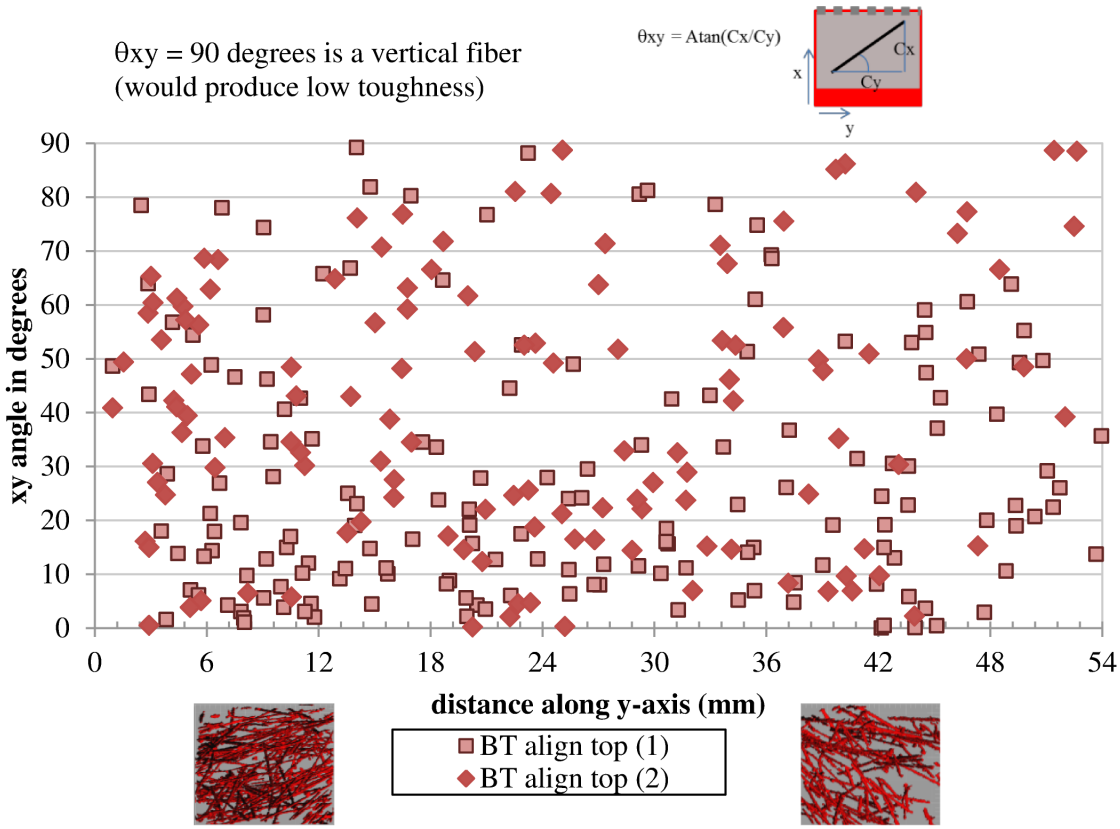


**Figure C-15 Example of the fiber orientation and centroid location within the xy plane.**

C.3.2. 3D Polar Orientation

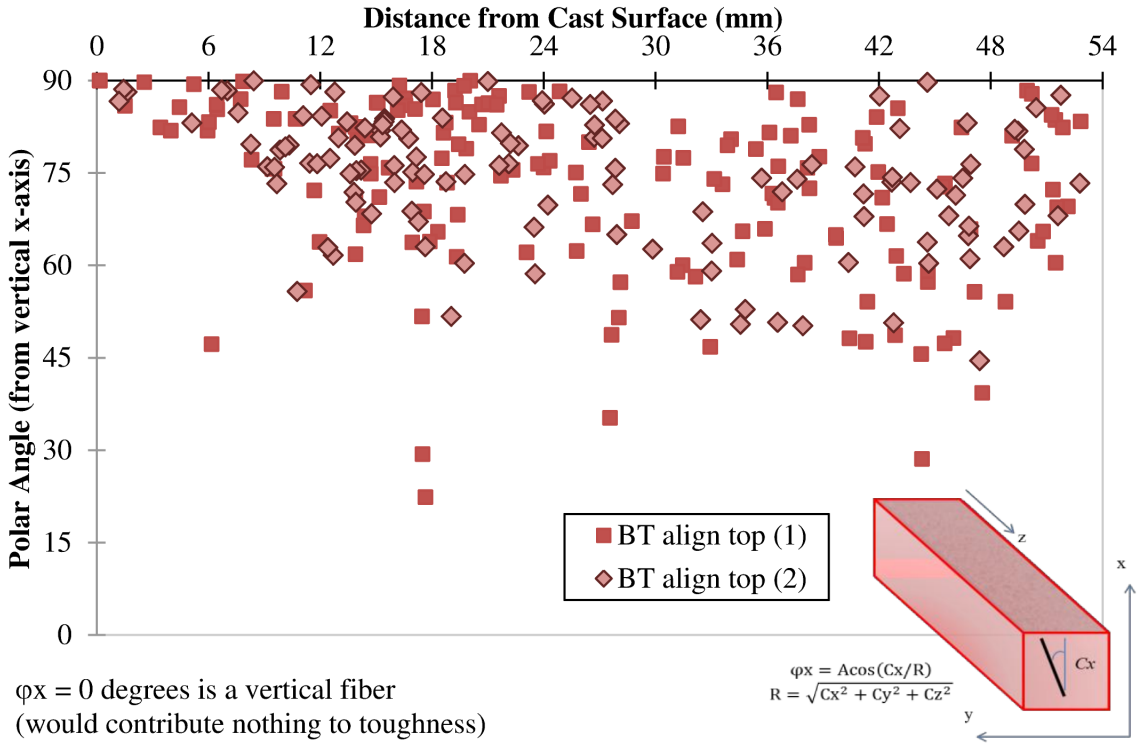


**Figure C-16 Polar angle of fibers versus the centroid location from the cast surface.**

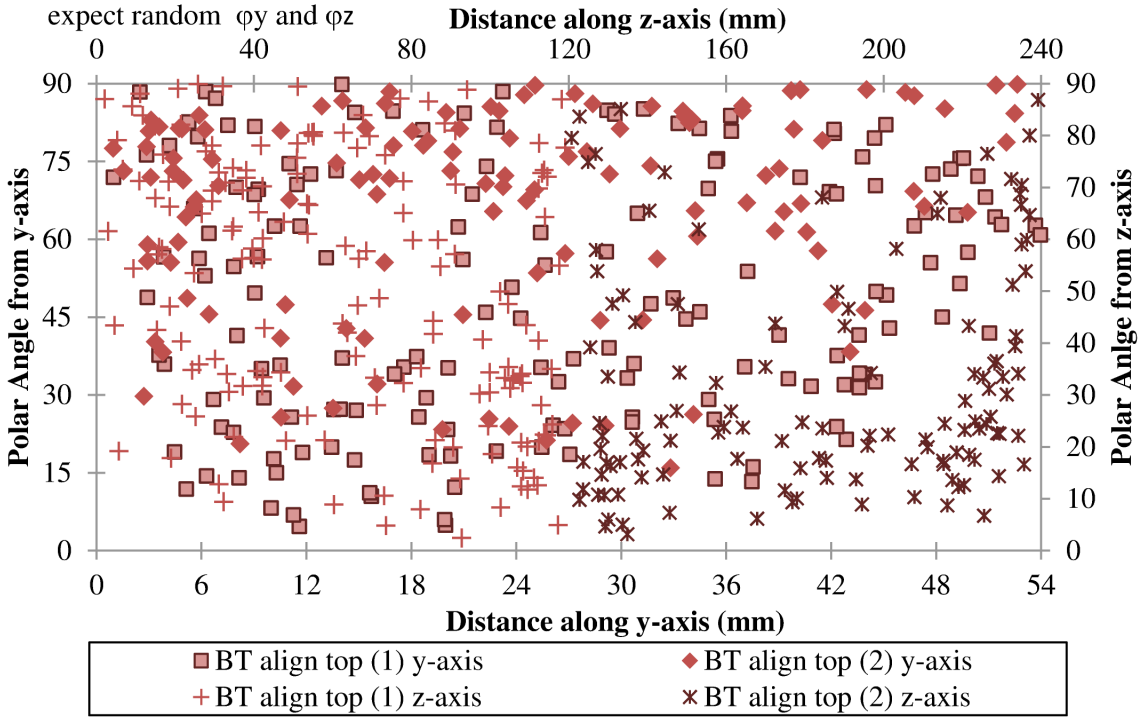


**Figure C-17 Polar angle distribution in y and z planes for 5 cm BT mixture beam cut from the top cast surface of a 15 cm beam.**

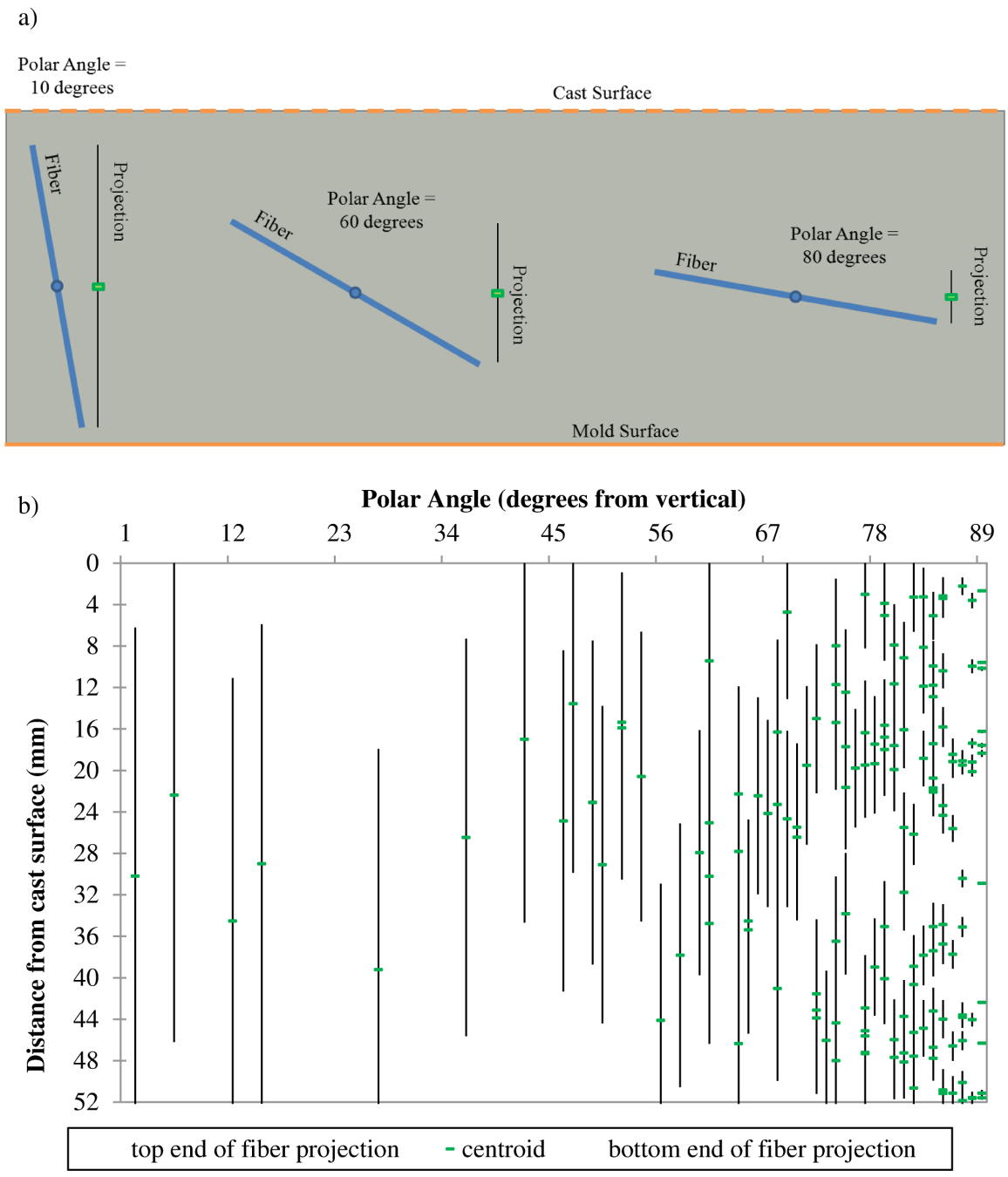


**Figure C-18 Projected fiber lengths and centroids are shown a) schematically and b) based on the randomly placed 5 cm plate specimen at corresponding polar angles and distance from the cast surface.**